Hybrid Nanoparticles for Anticancer Drug Delivery

Joseph Della Rocca

A dissertation submitted to the faculty of The University of North Carolina at Chapel Hill in partial fulfillment of the requirements for the degree of Doctor of Philosophy in the Department of Chemistry

Chapel Hill

2012

Approved by:

Dr. Wenbin Lin

Dr. Cynthia K. Schauer

Dr. Michel Gagné

Dr. Leaf Huang

Dr. Andrew Z. Wang

Abstract:

Joseph Della Rocca: Hybrid Nanoparticles for Anticancer Drug Delivery

(Under the Direction of Wenbin Lin)

Nanoparticle-based anticancer has the potential to improve cancer therapy as they generally show greater efficacy with less toxicity than their small molecules counterparts. In this work, the synthesis, characterization, *in vitro*, and *in vivo* evaluation of nanoparticle platforms to deliver platinum anticancer drugs are discussed.

First, cisplatin-containing co-condensed silica nanoparticles were developed. These nanoparticles could deliver up to 30 wt% cisplatin and could be targeted to cancer cells by the surface attachment of appropriate ligands. The targeted nanoparticles had comparable efficacy to cisplatin *in vitro*. A new nanoparticle platform, known as polysilsesquioxanes (PSQ) was developed to deliver the platinum anticancer drugs cisplatin and oxaliplatin. These nanoparticles have remarkably high drug loading, up to 47 wt% oxaliplatin and 42 wt% cisplatin, respectively, and can selectively release their cargos in the tumor environment. Both PSQ nanoparticles were functionalized with a polyethylene glycol (PEG) shell. *In vivo* evaluations against multiple xenograft models of pancreatic or lung cancers demonstrated that PSQ nanoparticles had comparable or better efficacy than oxaliplatin or cisplatin. Further development of all three nanoparticle platforms is ongoing to fully realize their clinical potential.

Acknowledgements

This dissertation would not have been possible without the support of many people. I would first like to thank my advisor, Dr. Wenbin Lin, for the opportunity to work in his lab on new and exciting projects and all of the invaluable discussions that we have had about my research over the last five years. Without his direction and constant support, I would have never completed all of the work that I did. I would also like to thank the other members of my committee, Dr. Cynthia Schauer, Dr. Michel Gagné, Dr. Leaf Huang, and Dr. Andrew Z. Wang for the consideration of this dissertation.

I'd also like to thank the present and former members of the Lin group for their help with these projects. I would like to especially thank Rachel Huxford-Phillips, Erica Comstock-Duggan, and Stephanie Kramer for carrying out the majority of the *in vitro* experiments conducted and for supporting the other aspects of my research. The UNC Animal Studies Core performed the majority of the *in vivo* experiments. I would also like to thank Liqing (Sam) Ma, B.J. Rieter, and Kathryn Taylor-Pashow for mentoring me at the onset of my career. Additionally, I would like to thank the undergraduate students that worked under me, Katie Weng, Asif Khan, and Honorio Lara, for their help. Finally I would like to thank the National Science Foundation, National Cancer Institute and the Carolina Center for Nanotechnology Excellence for funding.

Finally, I would not have made it to this point my life without the support of my family, especially my parents Vincent and Pamela Della Rocca. They have provided me with

the foundation that has shaped me into the person I am today and have supported me in all aspects of my life.

Table of Contents

Page

List of Tables

List of Figures

List of Abbreviations

2.1	Polysilsesquioxane nanoparticle containing an oxaliplatin derivative
3.1	Co-condensed silica nanoparticle with cisplatin and 5 molar equivalents of TEOS
3.2	Co-condensed silica nanoparticle containing cisplatin and 10 molar equivalents of TEOS
3.3	Co-condensed silica nanoparticle containing cisplatin and 15 molar equivalents of TEOS
3.4	Co-condensed silica nanoparticle containing cisplatin and 20 molar equivalents of TEOS
3.5	Co-condensed silica nanoparticle containing cisplatin and 5 molar equivalents of TEOS
3.6	Co-condensed silica nanoparticle containing cisplatin and 10 molar equivalents of TEOS
4.1	Polysilsesquioxane nanoparticle containing a cisplatin derivative
°C	degrees Celsius
α	alpha
λ_{ex}	wavelength of exciation
μ	micro-

A549	human lung adenocarcinoma cell line
AA	Anisamide
ACN	acetonitrile
AOT	bis(1-ethylhexyl)sulfosuccinate
APEG-**2.1**	an anisamide targeted, pegylated version of nanoparticle **2.1**
APEG-rhod-**2.1**	an anisamide targeted, pegylated version of nanoparticle rhod-**2.1**
APEG2k-**4.1**	an anisamide targeted, pegylated version of nanoparticle **4.1**
ASPC-1	human pancreatic ductal adenocarcinoma cell line
ATCC	American Type Culture Collection
BxPC-3	human pancreatic ductal adenocarcinoma cell line
BSA	Bovine serum albumin
c(RGDfK)	cyclic(arginine-glycine-aspartic acid-phenylalanine-lysine)
Dach	1,2-(*R*,*R*)-diaminocyclohexane
DACH-Si	$Pt(dach)Cl_2(triethoxysilylpropyl\ succinate)_2$
DLD-1	human colon adenocarcinoma cell line
DLS	Dynamic Light Scattering
DMF	Dimethylformamide

DMSO	Dimethylsulfoxide
DSCP	disuccinato cisplatin
DSCP-Si	*c,c,t*-$Pt(NH_3)_2Cl_2$(triethoxysilylpropyl succinate)$_2$
EDC	1-Ethyl-3-(3-dimethylaminopropyl) carbodiimide hydrochloride
EDS	Energy Dispersive X-ray Spectroscopy
FITC	Fluorescein isothiocyanate
g	gram
Gy	Gray
HBTU	*O*-(benzotriazol-1-yl)-1,1,3,3-tetramethyluronium hexafluorophosphate
hr	hour
HRTEM	High Resolution Transmission Electron Microscopy
HT-29	Human colon carcinoma cell line
IC_{50}	Inhibitory Concentration 50%
ICP-MS	Inductively Coupled Plasma-Mass Spectrometry
i.v.	intravenous
k	kilo-
L	Liter

m	milli-
M	Molar
min	minute
MOF	Metal Organic Framework
MTD	Maximum Tolerated Dose
MW	Molecular Weight
n	nano
NCI-H460	human large cell lung carcinoma cell line
NHS	N-hydroxysuccinimde
NMOF	nanoscale metal organic framework
NMR	Nuclear Magnetic Resonance
PBS	Phosphate Buffered Saline
PC-3	human prostate adenoncarcinoma cell line
PDI	Polydispersity Index
PEG	Polyethylene Glycol
PEG-**2.1**	a PEG coated version of nanoparticle **2.1**
PEG-rhod-**2.1**	a PEG coated version of nanoparticle rhod-**2.1**

PEG2k-**4.1**	a PEG (MW 2000) coated version of nanoparticle **4.1**
PEG5k-**4.1**	a PEG (MW 5000) coated version of nanoparticle **4.1**
PSQ	Polysilsesquioxane
R	a generic organic group
RGD-**2.1**	a cRGD targeted version of nanoparticle **2.1**
RGD-rhod-**2.1**	a cRGD targeted version of nanoparticle rhod-**2.1**
RGD-**3.6**	a cRGD targeted version of nanoparticle **3.6**
RGD-**4.1**	a cRGD targeted version of nanoparticle **4.1**
Rhod-**2.1**	a rhodamine containing version of nanoparticle **2.1**
r.t.	room temperature
SEM	scanning electron microscopy
$T_{1/2}$	half-life
TEA	triethylamine
TEM	Transmission Electron Microscopy
TEOS	tetraethylorthosilicate
TGA	Thermogravimetric Analysis
Triton X-100	t-octylphenoxypolyethyoxyethanol

W	water to surfactant ratio
X	multiplied (or enhanced) by
Zavg	Intensity-weighted cumulative nanoparticle diameter

Chapter 1:

Hybrid Nanoparticles for Anticancer Drug Delivery

1.1 Introduction

Cancer remains one of the deadliest diseases known to man, causing significant mortality and morbidity and costing hundreds of billions of dollars in healthcare expenses in the United States annually. Despite remarkable advances in our knowledge of the fundamental biology of cancer and the billions of dollars spent on drug research and development, there has not been a significant increase in overall patient survival for many types of cancer. A major reason for this dilemma is the lack of effective chemotherapeutic options. Over the past thirty years, the rate of new drug approvals has remained relatively constant (20-30 drugs annually). Most new approvals are reformulations, new applications, or new combinations of previously approved agents.[1] The treatment options for many cancers have remained nearly unchanged as a result of the lack of new drug approvals. Pharmaceutical development is limited by a number of factors including high research and development costs and regulatory barriers, but the lack of effective drug delivery vectors remains a major bottleneck. Many drug candidates identified through high throughput screenings do not possess sufficient solubility to be bioavailable,[2] and the biologically-derived agents (e.g., peptides, proteins, and siRNA) are degraded readily by endogenous enzymes in circulation. The currently approved agents, mostly small molecules, are limited by their nonspecific biodistribution, leading to dose-limiting side effects. There exists an

acute need to identify a method to make small molecule drugs more bioavailable, protect biologics from premature degradation, and increase tumor uptake of the agent while minimizing nonspecific uptake.

Nanoparticle-based chemotherapeutics are an emerging class of drug delivery systems which have the potential to revolutionize cancer chemotherapy. Broadly speaking, a nanoparticle- based chemotherapeutic (nanotherapeutic) consists of a therapeutic embedded within or attached to a nanoparticle matrix. A variety of nanocarriers have been developed to deliver a wide range of cancer chemotherapeutics.[3] Nanoparticles possess many advantages over conventional therapeutics such as extended systemic circulation times, increased tumor uptake due to the enhanced permeability and retention (EPR) effect, and targeted delivery to specific tissues with surface-conjugated ligands. Due to their size, nanotherapuetics cannot penetrate normal vasculatures and capillaries, leading to a lower nanoparticle dose to normal tissues such as skin, muscle, lungs, hearts and kidneys compared to small molecules. The clearance of nanotherapuetics generally occurs through the mononuclear phagocytic system (MPS), resulting in accumulation in the Kupffer cells of the liver and the macrophages of the spleen. This unique biodistribution generally results in lower systemic toxicity of nanotherapeutics. Additionally, nanoparticles can be engineered to incorporate multiple types of therapeutic or diagnostic agents, allowing for the synergistic therapeutic efficacy and real-time monitoring of therapeutic response. The promise of nanoparticle therapeutics is validated with the clinical success of multiple entities such as Doxil and Abraxane.[4]

The story of nanoparticle therapeutics cannot, however, be considered an unblemished success as clinically deployed nanotherapeutics have limitations. For example, Doxil has an improved safety profile, but not better efficacy, compared to doxorubicin.[5-6]

Abraxane shows improved efficacy compared to paclitaxel, but it is extremely expensive to manufacture and generally has not replaced paclitaxel clinically.[4, 7] Most nanocarriers can only be used to deliver drugs with specific properties (e.g., charge, hydrophobicity, etc) and have a fairly low threshold for drug incorporation, typically a few weight percent of active pharmaceutical ingredients (API). Most nanomedicines are in fact composed mostly of non-API components. The commercialization of nanotherapeutics is also hamstrung by high production costs and persistent manufacturing issues such as scalability to multi-kilogram batches and batch-to-batch consistency. The toxicological impact and biological persistence of many nanoparticles remain poorly investigated, posing long term issues from exposure to these materials.[8]

The nanoparticle platforms that have been extensively explored for biomedical applications are predominantly either purely inorganic or organic materials. The archetypical inorganic nanoparticles, quantum dots (QDs), are nanomaterials generally composed of elements from either groups II and VI or III and V.[9-13] They display unique optical properties, including sharp and symmetrical emission spectra, high quantum yields, broad absorption spectra, good chemical and photo-stability, and tunable size-dependent emission wavelengths.[11] As a result, they have been evaluated extensively for use as optical imaging probes both *in vitro* and *in vivo*. Another class of inorganic nanoparticles that have been evaluated for biomedical imaging applications are metal oxides, such as superparamagnetic iron oxide nanoparticles (SPIO). Iron oxide nanoparticles have been used as contrast agents for magnetic resonance imaging (MRI), and one formulation of SPIO has received FDA approval for clinical use.[14] Gold nanoparticles with controllable morphologies have been extensively used for biological imaging applications as they can be engineered to exhibit

strong absorption in the NIR region.[15-17] Gold nanoparticles have also been explored for photothermal therapy, where absorbed light by small gold nanoparticles (10-30 nm) is rapidly converted into thermal energy, leading to hyperthermia and cell death.

Purely organic nanoparticles have also found widespread use as imaging and therapeutic agents. Liposomes have been the most successful nanoparticle platform for biomedical applications, with several formulations clinically available.[18-19] These nanoparticles are composed of an aqueous core surrounded by a phospholipid bilayer and have been used to deliver a variety of therapeutic and imaging agents.[20-23] Surface modification of the lipid bilayer allows for long *in vivo* circulation times and targeting to specific regions.[24] There have been many reports on the use of polymeric hydrogel nanoparticles as delivery vehicles for imaging contrast agents and therapeutics.[25-35] Dendrimers and other hyper-branched organic polymers have also been extensively evaluated for their potential in imaging and drug delivery applications.[36-40]

Hybrid nanoparticles are composed of both inorganic and organic components that can not only retain the beneficial features of both inorganic and organic nanomaterials, but also possess unique advantages over the other two types. For example, the ability to combine a multitude of organic and inorganic components in a modular fashion allows for systematic tuning of the properties of the resultant hybrid nanomaterial. This chapter will cover two major classes of hybrid nanomaterials, namely silica-based nanomaterials and nanoscale metal-organic frameworks (NMOFs), which have been recently explored for therapeutic applications. While many nanoparticle platforms may be considered hybrid, we have chosen to restrict our discussion to silica-based nanomaterials and NMOFs that are closely examined in our laboratory for biomedical applications.

There are two major types of silica-based hybrid nanomaterials, solid silica particles and mesoporous silica nanoparticles (MSNs). Unlike solid silica particles, MSNs exhibit many unique properties such as high surface areas, tunable pore sizes, and large pore volumes. Imaging or therapeutic cargoes can either be directly incorporated in the silica matrix or grafted to the outer surface of the solid silica particles. MSNs can be functionalized with imaging or therapeutic agents in several ways, including loading of cargo into the pores, covalent grafting, and co-condensation of siloxy-derived cargoes.

NMOFs, also termed nanoscale coordination polymers (NCPs), are a new class of hybrid nanomaterials crafted from metal connecting points and organic bridging ligands. These materials can be tailored for biomedical applications by direct incorporation of functionalities into the framework or via post-synthesis modification of an existing framework structure.[41-44] Due to the presence of tunable pores and channels in many types of NMOF materials, it is also possible to encapsulate hydrophobic or charged agents into NMOFs through noncovalent interactions.[45-48] This chapter highlights recent advances in the design and synthesis of hybrid silica and NMOF nanoparticles and their applications in cancer chemotherapy.

1.2 Synthesis and Functionalization of Hybrid Nanomaterials

1.2.1 Silica Nanomaterials

The synthesis and functionalization of silica nanoparticles has been extensively reviewed elsewhere;[49-51] only the synthetic strategies will be briefly discussed here. Two major strategies are used to synthesize silica nanoparticles: the sol-gel synthesis and reverse microemulsion synthesis. The sol-gel synthesis of monodisperse solid silica particles ranging

in size from 50 nm to 2 μm was first reported in 1968 by Stöber and co-workers.[52] This method involves the controlled hydrolysis and condensation of a silica precursor, such as tetraethyl orthosilicate (TEOS), in ethanol using ammonia as a catalyst (Figure 1-1a). The particle size can be tuned by adjusting the reaction conditions. For example, adjusting the TEOS concentration from 0.05 M to 0.67 M while keeping the other reactant conditions constant affords silica particles from 20 to 880 nm in size.[53] These particles remain stable in solution due to electrostatic repulsion from the negatively-charged silica particles. Another common method for the synthesis of monodisperse silica nanoparticles uses reverse phase, or water-in-oil, microemulsions (Figure 1-1b).[53-56] Reverse phase microemulsions are highly tailorable systems that consist of nanometer-sized water droplets stabilized by a surfactant in a predominantly organic phase. The micelles in the microemulsion essentially act as "nanoreactors" that assist in controlling the kinetics of particle nucleation and growth. The size and number of micelles within the microemulsion can be tuned by varying the water to surfactant ratio (*W*). This method allows for careful control of particle size and polydispersity. The reverse microemulsion method is superior to the Stöber method for making monodisperse silica nanoparticles smaller than 100 nm.

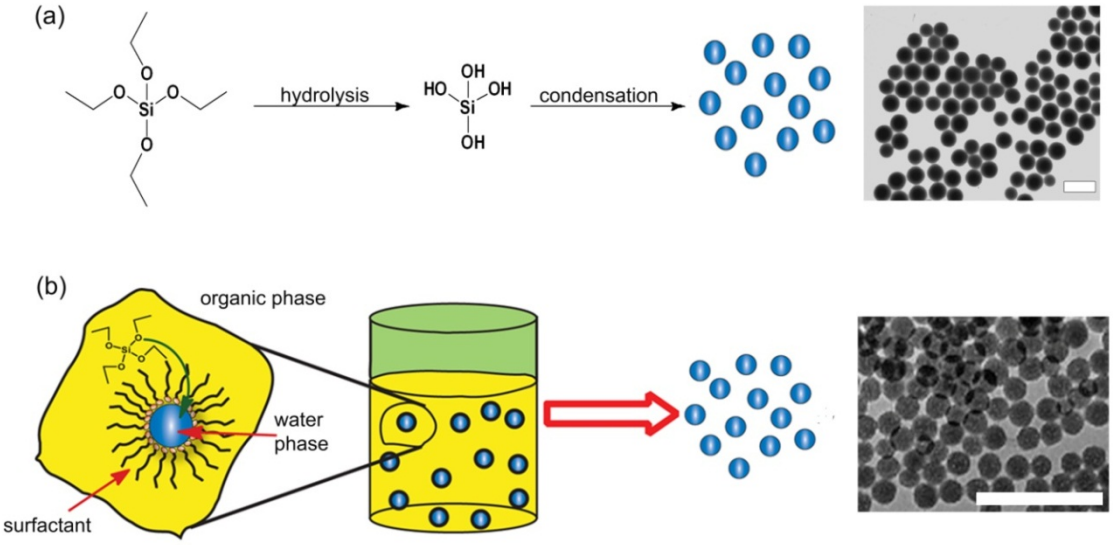

Figure 1-1: Methods for synthesizing solid silica nanoparticles. (a) The Stöber method, in which the hydrolysis and condensation of TEOS is facilitated by base in ethanol/water: TEM micrograph shows 125 nm silica nanoparticles.[57] (b) The reverse phase microemulsion, in which TEOS is hydrolyzed at the micellar interface and enters the aqueous droplet to form a silica nanoparticle within the micelle. TEM micrograph shows 37 nm silica nanoparticles.[56] The scale bars indicate 200 nm.

Solid silica nanoparticles can be functionalized for drug delivery using several strategies. The simplest method is to entrap hydrophillic functional molecules within the silica matrix via noncovalent interactions. This method was widely used to incorporate luminescent dyes (such as the cationic fluorophore $Ru(bpy)_3^{2+}$) within the anionic silica matrix.[58] However, the entrapped molecule can leach out of the nanoparticle under physiological conditions, limiting the stability and utility of the nanoconstruct. Alternatively, therapeutic agents can be covalently incorporated into silica nanoparticles by using trialkoxysilane-derived molecules that contain suitable moieties. These molecules are incorporated within the silica matrix through silanol linkages during particle synthesis, leading to stable hybrid silica nanoparticles with agents incorporated uniformly throughout the silica matrix. The silica nanoparticles can also be post-synthetically modified by reacting with trialkoxysilane molecules to introduce an active agent or functional group. Post-

synthesis grafting is particularly useful for modifying the particle surface selectively. The synthetic versatility also allows the incorporation of different cargoes in multi-step sequences. After the desired organic functionality is attached to the silica nanoparticles, the nanoparticles can be further modified using traditional conjugation chemistry. For example, an amine-modified particle can be reacted with various carboxylate-containing molecules to form a stable amide bond. The cargoes can also be conjugated to the nanoparticle surface by electrostatic interactions. Another popular strategy is to create a core-shell nanoparticle of a small inorganic nanoparticle or nanoparticles embedded within a silica matrix. [59-61]

1.2.2 Mesoporous Silica Nanoparticles

MSNs are typically synthesized using a surfactant-templated sol-gel method (Figure 1-2). [62-63] They provide a unique platform for the development of hybrid nanoparticles due to their high surface areas and tunable pore structures. MCM-41 type materials, for example, possess a hexagonal array of one dimensional channels with diameters that can be tuned from 2–10 nm.[64] Synthetic procedures have been developed for controlling the morphologies of MCM-41 materials,[65-66] leading to mesoporous silica nanospheres with diameters ranging from 60 to 1100 nm that have been utilized in a variety of applications, including catalysis,[67-68] drug delivery,[69-70] and imaging.[71-75]

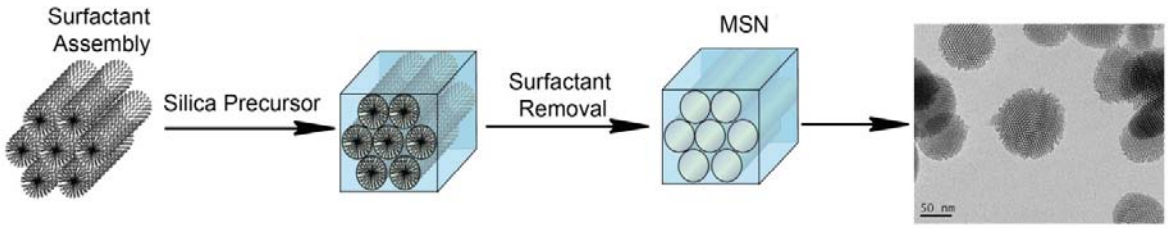

Figure 1-2: Schematic demonstrating the synthesis of MCM-41 type MSN particles. The cationic surfactant molecules self-assemble into hexagonal arrays in aqueous solution and the silica precursors then hydrolyze and condense along the exterior of the micelles to form a mesoporous material after surfactant removal.

MSNs can be covalently functionalized using two different approaches, either via co-condensation or by post-synthesis grafting. Victor Lin and coworkers have reported a co-condensation method for incorporating various organic functional groups into the pores of MSN.[63, 76-77] This co-condensation method has been extended in our lab to incorporate gadolinium chelates for MRI imaging.[74] The desired triethoxysilane is condensed into the walls of the MSNs during synthesis of the nanoparticle resulting in the uniform incorporation of the organic functionality throughout the particles. The degree of functionalization and particle size can be modified by adjusting the reagent concentration, size, and the hydrophobicity or hydrophillicity of the co-condensing reagents. However, not all types of MSN nanoparticles can be made by this method, as the organically-modified triethoxysilane can destabilize the surfactant templates during the synthesis, leading to large, rod-like particles (≈1000 nm).[77] The organic functionality can also have a pronounced effect on the pore structure of the nanoparticle.

Alternatively, as-synthesized MSNs can be functionalized via post-synthesis modification, for example, by reacting MSN nanoparticles with a variety of trialkoxysilanes to affect condensation with silanol groups on the silica surface. This method allows the particle morphology and pore structure to remain intact, but has been found to result in

inhomogeneous surface coverage of the nanoparticle, as the particle exterior surface and pore entrances are kinetically more accessible. This feature can also be exploited to selectively modify the exterior surface of the nanoparticles before the extraction of the surfactant in the channels. The surfactant is then removed and the interiors of the pores can then be differentially functionalized. The organically-modified MSN nanoparticles can be further modified with biomedically-relevant molecules.

1.2.3 Nanoscale Metal-Organic Frameworks

As the synthesis of nanoscale and microscale MOFs has recently been reviewed,[42, 44, 78] only general synthetic strategies will be outlined here. Four general methods have been utilized to synthesize NMOFs: nanoprecipitation, solvothermal, reverse microemulsion, and surfactant-templated solvothermal. The first method tends to yield amorphous materials, while the latter three methods can afford crystalline materials, owing to the ability to exert better control on nanoparticle nucleation and growth kinetics. The first two methods are surfactant free, whereas the last two methods rely on surfactants not only to control the particle synthesis but also to stabilize these particles.

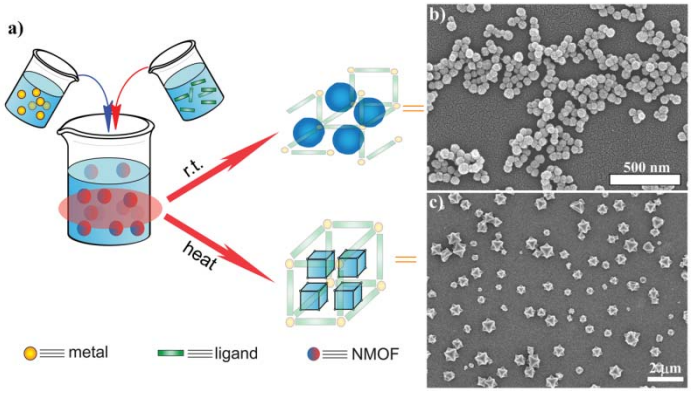

Figure 1-3: a) Surfactant-free synthesis of NMOFs by mixing NMOF precursors in appropriate solvents. In the nanoprecipitation method, the NMOF forms rapidly at room temperature, whereas in the solvothermal method, heating the solution leads to more controlled particle growth. b) and c) SEM images of amorphous[79] or crystalline[80] NMOFs.

In a typical NMOF synthesis, precursor solutions are mixed together to allow particle nucleation and growth (Figure 1-3a). In the nanoprecipitation method, nanoparticles form because the particles are insoluble in the solvent system whereas the individual precursors remain soluble. Due to the rapid particle growth, NMOFs produced by this method tend to be amorphous (Figure 1-3b). Solvothermal synthesis of NMOFs can be achieved with either conventional or microwave heating. Because high reaction temperatures are involved in the solvothermal method, more extensive transformations of the precursors typically occur before NMOF nanoparticle formation and favor the creation of more stable crystalline materials (Figure 1-3c). Temperature and heating rate provide additional parameters to control NMOF particle nucleation and growth. Surfactant-assisted synthesis of NMOFs can be carried out at either room or elevated temperatures. Because the building blocks for NMOFs are typically water soluble, reverse microemulsions provide another method to control the nucleation and growth kinetics of NMOF particles. Reverse microemulsions are formed by using surfactants to stabilize water droplets within a nonpolar organic phase (Figure 1-4a). Surfactant molecules can also be used to template the NMOF synthesis under

solvothermal conditions (Figure 1-4a) by coating the surfaces of growing NMOF particles. Surfactant molecules play an important role in defining NMOF morphologies. The four general methods described above have been adopted to synthesize a variety of NMOFs. With the ability to independently adjust NMOF precursors, reaction solvents, pH values, temperatures, surfactant or other templating molecules, *W* values, and other parameters, a range of NMOFs with well-defined compositions and morphologies have been synthesized. It has also been shown that surface termination can be an important parameter in defining NMOF morphologies.[46, 81] Although the synthesis of NMOFs has been phenomenologically described, there is little study on the NMOF growth mechanism and kinetics. Fundamental understanding of NMOF growth mechanism and kinetics will facilitate the development of NMOFs as a promising class of hybrid nanomaterials for biological and biomedical applications.

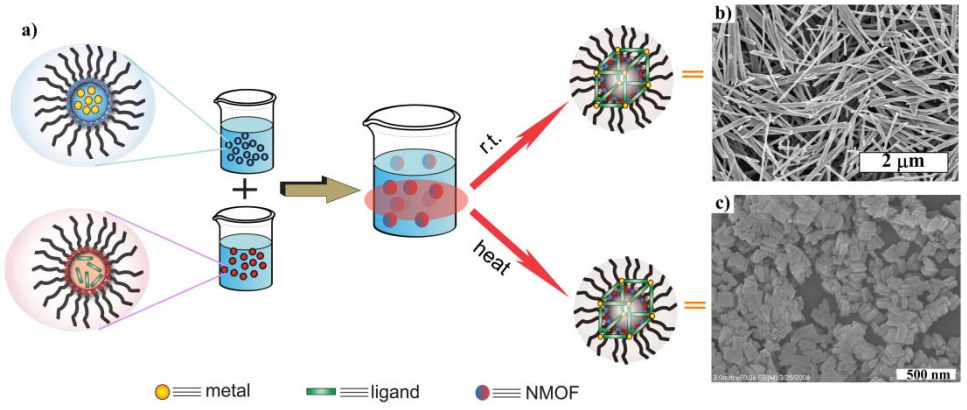

Figure 1.4: a) Surfactant-templated NMOF synthesis, either conducted with reverse microemulsions at room temperature or surfactant-assisted solvothermal reactions. b)[82] and c)[83] show SEM images of crystalline NMOFs synthesized by these methods.

NMOF materials tend to dissociate rapidly in aqueous media, so they must be stabilized to increase their utility in biological applications. Our group was able to

encapsulate NMOFs within a silica shell.[79-80, 84-86] Briefly, the as-synthesized NMOFs were treated with polyvinylpyrollidone, then coated with a shell of amorphous silica in basic ethanol. The silica shell thickness could be controlled by varying the reaction parameters and the silica shell could be further functionalized with a variety of silyl-derived molecules. An alternative procedure to coat NMOFs with silica also was developed using sodium silicate as the silica source in aqueous media for NMOFs that are unstable under basic conditions.[80] The silica shell could significantly retard, but not entirely prevent, NMOF decomposition. Our group has also developed a method to coat NMOFs with a lipid bilayer.[87] The lipid bilayer could drastically improve the stability of NMOFs under physiological conditions and could be functionalized to contain additional moieties (targeting molecules, fluorescent dyes). Several groups have demonstrated the coating of NMOFs with biocompatible polymers via coordination to surface metal centers. [46, 88-89] These polymers could be used to increase NMOF stability, improve biocompatibility, and modulate MRI relaxivity. Additional active agents or targeting molecules could be conjugated to the NMOF through these polymers.

1.3 Therapeutic Applications of Hybrid Materials

1.3.1 Silica Based Materials

Hybrid silica nanoparticles have been used in drug delivery and therapy applications. Prasad and coworkers described the use of an organically-modified silica nanoparticle for photodynamic therapy (PDT).[90] PDT is a light-activated treatment for cancer and other diseases, and works by utilizing light sensitive drugs (i.e. photosensitizers) that can be preferentially localized in malignant tissues. PDT's therapeutic effect is initiated by photoexcitation of the localized photosensitizer to generate cytotoxic species such as singlet

oxygen ($^1O_2$). This leads to selective and irreversible destruction of diseased tissues, without damaging adjacent healthy ones. The main drawback to this therapy is that currently approved PDT photosensitizers absorb in the visible spectral region below 700 nm, where light penetration into the skin is only a few millimeters. This problem can be overcome by combining a two-photon absorbing (TPA) dye with the photosensitizer. Here, the photosensitizer is indirectly excited through fluorescence resonance energy transfer (FRET). In this work, a known photosensitizer and a two-photon energy donor were co-encapsulated in a ~30 nm silica nanoparticle (Figure 1-5). Upon two-photon irradiation, the photosensitizer is excited as a result of intraparticle FRET from the two-photon absorbing dye, resulting in the generation of singlet oxygen and other reactive oxygen species. The uptake of these particles was demonstrated through fluorescence imaging of HeLa cells. Upon two-photon irradiation, HeLa cells that had been incubated with the nanoparticles exhibited drastic morphology changes associated with cell necrosis, apparently induced by the reactive oxygen species generated by the photosensitizer. Prasad and coworkers developed a similar system where a photosensitizer was covalently incorporated within a 20 nm silica nanoparticle.[91] These nanoparticles are rapidly taken up *in vitro* and demonstrate phototoxic action upon irridation.

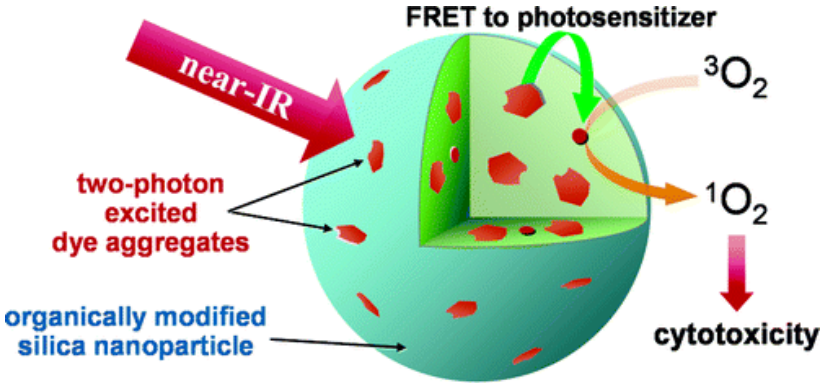

Figure 1.5: Schematic showing an organically-modified silica nanoparticle co-encapsulating two-photon absorbing fluorescent dye aggregates and a photosensitizing drug for two-photon photodynamic therapy.[90]

Silica nanoparticles have been extensively studied as DNA carriers for gene therapy.[62, 92-96] For example, Prasad and coworkers have developed a fluorescently-labeled silica nanoparticle with a cationic surface coating.[92, 95] Gel electrophoresis studies revealed that the particles efficiently bind DNA via electrostatic interactions and prevent enzymatic degradation of the encapsulated DNA. Confocal microscopy studies revealed that the nanoparticles were internalized by cells *in vitro* with the released DNA migrating to the nucleus. Further *in vivo* studies showed that the particles were able to successfully transfect and modulate the activity of neural cells in a murine model.[92] The transfection efficiency was equal to or exceeded that of a viral vector and no particle-related toxicity was observed after 4 weeks.

Jiang and coworkers have reported a system of hollow chitosan-silica nanospheres fabricated in aqueous medium.[97] The anticancer drug doxorubicin was loaded within the interior of the nanosphere (8.9 wt %). Drug release was found to be pH sensitive, with minimal release occurring at pH = 7.4; however, the drug is rapidly released at pH=4. Preliminary cytotoxicity assays demonstrated that the nanoparticles were more effective than

doxorubicin, presumably by more efficient drug uptake. A similar chitosan-silica nanosphere system was used for the treatment of breast cancer *in vitro* and *in vivo* with tumor necrosis factor alpha (TNF-α).[98] TNF-α was electrostatically bound to the nanosphere and a targeting antibody was covalently attached to the surface. The TNF-α conjugated nanospheres possessed time and concentration dependent cytotoxic effects on MCF-7 breast cancer cells (Figure 1-6) with targeting increasing nanoparticle localization to the cell surface. *In vivo* assays using a breast cancer xenograft model demonstrated that nanoparticle-bound TNF-α enhanced tumor growth inhibition compared to free TNF-α or the non-treated control.

Corma and coworkers have developed liposomal doxorubicin nanoparticles with a poly(silsesquioxane) shell.[99] *In vitro* assays against human glioma cells demonstrated that the nanospheres were able to kill the cells, reaching mortality rates of 44%, compared to 90% for the free drug. Fluorescence microscopy images revealed that the nanospheres enter the cells and release doxorubicin. Botella and coworkers designed a silica nanoparticle-based system for the systemic delivery of the anticancer drug camptothecin.[100] Camptothecin was covalently linked to the nanoparticle surface, which was further modified to contain a fluorescent dye. The nanoparticle-conjugate showed minimal background release. Preliminary *in vitro* cytotoxicity assays revealed that the nanoparticles were efficiently internalized by cells, but the efficacy of the nanoparticle conjuagate was less than free camptothecin. *In vivo* biodistribution and efficacy studies were performed in colon cancer xenografts. Nanoparticle conjugation increased tumor camptothecin concentration compared to the free drug. Additionally, nanoparticle-delivered camptothecin treatment delayed tumor growth and reduced side effects compared to free camptothecin.

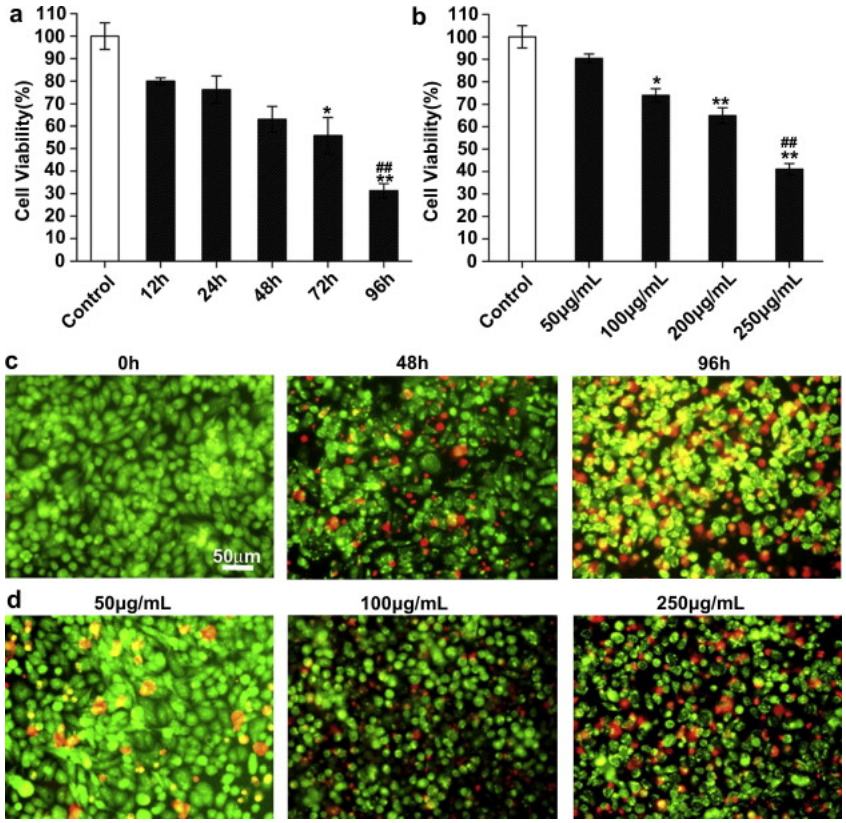

Figure 1-6: Cytotoxicity of TNF-α loaded chitosan-silica nanospheres. a) Cytotoxicity effect of TNF-α loaded chitosan-silica nanospheres at the same concentration (500 ng/mL TNF-α) with different incubation times. b) Concentration dependent cell viability of TNF-α loaded chitosan-silica nanospheres incubated for 4 hours. c) Fluorescent photos of MCF-7 cells demonstrating the time-dependent cytotoxicity effect of the nanocarriers by acridine orange (green color, live cells) and propidium iodide (red color, dead cells) staining. D) Fluorescent photos of MCF-7 cells demonstrating concentration dependent cytotoxicity effect after 48 hours incubation by acridine orange and propidium iodide stain. Scale bar is 50 μm.[98]

1.3.2 Mesoporous Silica Nanoparticles

Due to their unique properties, mesoporous silica nanoparticles have been extensively evaluated as drug delivery vehicles. Victor Lin and coworkers first demonstrated the use of MCM-41 nanoparticles for the delivery of a membrane impermeable protein, cytochrome C.[69] After removing the surfactants from large-pore (5.4 nm) MSN particles, cytochrome C (maximum loading = 41.5 wt%) was loaded into the pores. The release of the protein was

measured in PBS at two different pH values (7.4 and 5.2) over a 25 hour period. The total percentages of proteins that were released were 45 and 55% at pH values of 7.4 and 5.2, respectively. The difference in release was attributed to the extent of negative charge on the MSN surface, which favorably interacts with the positively-charged protein. No significant release of the protein was detected within the first 4 hours at pH 7.4, which allowed for the introduction of protein-loaded particles into cell culture at physiological pH without losing a large amount of the entrapped protein due to burst release. The released cytochrome C was found to retain catalytic activity for the oxidation of 2,2'-azino-bis(3-ethylbenzthiazoline-6-sulfonate) (ABTS) by hydrogen peroxide. HeLa cells could internalize the loaded MSN particles and confocal microscopy showed escape of the protein from endosomal entrapment. MSN systems were also used to deliver cysteine to cells.[101] The covalently attached cysteine does not release from the MSNs in the absence of a reducing agent; however, all cysteine was released within 1 h after the addition of a suitable reducing agent. *In vitro* assays against HeLa cells demonstrated that the conjugated nanoparticle was 444 times more effective in inhibiting cell growth than N-acetylcysteine, the standard molecule for cysteine therapy.

Figure 1-7: Schematic of the Au nanoparticle-capped MSN-based drug delivery system. The controlled release of the cargo is based on UV irradiation.[102]

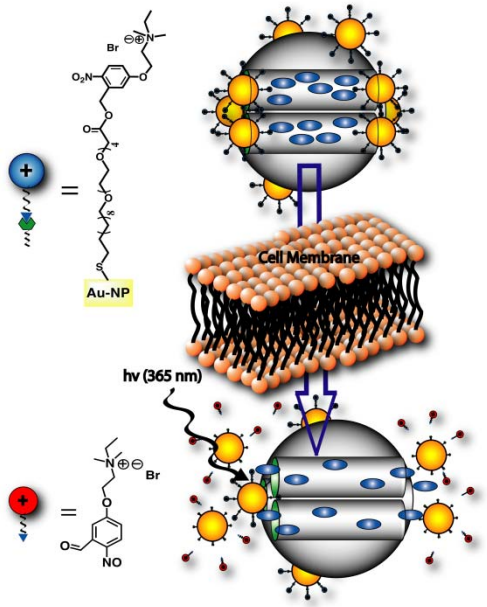

Victor Lin and coworkers pioneered the development of MSN-based drug delivery systems where the nanoparticle pores are capped by a stimuli-responsive system to allow controlled cargo release.[102-104] As an example shown in Figure 1-7, the gold nanoparticles were conjugated to the MSN materials with a photolabile linker.[102] The hybrid system will release the Au nanoparticle pore caps when exposed to UV irradiation. This system was used to deliver paclitaxel to human liver and fibroblast cells. After UV irradiation, significant decreases in cell viability were observed. Other drug molecules and neurotransmitters, such as vancomycin and adenosine triphosphate (ATP), have also been delivered using this strategy.[103-104]

A double drug delivery system was also developed based on capped MSN nanoparticles.[105] Boronic acid functionalized MSN nanoparticles were loaded with cyclic adenosine monophosphate (cAMP), an important cellular signaling molecule. The pores of

the material were then capped with fluorescein-labeled insulin. Release from the material was shown to be triggered by saccharides, as they form more stable conjugates with the boronic acids on the nanoparticles. In a 50 mM solution of glucose in PBS, 80% of the entrapped cAMP was released within 20 hours, with less than 10% released in the same time frame without glucose. Preliminary *in vitro* assays demonstrated that the materials showed low cytotoxicity and were able to deliver cAMP to pancreatic cells in a dose dependent manner.

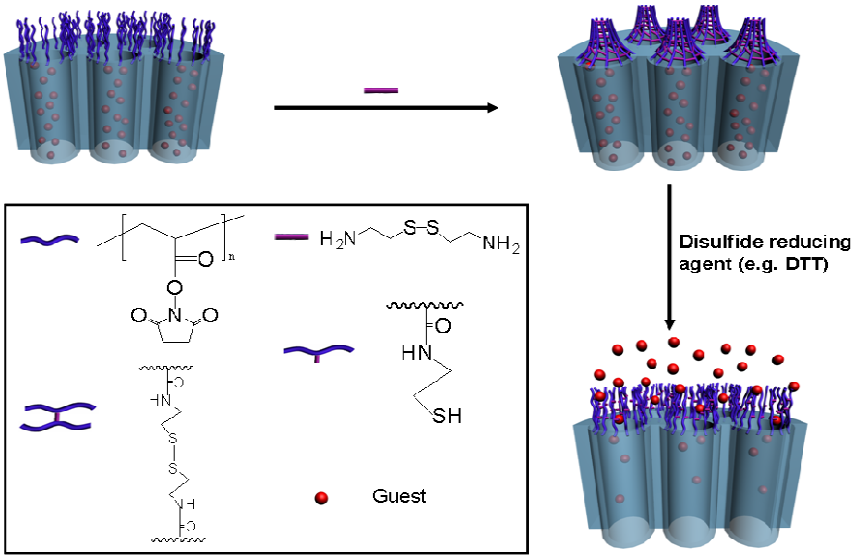

Figure 1-8: Schematic of a redox-responsive nanogated ensemble based on polymeric network capped mesoporous silica.[106]

Feng and coworkers demonstrated the use of a cross-linked polymer network as a "gatekeeper" for MSN (Figure 1-8).[106] Poly(*N*-acryloxysuccinimide) (2nm thick) was anchored to the MSN surface through reversible addition-fragmentation chain transfer (RAFT) polymerization and then cross-linked by adding cystamine. The ability to control the release of cargos was demonstrated by entrapping rhodamine B inside the MSN before cross-linking of the polymer. A light-activated nanoimpeller-controlled drug carrier based on

MSNs was recently designed by taking advantage of the well known cis-trans isomerization in the azobenzene derivative (4-phenylazoaniline).[107] The anti-cancer drug camptothecin loaded into this system could be trigger-released by irradiation at 413 nm. After incubating the cells with the drug-loaded MSN, cell death only was observed after irradiation. A related trigger release system based on MSN-supported polyelectrolyte multilayers (PEM) was developed by Wang and coworkers for the controlled delivery of doxorubicin *in vitro*.[108]

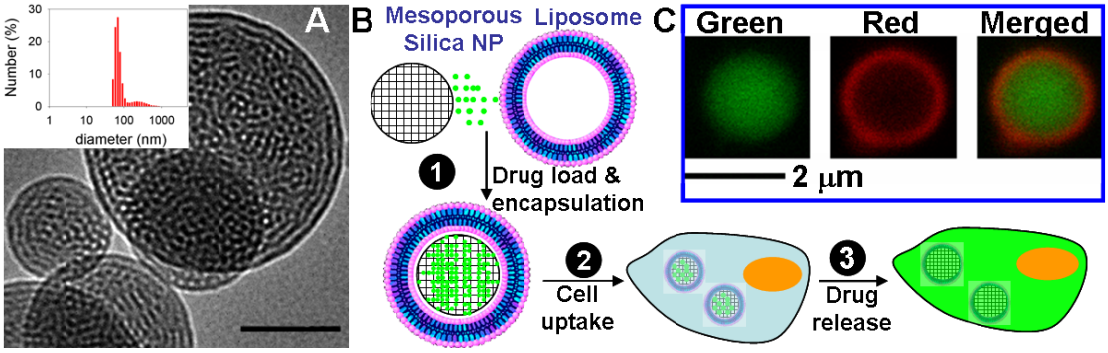

Figure 1-9: a) TEM image of MSN, scale bar= 50nm. Inset shows the dynamic light scattering histogram of these nanoparticles. b) Schematic representation of drug loading of MSN and encapsulation within a liposome to form a protocell, followed by cellular uptake and cargo release. c) Confocal images of the protocell: FITC-labeled MSN (green), Texas-Red labeled liposome (red) and the merged image showing the protocell.[109]

Brinker and coworkers have developed porous nanoparticle supported lipid bilayers (protocells) as delivery vehicles (Figure 1-9).[109] Liposome fusion on mesoporous particles was utilized to simultaneously load and seal cargo within the porous core. With the use of a cationic lipid (DOTAP) on an anionic silica particle, an anionic fluorescent dye (calcein) was effectively loaded into the particles. The loaded protocell particles were taken up efficiently by Chinese hamster ovary (CHO) cells. Calcein was effectively released inside endosomal compartments due to reduced pH. Brinker and coworkers have used the same approach to coat cationic mesoporous silica nanoparticles.[110] A cationic mesoporous material was

synthesized by incorporating 3-[2-(2-aminoethylamino)ethylamino]propyltriethoxysilane into the silica framework, and was then fused with anionic (DOPS) liposomes.

Subsequently, the protocell system was adapted for the delivery of small molecule chemotherapeutics.[111] A variety of different chemotherapeutic drugs and drug cocktails were loaded into the pores of a mesoprous silica nanoparticle before liposome coating. The protocell was modified with a targeting peptide for hepatocellular carcinoma. Targeting increased protocell uptake nearly 10,000 times in tumor cells compared to heptacytes, immune cells, and endothelial cells. *In vitro* assays demonstrated the protocells could improve treatment efficacy of multidrug-resistant hepatocellular carincoma by 10^6. The protocell system was also adapted for gene delivery.[112] Cationic liposomes were fused with solid silica nanoparticles of 30, 50, 80, and 130 nm in diameter to form silica-supported lipid bilayers. These particles were shown to bind to plasmid DNA in a size dependent manner, as measured by gel electrophoresis. It was observed that the transfection efficiency in the CHO cells decreased with particle size, with the 130 nm particles exhibiting no DNA transfection. Confocal microscopy studies revealed that the DNA needed to be released from the construct to induce transfection. For larger nanoparticles, the DNA appears to be trapped on the silica nanoparticles and does not leave the endosomal compartment, resulting in the lack of activity for the 130 nm nanoparticles. These protocell constructs protected the DNA from enzymatic degradation.

1.3.3 Nanoscale Metal-Organic Frameworks

Our group has developed two NMOF platforms to deliver cisplatin-based chemotherapeutics.[79-80] The first NMOF was built from a cisplatin prodrug (*c,c,t*-

$Pt(NH_3)_2Cl_2(succinate)_2$) and Tb^{3+} ions using a nanoprecipitation procedure. This cisplatin NMOF was coated with a thin layer of silica and targeted to cancer cells with a silyl-derived peptide. When placed in physiological medium, the framework decomposes and the cisplatin prodrug diffuses through the silica shell in a controlled manner (Figure 1-10a). The targeted peptide possessed similar cytotoxicity against human colon cancer cells as cisplatin, while the uncoated or untargeted NMOFs were less effective, presumably due to decreased uptake via receptor mediated endocytosis.

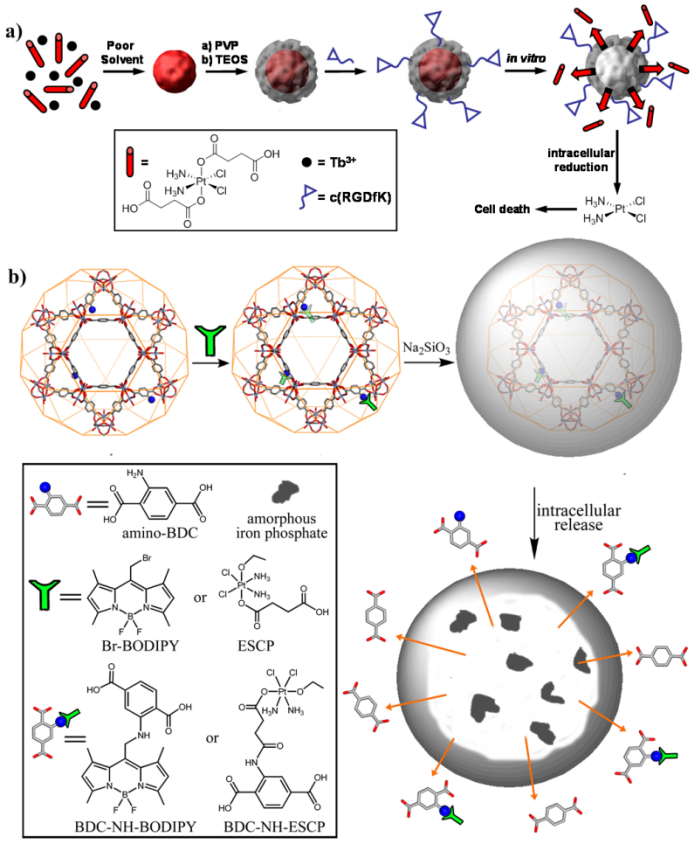

Figure 1-10: a) Schematic representation of the synthesis, post-synthetic modification and cisplatin release from Tb^{3+} based NMOF.[79] b) Schematic representation of the synthesis, post-synthetic modification, silica coating, and agent release from iron-carboxylate MIL101 NMOFs.[80]

Our group has also demonstrated a post-synthesis modification scheme to introduce therapeutic and imaging moieties into the iron-carboxylate NMOF, MIL-101 (Figure 1-10b).[80] Highly porous MIL-101 nanoparticles with amine-functionality were synthesized using a solvothermal method with microwave heating. A cisplatin prodrug, *c,c,t*-$Pt(NH_3)_2Cl_2(OEt)$(succinate) was also covalently incorporated into the framework via an amide linkage between the amine groups in the framework and the carboxylate of the anti-cancer prodrug. These nanoparticles were encapsulated in amorphous silica and tested *in vitro* against HT-29 human colon adenocarcinoma cells. Treatment of the cells with the Pt-loaded MIL-101 showed appreciable cytotoxicity (IC_{50} = 29 μM), but not as much as cisplatin under the same conditions (IC_{50} = 20 μM). Targeting of the nanoparticles with a silyl-derived cyclic RGD peptide as a targeting moiety increased the cytotoxicity to a value comparable to cisplatin (IC_{50} = 21 μM). An optical imaging agent, 1,3,5,7-tetramethyl-4,4-difluoro-8-bromoethyl-4-bora-3a,4a-diaza-s-indacene (Br-Bodipy) was loaded into the framework by covalent attachment to the amine groups in the framework. The Bodipy-loaded MIL-101 labeled colon cancer cells in a dose-dependent manner.

Horcajada and coworkers have developed a group of porous NMOF carriers for both drug delivery and imaging.[46] They synthesized five iron-carboxylate NMOFs under aqueous conditions (corresponding to the previously reported MIL-89, MIL-101_NH_2, MIL-88A, MIL-100, and MIL-53 bulk phases). These frameworks were rendered more biocompatible by coating with PEG, dextran, or chitosan. The MIL-88A particles showed low *in vitro* toxicity against murine macrophage cells (IC_{50} = 57 μg/mL). The *in vivo* toxicity of MIL-88A, MIL-100, MIL-88Bt was determined using the highest injectable amount (up to 220 mg/kg) in a rat model. Aside from a small increase of liver and spleen weights observed at

the onset of the study (which returned to control levels after a short period of time), no signs of toxicity were observed for 3 months.

These NMOFs were also evaluated as potential drug carriers. Four different anti-cancer or antiviral drugs (busulfan, azidothymidine triphosphate, cidofovir, and doxorubicin) were loaded into the NMOF pores via noncovalent interactions. This drug loading was highly efficient, with up to 90 wt% loading for azidothymidine triphosphate (AZT) into MIL-101_NH_2 particles. Release profile studies using MIL-100 nanoparticles loaded with cidofovir, doxorubicin, and AZT showed sustained release with no burst effects. The potential applicability of these NMOFs as drug delivery vehicles was evaluated *in vitro*. Experiments using human leukemia and myeloma cells showed that MIL-100 nanoparticles loaded with busulfan displayed comparable cytotoxicity to the free drug. Further *in vitro* tests using MIL-100 nanoparticles loaded with AZT showed significant anti-HIV activity only for those nanoparticles loaded with the active drug, with the nanocarrier showing no significant activity over the same concentration range.

The particle systems were also evaluated as T_2-weighted MRI contrast agents. Mössbauer spectroscopy demonstrated that the NMOFs themselves, not any iron oxide or hydroxide decomposition products, acted as the contrast agents and had r_2 values up to 95 mM^{-1} s^{-1} for MIL-88A-PEG NMOFs.[46] *In vivo* studies using Wistar rats demonstrated that the particles showed negative contrast in the major RES organs (liver and spleen) 30 minutes post injection of MIL-88A nanoparticles. This contrast disappeared 3 months post injection.

Our group has also developed a NMOF platform to deliver the chemotherapeutic methotrexate.[87] Methotrexate was incorporated into 3 different NMOF platforms at very high

drug loadings (up to 79.1 wt%), utilizing zinc, zirconium or gadolinium metal centers. The gadolinium-methotrexate NMOF could then be encapsulated within a functionalized lipid bilayer. *In vitro* assays demonstrated that the lipid-coated and targeted methotrexate NMOF had superior cytotoxicity to methotrexate in a leukemia cell line.

1.4 Theranostic Applications of Hybrid Nanomaterials

One of the unique advantages of nanomaterials over conventional small molecule therapeutics is the ability to incorporate multiple types of agents within the same nanoparticle. A popular trend is to create theranostic materials, which incorporate both an imaging contrast agent and a therapeutic agent. [113] Theranostic nanoparticles allow for the real-time monitoring of nanoparticle biodistribution, tumor uptake, tumor distribution and treatment efficacy. Someday, theranostic nanomaterials could provide clinicians important information as they attempt to assess the progress of chemotherapeutic treatments.

1.4.1 Silica Based Materials

Hai and coworkers prepared 105 nm silica particles with entrapped methylene blue (MB) dye for near-IR (NIR) imaging and photodynamic therapy.[114] Methylene blue is an effective photosensitizer due to its high quantum yield of $^1O_2$ generation, low dark toxicity, and wide NIR therapeutic window. PDT was demonstrated *in vitro* against HeLa cells. Significant cell death was only observed in cells treated with the MB nanoparticles and laser irradiation, with little toxicity observed when the cells were treated with either the nanoparticles or the laser alone. Both fluorescence imaging and PDT was observed *in vivo* in a mouse xenograft model. After intratumoral injection of the MB nanoparticles, fluorescent

imaging of the mice revealed that the tumor region was clearly defined and, after laser treatment, the tumor became necrotic (Figure 1-11).

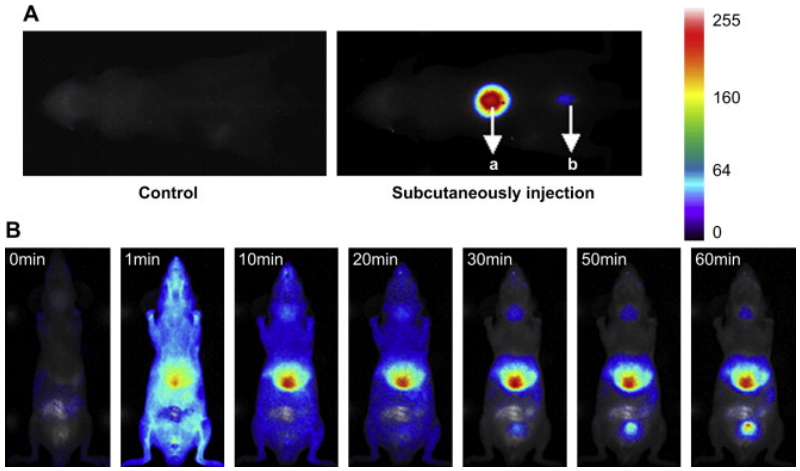

Figure 1-11: a) Images of control mice and the two subcutaneous injections of 100 µL MB-encapsulated PSiNPs with concentrations of 44 mg/mL (a) and 4.4 mg/mL (b). The acquisition was performed two minutes post-injection. b) Real time *in vivo* images of mice i.v. injected with 200 µL of MB-encapsulated PSiNPs (44 mg/mL) at different time points post-injection.[114]

Prasad and coworkers developed a novel drug carrier system for photodynamic therapy.[115] Organically-modified silica nanoparticles were used to encapsulate the photosensitizing anticancer drug 2-devinyl-2-(1-hexyloxyethyl)pyropheophorbide within the core of the nanoparticle. *In vitro* cell uptake studies demonstrated that the nanoparticles were internalized by HeLa cervical cancer cells and were found throughout the cytoplasm. Cytotoxicity studies with two different human cancer cell lines demonstrated that the photosensiziter-loaded nanoparticles displayed significant cytotoxic effects after laser irradiation and showed no toxicity in the absence of laser light. The unloaded silica nanoparticles demonstrated no toxic effects as well.

1.4.2 Mesoporous Silica Nanoparticles

Hyeon and coworkers synthesized particles containing a single iron oxide nanoparticle coated with a mesoporous silica shell. [71] SPIO nanoparticles provide T_2-weighed MR contrast enhancement, while the mesoporous silica serves as a drug carrier. Fluorescent dyes were also covalently attached to the silica shell and the anticancer drug doxorubicin was loaded into the pores. Preliminary *in vitro* assays revealed that the carrier possessed minimal cytotoxicity to cancer cells, while the doxorubicin-loaded nanoparticles showed a dose dependent cytotoxicity profile. *In vivo* assays on a murine xenograft model showed strong T_2 signal reduction at the tumor site up to 24 hours post injection, which was confirmed by *ex vivo* organ analysis by fluorescence microscopy (Figure 1-12). Hyeon and coworkers created a MSN nanoparticle capable of simultaneous drug delivery, MR imaging and fluorescent imaging.[116] Dye-doped MSN nanoparticles were surface functionalized with smaller iron oxide nanoparticles and the anticancer drug doxorubicin was loaded into the materials' pores. MRI relaxivity measurements demonstrated that the iron oxide@MSN nanoparticles possessed higher T_2 relaxivity than the iron oxide nanocrystals alone. The iron oxide@MSN nanoparticles were efficiently internalized into cells *in vitro* as measured by fluorescent imaging, Prussian blue staining, and MR imaging. The doxorubicin-loaded nanoparticles possessed similar cytotoxicity as free doxorubicin. *In vivo*, the MSN nanoparticles had high tumor accumulation and could be imaged by both MR and fluorescent imaging. Doxorubicin could also be delivered to the tumor region, but no tumor growth inhibition data was presented. In a subsequent publication, this system was modified to covalently attach doxorubicin to the MSN.[117]

Figure 1.12: a) *In vivo* T_2-weighted MR and b) fluorescence images of subcutaneously injected MCF-7 cells labeled with Fe_3O_4@MSN and control cells. (c) T_2-weighted MR (upper row) and color maps (lower row) of the tumor before and after the Fe_3O_4@MSN particles were intravenously injected into the tail vein of a nude mouse implanted with MCF-7 cells. A decrease in signal intensity was detected at the tumor site (arrows). (d) Photographic (left) and fluorescence (right) images of several organs and the tumor 24 hours after i.v. injection.[71]

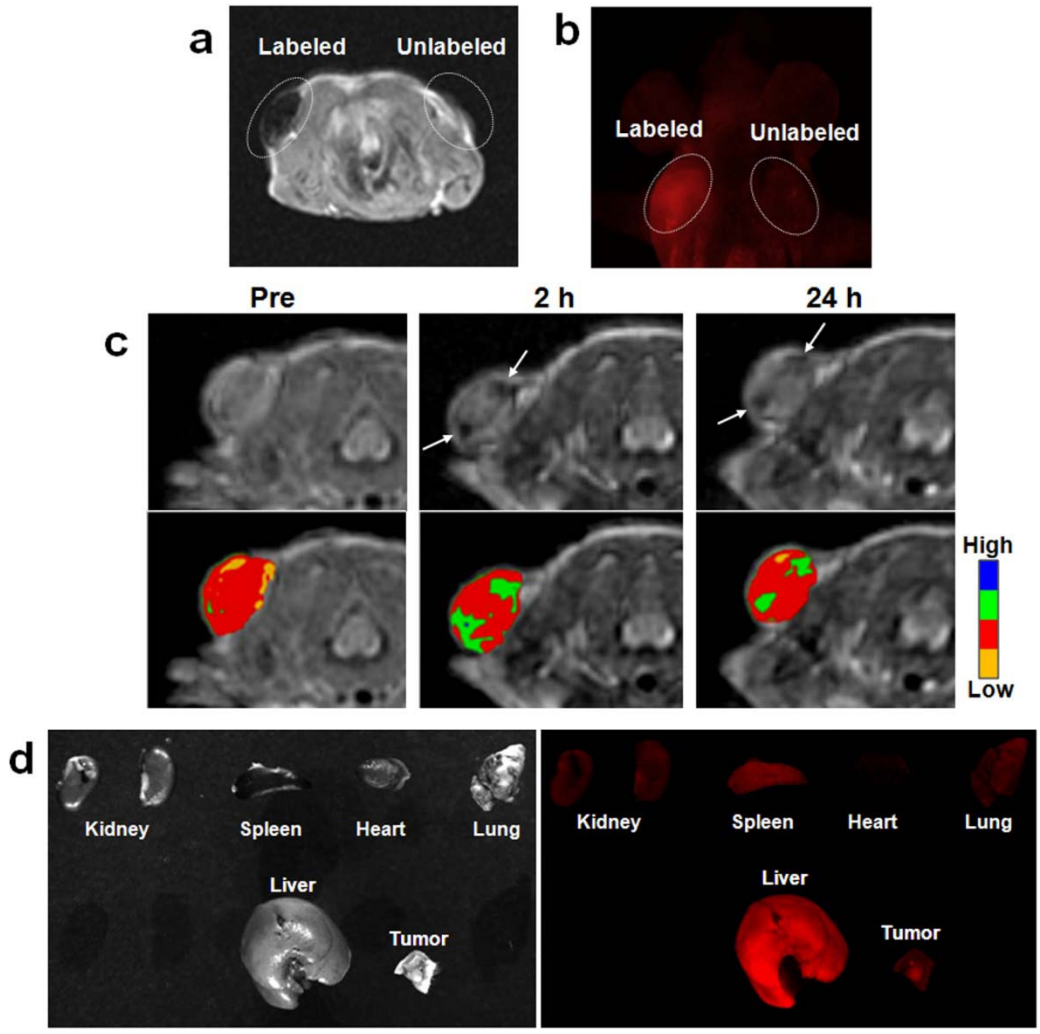

A similar report by Zink and coworkers described the encapsulation of SPIO nanocrystals inside mesostructured silica spheres that were labeled with fluorescent dye molecules and coated with hydrophilic groups (trihydroxysilylpropyl methylphosphonate) to prevent aggregation.[72] Water-insoluble anticancer drugs (camptothecin and paclitaxel) were delivered to human cancer cells; surface conjugation with cancer-specific targeting agents

increased the uptake into cancer cells relative to that in non-cancerous fibroblasts. Zink and coworkers studied this system *in vivo* in a murine xenograft model.[118] The biodistribution of the fluorescent MSN nanoparticles was evaluated by ICP-MS, histology, and fluorescent imaging. The nanoparticles were well tolerated and showed preferential tumor uptake. Camptothecin-loaded MSNs demonstrated statistically significant tumor growth inhibition compared to campthecin alone, while the unloaded nanoparticles did not affect tumor growth.

Chou, Chi, Hsiao, and coworkers have developed a multimodal system for MR imaging and photodynamic therapy.[119] Silica-coated SPIO nanoparticles were functionalized with an iridium photosensitizer and were evaluated *in vitro*. Confocal microscopy experiments revealed that the nanoparticles were efficiently uptaken by HeLa cells in a dose-dependent fashion. The nanoparticles also provided adequate T_2-weighted contrast using a 1.5 T scanner. Cytotoxicity assays revealed that the as-synthesized nanoparticles were not cytotoxic in the absence of irradiation; however, they exhibited significant cell death upon irradiation.

1.4.3 Nanoscale Metal Organic Frameworks

Boyes and coworkers have developed a multimodal system based on the NMOF particles developed in our group for targeted imaging and treatment of cancer.[89] Gadolinium-based NMOF particles were synthesized as described previously by our group[82] and were functionalized with PNIPAM-*co*-PNSOS-*co*-PFMA copolymers via vacant coordination sites on the Gd^{3+} metal centers. A chemotherapeutic, methotrexate (MTX), and a targeting peptide, glycine-arginine-glycine-aspartate-serine-NH_2 (GRGDS-NH_2), were conjugated to the copolymer. Preliminary *in vitro* assays were performed on canine FITZ-

HSA cells. Confocal microscopy experiments demonstrated that the targeted nanoparticles had significant localization at the cell surface after 1 hour of incubation, with internalization observed after 24 hours, while the unmodified nanoparticles had no significant fluorescence over the same time period. Cell growth inhibition studies demonstrated that the MTX-containing nanoparticles show a dose-dependent inhibition of growth similar to the free drug.

1.5 Conclusions

The effective delivery of chemotherapeutics to the tumor site remains a significant challenge for many difficult to treat cancers. Nanotherapeutics offer considerable promise in this area as they generally show higher tumor uptake, increased efficacy and reduced toxicity compared to their small molecule counterparts. Hybrid nanomaterials, combining the advantageous properties of both inorganic and organic nanoparticles, are an intriguing class of nanotherapeutics. Preliminary investigations reveal that hybrid nanomaterials are highly efficacious drug delivery agents for the delivery of a variety of different therapeutic classes. Hybrid nanomaterials can also be developed as theranostic agents, combining both imaging and drug delivery functionalities. However, many of these materials still need to undergo systemic *in vivo* investigation to fully realize their clinical potential as drug delivery vehicles.

1.6 References

1. Bawa, R., Patents and Nanomedicine. *Nanomedicine (London)* **2007,** *2* (3), 351-374.

2. Lipinski, C. A.; Lombardo, F.; Dominy, B. W.; Feeney, P. J., Experimental and Computational Approaches to Estimate Solubility and Permeability in Drug Discovery and Development Settings. *Adv. Drug Delivery Rev.* **1997,** *23* (1-3), 3-25.

3. Peer, D.; Karp, J. M.; Hong, S.; Farokhzad, O. C.; Margalit, R.; Langer, R., Nanocarriers as an emerging platform for cancer therapy. *Nat. Nanotechnol.* **2007,** *2* (12), 751-760.

4. Wang, A. Z.; Langer, R.; Farokhzad, O. C., Nanoparticle Delivery of Anticancer Drugs. *Ann. Rev. Med.* **2012,** *63*, 7.1-7.14.

5. Judson, I.; Radford, J. A.; Harris, M.; Blay, J.-Y.; van Hoesel, Q.; le Cesne, A.; van Oosterom, A. T.; Clemons, M. J.; Kamby, C.; Hermans, C.; Whittaker, J.; Donato di Paola, E.; Verweij, J.; Nielson, S., Randomised phase II trial of pegylated liposomal doxorubicin (DOXIL/CAELYX) versus doxorubicin in the treatment of advanced or metastatic soft tissue sarcoma: a study by the EORTC soft tissue and bone sarcoma group. *Eur. J. Cancer* **2001,** *37* (7), 870-877.

6. O'Brien, M. E. R.; Wigler, N.; Inbar, M.; Rosso, R.; Grischke, E.; Santoro, A.; Catane, R.; Kieback, D. G.; Tomczak, P.; Ackland, S. P.; Orlandi, F.; Mellars, L.; Alland, L.; Tendler, C., Reduced cardiotoxicity and comparable efficacy in a phase III trial of pegylated liposomal doxorubicin HCL (CAELYX^{TM}/Doxil^{R}) versus conventional doxorubicin for first-line treatment of metastatic breast cancer. *Annal. Oncol.* **2004,** *15* (3), 440-449.

7. Liu, F.; Park, J.-Y.; Zhang, Y.; Conwell, C.; Liu, Y.; Bathula, S. R.; Huang, L., Targeted Cancer Therapy with Novel High Drug-Loading Nanocrystals. *J. Pharm. Sci.* **2010,** *99* (8), 3542-3551.

8. Dobrovolskaia, M. A.; Germolec, D. R.; Weaver, J. L., Evaluation of nanoparticle immunotoxicity. *Nat. Nanotechnol.* **2009,** *4* (7), 411-414.

9. Biju, V.; Itoh, T.; Anas, A.; Sujith, A.; Ishikawa, M., Semiconductor quantum dots and metal nanoparticles: syntheses, optical properties, and biological applications. *Anal. Bioanal. Chem.* **2008,** *391* (7), 2469-2495.

10. Smith, A. M.; Duan, H.; Mohs, A. M.; Nie, S., Bioconjugated quantum dots for in vivo molecular and cellular imaging. *Adv. Drug Delivery Rev.* **2008,** *60* (11), 1226-1240.

11. Weng, J.; Ren, J., Luminescent Quantum Dots: A Very Attractive and Promising Tool in Biomedicine. *Curr. Med. Chem.* **2006,** *13* (8), 897-909.

12. Yu, W. W.; Chang, E.; Drezek, R.; Colvin, V. L., Water-soluble quantum dots for biomedical applications. *Biochem. Biophys. Res. Commun.* **2006,** *348* (3), 781-786.

13. Zhang, H.; Yee, D.; Wang, C., Quantum dots for cancer diagnosis and therapy: biological and clinical perspectives. *Nanomedicine (London, U.K.)* **2008,** *3* (1), 83-91.

14. Yavuz, M. S.; Cheng, Y.; Chen, J.; Cobley, C. M.; Zhang, Q.; Rycenga, M.; Xie, J.; Kim, C.; Song, K. H.; Schwartz, A. G.; Wang, L. V.; Xia, Y., Gold nanocages covered by smart polymers for controlled release with near-infrared light. *Nat. Mater.* **2009,** *8* (12), 935-939.

15. Boisselier, E.; Astruc, D., Gold nanoparticles in nanomedicine: preparations, imaging, diagnostics, therapies and toxicity. *Chem. Soc. Rev.* **2009,** *38* (6), 1759-1782.

16. Hu, M.; Chen, J.; Li, Z.-Y.; Au, L.; Hartland, G. V.; Li, X.; Marquez, M.; Xia, Y., Gold nanostructures: engineering their plasmonic properties for biomedical applications. *Chem. Soc. Rev.* **2006,** *35* (11), 1084-1094.

17. Jain, P. K.; Huang, X.; El-Sayed, I. H.; El-Sayed, M. A., Noble Metals on the Nanoscale: Optical and Photothermal Properties and Some Applications in Imaging, Sensing, Biology, and Medicine. *Acc. Chem. Res.* **2008,** *41* (12), 1578-1586.

18. Mulder, W. J. M.; Strijkers, G. J.; van Tilborg, G. A. F.; Cormode, D. P.; Fayad, Z. A.; Nicolay, K., Nanoparticulate Assemblies of Amphiphiles and Diagnostically Active Materials for Multimodality Imaging. *Acc. Chem. Res.* **2009,** *42* (7), 904-914.

19. Torchilin, V. P., Recent advances with liposomes as pharmaceutical carriers. *Nat. Rev. Drug Discovery* **2005,** *4* (2), 145-160.

20. Burger, K. N. J.; Staffhorst, R. W. H. M.; de Vijlder, H. C.; Velinova, M. J.; Bomans, P. H.; Frederik, P. M.; de Kruijff, B., Nanocapsules: Lipid Coated Aggregates of Cisplatin with High Toxicity. *Nat. Med.* **2002,** *8* (1), 81-84.

21. Stanimirovic, D. B.; Markovic, M.; Micic, D. V.; Spatz, M.; Mrsulja, B. B., Liposome-entrapped superoxide dismutase reduces ischemia/reperfusion 'oxidative stress' in gerbil brain. *Neurochem. Res.* **1994,** *19* (12), 1473-1478.

22. Torchilin, V. P., Surface-modified liposomes in gamma- and MR-imaging. *Adv. Drug Delivery Rev.* **1997,** *24* (2–3), 301-313.

23. Tseng, Y.-C.; Mozumdar, S.; Huang, L., Lipid-based systemic delivery of siRNA. *Adv. Drug Delivery Rev.* **2009,** *61* (9), 721-731.

24. Li, S.-D.; Huang, L., Pharmacokinetics and Biodistribution of Nanoparticles. *Mol. Pharmaceutics* **2008,** *5* (4), 496-504.

25. Chiellini, F.; Bartoli, C.; Dinucci, D.; Piras, A. M.; Anderson, R.; Croucher, T., Bioeliminable polymeric nanoparticles for proteic drug delivery. *Int. J. Pharm.* **2007,** *343* (1–2), 90-97.

26. Dai, H.; Chen, Q.; Qin, H.; Guan, Y.; Shen, D.; Hua, Y.; Tang, Y.; Xu, J., A Temperature-Responsive Copolymer Hydrogel in Controlled Drug Delivery. *Macromolecules* **2006,** *39* (19), 6584-6589.

27. Duncan, R., Polymer conjugates as anticancer nanomedicines. *Nat. Rev. Cancer* **2006,** *6* (9), 688-701.

28. Gao, D.; Xu, H.; Philbert, M. A.; Kopelman, R., Ultrafine Hydrogel Nanoparticles: Synthetic Approach and Therapeutic Application in Living Cells. *Angew. Chem. Int. Ed.* **2007,** *46* (13), 2224-2227.

29. Hamidi, M.; Azadi, A.; Rafiei, P., Hydrogel nanoparticles in drug delivery. *Adv. Drug Delivery Rev.* **2008,** *60* (15), 1638-1649.

30. Hidaka, M.; Kanematsu, T.; Ushio, K.; Sunamoto, J., Selective and Effective Cytotoxicity of Folic Acidconjugated Cholesteryl Pullulan Hydrogel Nanoparticles Complexed with Doxorubicin in *In Vitro* and *In Vivo* Studies. *J. Bioact. Compat. Polym.* **2006,** *21* (6), 591-602.

31. McAllister, K.; Sazani, P.; Adam, M.; Cho, M. J.; Rubinstein, M.; Samulski, R. J.; DeSimone, J. M., Polymeric Nanogels Produced via Inverse Microemulsion Polymerization as Potential Gene and Antisense Delivery Agents. *J. Am. Chem. Soc.* **2002,** *124* (51), 15198-15207.

32. Missirlis, D.; Kawamura, R.; Tirelli, N.; Hubbell, J. A., Doxorubicin encapsulation and diffusional release from stable, polymeric, hydrogel nanoparticles. *Eur. J. Pharm. Sci.* **2006,** *29* (2), 120-129.

33. Nayak, S.; Lyon, L. A., Soft Nanotechnology with Soft Nanoparticles. *Angew. Chem. Int. Ed.* **2005,** *44* (47), 7686-7708.

34. Sahiner, N.; Alb, A. M.; Graves, R.; Mandal, T.; McPherson, G. L.; Reed, W. F.; John, V. T., Core–shell nanohydrogel structures as tunable delivery systems. *Polymer* **2007,** *48* (3), 704-711.

35. Zeng, Y. I.; Pitt, W. G., Poly(ethylene oxide)-b0poly(N-isopropylacrylamide) nanoparticles with cross-linked cores as drug carriers. *J. Biomater. Sci., Polym. Ed.* **2005,** *16* (3), 371-380.

36. Cheng, J.; Teply, B. A.; Sherifi, I.; Sung, J.; Luther, G.; Gu, F. X.; Levy-Nissenbaum, E.; Radovic-Moreno, A. F.; Langer, R.; Farokhzad, O. C., Formulation of functionalized PLGA–PEG nanoparticles for in vivo targeted drug delivery. *Biomaterials* **2007,** *28* (5), 869-876.

37. Gupta, U.; Agashe, H. B.; Asthana, A.; Jain, N. K., A review of in vitro–in vivo investigations on dendrimers: the novel nanoscopic drug carriers. *Nanomedicine: Nanotechnol. Biol. Med.* **2006,** *2* (2), 66-73.

38. Lee, C. C.; MacKay, J. A.; Frechet, J. M. J.; Szoka, F. C., Designing dendrimers for biological applications. *Nat. Biotechnol.* **2005,** *23* (12), 1517-1526.

39. Yang, A.; Yang, L.; Liu, W.; Li, Z.; Xu, H.; Yang, X., Tumor necrosis factor alpha blocking peptide loaded PEG-PLGA nanoparticles: Preparation and in vitro evaluation. *Int. J. Pharm.* **2007,** *331* (1), 123-132.

40. Yang, H.; Lopina, S.; DiPersio, L.; Schmidt, S., Stealth dendrimers for drug delivery: correlation between PEGylation, cytocompatibility, and drug payload. *J. Mater. Sci.: Mater. Med.* **2008,** *19* (5), 1991-1997.

41. Huxford, R. C.; Della Rocca, J.; Lin, W., Metal–organic frameworks as potential drug carriers. *Curr. Opin. Chem. Biol.* **2010,** *14* (2), 262-268.

42. Lin, W.; Rieter, W. J.; Taylor, K. M. L., Modular Synthesis of Functional Nanoscale Coordination Polymers. *Angew. Chem. Int. Ed.* **2009,** *48* (4), 650-658.

43. Della Rocca, J.; Lin, W. B., Nanoscale Metal-Organic Frameworks: Magnetic Resonance Imaging Contrast Agents and Beyond. *Eur. J. Inorg. Chem.* **2010,** (24), 3725-3734.

44. Della Rocca, J.; Liu, D. M.; Lin, W. B., Nanoscale Metal-Organic Frameworks for Biomedical Imaging and Drug Delivery. *Acc. Chem. Res.* **2011,** *44* (10), 957-968.

45. An, J.; Geib, S. J.; Rosi, N. L., Cation-Triggered Drug Release from a Porous Zinc−Adeninate Metal−Organic Framework. *J. Am. Chem. Soc.* **2009,** *131* (24), 8376-8377.
46. Horcajada, P.; Chalati, T.; Serre, C.; Gillet, B.; Sebrie, C.; Baati, T.; Eubank, J. F.; Heurtaux, D.; Clayette, P.; Kreuz, C.; Chang, J.-S.; Hwang, Y. K.; Marsaud, V.; Bories, P.-N.; Cynober, L.; Gil, S.; Ferey, G.; Couvreur, P.; Gref, R., Porous metal-organic-framework nanoscale carriers as a potential platform for drug delivery and imaging. *Nat. Mater.* **2010,** *9* (2), 172-178.

47. Horcajada, P.; Serre, C.; Maurin, G.; Ramsahye, N. A.; Balas, F.; Vallet-Regí, M. a.; Sebban, M.; Taulelle, F.; Férey, G. r., Flexible Porous Metal-Organic Frameworks for a Controlled Drug Delivery. *J. Am. Chem. Soc.* **2008,** *130* (21), 6774-6780.
48. Horcajada, P.; Serre, C.; Vallet-Regí, M.; Sebban, M.; Taulelle, F.; Férey, G., Metal–Organic Frameworks as Efficient Materials for Drug Delivery. *Angew. Chem. Int. Ed.* **2006,** *45* (36), 5974-5978.

49. Jin, Y.; Li, A.; Hazelton, S. G.; Liang, S.; John, C. L.; Selid, P. D.; Pierce, D. T.; Zhao, J. X., Amorphous silica nanohybrids: Synthesis, properties and applications. *Coord. Chem. Rev.* **2009,** *253* (23–24), 2998-3014.

50. Wang, L.; Wang, K.; Santra, S.; Zhao, X.; Hilliard, L. R.; Smith, J. E.; Wu, Y.; Tan, W., Watching Silica Nanoparticles Glow in the Biological World. *Anal. Chem.* **2006,** *78* (3), 646-654.

51. Wang, L.; Zhao, W.; Tan, W., Bioconjugated silica nanoparticles: Development and applications. *Nano Res.* **2008,** *1* (2), 99-115.

52. Stöber, W.; Fink, A.; Bohn, E., Controlled growth of monodisperse silica spheres in the micron size range. *J. Colloid Interface Sci.* **1968,** *26* (1), 62-69.

53. Wang, X.-D.; Shen, Z.-X.; Sang, T.; Cheng, X.-B.; Li, M.-F.; Chen, L.-Y.; Wang, Z.-S., Preparation of spherical silica particles by Stöber process with high concentration of tetra-ethyl-orthosilicate. *J. Colloid Interface Sci.* **2010,** *341* (1), 23-29.

54. Arriagada, F. J.; Osseo-Asare, K., Phase and dispersion stability effects in the synthesis of silica nanoparticles in a non-ionic reverse microemulsion. *Colloid Surf.* **1992,** *69* (2–3), 105-115.

55. Arriagada, F. J.; Osseo-Asare, K., Synthesis of Nanosize Silica in a Nonionic Water-in-Oil Microemulsion: Effects of the Water/Surfactant Molar Ratio and Ammonia Concentration. *J. Colloid Interface Sci.* **1999,** *211* (2), 210-220.

56. Rieter, W. J.; Kim, J. S.; Taylor, K. M. L.; An, H.; Lin, W.; Tarrant, T.; Lin, W., Hybrid Silica Nanoparticles for Multimodal Imaging. *Angew. Chem. Int. Ed.* **2007,** *46* (20), 3680-3682.

57. Chung, Y.; Jeon, M.; Kim, C., Fabrication of nearly monodispersed silica nanoparticles by using poly(1-vinyl-2-pyrrolidinone) and their application to the preparation of nanocomposites. *Macromol. Res.* **2009,** *17* (1), 37-43.

58. Bagwe, R. P.; Yang, C.; Hilliard, L. R.; Tan, W., Optimization of Dye-Doped Silica Nanoparticles Prepared Using a Reverse Microemulsion Method. *Langmuir* **2004,** *20* (19), 8336-8342.

59. Bridot, J.-L.; Faure, A.-C.; Laurent, S.; Rivière, C.; Billotey, C.; Hiba, B.; Janier, M.; Josserand, V.; Coll, J.-L.; Vander Elst, L.; Muller, R.; Roux, S.; Perriat, P.; Tillement, O., Hybrid Gadolinium Oxide Nanoparticles: Multimodal Contrast Agents for in Vivo Imaging. *J. Am. Chem. Soc.* **2007,** *129* (16), 5076-5084.

60. Gerion, D.; Herberg, J.; Bok, R.; Gjersing, E.; Ramon, E.; Maxwell, R.; Kurhanewicz, J.; Budinger, T. F.; Gray, J. W.; Shuman, M. A.; Chen, F. F., Paramagnetic Silica-Coated Nanocrystals as an Advanced MRI Contrast Agent. *J. Phys. Chem. C* **2007,** *111* (34), 12542-12551.

61. Ma, D.; Guan, J.; Dénommée, S.; Enright, G.; Veres, T.; Simard, B., Multifunctional Nano-Architecture for Biomedical Applications. *Chem. Mater.* **2006,** *18* (7), 1920-1927.

62. Slowing, I. I.; Vivero-Escoto, J. L.; Wu, C.-W.; Lin, V. S. Y., Mesoporous silica nanoparticles as controlled release drug delivery and gene transfection carriers. *Adv. Drug Delivery Rev.* **2008,** *60* (11), 1278-1288.

63. Trewyn, B. G.; Slowing, I. I.; Giri, S.; Chen, H.-T.; Lin, V. S. Y., Synthesis and Functionalization of a Mesoporous Silica Nanoparticle Based on the Sol–Gel Process and Applications in Controlled Release. *Acc. Chem. Res.* **2007,** *40* (9), 846-853.

64. Kresge, C. T.; Leonowicz, M. E.; Roth, W. J.; Vartuli, J. C.; Beck, J. S., Ordered mesoporous molecular sieves synthesized by a liquid-crystal template mechanism. *Nature* **1992,** *359* (6397), 710-712.

65. Cai, Q.; Luo, Z.-S.; Pang, W.-Q.; Fan, Y.-W.; Chen, X.-H.; Cui, F.-Z., Dilute Solution Routes to Various Controllable Morphologies of MCM-41 Silica with a Basic Medium†. *Chem. Mater.* **2001,** *13* (2), 258-263.

66. Grün, M.; Unger, K. K.; Matsumoto, A.; Tsutsumi, K., Novel pathways for the preparation of mesoporous MCM-41 materials: control of porosity and morphology. *Microporous Mesporous Mater.* **1999,** *27* (2–3), 207-216.

67. Chen, H.-T.; Huh, S.; Wiench, J. W.; Pruski, M.; Lin, V. S. Y., Dialkylaminopyridine-Functionalized Mesoporous Silica Nanosphere as an Efficient and Highly Stable Heterogeneous Nucleophilic Catalyst. *J. Am. Chem. Soc.* **2005,** *127* (38), 13305-13311.

68. Mihalcik, D. J.; Lin, W., Mesoporous Silica Nanosphere Supported Ruthenium Catalysts for Asymmetric Hydrogenation. *Angew. Chem. Int. Ed.* **2008,** *47* (33), 6229-6232.

69. Slowing, I.; Trewyn, B. G.; Lin, V. S. Y., Effect of Surface Functionalization of MCM-41-Type Mesoporous Silica Nanoparticles on the Endocytosis by Human Cancer Cells. *J. Am. Chem. Soc.* **2006,** *128* (46), 14792-14793.

70. Argyo, C.; Cauda, V.; Engelke, H.; Rädler, J.; Bein, G.; Bein, T., Heparin-Coated Colloidal Mesoporous Silica Nanoparticles Efficiently Bind to Antithrombin as an Anticoagulant Drug-Delivery System. *Chem.-Eur. J.* **2012,** *18* (2), 428-432.

71. Kim, J.; Kim, H. S.; Lee, N.; Kim, T.; Kim, H.; Yu, T.; Song, I. C.; Moon, W. K.; Hyeon, T., Multifunctional Uniform Nanoparticles Composed of a Magnetite Nanocrystal Core and a Mesoporous Silica Shell for Magnetic Resonance and Fluorescence Imaging and for Drug Delivery. *Angew. Chem. Int. Ed.* **2008,** *47* (44), 8438-8441.

72. Liong, M.; Lu, J.; Kovochich, M.; Xia, T.; Ruehm, S. G.; Nel, A. E.; Tamanoi, F.; Zink, J. I., Multifunctional Inorganic Nanoparticles for Imaging, Targeting, and Drug Delivery. *ACS Nano* **2008,** *2* (5), 889-896.

73. Taylor, K. M. L.; Kim, J. S.; Rieter, W. J.; An, H.; Lin, W.; Lin, W., Mesoporous Silica Nanospheres as Highly Efficient MRI Contrast Agents. *J. Am. Chem. Soc.* **2008,** *130* (7), 2154-2155.

74. Taylor-Pashow, K. M. L.; Della Rocca, J.; Lin, W. B., Mesoporous Silica Nanoparticles with Co-condensed Gadolinium Chelates for Multimodal Imaging. *Nanomaterials* **2012,** *2* (1), 1-14.

75. Vivero-Escoto, J. L.; Taylor-Pashow, K. M. L.; Huxford, R. C.; Della Rocca, J.; Okoruwa, C.; An, H.; Lin, W.; Lin, W., Multifunctional Mesoporous Silica Nanospheres with Cleavable Gd(III) Chelates as MRI Contrast Agents: Synthesis, Characterization, Target-Specificity, and Renal Clearance. *Small* **2011,** *7* (24), 3519-3528.

76. Huh, S.; Wiench, J. W.; Trewyn, B. G.; Song, S.; Pruski, M.; Lin, V. S. Y., Tuning of particle morphology and pore properties in mesoporous silicas with multiple organic functional groups. *Chem. Commun. (Cambridge, UK)* **2003,** (18), 2364-2365.

77. Huh, S.; Wiench, J. W.; Yoo, J.-C.; Pruski, M.; Lin, V. S. Y., Organic Functionalization and Morphology Control of Mesoporous Silicas via a Co-Condensation Synthesis Method. *Chem. Mater.* **2003,** *15* (22), 4247-4256.

78. Spokoyny, A. M.; Kim, D.; Sumrein, A.; Mirkin, C. A., Infinite coordination polymer nano- and microparticle structures. *Chem. Soc. Rev.* **2009,** *38* (5), 1218-1227.

79. Rieter, W. J.; Pott, K. M.; Taylor, K. M. L.; Lin, W., Nanoscale Coordination Polymers for Platinum-Based Anticancer Drug Delivery. *J. Am. Chem. Soc.* **2008,** *130* (35), 11584-11585.

80. Taylor-Pashow, K. M. L.; Della Rocca, J.; Xie, Z.; Tran, S.; Lin, W., Postsynthetic Modifications of Iron-Carboxylate Nanoscale Metal−Organic Frameworks for Imaging and Drug Delivery. *J. Am. Chem. Soc.* **2009,** *131* (40), 14261-14263.

81. Tanaka, D.; Kitagawa, S., Template Effects in Porous Coordination Polymers. *Chem. Mater.* **2007,** *20* (3), 922-931.

82. Rieter, W. J.; Taylor, K. M. L.; An, H.; Lin, W.; Lin, W., Nanoscale Metal−Organic Frameworks as Potential Multimodal Contrast Enhancing Agents. *J. Am. Chem. Soc.* **2006,** *128* (28), 9024-9025.

83. Taylor, K. M. L.; Jin, A.; Lin, W., Surfactant-Assisted Synthesis of Nanoscale Gadolinium Metal–Organic Frameworks for Potential Multimodal Imaging. *Angew. Chem. Int. Ed.* **2008,** *47* (40), 7722-7725.

84. Liu, D.; Huxford, R. C.; Lin, W., Phosphorescent Nanoscale Coordination Polymers as Contrast Agents for Optical Imaging. *Angew. Chem. Int. Ed.* **2011,** *50* (16), 3696-3700.

85. Rieter, W. J.; Taylor, K. M. L.; Lin, W., Surface Modification and Functionalization of Nanoscale Metal-Organic Frameworks for Controlled Release and Luminescence Sensing. *J. Am. Chem. Soc.* **2007,** *129* (32), 9852-9853.

86. Taylor, K. M. L.; Rieter, W. J.; Lin, W., Manganese-Based Nanoscale Metal−Organic Frameworks for Magnetic Resonance Imaging. *J. Am. Chem. Soc.* **2008,** *130* (44), 14358-14359.

87. Huxford, R. C.; deKrafft, K. E.; Boyle, W. S.; Liu, D.; Lin, W., Lipid-coated nanoscale coordination polymers for targeted delivery of antifolates to cancer cells. *Chem. Sci.* **2012,** *3* (1), 198-204.

88. Rowe, M. D.; Chang, C.-C.; Thamm, D. H.; Kraft, S. L.; Harmon, J. F.; Vogt, A. P.; Sumerlin, B. S.; Boyes, S. G., Tuning the Magnetic Resonance Imaging Properties of Positive Contrast Agent Nanoparticles by Surface Modification with RAFT Polymers. *Langmuir* **2009,** *25* (16), 9487-9499.

89. Rowe, M. D.; Thamm, D. H.; Kraft, S. L.; Boyes, S. G., Polymer-Modified Gadolinium Metal-Organic Framework Nanoparticles Used as Multifunctional Nanomedicines for the Targeted Imaging and Treatment of Cancer. *Biomacromolecules* **2009,** *10* (4), 983-993.

90. Kim, S.; Ohulchanskyy, T. Y.; Pudavar, H. E.; Pandey, R. K.; Prasad, P. N., Organically Modified Silica Nanoparticles Co-encapsulating Photosensitizing Drug and Aggregation-Enhanced Two-Photon Absorbing Fluorescent Dye Aggregates for Two-Photon Photodynamic Therapy. *J. Am. Chem. Soc.* **2007,** *129* (9), 2669-2675.

91. Ohulchanskyy, T. Y.; Roy, I.; Goswami, L. N.; Chen, Y.; Bergey, E. J.; Pandey, R. K.; Oseroff, A. R.; Prasad, P. N., Organically Modified Silica Nanoparticles with Covalently Incorporated Photosensitizer for Photodynamic Therapy of Cancer. *Nano Lett.* **2007,** *7* (9), 2835-2842.

92. Bharali, D. J.; Klejbor, I.; Stachowiak, E. K.; Dutta, P.; Roy, I.; Kaur, N.; Bergey, E. J.; Prasad, P. N.; Stachowiak, M. K., Organically modified silica nanoparticles: A nonviral vector for in vivo gene delivery and expression in the brain. *Proc. Natl. Acad. Sci. U.S.A.* **2005,** *102* (32), 11539-11544.

93. Hom, C.; Lu, J.; Tamanoi, F., Silica nanoparticles as a delivery system for nucleic acid-based reagents. *J. Mater. Chem.* **2009,** *19* (35), 6308-6316.

94. Mintzer, M. A.; Simanek, E. E., Nonviral Vectors for Gene Delivery. *Chem. Rev. (Washington, DC, U.S.)* **2008,** *109* (2), 259-302.

95. Roy, I.; Ohulchanskyy, T. Y.; Bharali, D. J.; Pudavar, H. E.; Mistretta, R. A.; Kaur, N.; Prasad, P. N., Optical tracking of organically modified silica nanoparticles as DNA carriers: A nonviral, nanomedicine approach for gene delivery. *Proc. Natl. Acad. Sci. U.S.A.* **2005,** *102* (2), 279-284.

96. Sokolova, V.; Epple, M., Inorganic Nanoparticles as Carriers of Nucleic Acids into Cells. *Angew. Chem. Int. Ed.* **2008,** *47* (8), 1382-1395.

97. Yan, E.; Ding, Y.; Chen, C.; Li, R.; Hu, Y.; Jiang, X., Polymer/silica hybrid hollow nanospheres with pH-sensitive drug release in physiological and intracellular environments. *Chem. Commun. (Cambridge, UK)* **2009,** (19), 2718-2720.

98. Deng, Z.; Zhen, Z.; Hu, X.; Wu, S.; Xu, Z.; Chu, P. K., Hollow chitosan–silica nanospheres as pH-sensitive targeted delivery carriers in breast cancer therapy. *Biomaterials* **2011,** *32* (21), 4976-4986.

99. Corma, A.; Díaz, U.; Arrica, M.; Fernández, E.; Ortega, Í., Organic–Inorganic Nanospheres with Responsive Molecular Gates for Drug Storage and Release. *Angew. Chem. Int. Ed.* **2009,** *48* (34), 6247-6250.

100. Botella, P.; Abasolo, I.; Fernández, Y.; Muniesa, C.; Miranda, S.; Quesada, M.; Ruiz, J.; Schwartz Jr, S.; Corma, A., Surface-modified silica nanoparticles for tumor-targeted delivery of camptothecin and its biological evaluation. *J. Controlled Release* **2011,** *156* (2), 246-257.

101. Mortera, R.; Vivero-Escoto, J.; Slowing, I. I.; Garrone, E.; Onida, B.; Lin, V. S. Y., Cell-induced intracellular controlled release of membrane impermeable cysteine from a mesoporous silica nanoparticle-based drug delivery system. *Chem. Commun. (Cambridge, UK)* **2009,** (22), 3219-3221.

102. Vivero-Escoto, J. L.; Slowing, I. I.; Wu, C.-W.; Lin, V. S. Y., Photoinduced Intracellular Controlled Release Drug Delivery in Human Cells by Gold-Capped Mesoporous Silica Nanosphere. *J. Am. Chem. Soc.* **2009,** *131* (10), 3462-3463.

103. Giri, S.; Trewyn, B. G.; Stellmaker, M. P.; Lin, V. S. Y., Stimuli-Responsive Controlled-Release Delivery System Based on Mesoporous Silica Nanorods Capped with Magnetic Nanoparticles. *Angew. Chem. Int. Ed.* **2005,** *44* (32), 5038-5044.

104. Lai, C.-Y.; Trewyn, B. G.; Jeftinija, D. M.; Jeftinija, K.; Xu, S.; Jeftinija, S.; Lin, V. S. Y., A Mesoporous Silica Nanosphere-Based Carrier System with Chemically Removable CdS Nanoparticle Caps for Stimuli-Responsive Controlled Release of Neurotransmitters and Drug Molecules. *J. Am. Chem. Soc.* **2003,** *125* (15), 4451-4459.

105. Zhao, Y.; Trewyn, B. G.; Slowing, I. I.; Lin, V. S. Y., Mesoporous Silica Nanoparticle-Based Double Drug Delivery System for Glucose-Responsive Controlled Release of Insulin and Cyclic AMP. *J. Am. Chem. Soc.* **2009,** *131* (24), 8398-8400.

106. Liu, R.; Zhao, X.; Wu, T.; Feng, P., Tunable Redox-Responsive Hybrid Nanogated Ensembles. *J. Am. Chem. Soc.* **2008,** *130* (44), 14418-14419.

107. Lu, J.; Choi, E.; Tamanoi, F.; Zink, J. I., Light-Activated Nanoimpeller-Controlled Drug Release in Cancer Cells. *Small* **2008,** *4* (4), 421-426.

108. Zhu, C.-L.; Song, X.-Y.; Zhou, W.-H.; Yang, H.-H.; Wen, Y.-H.; Wang, X.-R., An efficient cell-targeting and intracellular controlled-release drug delivery system based on MSN-PEM-aptamer conjugates. *J. Mater. Chem.* **2009,** *19* (41), 7765-7770.

109. Liu, J.; Stace-Naughton, A.; Jiang, X.; Brinker, C. J., Porous Nanoparticle Supported Lipid Bilayers (Protocells) as Delivery Vehicles. *J. Am. Chem. Soc.* **2009,** *131* (4), 1354-1355.

110. Liu, J.; Jiang, X.; Ashley, C.; Brinker, C. J., Electrostatically Mediated Liposome Fusion and Lipid Exchange with a Nanoparticle-Supported Bilayer for Control of Surface Charge, Drug Containment, and Delivery. *J. Am. Chem. Soc.* **2009,** *131* (22), 7567-7569.

111. Ashley, C. E.; Carnes, E. C.; Phillips, G. K.; Padilla, D.; Durfee, P. N.; Brown, P. A.; Hanna, T. N.; Liu, J.; Phillips, B.; Carter, M. B.; Carroll, N. J.; Jiang, X.; Dunphy, D. R.; Willman, C. L.; Petsev, D. N.; Evans, D. G.; Parikh, A. N.; Chackerian, B.; Wharton, W.; Peabody, D. S.; Brinker, C. J., The targeted delivery of multicomponent cargos to cancer cells by nanoporous particle-supported lipid bilayers. *Nat. Mater.* **2011,** *10* (5), 389-397.

112. Liu, J.; Stace-Naughton, A.; Brinker, C. J., Silica nanoparticle supported lipid bilayers for gene delivery. *Chem. Commun. (Cambridge, UK)* **2009,** (34), 5100-5102.

113. Janib, S. M.; Moses, A. S.; MacKay, J. A., Imaging and drug delivery using theranostic nanoparticles. *Adv. Drug Delivery Rev.* **2010,** *62* (11), 1052-1063.

114. He, X.; Wu, X.; Wang, K.; Shi, B.; Hai, L., Methylene blue-encapsulated phosphonate-terminated silica nanoparticles for simultaneous in vivo imaging and photodynamic therapy. *Biomaterials* **2009,** *30* (29), 5601-5609.

115. Roy, I.; Ohulchanskyy, T. Y.; Pudavar, H. E.; Bergey, E. J.; Oseroff, A. R.; Morgan, J.; Dougherty, T. J.; Prasad, P. N., Ceramic-Based Nanoparticles Entrapping Water-Insoluble Photosensitizing Anticancer Drugs: A Novel Drug−Carrier System for Photodynamic Therapy. *J. Am. Chem. Soc.* **2003,** *125* (26), 7860-7865.

116. Lee, J. E.; Lee, N.; Kim, H.; Kim, J.; Choi, S. H.; Kim, J. H.; Kim, T.; Song, I. C.; Park, S. P.; Moon, W. K.; Hyeon, T., Uniform Mesoporous Dye-Doped Silica Nanoparticles Decorated with Multiple Magnetite Nanocrystals for Simultaneous Enhanced Magnetic Resonance Imaging, Fluorescence Imaging, and Drug Delivery. *J. Am. Chem. Soc.* **2009,** *132* (2), 552-557.

117. Lee, J. E.; Lee, D. J.; Lee, N.; Kim, B. H.; Choi, S. H.; Hyeon, T., Multifunctional mesoporous silica nanocomposite nanoparticles for pH controlled drug release and dual modal imaging. *J. Mater. Chem.* **2011,** *21* (42), 16869-16872.

118. Lu, J.; Liong, M.; Li, Z.; Zink, J. I.; Tamanoi, F., Biocompatibility, Biodistribution, and Drug-Delivery Efficiency of Mesoporous Silica Nanoparticles for Cancer Therapy in Animals. *Small* **2010,** *6* (16), 1794-1805.

119. Lai, C.-W.; Wang, Y.-H.; Lai, C.-H.; Yang, M.-J.; Chen, C.-Y.; Chou, P.-T.; Chan, C.-S.; Chi, Y.; Chen, Y.-C.; Hsiao, J.-K., Iridium-Complex-Functionalized Fe3O4/SiO2 Core/Shell Nanoparticles: A Facile Three-in-One System in Magnetic Resonance Imaging, Luminescence Imaging, and Photodynamic Therapy. *Small* **2008,** *4* (2), 218-224.

Chapter 2:

Polysilsesquioxane Nanoparticles for Targeted Oxaliplatin-Based Cancer Chemotherapy by Triggered Release

2.1 Introduction

Since the discovery of cisplatin by Rosenberg in the 1960's, platinum anticancer drugs have played an important role in cancer chemotherapy.[1] Cisplatin is used to treat a variety of cancers such as testicular, lung, breast, and ovarian cancer. The success of cisplatin has led to the synthesis and biological evaluation of thousands of platinum complexes; however, only two additional complexes−carboplatin and oxaliplatin−are approved for clinical use by the FDA.[2-4] The clinical efficacy of platinum-based anticancer drugs is limited by their poor pharmacokinetic properties. High doses of platins are needed, which often lead to severe side effects. Furthermore, many tumors display inherent or acquired resistance to platinum-based therapies. There exists a need to develop alternative strategies to effectively deliver, with fewer side effects, platinum drugs to the tumor.

Nanomaterials offer one possible solution. Nanoparticulate imaging and therapeutic agents have several advantages over traditional small molecule agents, including high agent loading, tunable size, tailorable surface properties, controllable drug release kinetics, and improved pharmacokinetics. [5-12] Nanoparticles also tend to have increased accumulation in tumors as a result of the enhanced permeability and retention (EPR) effect that results from

the leaky tumor neovasculatures. Additionally, nanoparticles can be specifically targeted to cancer cells by surface conjugation of an appropriate ligand to further enhance their tumor accumulation. The clinical success of nanoparticle therapeutics such as Doxil illustrates the potential of nanomaterials in anticancer drug delivery. Our lab has previously developed nanoscale coordination polymers (NCP) as a potential delivery vehicle for cisplatin prodrugs.[13-14] These materials demonstrated high agent loading and comparable cytotoxicity to cisplatin *in vitro*. However, these materials readily degrade under physiological conditions, limiting their potential for *in vivo* applications. We sought to develop a new nanoparticle platform which would possess minimal drug release and nanoparticle decomposition when circulating in the blood stream, but would also readily release the drugs upon cellular internalization. This chapter describes the development of bridged polysilsesquioxane (PSQ) nanoparticles as a platform for oxaliplatin delivery.

PSQs are a type of hybrid material composed of silsesquioxane networks with organic or metal-organic bridging ligands. These materials are synthesized from bis-trialkoxysilanes [$(R'O)_3$-Si-R-Si-$(OR')_3$] by sol-gel chemistry.[15-17] PSQs have been well studied as bulk materials for a number of applications, but have only recently been prepared as nanomaterials.[18-22] PSQs offer similar biocompatiblity as silica-based materials, which have been extensively studied for biomedical applications.[23-26] However, as a homopolymer of $(R'O)_3$-Si-R-Si-$(OR')_3$, PSQ materials allow much higher drug loadings than silica-based materials with grafted drugs only on their surfaces. The physicochemical properties of PSQ materials can be more easily tuned by changing the monomer properties than in a silica-based material.

The goal of this research is to develop PSQ nanoparticles for the delivery of platinum anticancer drugs based on the FDA-approved anticancer drug oxaliplatin. The development of these PSQ nanoparticles starts with the synthesis of a platinum(IV) precursor molecule. The platinum complex is then polymerized within an anionic reverse microemulsion to form the PSQ nanoparticles. The PSQ nanoparticles are then post-synthetically modified to include either a cancer targeting peptide or a passivating polymer. The functionalized nanoparticles are then evaluated *in vitro* against a panel of cancer cell lines and *in vivo* against two mouse xenograft models.

2.2 Results and Discussion

2.2.1 Synthesis of Platinum Complexes

The platinum(IV) complex Pt(dach)Cl_2(triethoxysilylpropyl succinate)$_2$ (dachPtSi, where dach = *R*,*R*-diaminocyclohexane) was synthesized starting from the readily available platinum(II) starting material, $K_2[PtCl_4]$, by following established procedures with minor modifications (Scheme 2-1).[27-30] First, $K_2[PtCl_4]$ was converted into Pt(dach)Cl_2 in high yield (typically ≈95 %) by a modification of Dhara's procedure for the synthesis of cisplatin, going through an isolatable Pt(dach)I_2 intermediate complex (Scheme 2-1, steps 1 and 2).[27] Pt(dach)Cl_2 could then be oxidized to Pt(dach)$Cl_2(OH)_2$ with hydrogen peroxide in water (Scheme 2-1, step 3). The platinum complex dachPtSi was synthesized in 50-60% yield by reacting Pt(dach)$Cl_2(OH)_2$ with excess triethoxysilylpropyl succinic anhydride in DMSO (Scheme 2-1, step 4). The OH groups on Pt(dach)$Cl_2(OH)_2$ act as nucleophiles and add to the electrophilic carbonyl carbons within the anhydride. The dachPtSi monomer contains a platinum(IV) complex, which is known to be inert under non-reducing conditions, but will be rapidly reduced by endogenous molecules to the active Pt(II) complex.[31] Additionally,

dachPtSi contains orthogonal carboxylic acid functionalities, which can be used to modify the nanoparticle post-synthetically.

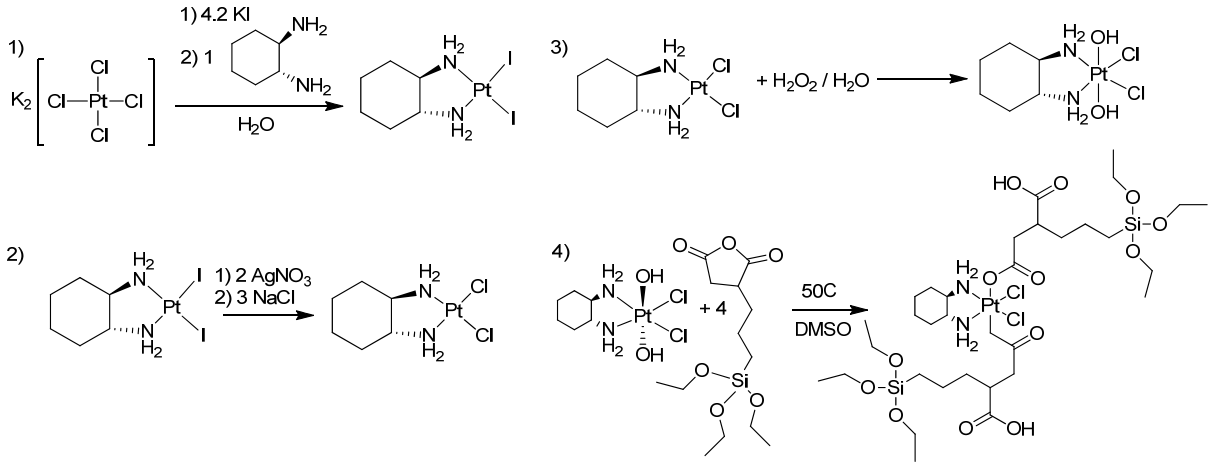

Scheme 2-1: Synthesis of platinum complexes used for the synthesis of the PSQ nanoparticle **2.1.**

2.2.2 Synthesis of PSQ nanoparticle 2.1

PSQ nanoparticles **2.1** were synthesized by base-catalyzed sol-gel polymerization in an anionic reverse microemulsion (Scheme 2-2). Briefly, dachPtSi (29 μmol) was dissolved in 3.75 mL of ammonium hydroxide solution. This solution was then added to 125 mL of 0.3 M docusate sodium salt in hexanes. After 24 hours of reaction, the nanoparticles were precipitated from the reverse microemulsion by the addition of an equal volume of ethanol. Particles of **2.1** were isolated by centrifugation and washed repeatedly with ethanol. The particle size and morphology could be tuned by adjusting the reaction time, water to surfactant molar ratio (w), and the concentration of ammonia or Pt complex in the aqueous phase. The nanoparticles of **2.1** were characterized by transmission electron microscopy (TEM), dynamic light scattering (DLS), thermogravimetric analysis (TGA), and inductively-coupled plasma mass spectrometry (ICP-MS). As shown in Figure 2-1, TEM analysis of **2.1**

showed spherical nanoparticles of 50-100 nm in diameter. The nanoparticles appear to be aggregated on the TEM slides, but this aggregation is induced by solvent evaporation. DLS measurements of **2.1** gave an average diameter of 78 nm (PDI: 0.074) (Figure 2-2, Table 2-1). The zeta potential of **2.1** was -20.7 mV in PBS. TGA analysis gave 48% weight loss for the organics (Figure 2-3), which is slightly lower than 52% expected for the homopolymer of dachPtSi. We believe that the lower weight loss can be attributed to the presence of sodium ions in **2.1** (from the surfactant used in the synthesis), which was confirmed by energy dispersive X-ray spectroscopic (EDS) measurements. ICP-MS measurements of **2.1** gave a Pt loading of 18-24 wt% by weight (expected 24 wt% for the homopolymer), yielding an active agent loading [$Pt(dach)Cl_2$] of 35-47 wt%. Each particle of **2.1** contains approximately 1.5×10^5 $Pt(dach)Cl_2$ molecules, which is several thousand times the drug loading of known nanoparticle platforms that deliver Pt(IV) prodrugs.[32-36]

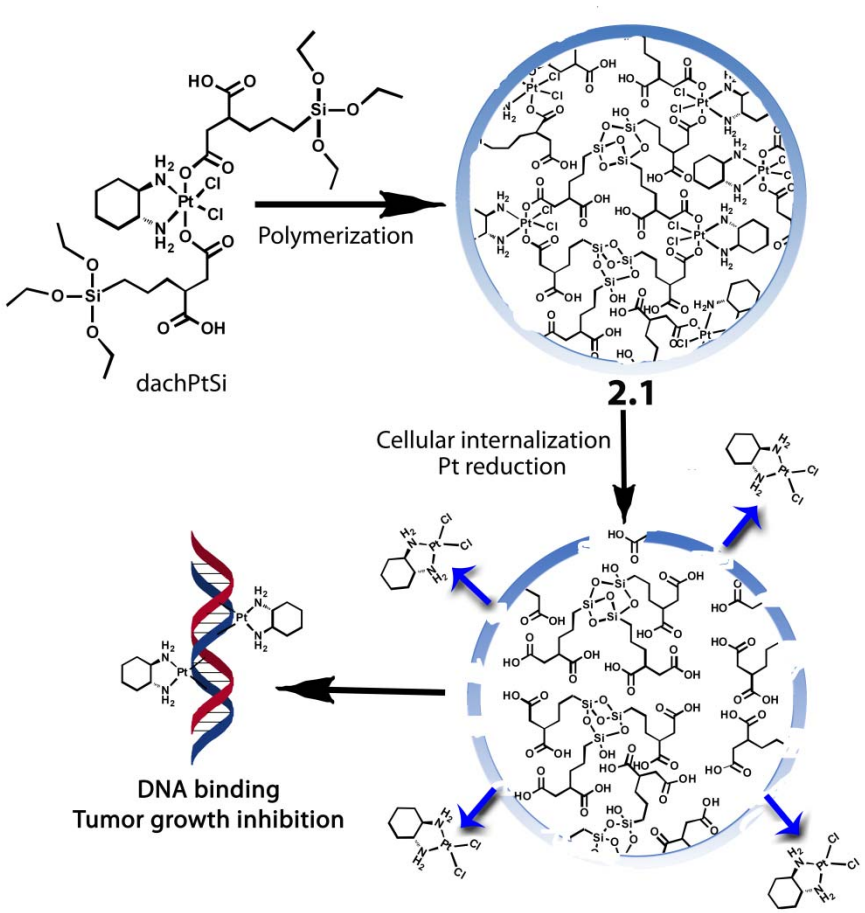

Scheme 2-2: Schematic demonstrating the synthesis, platinum release and tumor growth inhibition mechanism of **2.1**

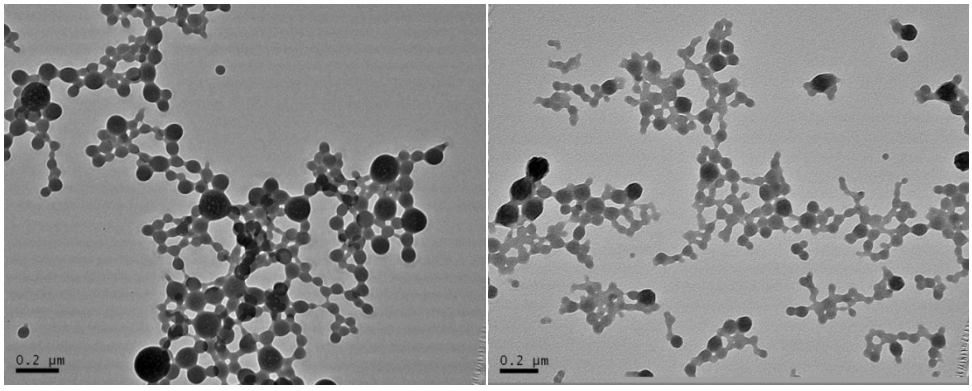

Figure 2-1: TEM micrographs of **2.1**

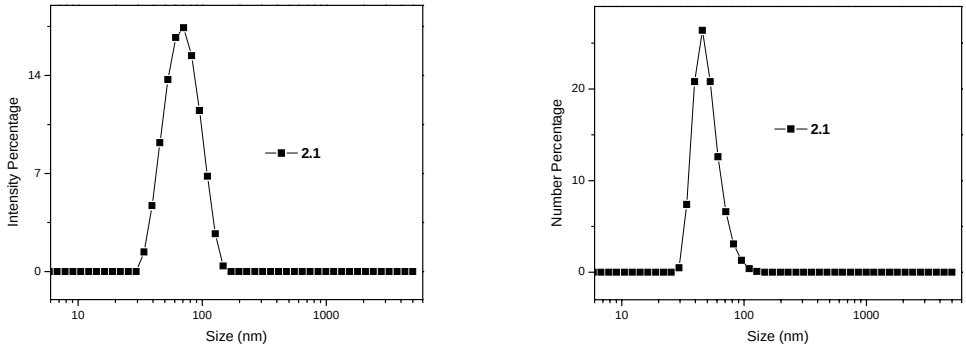

Figure 2-2: Intensity(left) and number (right) weighted DLS spectra of **2.1**

Table 2-1: Hydrodynamic diameters and zeta potential of various forms of **2.1** in PBS

Particle ID	Zavg (nm)	PDI	Intensity Average (nm)	Number Average (nm)	Zeta Potential (mV)
2.1	77.8 ± 0.3	0.07 ± 0.01	84.5 ± 0.3	62.3 ± 0.2	-20.7 ±1.4
Rhod-**2.1**	105.2 ± 0.5	0.09 ± 0.19	113.9 ± 0.8	90.3 ± 3	-21.8 ±1.1
RGD-**2.1**	100.0±2.3	0.25± 0.05	102.9± 1.8	97.5±7.7	-18.2
PEG-**2.1**	91.3±6.2	0.15± 0.03	95.2± 6.2	82.8±2.9	-5.5± 1.3
APEG-**2.1**	92.6± 0.4	0.16 ± 0.05	94.8± 9.8	81.6±7.8	-5.0± 1.4

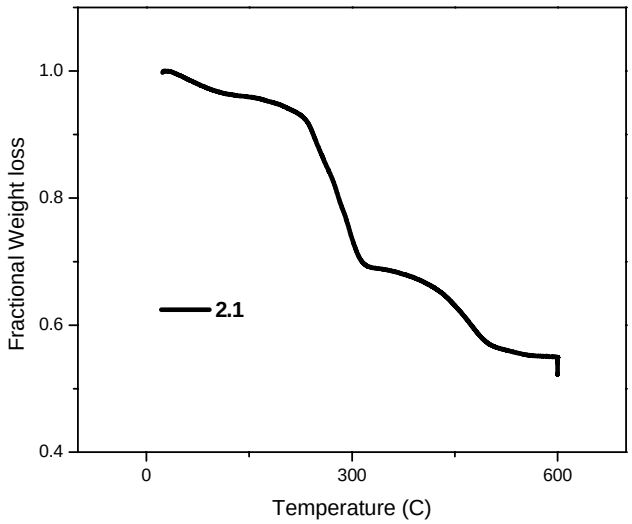

Figure 2-3: TGA weight loss curve for **2.1**.

Dye-doped particles of **2.1** (rhod-**2.1**) were obtained by incorporating a fraction of silyl-derived rhodamine B into the microemulsion during the synthesis. Particles of rhod-**2.1** had a similar size distribution as **1** (Figures 2-4 and 2-5, Table 2.-) but contained rhodamine B to facilitate confocal imaging studies. Rhod-**2.1** had a slightly higher TGA weight loss as expected due to the incorporation of the organic dye (Figure 2-6) in the synthesis and also was fluorescent in the same wavelengths as the free dye (Figure 2-7).

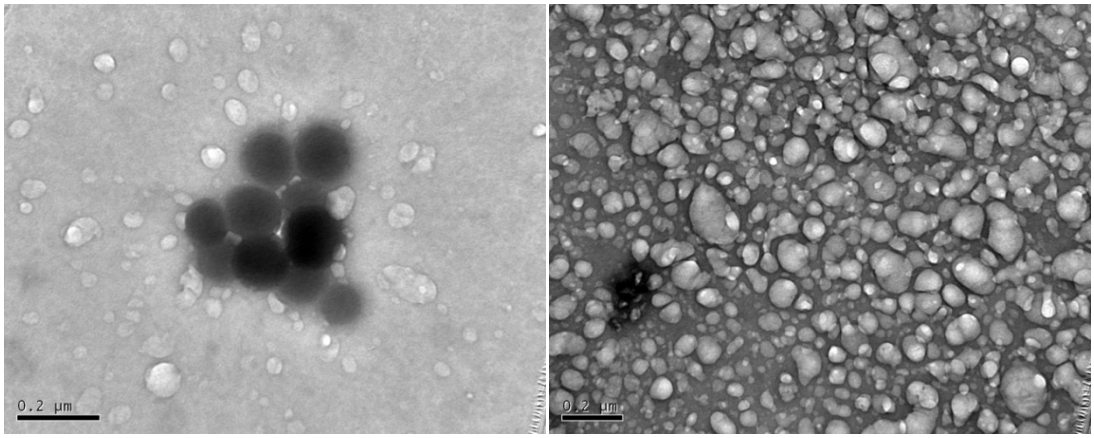

Figure 2-4: TEM micrographs of rhod-**2.1**

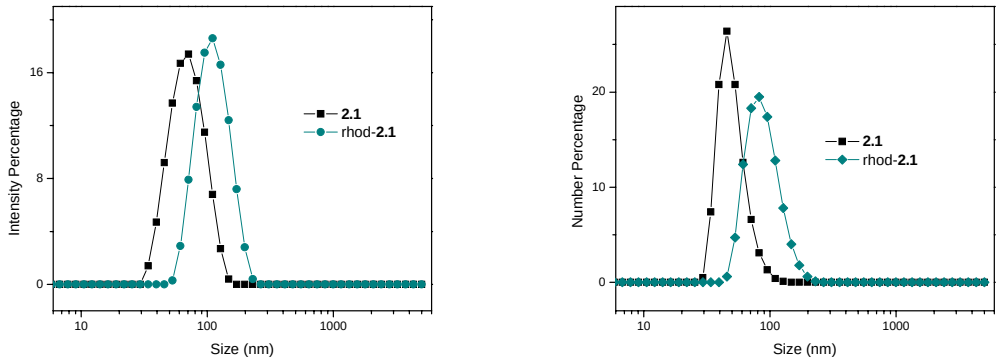

Figure 2-5: Intensity (left) and number (right) weighted DLS spectra of **2.1** (black) and rhod-**2.1** (cyan) in PBS.

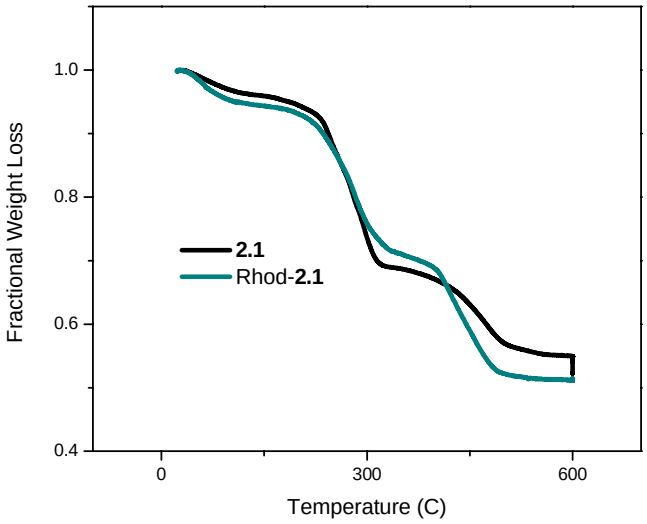

Figure 2-6: TGA weight loss curves for **2.1** (black) and rhod-**2.1** (cyan).

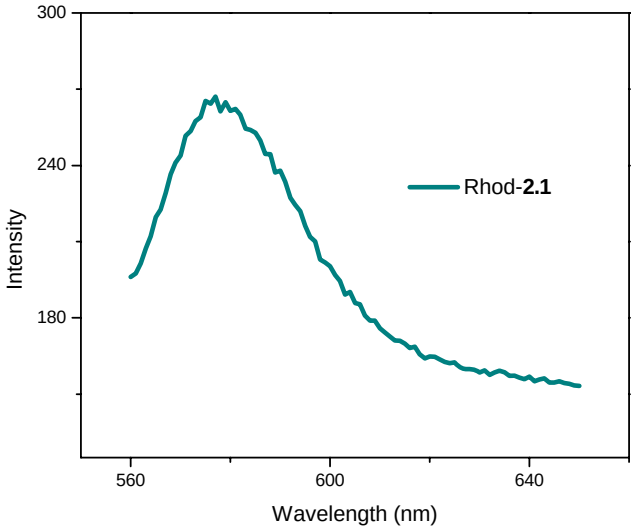

Figure 2-7: Fluorescence spectra of rhod-**2.1** as a dispersion in PBS. The excitation wavelength was 555 nm.

2.2.3 Platinum release from Nanoparticle 2.1

We expect that **2.1** will be stable under normal physiological conditions, but the Pt(IV) prodrug in **2.1** can be rapidly reduced by endogenous biomolecules, such as glutathione and cysteine, to release (dach)$PtCl_2$, which can then undergo hydrolysis (assisted by the low intracellular Cl^- concentration) and DNA binding (Scheme 2.2). Release profile experiments revealed that **1** is stable in the absence of a reducing agent, with only 10% background release over 24 h (Figure 2.8). However, with the addition of 10 mM cysteine, ~30% of the platin cargo was quickly released, followed by a more gradual release of the cargo. ~80% of the payload was released after two days of incubation with cysteine. When in circulation, **2.1** would only encounter low concentrations of reducing agents (typically μM concentrations), so only a small amount of platinum would be released nonspecifically. However, the tumor microenvironment is generally highly reducing, so Pt(dach)Cl_2 would be released locally to provide cancer chemotherapy. Also cellular endosomes have millimolar concentrations of reducing agents, so the platinum payload would also be released after endocytosis.

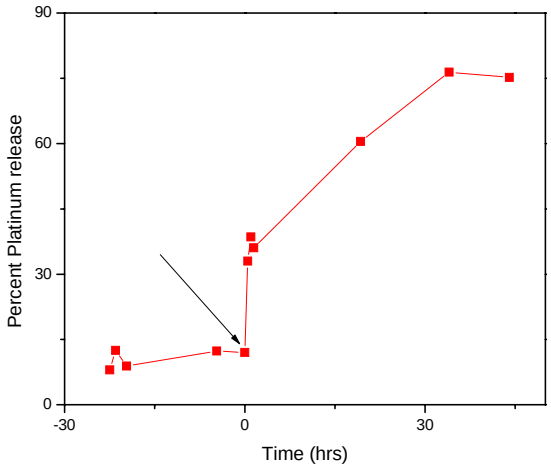

Figure 2.8: Platinum release profile from **2.1** in the absence and presence of 10mM L-cysteine. The reducing agent was added where indicated by the arrow.

2.2.4 Post-Synthetic Modification

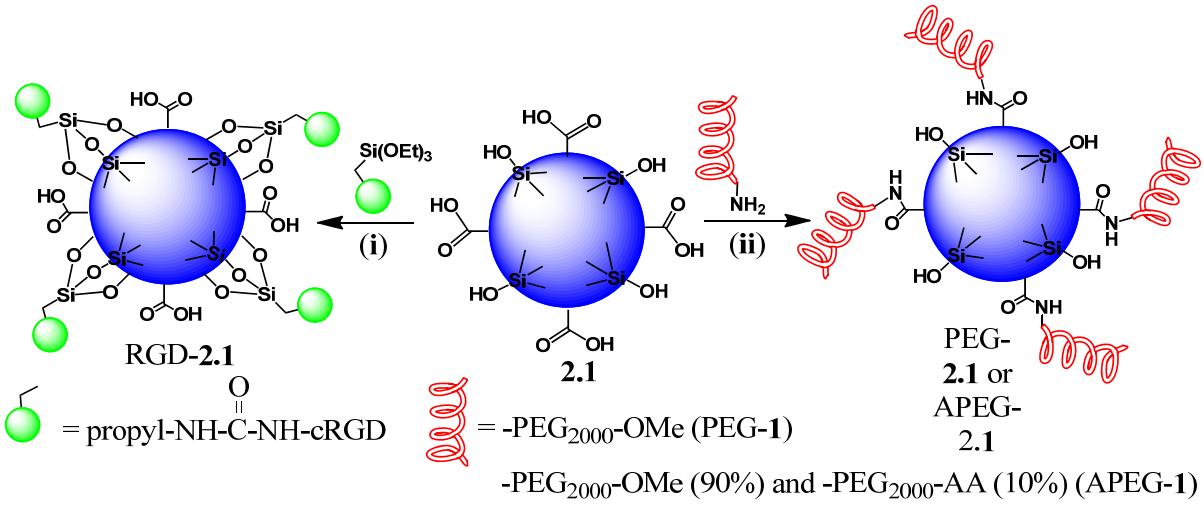

Scheme 2.3: Post-synthetic modification strategies for **2.1** through either surface silanol groups (i) or carboxylic acids(ii).

2.1 possesses two surface functional groups, silanol groups and carboxylic acids, which were used for post-synthesis grafting of cyclic arginine-glycine-aspartate (cRGD) peptide and polyethylene glycol (Scheme 2-3). The surface silanol groups allow for the

functionalization of **2.1** with a variety of silanol derived molecules through traditional siloxane chemistry (Scheme 2-3, i).[37-38] The carboxylic acids in **2.1** allows for the attachment of molecules through traditional coupling chemistry (Scheme 2-3, ii).[39] **2.1** was functionalized with silyl-derived cRGD by base-catalyzed condensation to afford RGD-**2.1** (Scheme 2-3, method i). The cRGD peptide targets the $\alpha_v\beta_3$ integrin, which is upregulated in many angiogenic tumor cells.[40-42] DLS measurements showed an increase in particle size to 100 nm, most likely due to slight particle aggregation after the peptide conjugation (Figure 2-9, Table 2.1). The zeta potential slightly increased to -18.2 mV, consistent with the grafting of the neutral cRGD peptide (Table 2-1).

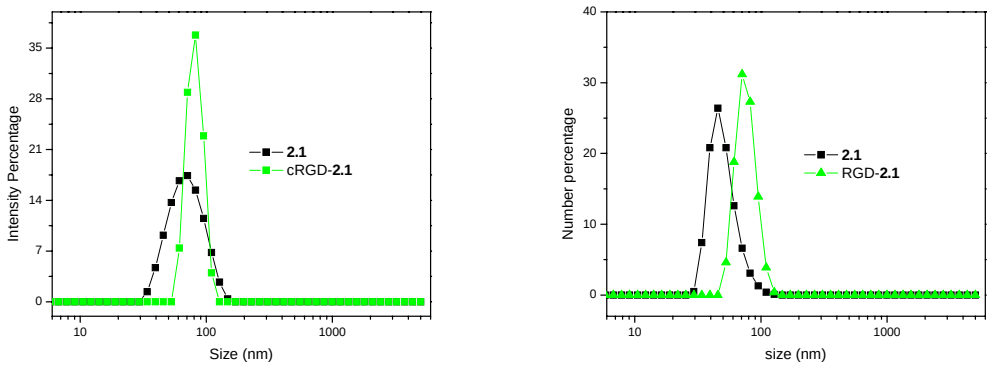

Figure 2-9: Intensity (left) and number (right) weighted DLS size distributions for **2.1** (black) and RGD-**2.1** (green) in PBS

2.1 was also surface-modified with polyethylene glycol (PEG). PEG is an inert, nontoxic, and non-immunogenic hydrophilic polymer.[43] Numerous studies of PEG-modified nanoparticles have demonstrated that the PEG coating sterically stabilizes the nanoparticle and imparts stealth properties such as prolonged circulation half-life, reduced serum protein binding, and avoidance of the mononuclear phagocytic system (MPS).[5, 8, 12] Repeated attempts to pegylate **2.1** through surface silanol groups were unsuccessful, so PEG was

attached to the nanoparticle surface by an EDC-mediated coupling (EDC= 1-ethyl-3-(3-dimethylaminopropyl)carbodiimide) between surface carboxylic acids on **2.1** and amino-PEG_{2000}-methyl ether (PEG-**2.1**). PEG-**2.1** was characterized by TEM, DLS, zeta potential, and TGA. DLS measurements gave a hydrodynamic diameter of 91 nm for PEG-**2.1**, while the TEM micrograph showed minimal changes in the particle morphology (Figures 2-10 and 2-11, Table 2-1). The zeta potential of PEG-**2.1** increased to -5.5 mV (Table 2-1). This positive shift in the zeta potential to near neutral values is indicative of the formation of a dense PEG layer which shields the surface charge of the nanoparticles. A slight increase in the particle size was observed for PEG-**2.1**, probably resulting from the extension of the PEG chains from the nanoparticle surface. TGA analysis of PEG-**2.1** gave an increase in organic weight loss of 8%, which corresponds to a coverage density of 1 PEG per 2.7 nm^2 (Figure 2-12).

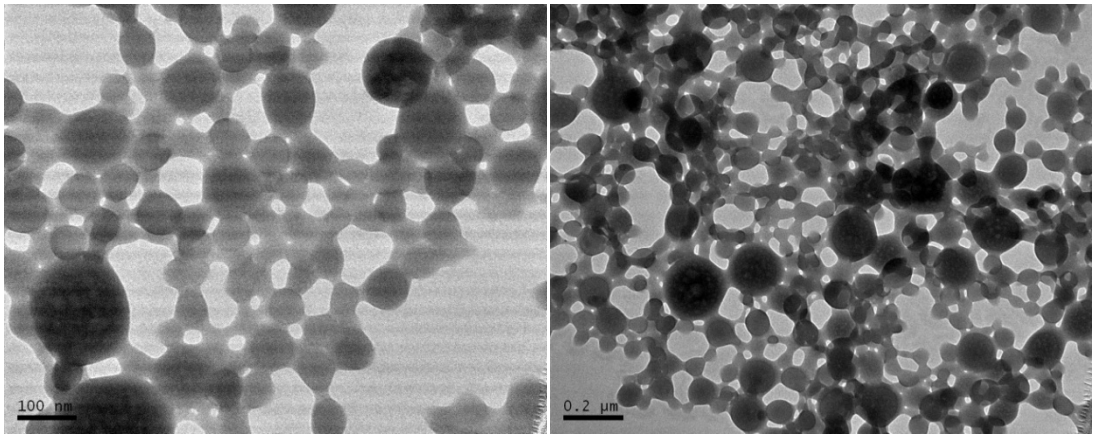

Figure 2-10: TEM micrographs of PEG-**2.1**.

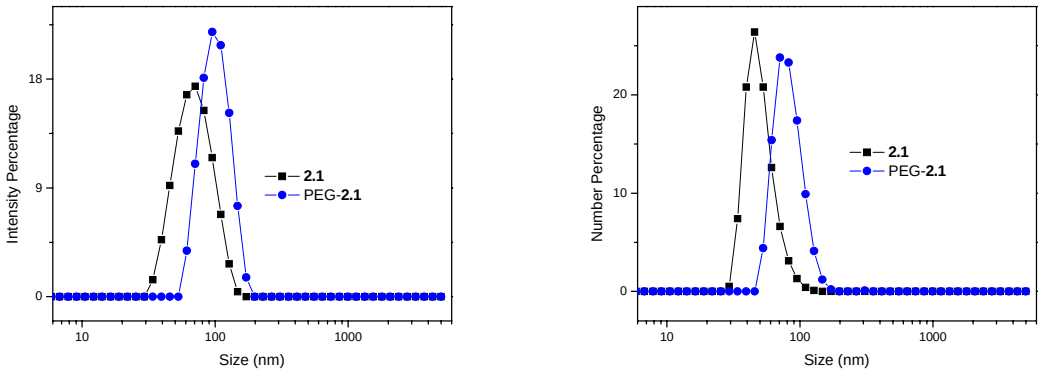

Figure 2-11: Intensity (left) and number (right) weighted DLS spectra of **2.1** (black) and PEG-**2.1** (blue) obtained in PBS.

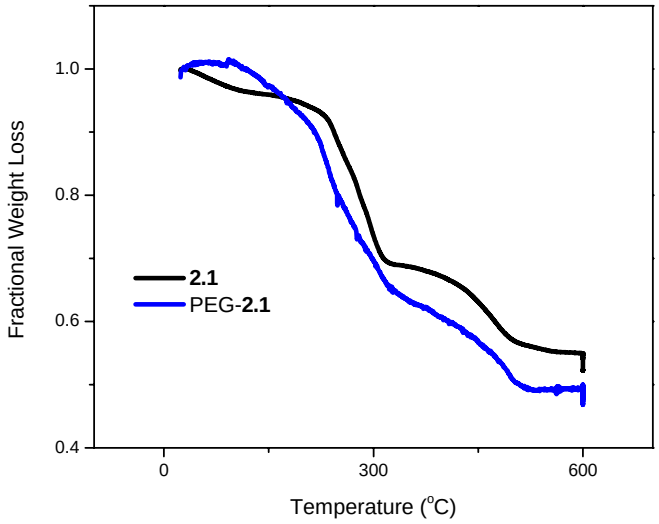

Figure 2-12: TGA weight loss curves for **2.1** (black) and PEG-**2.1** (blue)

The anisamide (AA) ligand was also attached to the surface of **2.1** by an amide coupling between the carboxylic acid groups of **2.1** and amino-PEG_{2000}-AA. The AA ligand is an effective targeting agent for the sigma receptor, an opioid receptor overexpressed on many cancers.[44-49] AA-targeted PEG-**2.1** (APEG-**2.1**) was prepared by the EDC coupling of **2.1** with amino-PEG_{2000}-methyl ether and amino-PEG_{2000}-AA (in a 9:1 weight ratio) under

the same conditions as the above pegylation reaction. TEM analysis demonstrated no change in particle size or morphology (Figure 2-13). APEG-**2.1** particles exhibited a DLS diameter of 93 nm and a zeta potential of -5.0 mV (Figure 2-14 and Table 2-1). TGA showed an increase in organic weight loss of 8%, suggesting nearly identical PEG surface coverage in APEG-**2.1** to that in PEG-**2.1** (Figure 2-15).

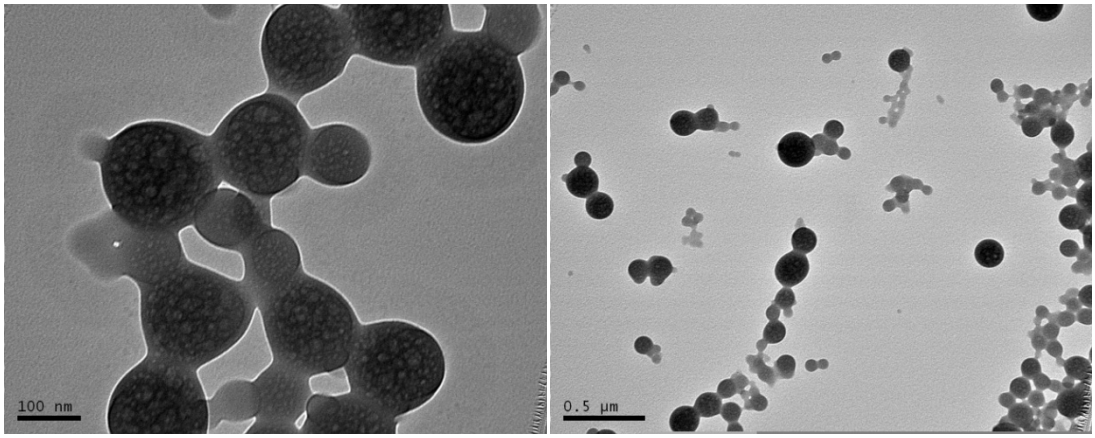

Figure 2-13: TEM micrographs of APEG-**2.1**

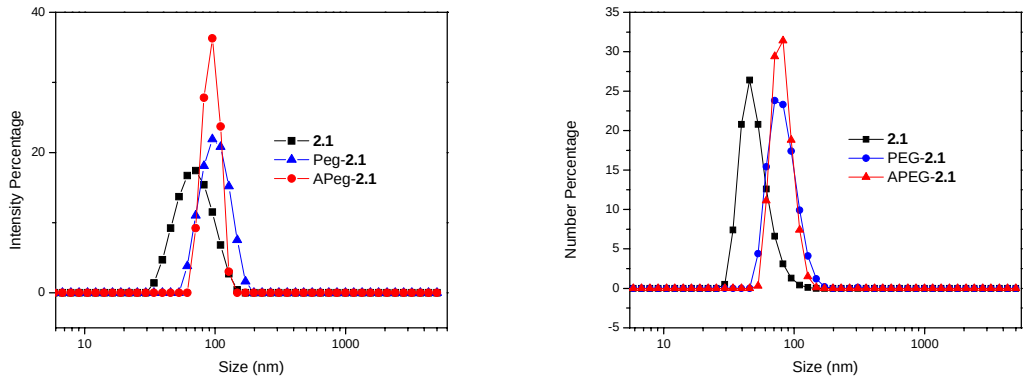

Figure 2-14: Intensity (left) and number (right) weighted DLS spectra of **2.1** (black), PEG-**2.1** (blue), and APEG-**2.1** (red) obtained in PBS.

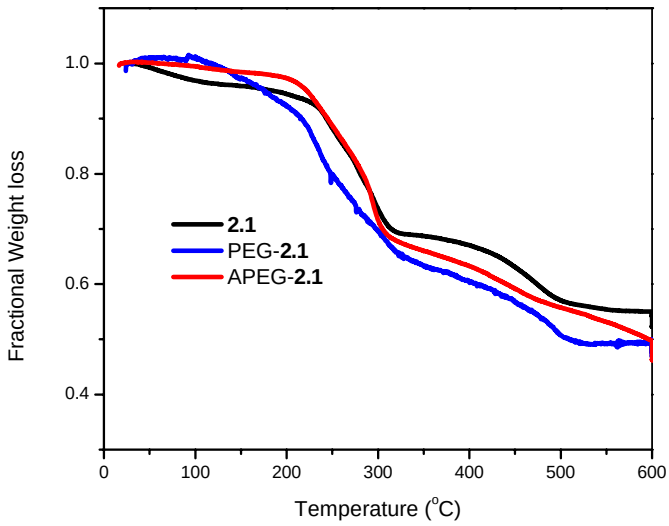

Figure 2-15: TGA weight loss curves for **2.1** (black)**, PEG-2.1** (blue) and APEG-**2.1** (red)

2.2.5 *In Vitro* Cytotoxicity Studies

The cytotoxicity of **2.1** was evaluated *in vitro* against several human colon and pancreatic cancer lines, because oxaliplatin is used clinically to treat colon cancer and has been studied as a potential therapy for pancreatic cancer.[50-52] Oxaliplatin, **2.1**, and RGD-**2.1** were evaluated against two colon adenocarcinoma cell lines: DLD-1 and HT-29 (Figures 2-16 and 2-17). Against the DLD-1 cell line, oxaliplatin was highly effective, with an IC_{50} of 0.14 μM, while **2.1** had slightly better efficacy, with an IC_{50} of 0.11 μM. RGD-**2.1** showed a 10-fold increase in cytotoxicity compared to both **2.1** and oxaliplatin, exhibiting an extremely low IC_{50} of 0.01 μM (Figure 2-16). Against the HT-29 cell line, oxaliplatin and **2.1** showed comparable cytotoxicity (IC_{50}=0.175 and 0.145 μM, respectively), while RGD-**2.1** was more than twice as cytotoxic (IC_{50}=0.081 μM) (Figure 2-17). These results clearly indicate the ability to target particles of **2.1** to colon cancer cells with the cRGD ligand.

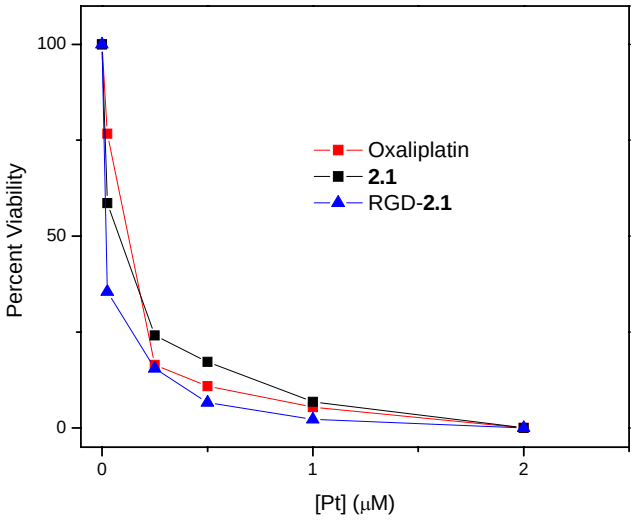

Figure 2-16: Cell viability assays of oxaliplatin (red), **2.1** (black) and RGD-**2.1** (blue) evaluated against DLD-1 human colon adenocarcinoma cells.

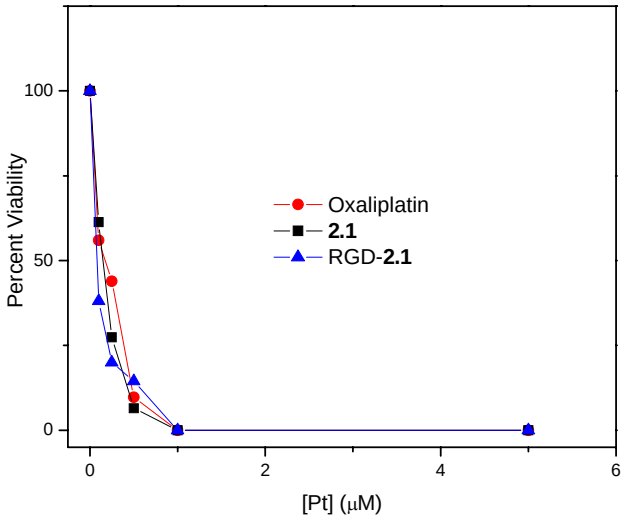

Figure 2-17: Cell viability assays of oxaliplatin (red), **2.1** (black) and RGD-**2.1** (blue) evaluated against HT-29 human colon adenocarcinoma cells.

Two pancreatic ductal adenocarcinoma cell lines, AsPC-1 and BxPC-3, were chosen to evaluate the cytotoxicity of **2.1**, RGD-**2.1,** and oxaliplatin (Figures 2-18 and 2-19). Against

the AsPC-1 cell line, **2.1** and RGD-**2.1** exhibited IC_{50} values of 0.75 and 0.6 μM, respectively (Figure 2-18). They were about three times as cytotoxic as oxaliplatin (IC_{50} = 2 μM). Oxaliplatin, **2.1**, and RGD-**2.1** showed comparable cytotoxicity against the BxPC-3 cell line, with an IC_{50} of 1, 0.8, and 1 μM, respectively (Figure 2-19). RGD-**2.1** is not expected to show an increase in cytotoxicity compared to **2.1**, as these cell lines do not express high levels of the $\alpha_v\beta_3$ integrin.[53-54] Instead, we hypothesized that AA can be used to target AsPC-1 cells which were shown previously to be sigma receptor positive.[55] PEG-**2.1** and oxaliplatin showed identical IC_{50} values of 0.52 and 0.37 μM, respectively (Figure 2-20), while anisamide targeting decreased the IC_{50} value of APEG-**2.1** to 0.17 μM, equivalent to more than a 3-fold increase in cytotoxicity.

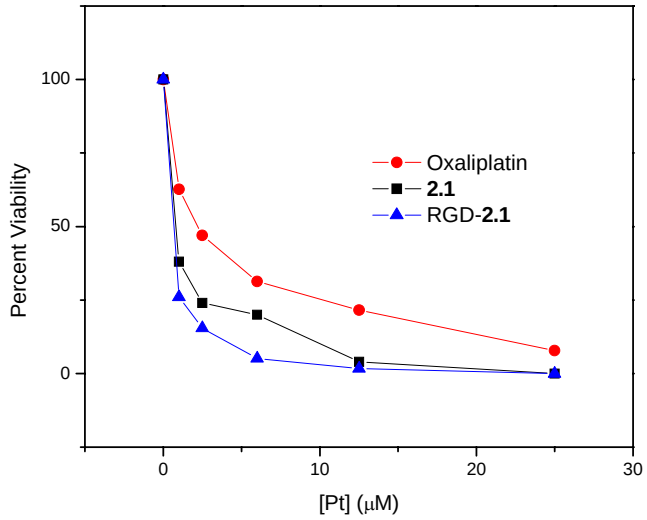

Figure 2-18: Cell viability assay of oxaliplatin (red), **2.1** (black), and RGD-**2.1** (blue) evaluated against AsPC-1 pancreatic ductal adenocarcinoma cells.

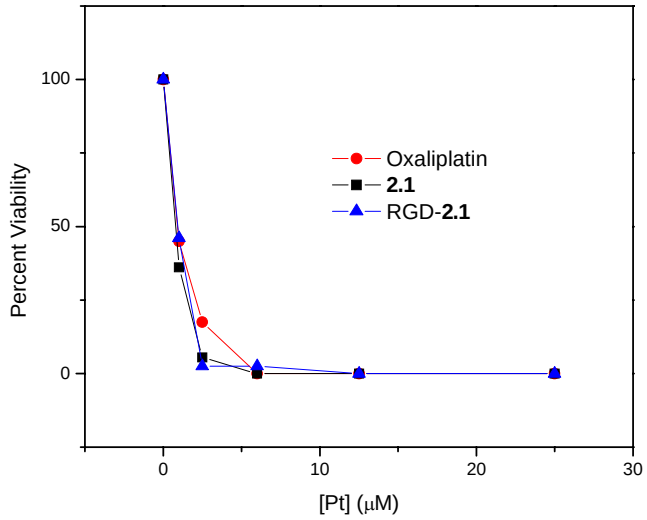

Figure 2-19: Cell viability assay of oxaliplatin (red), **2.1** (black), and RGD-**2.1** (blue) evaluated against BxPc-3 pancreatic ductal adenocarcinoma cells.

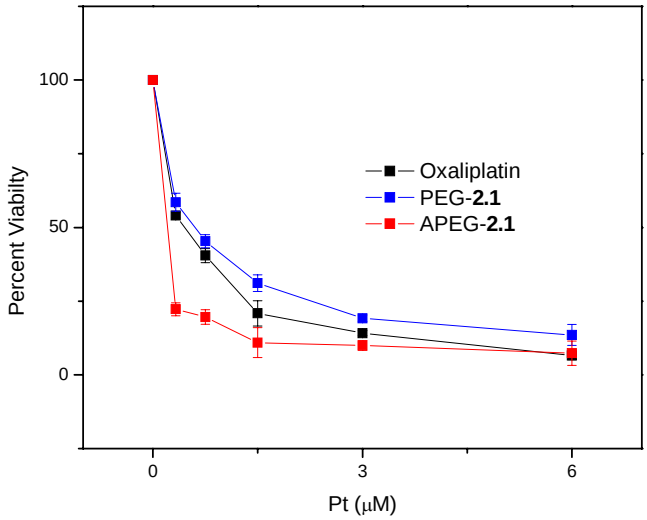

Figure 2-20: Cell viability assay of oxaliplatin (black), PEG-**2.1** (blue) and APEG-**2.1** (red) evaluated against AsPc-1 pancreatic ductal adenocarcinoma cells.

2.2.6: *In Vitro* Confocal Microscopy Studies

The *in vitro* cytotoxicity assay results clearly indicated the increased uptake of **2.1** by DLD-1 and HT-29 human colon cancer cells via integrin receptor targeting and by AsPC-1 human pancreatic cancer cells via sigma receptor targeting, presumably through receptor-

mediated endocytosis. The cellular localization and effect of RGD targeting of **2.1** was investigated by confocal microscopy. DLD-1 cells were incubated with either rhod-**2.1** or RGD-rhod-**2.1** for 10 minutes before being washed extensively to remove any unbound nanoparticles. This short reaction time was necessary because of the effectiveness of **2.1** in inducing apoptosis in DLD-1cells. Experiments using longer incubation times produced significant cell death, and few viable cells were located on the microscope slide. DLD-1 cells showed increased cellular localization and uptake of RGD-rhod-**1** particles compared to the untargeted rhod-**1** particles (Figure 2-21). The nanoparticles appear to be located in discrete areas within DLD-1 cells, most likely cellular endosomes.

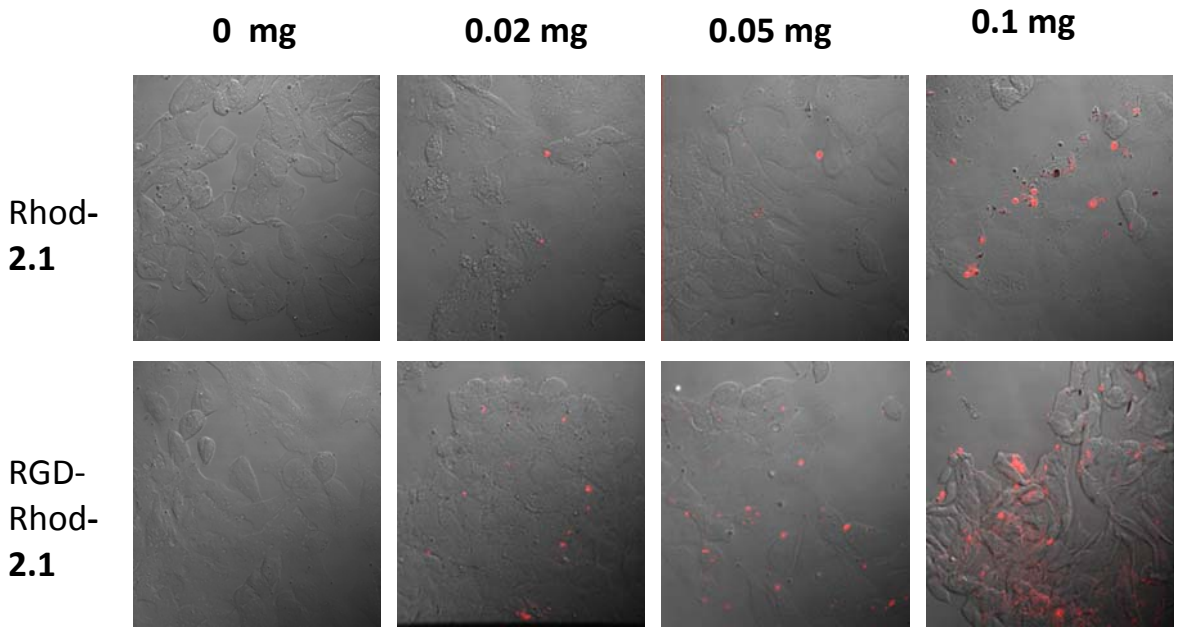

Figure 2.21: Overlaid confocal microscopy images of rhod-**2.1** (top) and RGD-rhod-**2.1** (bottom) incubated with DLD-1 colon cancer cells at 0, 0.02, 0.05 and 0.1 mg nanoparticle per well.

The cellular localization, time dependence of internalization and induction of apoptosis by **2.1** was investigated in AsPC-1 cells by confocal microscopy (Figures 2-22 and

2-23). Cells were treated with nanoparticle for either 1 hour or 5.5 hours at a fixed platinum concentration. The media was then removed and the cells were washed to remove any unbound nanoparticles. A FITC-Annexin V conjugate was then used to monitor cellular apoptosis. Annexin V is a protein with a high affinity for the phospholipid phosphatidylserine. During apopotosis, phosphatidylserine becomes translocated from the inner cell membrane to the outer allowing for the detection of apopotosis.[56] After 1 hour of incubation, no fluorescence was evident in the rhodamine B channel for cells incubated with rhod-**2.1**, but significant rhodamine B fluorescence was found for the cells incubated with PEG-rhod-**2.1** and APEG-rhod-**2.1** (Figure 2-22). Consistent with the efficient uptake of PEG-rhod-**2.1** and APEG-rhod-2.**1** particles, the FITC channels showed strong green fluorescence in both cases, indicating significant cell apoptosis induced by the released oxaliplatin from the endocytosed particles. In contrast, no apoptosis was observed for the cells incubated with no particles or rhod-**2.1** particles. These results would suggest that the negatively charged rhod-**2.1** nanoparticles cannot efficiently enter cells compared to the neutral pegylated nanoparticles. Additionally, these results confirm the triggered release capabilities of **2.1** as only internalized nanoparticles appear to be able to release their platinum payloads to cause apoptosis. Confocal images of the cells incubated for 5.5 hours with rhod-**2.1** particles indicated a low level of particle uptake and cell apoptosis (much less than the cells that were treated with PEG-rhod-**2.1** and APEG-rhod-2.**1**) (Figure 2-23). The confocal microscope imaging studies thus provided additional evidence for the enhanced uptake of PEG-rhod-**2.1** and APEG-rhod-2.**1** particles and triggered release of the platin cargoes in the AsPC-1 cells. The enhanced uptake of PEG-rhod-**2.1** and APEG-rhod-**2.1** was

surprising because pegylation would be expected to decrease cellular uptake; however, it is possible that these nanoparticles were insufficiently pegylated to reduce cell uptake.

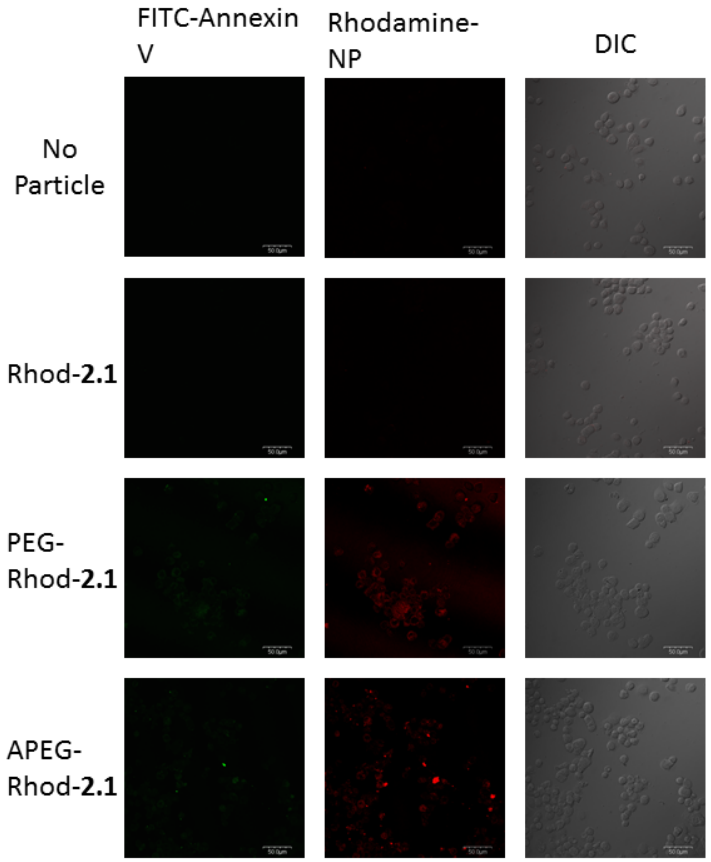

Figure 2-22: Laser scanning confocal microscopy images of AsPC-1 cells incubated with no particle, rhod-**2.1**, PEG-rhod-**2.1**, and APEG-rhod-**2.1** for 1 hr (5μM Pt concentration) and then treated with Annexin V/FITC. The green fluorescence arises from FITC and the red fluorescence arises from rhodamine B. Scale bars= 50μm.

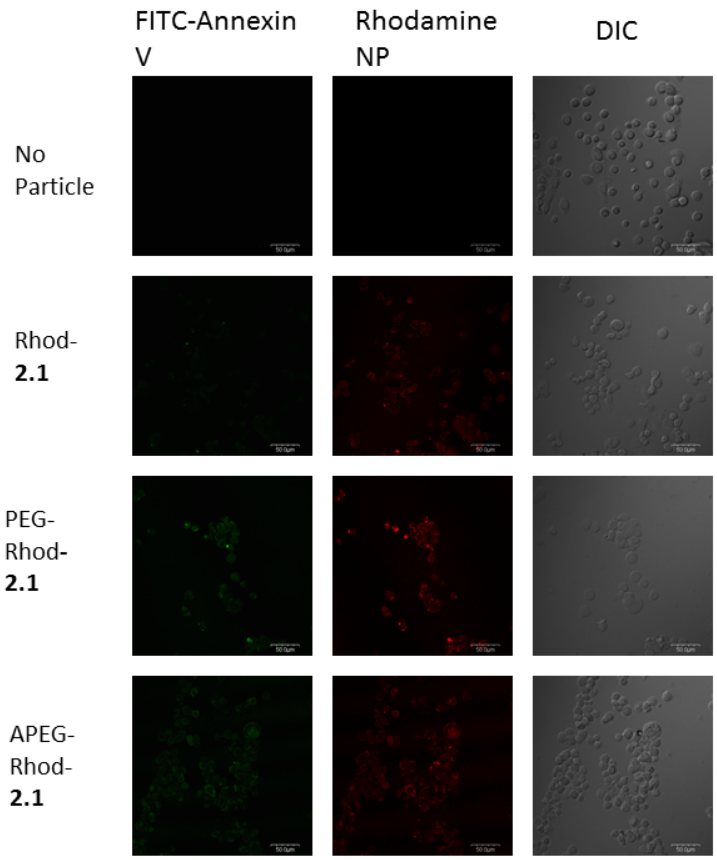

Figure 2-23: Laser scanning confocal microscopy images of AsPC-1 cells incubated with no particle, rhod-**2.1**, PEG-rhod-**2.1**, and APEG-rhod-**2.1** for 5.5 hours at 5μM Pt. The cells were stained with FITC-Annexin V (green channel) to mark cellular apoptosis. Nanoparticle fluorescence is the red channel, and the scale bars indicate 50μm.

2.2.7 *In Vivo* Studies

Encouraged by the promising *in vitro* results, we have evaluated the *in vivo* tumor growth inhibition efficacy of PEG-**2.1** and APEG-**2.1** against a murine model of pancreatic cancer. Female athymic nude mice were injected in both flanks with 1×10^6 AsPC-1 cells and the tumors grew until palpable in both flanks (typically 16-21 days after cell injection). The mice were randomly split into 4 groups (4-6 mice per group) and received three weekly doses of oxaliplatin (5 mg Pt/kg), PEG-**1** (5 mg Pt/kg), APEG-**1** (5 mg Pt/kg), or PBS control. These platinum doses are equivalent to the maximum tolerated dose of oxaliplatin for this

injection schedule.[57] Figure 2-24 shows the effect of the treatments on tumor growth. Mice which received no treatment demonstrated sustained tumor growth, reaching the maximum size allowed by the UNC institutional animal care and use committee guidelines 21 days after the commencement of the treatment. Oxaliplatin appeared to slightly inhibit tumor growth over the study period (75% of the volume of untreated tumors), but the effect was not statistically significant. However, mice which received either PEG-**1** or APEG-**1** showed a statistically significant reduction in tumor growth (α =0.06 for PEG-**1** and α=0.02 for APEG-**1**), thus limiting the average tumor volume to approximately 50% and 40% of the volume for untreated control mice, respectively. Throughout the duration of the study, no weight loss was observed in any of the treatment groups (Figure 2-25). The antitumor efficacy of PEG-**1** and APEG-**1** was confirmed by histological analysis of the resected tumors (Figures 2-26- 2-29). Both the untreated and oxaliplatin-treated tumors were very large and composed of large regions of viable tumor cells (Figures 2-26- 2-29 a and b). The tumors from the oxaliplatin-treated mice showed small necrotic regions around the center of the tumor mass. In contrast, mice which received PSQ nanoparticle treatment (Figures 2-26- 2-29 c and d) had smaller tumors composed of large regions of necrotic (scarred) tissue. Mice which received APEG-**1** showed much larger regions of necrotic tissue. These results suggest that PSQ nanoparticles are potentially useful therapies for the treatment of pancreatic cancer.

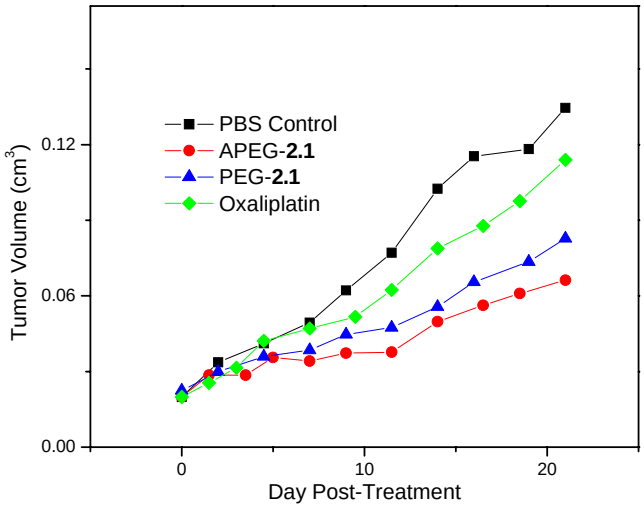

Figure 2-24: Tumor growth inhibition curves of oxaliplatin (green), PEG-**2.1** (blue), APEG-**2.1** (red) and PBS control (black) administered by tail vein injection at 5mg Pt/kg on days 0,7, and 14 against an AsPc-1 subcutaneous xenograft.

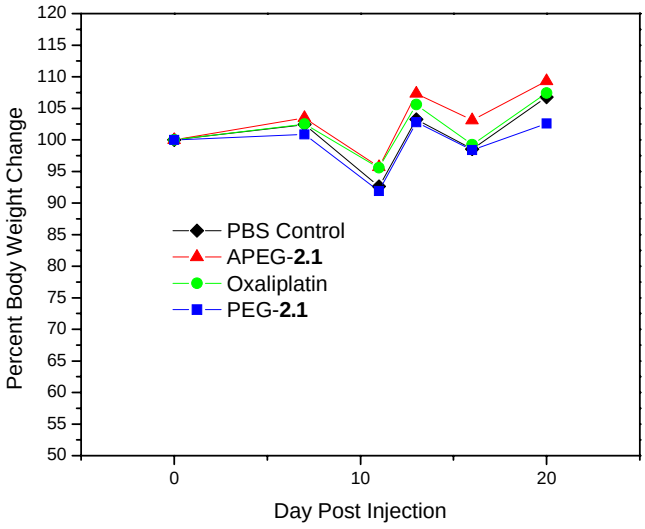

Figure 2-25: Mouse body weights of groups treated with oxaliplatin (green), PEG-**2.1** (blue), APEG-**2.1** (red) and PBS control (black) administered i.v. at 5mg Pt/kg. Treatment was administered on days 0, 7, and 14 against an AsPC-1 subcutaneous xenograft. Error bars are omitted for clarity.

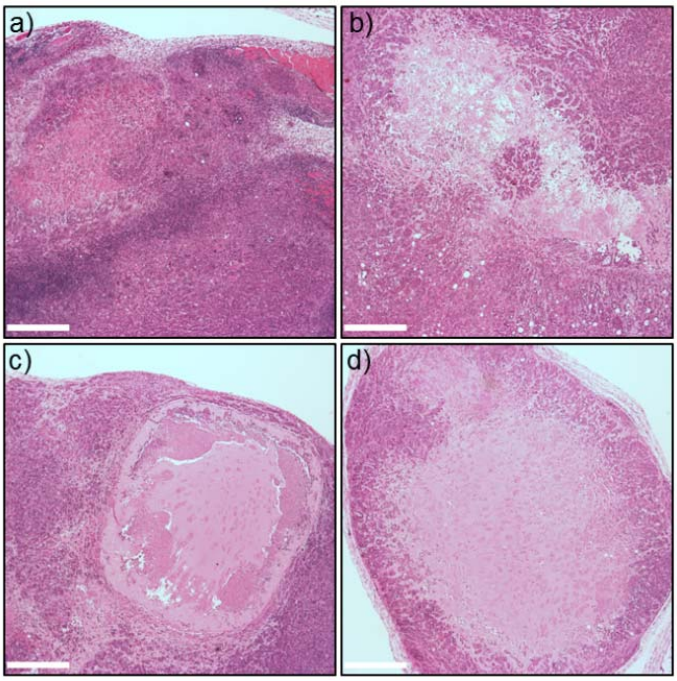

Figure 2-26: Histology images of resected AsPc-1 tumors with H&E staining from mice receiving PBS control (a), oxaliplatin (b), PEG-**2.1** (c), and APEG-**2.1** (d). The scale bars indicated 0.5 mm. The blue-purple dots result from nuclear staining of viable cancer cells whereas the pinkish areas indicate necrotic tumor tissue with no viable cells or nuclear material.

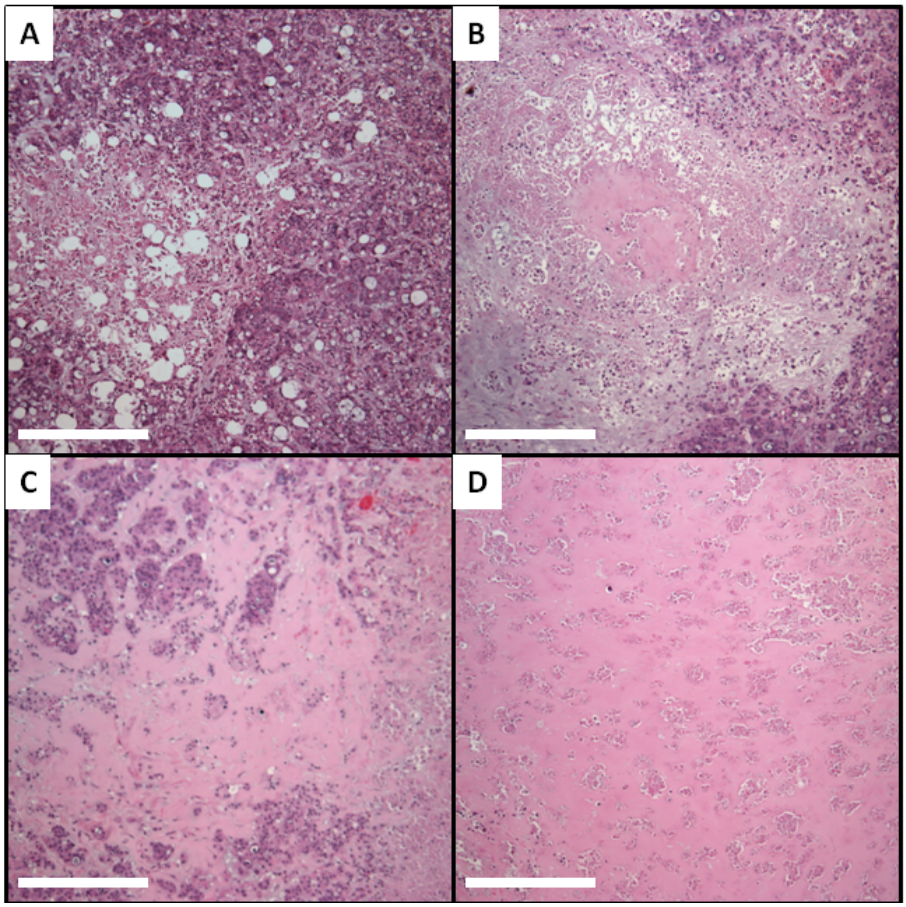

Figure 2-27: AsPc-1 tumor histology images taken at 10x magnification for mice receiving PBS(A), oxaliplatin (B), PEG-**2.1** (C), or APEG-**2.1** (D). The blue purple dots result from viable cancer cells, the pink areas indicate regions of complete cellular necrosis, leaving no nuclear material to be stained purple and conversion of the area to an abscess and the white areas are regions of deposited fatty tissue. The scale bar indicates 500 μm.

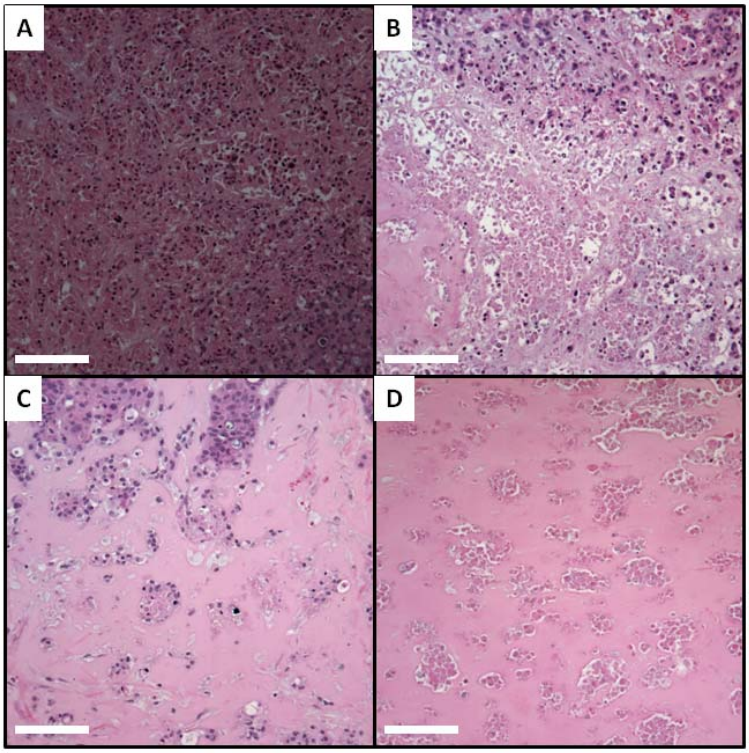

Figure 2-28: AsPc-1 tumor histology images taken at 20x magnification for mice receiving PBS(A), oxaliplatin (B), PEG-**2.1** (C), or APEG-**2.1** (D). The blue purple dots result from viable cancer cells, the pink areas indicate regions of complete cellular necrosis, leaving no nuclear material to be stained purple and conversion of the area to an abscess and the white areas are regions of deposited fatty tissue. The scale bar indicates 120 μm.

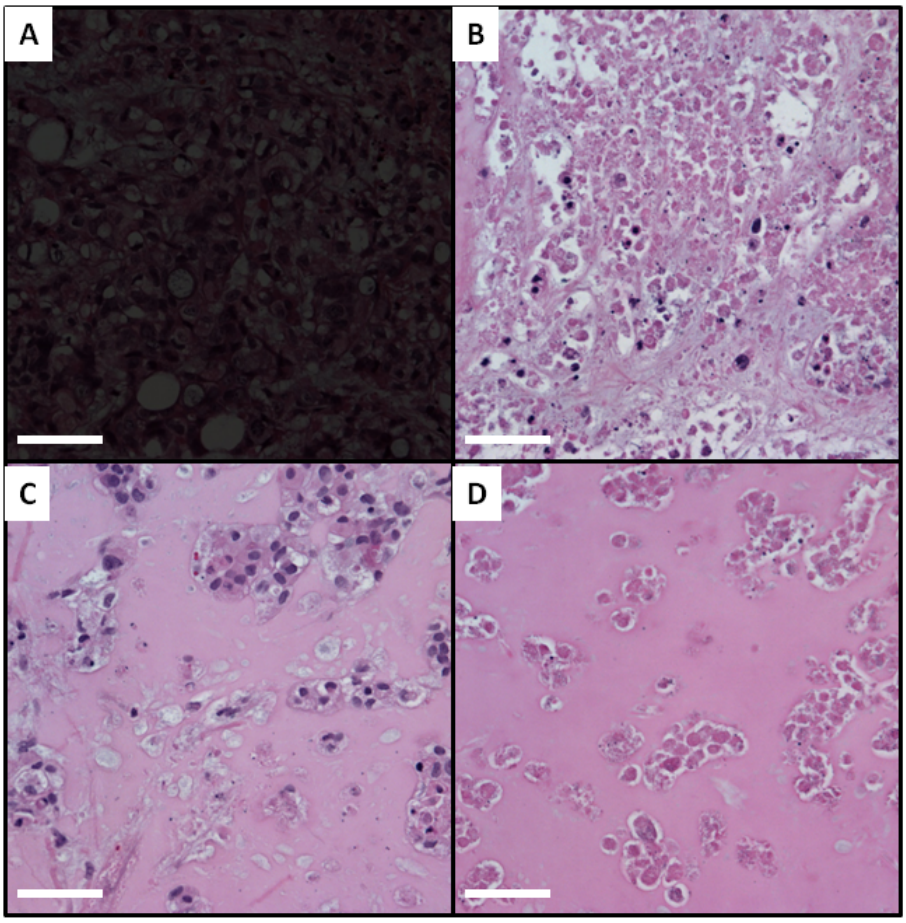

Figure 2-29: AsPc-1 tumor histology images taken at 40x magnification for mice receiving PBS(A), oxaliplatin (B), PEG-**2.1** (C), or APEG-**2.1** (D). The blue purple dots result from viable cancer cells, the pink areas indicate regions of complete cellular necrosis, leaving no nuclear material to be stained purple and conversion of the area to an abscess and the white areas are regions of deposited fatty tissue. The scale bar indicates 60 μm.

PEG-**2.1** was further evaluated against an orthotopic model of pancreatic cancer. In an orthotopic model, the cancer cells are implanted within their derived organ instead of the flanks of the mouse. Orthotopic models mimic the natural organ microenvironment of the human cancer cells. This can influence the tumor's growth characteristics, metastatic potential, and response to chemotherapy.[58] Luciferase expressing AsPC-1 cells were orthotopically implanted (i.e., injected into the pancreas in this case) within nu/nu mice and the tumors were allowed to grow until detected by fluorescent imaging. Mice were then split into 3 groups (5 mice per group) and received PBS control, oxaliplatin or PEG-**2.1**at 5mg

Pt/kg for three weekly doses. APEG-**2.1** was not included in this study due to both mouse availability only allowing three treatment groups for statistically significant results and the modest increase in efficacy brought upon by anisamide targeting. The mice were injected with luciferin weekly and imaged. Tumor growth was determined by the relative increase in fluorescence compared to the day-1 fluorescence. As seen in figure 2-30, the fluorescence intensity of mice receiving no treatment increased nearly 3 times over the course of the study. Oxaliplatin appeared to have had no tumor growth inhibition effect, while administration of PEG-**2.1** seemed to only result in a modest increase in tumor volume (29%). However, the error within the measurements was too large to achieve any statically significant results. This study was terminated early due to technical issues arising from repeated injections so long term tumor growth or survival data was not obtained.

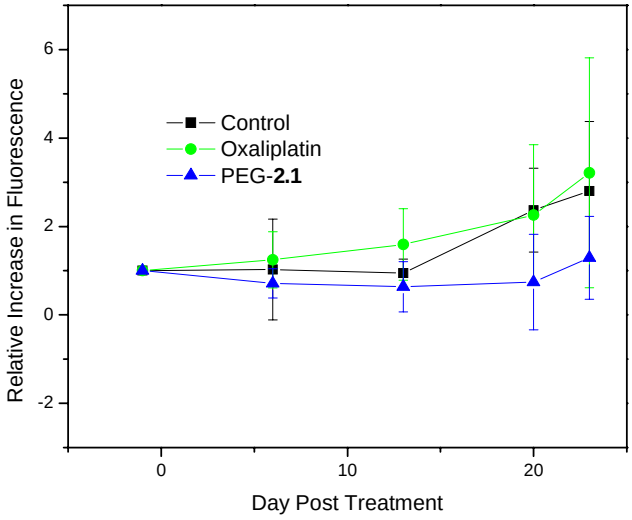

Figure 2-30: Luminescence intensity increases of mice orthotopically implanted with luciferase expressing AsPc-1 tumors and receiving either PBS (black), oxaliplatin (green), or PEG-**2.1** (blue) via tail vein injection at 5mg Pt/kg. The study was terminated prematurely due to adverse effects from repeated tail vein injection.

2.3 Conclusions

In conclusion, we have synthesized PSQ nanoparticles containing extremely high loadings of oxaliplatin-based chemotherapeutics. These nanoparticles are highly stable under normal physiological conditions, but can be readily reduced to release the platin cargoes in highly reducing tumor microenvironments. The Pt(IV) centers within the PSQ nanoparticle would allow the cargo to remain inside of cancer cells in circulation, but could be reduced inside of the tumor environment. The PSQ particles contained both surface silanol and carboxylic acid groups to allow further functionalization with PEG and targeting ligands. The PSQ particles exhibited superior cytotoxicity to oxaliplatin against four cancer cell lines *in vitro*, and the RGD- and anisamide-targeting further enhanced the cytotoxicity. In a pancreatic cancer xenograft mouse model, the pegylated and anisamide-targeted PSQ particles showed drastically superior efficacy to oxaliplatin in inhibiting tumor growth. These results were tentatively extended to an orthotopic model of pancreatic cancer. This work highlights the potential of PSQ nanoparticles as excellent delivery vehicles for cancer therapeutics.

2.4 Materials and Methods

2.4.1 General Materials and Methods

All chemicals were purchased from Fisher or Aldrich and used without further purification unless noted. Oxaliplatin was purchased from AK scientific. Tetrahydrofuran was dried by the sodium metal/benzophenone method. Thermogravimetric analysis was performed using a Shimadzu TGA-50 equipped with a platinum pan and heated at 3°C per minute in air. A JEM 100CX-2 transmission electron microscope (TEM) was used to

determine particle size and morphology. TEM samples were prepared from ethanolic suspensions of the nanoparticles dropped onto amorphous carbon coated copper grids. The solvent was then allowed to evaporate. Dynamic light scattering (DLS) and zeta potential measurements were made using a Malvern Instruments Zetasizer Nano. Inductively-Coupled Plasma Mass Spectrometry (ICP-MS) measurements were made using a Varian 820-MS Inductively-Coupled Plasma Mass Spectrometer. ICP-MS samples were prepared by digesting a known amount of sample in concentrated nitric acid overnight, and then diluted with water to 2% nitric acid by volume.

2.4.2 Synthesis of Platinum Complexes

Synthesis of Pt(dach)Cl$_2$: Pt(dach)Cl$_2$ was synthesized using Dhara's method.[27] K_2PtCl_4 (2.07 g, .005 mol) was dissolved in 60 mL of H_2O and allowed to stir for 10 min. KI (3.20 g, .019 mol, 3.8 eq) was dissolved in 10 mL of H_2O and added to the mixture, resulting in a violet solution that was stirred for 15 min. R,R-diaminocyclohexane (dach) (591.5 mg, 0.0052 mol, 1 eq) was dissolved in 10 mL of H_2O and added to the mixture dropwise, resulting in the yellow Pt(dach)I_2 precipitate, which was stirred overnight, at room temperature, in the dark. Pt(dach)I_2 was filtered by vacuum and washed with H_2O, acetone, and ethanol (2.71 g, .0047 mol, 95% yield). Pt(dach)I_2 was suspended in 60 mL of H_2O, and $AgNO_3$ (1.71 g, .010 mol, 2 eq) dissolved in 10 mL H_2O was added to the slurry and stirred for 24 h at room temperature. The AgI precipitate was removed by vacuum filtration, and a saturated NaCl solution was added dropwise until the yellow Pt(dach)Cl_2 precipitated and was filtered and washed with H_2O, EtOH, and acetone. Yield = 95%. IR spectra (3320, 3200, 2960, 2880 cm^{-1})

Synthesis of Pt(dach)$Cl_2(OH)_2$: Pt(dach)$Cl_2(OH)_2$ was synthesized by a modification of a previously reported procedure.[28] Pt(dach)Cl_2 (1.48 g, .0039 mol) was suspended in 60 mL H_2O, followed by the addition of 14 mL of 30% H_2O_2 in water. The slurry was heated at 70 °C overnight, in the dark. The white product was filtered and washed with H_2O and acetone. Yield = 68%.

Synthesis of c,c,t-Pt(dach)Cl_2(propyltriethoxysilane succinic acid)$_2$ (DachPt-Si): c,c,t- Pt(Dach)$Cl_2(OH)_2$ (0.2 g, .0004 mol) was dried under vacuum for several hours. The Pt complex was then suspended in 6 mL of anhydrous DMSO and triethoxysilylpropyl succinic anhydride (600 µL, 0.002 mol, 4 eq) was added. The mixture was heated under argon at 50 °C for 4 days, yielding a brown solution. The solvent was removed by lyophilization. The residue was dissolved in ethanol and precipitated with hexane. The brown solid was washed twice with diethyl ether and dried under vacuum for several hours. Yield: 247 mg, 50%. ^{1}H NMR (400 MHz, DMSO-d_6): δ 12.22 (2 H, COOH), 8.19 (4H, NH_2), 4.041 (4H, Si-OH), 3.737 (4H, Si-OCH_2), 3.07 (2H), 2.33 (2H), 2.19 (2H), 1.501 (8H), 1.375 (8H), 1.15 (6H), 0.582 (4H).

2.4.3 Synthesis of Silyl-Derived Molecules

Synthesis of Rhodamine-APS: Rhodamine B-APS was synthesized by an established procedure.[59] Rhodamine B (6.8 mg, $1.4x10^{-5}$ mol) was dissolved into 1.1 mL of absolute ethanol. 3-aminopropyltriethoxysilane (3.3 µL, $1.4x10^{-5}$ mol) was added and the reaction was stirred under nitrogen for 24 h at room temperature, in the dark. The solution was then diluted to a total volume of 2 mL with additional ethanol to make a 6 mM solution.

Synthesis of triethoxysilylpropyl carbomoyl c(RGDfK): Triethoxysiylpropyl carbomoyl c(RGDfK) was synthesized by an established method.[13] Cyclic(RGDfK) (2.0 mg, 3.3 μmol) was added to a small round-bottom flask and dried under high vacuum for 1 h. Anhydrous DMSO (500 μL) and triethylamine (0.20 μL) were added to the round-bottom flask, followed by (3-isocyanatopropyl)triethoxysilane (0.86 μL, 3.44 μmol). The mixture was magnetically stirred under argon for 24 h. The solution (4 mg c(RGDfK)/mL DMSO) was placed in a freezer for later use.

2.4.4: Synthesis of Polyethylene Glycol (MW=2000) Derivatives

Synthesis of MeO-PEG_{2000}-NH_2: Methoxy-PEG_{2000} –amino was synthesized by a modification of a previously reported protocol.[60] Peg_{2000} monomethylether (10 g, 5.0 mmol) was co-evaporated with 50 mL of toluene to remove water. The PEG was dissolved into 50 mL of anhydrous THF with 1.2 mL (15.5 mmol) of methane sulfonyl chloride. The solution was cooled to 0°C on an ice bath, then 2.3 mL (16.5 mmol) of triethylamine dissolved in 20 mL THF was added dropwise. The solution was stirred from 0°C to room temperature overnight. Water (50 mL) was added and the solution was cooled back to 0°C. Sodium bicarbonate solution (5 mL, 1 M) was added, followed by sodium azide (1.3 g, 20 mmol). The THF was removed by rotary evaporation. The remaining aqueous solution was refluxed for 24 h. The PEG was extracted with dichloromethane (4×100 mL). The DCM layers were collected, concentrated, and extracted once with brine. The dichloromethane was then removed by rotary evaporation, yielding solid methoxy-PEG_{2000}-azide (8.9 g, 89% yield). The methoxy-PEG_{2000}-azide was dissolved into 55 mL THF and triphenylphosphine (3.42 g, 13 mmol) was added. The solution was stirred for 10 h at room temperature, and then water (3.3 mL) was added. The solution was stirred at room temperature overnight, and then the

THF was removed by rotary evaporation. Water (100 mL) was added to precipitate triphenylphosphine oxide, which was then removed by filtration. The water was removed by rotary evaporation. Yield: 6 g (60% vs. Peg_{2000} monomethylether). ^1H NMR: (400MHz, $CDCl_3$) 3.615 (180 H), 3.43 (2H), 3.35 (3H).

Synthesis of Anisamide-PEG_{2000}-NH_2: $DiaminoPEG_{2000}$ was synthesized by a previously reported method.[60] $DiaminoPEG_{2000}$ (2 g, 1 mmol) were dissolved into 100 mL of dichoromethane. Subsequently, 4-methoxybenzoic acid (182.4 mg, 1.1 eq), dicyclohexylcarbodiimide (308 mg, 1.5 mmol) and 4-dimethyl-aminopyridine (140 mg, 1.1 mmol) were dissolved into the PEG solution. The solution was stirred at room temperature for 24 h, and then the dicyclohexylurea byproduct was removed by filtration. The dichloromethane was removed by rotary evaporation. The desired anisamide-PEG_{2000}-NH_2 product was isolated by silica gel chromatography using 10% MeOH in CH_2Cl_2. Yield: 700 mg, 33%. ^1H NMR (400MHz, $CDCl_3$), 7.767 (2H), 6.891 (2H), 3.82 (2H), 3.61 (180H), 3.44 (2H)

2.4.5: Nanoparticle Synthesis

*Synthesis of Pt(Dach)-based polysilsesquioxane nanoparticles (**2.1**):* DachPt-Si (30 mg, $2.9x10^{-5}$ mol) was dissolved in 3.25 mL ammonium hydroxide (33%) aqueous solution and then added to 125 mL of a 0.3 M AOT solution in hexanes. The microemulsion was stirred for 10 min, until it became optically transparent. An additional 500 μL of ammonium hydroxide was added. The microemulsion was stirred for 24 h, in the dark. An equal volume of ethanol was added to quench the reaction and precipitate the nanoparticles. The particles were isolated by centrifugation and washed three times with ethanol. The particles were

stored as an ethanolic suspension. The nanoparticles were characterized by DLS, TEM, TGA and ICP-MS.

*Synthesis of rhodamine-tagged nanoparticles **(Rhod-2.1)**:* DachPt-Si (12 mg, $1.1x10^{-5}$ mol) was dissolved in 1.3 mL ammonium hydroxide (33%), and then added to 50 mL of a 0.3 M AOT solution in hexanes. Rhodamine-APS solution (100 μL, $5.8x10^{-7}$ mol) was added. The microemulsion was stirred for 10 min, until optically transparent. An additional 200 μL of ammonium hydroxide was added. The microemulsion was stirred for 24 h. An equal volume of ethanol was added to quench the reaction and the particles were isolated by centrifugation and washed twice with ethanol. All subsequent post-synthetic modification of **rhod-2.1** followed the same procedures listed below for **2.1**.

2.4.6: Nanoparticle Surface Functionalization

*Conjugation of triethoxysilylpropyl carbomoyl c(RGDfK) to **2.1 (RGD-2.1)**:* **2.1** was dispersed in ethanol at a concentration of 2mg/mL. Tri(ethoxy)silylpropyl carbomoyl c(RGDfK) solution was added (5% by mass). The pH of the solution was adjusted to 10 with aqueous ammonium hydroxide, and the resulting suspension was stirred for 24 h, in the dark. The particles were isolated by centrifugation and washed twice with ethanol. The resulting particles were analyzed by DLS and zeta potential.

*Pegylation of **2.1 (PEG-2.1)**:* **2.1** was redispersed into an acetonitrile solution containing 7 mM EDC and Peg2000-NH_2 (1.65 mM) at 2mg/mL. The suspension was stirred at 50°C for 24 h, in the dark. The particles were isolated by centrifugation and washed twice with ethanol. The particles were analyzed by DLS and zeta potential.

*Synthesis of anisamide-targeted-Pegylated **2.1** (**APEG-2.1**):* **2.1** was re-dispersed at 2mg/mL into an acetonitrile solution containing 7 mM EDC, 0.165 mM anisamide-PEG_{2000}-NH_2, and 1.65 mM PEG_{2000}-NH_2. The suspension was stirred at 50°C for 24 h, in the dark. The particles were isolated by centrifugation and washed twice with ethanol. The particles were analyzed by DLS and zeta potential.

2.4.7 Platinum Release from 2.1

Two milligrams of 2.**1** were redispersed into 1 mL 2 mM HEPES buffer (pH=7.4). The nanoparticle suspension was placed into a 3500 MW cutoff dialysis bag, and the bag was placed into 360 mL 2 mM HEPES buffer at 37°C. The solution was sparged with argon and sealed within an air-free apparatus. The solution was incubated at 37°C for 22.5 h, with dialysate aliquots removed periodically. L-cysteine was added in deoxygenated HEPES for a total concentration of 5mM. The dialysate was incubated at 37°C, with aliquots removed periodically. Platinum release was determined by ICP-MS.

2.4.8 *In Vitro* Assays

General: DLD-1 human colorectal adenocarcinoma cells (ATCC# CCL-221) and HT-29 human colorectal adenocarcinoma cells (ATCC# HTB-38) were purchased from the Tissue Culture Facility of the Lineberger Comprehensive Cancer Center at the University of North Carolina at Chapel Hill. DLD-1 cells were cultured in RPMI-1640 growth medium (Cellgro) supplemented with 10% fetal bovine serum (Sigma) and 2% pencillin-streptomycin (Sigma). HT-29 cells were cultured in McCoys 5A 1X growth medium (Mediatech) supplemented with 10%FBS (Mediatech) and 2% penicillin-streptomycin solution. AsPC-1 human pancreatic adenocarcinoma cells (ATCC# CRL-1682) and BxPC-3 human pancreatic

adenocarcinoma cells (ATCC# CRL-1687) were received from the laboratory of Dr. Jen Jen Yeh at the University of North Carolina at Chapel Hill. AsPC-1 and BxPC-3 cells were cultured in RPMI-1640 growth medium supplemented with 10% FBS and 2% pencillin-streptomycin.

DLD-1 Colon cancer cell viability assay: Confluent DLD-1 cells were trypsinized and counted with a hematocytometer. Cells were plated in 6-well plates at a cell density of 50,000 cells/well and 3 mL of complete growth medium. Plates were incubated at 37°C, 5% CO_2, overnight. Media was removed from wells, and each well was washed with 2 mL of PBS. Drug/particle solutions were prepared in media containing 5% PBS. Aliquots of drug/particle solutions and media (5% PBS) were given to each well to result in drug/particle concentrations of 0, 0.025, 0.25, 0.5, 1, and 2 μM. Plates were incubated for 3 days, and viability was determined via the trypan blue exclusion assay.

HT-29 colon cancer cell cell viability assay: HT-29 cells were plated in 6-well plates in 3 mL of media at a cell density of 100,000cells/well, and were incubated for 12 h to promote cell attachment. Media was removed from the wells and each well was washed with 2 mL PBS. 5 μM drug stock solutions were prepared with oxaliplatin, **2.1,** and **RGD-2.1,** and these were added to wells, along with additional media, resulting in concentrations of 0, 0.1, 0.25, 0.5, 1 and 5 μM. The plates were incubated for 48 h, and cell viability was determined using the trypan blue exclusion assay.

BxPc-3 pancreatic cancer cell viability assay: Confluent BxPC-3 cells were trypsinized and counted using a hemocytometer. Cells were plated in 6-well plates at a cell density of 100,000 cells/well and 3 mL of complete growth medium. Plates were incubated at 37°C, 5%

CO_2, overnight. Media was removed from wells, and each well was washed with 2 mL PBS. Drug/particle solutions were prepared in media containing 5% PBS. Aliquots of drug/particle solutions and media (5% PBS) were distributed to each well, resulting in drug/particle concentrations of 0, 1, 2.5, 6, 12.5, and 25 μM. Plates were incubated for 3 days, and viability was determined using the trypan blue exclusion assay.

AsPC-1 pancreatic cancer cell viability assay: Confluent AsPC-1 cells were trypsinized and counted using a hemocytometer. Cells were plated in 6-well plates at a cell density of 100,000 cells/well and 2 mL of complete growth medium. Plates were incubated at 37°C, 5% CO_2, overnight. Media was removed from wells, and each well was washed with 2 mL PBS. Drug/particle solutions were prepared in media containing 5% PBS. Aliquots of drug/particle solutions and media (5% PBS) were given to each well, resulting in drug/particle concentrations of 0, 1, 2.5, 6, 12.5, and 25 μM. Plates were incubated for 3 days, and viability was determined via the trypan blue exclusion assay.

Confocal Microscopy-DLD-1 cancer cells: Glass microscope coverslips were silanized by a reported protocol.[61] Confluent DLD-1 cells were trypsinized and counted using a hemocytometer. Cells were plated in 6-well plates containing coverslips at a cell density of 300,000 cells/well and 3 mL of complete growth medium. Plates were incubated at 37°C, 5% CO_2, overnight. Media was removed from the plates and each well was washed with 2 mL PBS. Particle dispersions were prepared in PBS. Wells were given aliquots of particle dispersion, PBS, and media to yield concentrations of 0, 0.02, 0.05, and 0.1 mg/well. Wells were incubated at 37°C, 5% CO_2, for 10 minutes. The media was removed, each well washed with 2 mL PBS, and 1 mL fresh media added to each well. The coverslips were adhered on slides and imaged on a Zeiss Pascal laser scanning confocal microscope at the Microscopy

Services Laboratory of the Department of Pathology and Laboratory Medicine at UNC-Chapel Hill.

Confocal Microscopy AsPC-1 pancreatic cells: Glass coverslips were silanized by a previously reported protocol[61] and placed within the wells of a 6-well plate. AsPC-1 cells were collected by trypsinization and counted using a hemocytometer. Cells were plated at a cell density of 250,000 cells/well (3 mL media). The plates were incubated at 37°C, 5% CO_2, overnight to promote cell adhesion. The media was removed, and the wells were washed twice with 1 mL PBS. The plates were refilled with media (2 mL) containing rhod-**2.1**, PEG-rhod-**2.1**, or APEG-rhod-**2.1** at a Pt concentration of 5 μM or no nanoparticle (as a control). The plates were incubated for either 1 or 5.5 hours. After the incubation period, the media was removed, and each well was washed with 1 mL PBS. The wells were refilled with 1 mL media containing 15 μL FITC-Annexin V (Invitrogen). The plates were incubated for 15 min, the media was removed, and each well was washed with 1 mL PBS. The coverslips were removed from each well and the cells were mounted onto glass slides. Cells were imaged at the Microscopy Services Laboratory at the University of North Carolina at Chapel Hill on an Olympus FV500 laser scanning confocal microscope.

2.4.9 *In Vivo* Assays

AsPC-1 subcutaneous mouse xenografts: Female athymic nude mice (6-8 weeks old) were purchased from Jackson Laboratories. Mice were cared for according to an approved protocol by the institutional animal care and use committee. AsPC-1 cells were suspended in 50% matrigel (BD Biosciences) and 50% RPMI-1640 medium at 1,000,000 cells/mL. The cells were injected subcutaneously in both flanks with 100 μL of the cell suspension. Tumor

growth was measured every Monday, Wednesday, and Friday, and treatment commenced when tumors were palpable in each flank. Treatments were administered by tail vein injection with 100 μL PBS. The mice were divided into 4 groups (4-6 mice per group) and received PBS (control), oxaliplatin (5 mg Pt/kg), PEG-**1** (5mg Pt/kg) or APEG-**1** (5 mg Pt/kg) The mice received treatments once a week for three weeks (days 0, 7, and 14). Tumor volume was calculated by the formula (a x b x c)/2, where a, b, and c are the tumor dimensions in three directions. Tumor growth was monitored every Monday, Wednesday, and Friday until the tumor size reached the maximum allowed size. Mice weights were recorded weekly throughout the study. The mice were euthanized by CO_2 inhalation and cervical dislocation. The tumors were then removed and fixed in formalin.

AsPc-1 orthotopic pancreatic cancer model: AsPC-1-luciferase cells were orthotopically implanted within the pancreas of nu/nu mice (100,000 cells) and the tumors were allowed to grow until detected by optical imaging. Mice were injected with either oxaliplatin (5mg Pt), PEG-**2.1** (5mg Pt/kg), or PBS control through the tail vein (100μL total volume) on study days 0, 7, 14, and 21. Tumor growth was monitored weekly by luciferin injections (100μL) and imaged post-injection on a IVIS-100 system. The data was analyzed using Xenogen Living Image software by analyzing the total luminescent counts and normalizing against the background image. Luminescence intensities were normalized compared to the day -1 luminescence intensity.

2.4.10 *Ex Vivo* Tissue Histology

Tumors were received in a formalin solution. For histology, the tumors were placed in labeled cassettes and flushed with water for 20 min. The tumors were then transported to

the Lineberger Comprehensive Cancer Center Animal Histopathology Core Lab in a 70% ethanol solution where they were pariffinized, cut, and H&E stained. The stained tumors were imaged at the UNC Microscopy Services Laboratory using an Olympus BX61 Upright Fluorescence Microscope equipped with Improvision's Volocity software. Images were captured using a QImaging RETIGA 4000R color camera.

2.5 References

1. Rosenberg, B.; Van Camp, L.; Krigas, T., Inhibition of Cell Division in *Escherichia coli* by Electrolysis Products from a Platinum Electrode. *Nature* 1965, *205* (4972), 698-699.

2. Kelland, L., The resurgence of platinum-based cancer chemotherapy. *Nat Rev Cancer* 2007, *7* (8), 573-584.

3. Jung, Y.; Lippard, S. J., Direct Cellular Responses to Platinum-Induced DNA Damage. *Chem. Rev.* 2007, *107* (5), 1387-1407.

4. Wang, D.; Lippard, S. J., Cellular processing of platinum anticancer drugs. *Nat. Rev. Drug Discovery* 2005, *4* (4), 307-320.

5. Alexis, F.; Pridgen, E.; Molnar, L. K.; Farokhzad, O. C., Factors Affecting the Clearance and Biodistribution of Polymeric Nanoparticles. *Mol. Pharmaceutics* 2008, *5* (4), 505-515.

6. Cheon, J.; Lee, J.-H., Synergistically Integrated Nanoparticles as Multimodal Probes for Nanobiotechnology. *Acc. Chem. Res.* 2008, *41* (12), 1630-1640.

7. Lee, J. E.; Lee, N.; Kim, H.; Kim, J.; Choi, S. H.; Kim, J. H.; Kim, T.; Song, I. C.; Park, S. P.; Moon, W. K.; Hyeon, T., Uniform Mesoporous Dye-Doped Silica Nanoparticles Decorated with Multiple Magnetite Nanocrystals for Simultaneous Enhanced Magnetic Resonance Imaging, Fluorescence Imaging, and Drug Delivery. *J. Am. Chem. Soc.* 2009, *132* (2), 552-557.

8. Li, S.-D.; Huang, L., Pharmacokinetics and Biodistribution of Nanoparticles. *Mol. Pharmaceutics* 2008, *5* (4), 496-504.

9. Liu, R.; Zhang, Y.; Zhao, X.; Agarwal, A.; Mueller, L. J.; Feng, P., pH-Responsive Nanogated Ensemble Based on Gold-Capped Mesoporous Silica through an Acid-Labile Acetal Linker. *J. Am. Chem. Soc.* 2010, *132* (5), 1500-1501.

10. Sajja, H. K.; East, M. P.; Mao, H.; Wang, Y. A.; Nie, S.; Yang, L., Development of Multifunctional Nanoparticles for Targeted Drug Delivery and Noninvasive Imaging of Therapeutic Effect. *Curr. Drug Discovery Technol.* 2009, *6* (1), 43-51.

11. Yavuz, M. S.; Cheng, Y.; Chen, J.; Cobley, C. M.; Zhang, Q.; Rycenga, M.; Xie, J.; Kim, C.; Song, K. H.; Schwartz, A. G.; Wang, L. V.; Xia, Y., Gold nanocages covered by smart polymers for controlled release with near-infrared light. *Nat Mater* 2009, *8* (12), 935-939.

12. Peer, D.; Karp, J. M.; Hong, S.; Farokhzad, O. C.; Margalit, R.; Langer, R., Nanocarriers as an emerging platform for cancer therapy. *Nat. Nanotechnol.* 2007, *2* (12), 751-760.

13. Rieter, W. J.; Pott, K. M.; Taylor, K. M. L.; Lin, W., Nanoscale Coordination Polymers for Platinum-Based Anticancer Drug Delivery. *J. Am. Chem. Soc.* 2008, *130* (35), 11584-11585.

14. Taylor-Pashow, K. M. L.; Della Rocca, J.; Xie, Z.; Tran, S.; Lin, W., Postsynthetic Modifications of Iron-Carboxylate Nanoscale Metal−Organic Frameworks for Imaging and Drug Delivery. *J. Am. Chem. Soc.* 2009, *131* (40), 14261-14263.

15. Hu, L. C.; Shea, K. J., Organo-silica hybrid functional nanomaterials: how do organic bridging groups and silsesquioxane moieties work hand-in-hand? *Chem. Soc. Rev.* 2011, *40* (2), 688-695.

16. Shea, K. J.; Loy, D. A., Bridged polysilsesquioxanes. Molecular-engineered hybrid organic-inorganic materials. *Chem. Mater.* 2001, *13* (10), 3306-3319.

17. Shea, K. J.; Loy, D. A., Bridged polysilsesquioxanes: Molecular engineering of hybrid organic-inorganic materials. *MRS Bull.* 2001, *26* (5), 368-376.

18. Hu, L. C.; Khiterer, M.; Huang, S. J.; Chan, J. C. C.; Davey, J. R.; Shea, K. J., Uniform, Spherical Bridged Polysilsesquioxane Nano- and Microparticles by a Nonemulsion Method. *Chem. Mater.* 2010, *22* (18), 5244-5250.

19. Khiterer, M.; Shea, K. J., Spherical, monodisperse, functional bridged polysilsesquioxane nanoparticles. *Nano Lett.* 2007, *7* (9), 2684-2687.

20. Zhao, L. H.; Loy, D. A.; Shea, K. J., Photodeformable spherical hybrid nanoparticles. *J. Am. Chem. Soc.* 2006, *128* (44), 14250-14251.

21. Corma, A.; Diaz, U.; Arrica, M.; Fernandez, E.; Ortega, I., Organic-Inorganic Nanospheres with Responsive Molecular Gates for Drug Storage and Release. *Angew. Chem., Int. Ed.* 2009, *48* (34), 6247-6250.

22. Urata, C.; Yamada, H.; Wakabayashi, R.; Aoyama, Y.; Hirosawa, S.; Arai, S.; Takeoka, S.; Yamauchi, Y.; Kuroda, K., Aqueous Colloidal Mesoporous Nanoparticles with Ethenylene-Bridged Silsesquioxane Frameworks. *J. Am. Chem. Soc.* 2011, *133* (21), 8102-8105.

23. Ambrogio, M. W.; Thomas, C. R.; Zhao, Y.-L.; Zink, J. I.; Stoddart, J. F., Mechanized Silica Nanoparticles: A New Frontier in Theranostic Nanomedicine. *Acc. Chem. Res.* 2011, *44* (10), 903-913.

24. Ashley, C. E.; Carnes, E. C.; Phillips, G. K.; Padilla, D.; Durfee, P. N.; Brown, P. A.; Hanna, T. N.; Liu, J.; Phillips, B.; Carter, M. B.; Carroll, N. J.; Jiang, X.; Dunphy, D. R.; Willman, C. L.; Petsev, D. N.; Evans, D. G.; Parikh, A. N.; Chackerian, B.; Wharton, W.; Peabody, D. S.; Brinker, C. J., The targeted delivery of multicomponent cargos to

cancer cells by nanoporous particle-supported lipid bilayers. *Nat Mater* 2011, *10* (5), 389-397.

25. Kim, T.; Momin, E.; Choi, J.; Yuan, K.; Zaidi, H.; Kim, J.; Park, M.; Lee, N.; McMahon, M. T.; Quinones-Hinojosa, A.; Bulte, J. W. M.; Hyeon, T.; Gilad, A. A., Mesoporous Silica-Coated Hollow Manganese Oxide Nanoparticles as Positive T1 Contrast Agents for Labeling and MRI Tracking of Adipose-Derived Mesenchymal Stem Cells. *J. Am. Chem. Soc.* 2011, *133* (9), 2955-2961.

26. Taylor-Pashow, K. M. L.; Della Rocca, J.; Huxford, R. C.; Lin, W., Hybrid nanomaterials for biomedical applications. *Chem. Commun.* 2010, *46* (32), 5832-5849.

27. Dhara, S. C., A rapid method for the synthesis of *cis*-[$PtCl_2(NH_3)_2$]. *Indian J. Chem.* 1970, *8* (193-194).

28. Ali Khan, S. R.; Huang, S.; Shamsuddin, S.; Inutsuka, S.; Whitmire, K. H.; Siddik, Z. H.; Khokhar, A. R., Synthesis, characterization and cytotoxicity of new platinum(IV) axial carboxylate complexes: crystal structure of potential antitumor agent [PtIV(trans-1R,2R-diaminocyclohexane)trans(acetate)2Cl2]. *Bioorg. Med. Chem.* 2000, *8* (3), 515-521.

29. Barnes, K. R.; Kutikov, A.; Lippard, S. J., Synthesis, Characterization, and Cytotoxicity of a Series of Estrogen-Tethered Platinum(IV) Complexes. *Chem. Biol.* 2004, *11* (4), 557-564.

30. Giandomenico, C. M.; Abrams, M. J.; Murrer, B. A.; Vollano, J. F.; Rheinheimer, M. I.; Wyer, S. B.; Bossard, G. E.; Higgins, J. D., Carboxylation of Kinetically Inert Platinum(IV) Hydroxy Complexes. An Entr.acte.ee into Orally Active Platinum(IV) Antitumor Agents. *Inorg. Chem.* 1995, *34* (5), 1015-1021.

31. Hall, M. D.; Mellor, H. R.; Callaghan, R.; Hambley, T. W., Basis for Design and Development of Platinum(IV) Anticancer Complexes. *J. Med. Chem.* 2007, *50* (15), 3403-3411.

32. Brown, S. D.; Nativo, P.; Smith, J.-A.; Stirling, D.; Edwards, P. R.; Venugopal, B.; Flint, D. J.; Plumb, J. A.; Graham, D.; Wheate, N. J., Gold Nanoparticles for the Improved Anticancer Drug Delivery of the Active Component of Oxaliplatin. *J. Am. Chem. Soc.* 2010, *132* (13), 4678-4684.

33. Dhar, S.; Daniel, W. L.; Giljohann, D. A.; Mirkin, C. A.; Lippard, S. J., Polyvalent Oligonucleotide Gold Nanoparticle Conjugates as Delivery Vehicles for Platinum(IV) Warheads. *J. Am. Chem. Soc.* 2009, *131* (41), 14652-14653.

34. Dhar, S.; Gu, F. X.; Langer, R.; Farokhzad, O. C.; Lippard, S. J., Targeted delivery of cisplatin to prostate cancer cells by aptamer functionalized Pt(IV) prodrug-PLGA–PEG nanoparticles. *Proc. Natl. Acad. Sci. U.S.A.* 2008, *105* (45), 17356-17361.

35. Feazell, R. P.; Nakayama-Ratchford, N.; Dai, H.; Lippard, S. J., Soluble Single-Walled Carbon Nanotubes as Longboat Delivery Systems for Platinum(IV) Anticancer Drug Design. *J. Am. Chem. Soc.* 2007, *129* (27), 8438-8439.

36. Min, Y.; Mao, C.; Xu, D.; Wang, J.; Liu, Y., Gold nanorods for platinum based prodrug delivery. *Chem. Commun.* 2010, *46* (44), 8424-8426.

37. Tallury, P.; Payton, K.; Santra, S., Silica-based multimodal/multifunctional nanoparticles for bioimaging and biosensing applications. *Nanomedicine* 2008, *3* (4), 579-592.

38. Yan, J. L.; Estevez, M. C.; Smith, J. E.; Wang, K. M.; He, X. X.; Wang, L.; Tan, W. H., Dye-doped nanoparticles for bioanalysis. *Nano Today* 2007, *2* (3), 44-50.

39. Hermanson, G. T., *Bioconjugate Techniques*. 1st ed.; Academic Press: San Diego, CA, 1996; Vol. 1.

40. Liu, S., Radiolabeled Multimeric Cyclic RGD Peptides as Integrin αvβ3 Targeted Radiotracers for Tumor Imaging. *Mol. Pharmaceutics* 2006, *3* (5), 472-487.

41. Schottelius, M.; Laufer, B.; Kessler, H.; Wester, H.-J. r., Ligands for Mapping αvβ3-Integrin Expression in Vivo. *Acc. Chem. Res.* 2009, *42* (7), 969-980.

42. Temming, K.; Schiffelers, R. M.; Molema, G.; Kok, R. J., RGD-based strategies for selective delivery of therapeutics and imaging agents to the tumour vasculature. *Drug Resist. Updates* 2005, *8* (6), 381-402.

43. Zalipsky, S., Functionalized Poly(ethylene glycols) for Preparation of Biologically Relevant Conjugates. *Bioconjugate Chem.* 1995, *6* (2), 150-165.

44. Aydar, E.; Palmer, C. P.; Djamgoz, M. B. A., Sigma Receptors and Cancer. *Cancer Res.* 2004, *64* (15), 5029-5035.

45. Banerjee, R.; Tyagi, P.; Li, S.; Huang, L., Anisamide-targeted stealth liposomes: A potent carrier for targeting doxorubicin to human prostate cancer cells. *Int. J. Cancer* 2004, *112* (4), 693-700.

46. John, C. S.; Vilner, B. J.; Geyer, B. C.; Moody, T.; Bowen, W. D., Targeting Sigma Receptor-binding Benzamides as in Vivo Diagnostic and Therapeutic Agents for Human Prostate Tumors. *Cancer Res.* 1999, *59* (18), 4578-4583.

47. Li, S.-D.; Huang, L., Targeted Delivery of Antisense Oligodeoxynucleotide and Small Interference RNA into Lung Cancer Cells. *Mol. Pharmaceutics* 2006, *3* (5), 579-588.

48. Nakagawa, O.; Ming, X.; Huang, L.; Juliano, R. L., Targeted Intracellular Delivery of Antisense Oligonucleotides via Conjugation with Small-Molecule Ligands. *J. Am. Chem. Soc.* 2010, *132* (26), 8848-8849.

49. Vilner, B. J.; John, C. S.; Bowen, W. D., Sigma-1 and Sigma-2 Receptors Are Expressed in a Wide Variety of Human and Rodent Tumor Cell Lines. *Cancer Res.* 1995, *55* (2), 408-413.

50. Capdevila, J.; Elez, E.; Peralta, S.; Macarulla, T.; Ramos, F. J.; Tabernero, J., Oxaliplatin-based chemotherapy in the management of colorectal cancer. *Exp. Rev. Anticancer Ther.* 2008, *8* (8), 1223-1236.

51. Sanchez, S. E.; Trevino, J. G., Current Adjuvant and Targeted Therapies for Pancreatic Adenocarcinoma. *Curr. Med. Chem.* 2008, *15* (17), 1674-1683.

52. STATHOPOULOS, G. P.; ANDROULAKIS, N.; SOUGLAKOS, J.; STATHOPOULOS, J.; GEORGOULIAS, V., Present Treatment and Future Expectations in Advanced Pancreatic Cancer. *Anticancer Res.* 2008, *28* (2B), 1303-1308.

53. Löhr, M.; Trautmann, B.; Göttler, M.; Peters, S.; Zauner, I.; Maier, A.; Klöppel, G.; Liebe, S.; Kreuser, E.-D., Expression and Function of Receptors for Extracellular Matrix Proteins in Human Ductal Adenocarcinomas of the Pancreas. *Pancreas* 1996, *12* (3), 248-259.

54. Mukhopadhyay, S.; Barnés, C. M.; Haskel, A.; Short, S. M.; Barnes, K. R.; Lippard, S. J., Conjugated Platinum(IV)−Peptide Complexes for Targeting Angiogenic Tumor Vasculature. *Bioconjugate Chem.* 2007, *19* (1), 39-49.

55. Kashiwagi, H.; McDunn, J.; Simon, P.; Goedegebuure, P.; Xu, J.; Jones, L.; Chang, K.; Johnston, F.; Trinkaus, K.; Hotchkiss, R.; Mach, R.; Hawkins, W., Selective sigma-2 ligands preferentially bind to pancreatic adenocarcinomas: applications in diagnostic imaging and therapy. *Mol. Cancer* 2007, *6* (1), 48.

56. Vermes, I.; Haanen, C.; Steffens-Nakken, H.; Reutellingsperger, C., A novel assay for apoptosis Flow cytometric detection of phosphatidylserine expression on early apoptotic cells using fluorescein labelled Annexin V. *J. Immunol. Methods* 1995, *184* (1), 39-51.

57. Rice, J. R.; Gerberich, J. L.; Nowotnik, D. P.; Howell, S. B., Preclinical Efficacy and Pharmacokinetics of AP5346, A Novel Diaminocylohexane-Platinum Tumor-Targeting Drug Delivery System. *Clin. Cancer. Res.* 2006, *12* (7), 2248-2254.

58. Talmadge, J. E.; Singh, R. K.; Fidler, I. J.; Raz, A., Murine Models to Evaluate Novel and Conventional Therapeutic Strategies for Cancer. *Am. J. Pathol.* 2007, *170* (3), 793-804.

59. Taylor, K. M. L.; Rieter, W. J.; Lin, W., Manganese-Based Nanoscale Metal−Organic Frameworks for Magnetic Resonance Imaging. *J. Am. Chem. Soc.* 2008, *130* (44), 14358-14359.

60. Kikkeri, R.; Lepenies, B.; Adibekian, A.; Laurino, P.; Seeberger, P. H., In Vitro Imaging and in Vivo Liver Targeting with Carbohydrate Capped Quantum Dots. *J. Am. Chem. Soc.* 2009, *131* (6), 2110-2112.

61. Cold Spring Harbor Protocols, Silanization of microscope coverslips. doi:10.1101/pdb.prot4988

Chapter 3: Co-condensed Silica Nanoparticles for Platinum-based Anticancer Drug Delivery

3.1 Introduction

Since its discovery in 1960 by Rosenberg and coworkers, cisplatin has played a major role in cancer chemotherapy.[1] Cisplatin is clinically used against a variety of different cancers such as testicular, breast, lung, cervical, head and neck, and ovarian cancers.[2-6] It is one of the most widely used and potent cancer chemotherapies, but cisplatin chemotherapy is limited by its high general toxicity and severe side effects. Some cancers also display inherent or acquired resistance to cisplatin therapy.[7-8] Despite an intense research effort of screening thousands of platinum compounds in the past few decades, only two additional platinum complexes, carboplatin and oxaliplatin, have been approved by the FDA.[9] There exists an acute need to develop strategies to effectively deliver platinum drugs to the tumor while limiting side effects.

Nanomaterials offer a potential solution. Nanoparticle therapeutics generally have a superior biodistribution over small molecule therapies due to longer circulation times. Resulting from their size, nanomaterials cannot penetrate normal vasculatures and capillaries, leading to a lower nanoparticle effective dose to healthy organs such as the skin, muscle, lungs and heart compared to small molecules, which would reduce side effects. Nanomaterials also have higher tumor uptake, due to the enhanced permeability and retention

effect, and tumor uptake can be enhanced with the conjugation of targeting ligands to the nanoparticle surface.[10] Nanoparticulate therapeutic agents offer tailorable size, surface properties, and drug release rates which would allow for the optimization of nanoparticle efficacy.[11-13] Our lab has recently developed two nanoscale coordination polymers (NCPs) as potential delivery vectors for cisplatin therapy.[14-15] These materials demonstrated high drug loading and comparable cytotoxicity to cisplatin *in vitro*; however, NCPs readily degrade under physiological conditions, limiting their *in vivo* utility. We sought to develop a more stable nanoparticle platform for cisplatin delivery, which would be stable under normal physiological conditions. The drug can be triggered to be released from the nanoparticles once they reach the tumor microenvironment.

Silica-based nanomaterials have received an increasing amount of attention for biomedical applications.[16-22] Silica is an inert, biocompatible matrix material that can be functionalized by a variety of covalent and non-covalent strategies.[16, 21, 23-25] Our lab has developed several solid or mesoporous silica nanoparticle platforms for magnetic resonance and optical imaging.[26-30] A silica-based material, known as Cornell dots (C-dots), is undergoing clinical investigation as an optical contrast agent.[31] This chapter reports the development of hybrid silica nanospheres for cisplatin delivery. The development of these silica nanoparticles begins with the synthesis of a platinum(IV) cisplatin prodrug. The prodrug is incorporated covalently into a silica nanoparticle by co-condensation of the silica and platinum precursors. The silica nanoparticles can be post-synthetically modified to include a cancer-targeting peptide and are evaluated *in vitro* against human non-small cell lung cancer cell lines.

3.2 Results and Discussion

3.2.1 Platinum Complex Synthesis

The platinum(IV) complex *c,c,t*-$Pt(NH_3)_2Cl_2$(triethoxysilylpropyl succinate)$_2$ (DSCP-Si) was synthesized from commercially available cisplatin (Scheme 3-1). Cisplatin was oxidized using hydrogen peroxide in water to form *c,c,t*-$Pt(NH_3)_2Cl_2(OH)_2$ in good yields (typically around 75%) (Scheme 3.1, i). The hydroxyl groups in *c,c,t*-$Pt(NH_3)_2Cl_2(OH)_2$ act as nucleophiles and react with electrophilic groups, [32-33] in this case, the carbonyl groups of triethoxysilylpropyl succinic anhydride, to form DSCP-Si at a 78% yield (Scheme 3-1, ii). This platinum complex has two orthogonal functional groups: triethoxysilyl groups to allow for covalent attachment within the silica matrix and carboxylic acids to allow for post-synthetic modification of the synthesized nanoparticles.

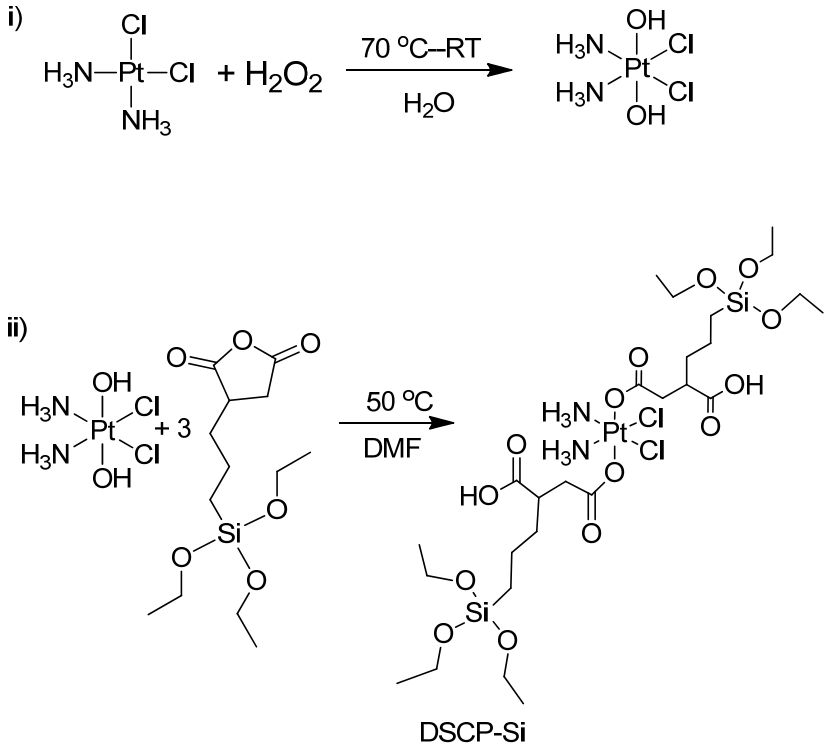

Scheme 3-1: Schematic of the synthesis of the platinum complexes used i) cisplatin is oxidized with hydrogen peroxide in water to form *c,c,t*-$Pt(NH_3)_2Cl_2(OH)_2$. ii) *c,c,t*-$Pt(NH_3)_2Cl_2(OH)_2$ reacts with triethoxysilyl propyl succinic anhydride to form DSCP-Si.

3.2.2: Synthesis of Co-condensed Silica Nanoparticles

A water-in-oil, or reverse, microemulsion was used to synthesize the silica nanoparticles with DSCP-Si and tetraethylorthosilicate (TEOS) as the silica source. Reverse microemulsions are a common way to synthesize silica nanoparticles with diameters under 50 nm and have been used by our group, and others, to synthesize a variety of functional, monodisperse silica nanoparticles of different sizes.[16, 23, 28, 34-35] To synthesize silica nanoparticles with co-condensed platinum complexes, we employed a reverse microemulsion based on the neutral surfactant Triton X100, with 1-hexanol as the co-surfactant and cyclohexanes as the oil phase. DSCP-Si was dissolved into the water phase and added to the

oil phase to create the microemulsion (Scheme 3-2). TEOS was then added to the reaction mixture, followed by ammonium hydroxide. Hydrophobic TEOS molecules remain in the oil phase of the microemulsion, diffusing to the oil-water interface. TEOS is hydrolyzed, entering the water phase. Subsequent condensation of orthosilicic acid and DSCP-Si affords the co-condensed silica nanoparticles (Scheme 3-2). The reaction is quenched by the addition of an equal volume of ethanol and the particles are isolated by centrifugation.

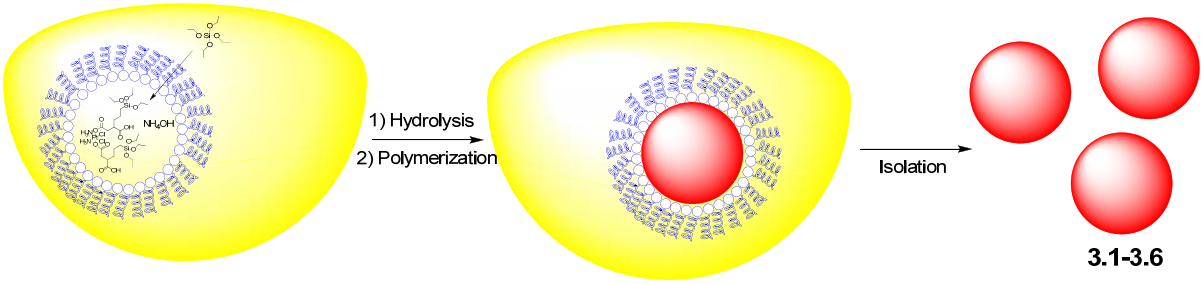

Scheme 3-2: Schematic demonstrating the synthesis of co-condensed silica nanoparticles. TEOS diffuses into the water droplets and subsequent hydrolysis and condensation leads to the creation of the Pt-containing nanoparticles within the water droplets.

Nanoparticles **3.1**, **3.2**, **3.3**, and **3.4** were synthesized within a 0.3 M Triton X100 and 1.5 M 1-hexanol in cyclohexanes reverse microemulsion using ammonia as a base catalyst. The *W* value (water to surfactant molar ratio) of this microemulsion was 7.5. Particles **3.1**, **3.2**, **3.3**, and **3.4** correspond to the molar equivalents of TEOS of 5, 10, 15, and 20, respectively. Ethanol was added after 3 hours after the initiation of the particle synthesis to quench the reaction; the particles were isolated by centrifugation and washed with ethanol to remove any residual surfactants. SEM images of the as-synthesized nanoparticles showed a change in nanoparticle morphology as a result of the different amount of TEOS added to the microemulsion (Figure 3-1). **3.1** had a fused and fiber-like morphology with no clearly-defined individual nanoparticles (Figure 3-1 A). Nanoparticles with 10 equivalents of TEOS (**3.2**) were spherical and approximately 50-75 nm in diameter. There was some degrees of

polydispersity, as there were a few larger nanoparticles present (Figure 3-1 B). **3.3** was in the same size regime, with some larger fiber-like nanoparticles present (Figure 3-1 C). **3.4** yielded smaller nanoparticles that were approximately 30 nm in diameter (Figure 3-1 D). Dynamic light scattering (DLS) measurements of **3.2**, **3.3**, and **3.4** in 5 mM PBS (pH= 7.4) demonstrated that all three nanoparticles had multimodal intensity distributions (Figure 3-2, Table 3-1). This is due to the presence of a small amount of larger nanoparticles, which could not be completely removed from the synthesis and/or salt-induced aggregation of the nanoparticles. However, the number-weighted distribution data of all three nanoparticles was unimodal and corresponded roughly to the SEM diameter (Figure 3-2, Table 3-1). Inductively-coupled plasma-mass spectrometry (ICP-MS) measurements of **3.2**-**3.4** demonstrated a modest cisplatin loading of 9.2-18.4 wt%; however, the thermogravimetric analysis (TGA) weight loss curves gave much higher organic weight loss than expected, due to incompletely hydrolyzed silica species within the nanoparticle (Figure 3-3). This hypothesis was supported by TGA analysis of pure silica nanoparticles synthesized under the same conditions, which had considerable organic weight loss.

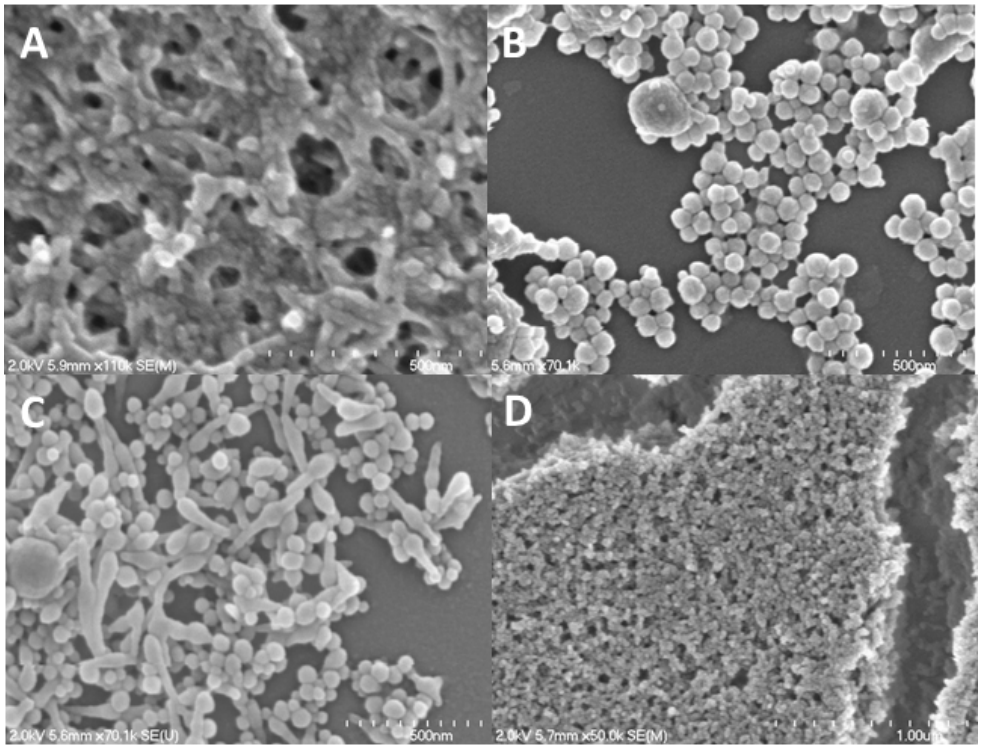

Figure 3-1: SEM images of as synthesized **3.1** (A), **3.2** (B), **3.3** (C), and **3.4** (D).

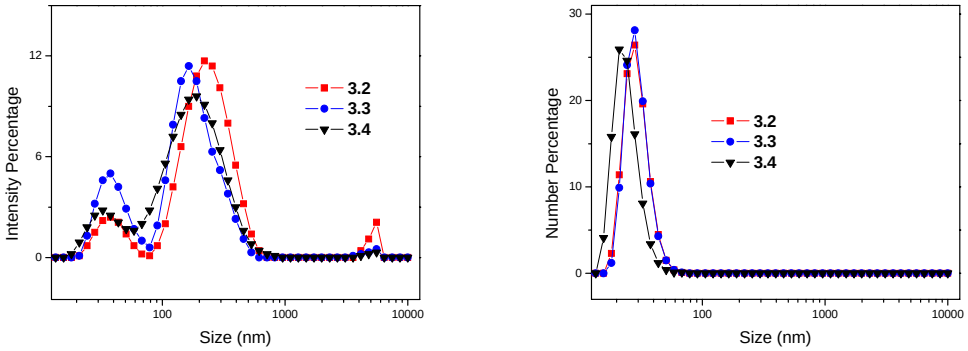

Figure 3-2: Intensity (left) and number (right) weighted DLS spectra of **3.2** (red), **3.3** (blue) and **3.4** (black) obtained in PBS.

Table 3-1: Hydrodynamic diameters of different forms of nanoparticles obtained in PBS. The numbers in parentheses are the average percent volumes for multimodal size distributions. All measurements are the average of 3 independent measurements. N.A.= not available

Particle ID	Zavg (nm)	PDI	Intensity Average (nm)	Number Average (nm)	Zeta Potential (mV)
3.2	185 ± 5	.39 ± 0.01	248± 12 (85) 39 ± 5 (11) 5178± 98 (4)	29 ± 3	N.A
3.3	136 ± 44	0.47 ± .06	200 ± 44 (74) 39± 8 (25) 4964 (1)	30 ± 1.5	N.A
3.4	114 ± 5	0.44± 0.04	199 ± 22 (86) 34 ± 2 (13) 5020 (1)	24 ± 2	N.A.
3.5	108 ± 1	0.33 ± .01	142 ± 33 (92) 682 (5) 4849± 33 (3)	54 ± 4	-25.1 ± 1.1
3.6	193 ± 0.3	0.12 ± .12	221 ± 1	137 ± 3	-29.75 ± 0.5
RGD-**3.6**	222 ± 3	0.17 ± 0.03	243 ± 15	166 ± 0.3	-21.1 ± 0.4

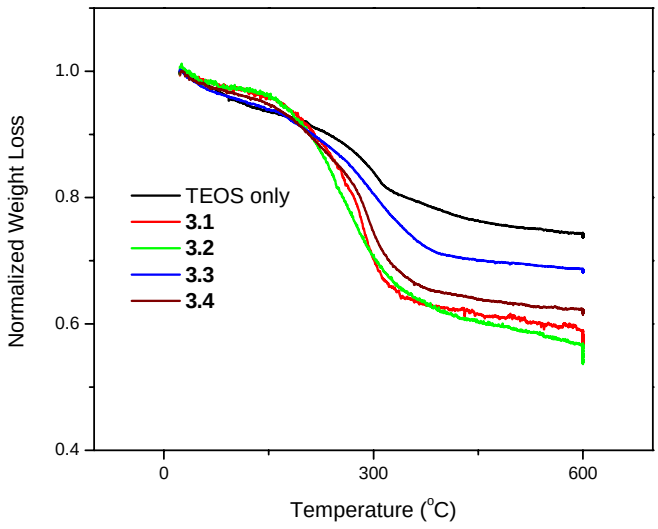

Figure 3-3: TGA weight loss curves for silica nanoparticles synthesized under the same reaction conditions TEOS only (black), **3.1** (red), **3.2** (green), **3.3** (blue) and **3.4** (maroon).

In order to increase the extent of silanol condensation, the reaction time was extended to 24 hours. The nanoparticles **3.5** and **3.6** were synthesized by the same reverse microemuslion method described above with 5 and 10 molar equivalents of TEOS, respectively. Additionally, we expected that these nanoparticles would be slightly larger than those synthesized in three hours, owing to the increased particle growth. SEM images of **3.5** and **3.6** showed well-defined spherical nanoparticles of 40-100 nm and 75-100 nm in diameter, respectively (Figure 3-4). TEM and HRTEM images of **3.5** and **3.6** confirmed the SEM size measurements and distributions. Additionally, the internal structure of **3.5** and **3.6** could be probed by TEM; both nanoparticles possessed a solid, uniform structure which confirms that the DSCP-Si is homogeneously distributed throughout the nanoparticle interior (Figures 3-5 and 3-6). Under physiological conditions, **3.5** is 108 nm in diameter (Table 3-1, Figure 3-7) due to slight aggregation of the nanoparticles, evidenced by both the intensity-weighted size distribution (in which larger nanoparticles have a much greater effect) and the PDI (0.332). **3.6** was larger, 193 nm in diameter by DLS (Table 3-1, Figure 3-7) but has a monodisperse size distribution with a polydispersity index (PDI) of 0.122. These results suggest that **3.6** forms discrete nanoparticles in solution, which exhibit some hydrogel-like behavior with the negatively-charged silanol and carboxylic acid groups within **3.6** repelling each other in aqueous solution. The higher equivalents of TEOS in **3.6** would make the nanoparticles behave more like silica nanoparticles, which tend to form discrete nanoparticles under these synthesis conditions. The zeta potentials of **3.5** and **3.6** were -25.1 and -29.75 due to the negatively charged silanol and carboxylic acids present on the nanoparticle surface. TGA analysis of **3.5** closely matched the feed conditions, with 4.7 SiO_2 molecules per platinum (Figure 3-8) and ICP-MS further confirmed the cisplatin loading of 25.4- 30.8%

cisplatin by weight (hypothetical 29.9%). **3.6** had a slight overincorporation of TEOS compared to the hypothetical with 12.5 SiO_2 units per platinum center (Figure 3-8). The cisplatin loading of **3.6** was 14-20 wt% (hypothetical 20.3%). These platinum loadings translate into approximately 62,500 (**3.5**) or 106,000 (**3.6**) cisplatins per nanoparticle, which is much higher than other nanoparticle systems for cisplatin delivery[36-40] and rivals other high platinum loading platforms. [14, 41-43]

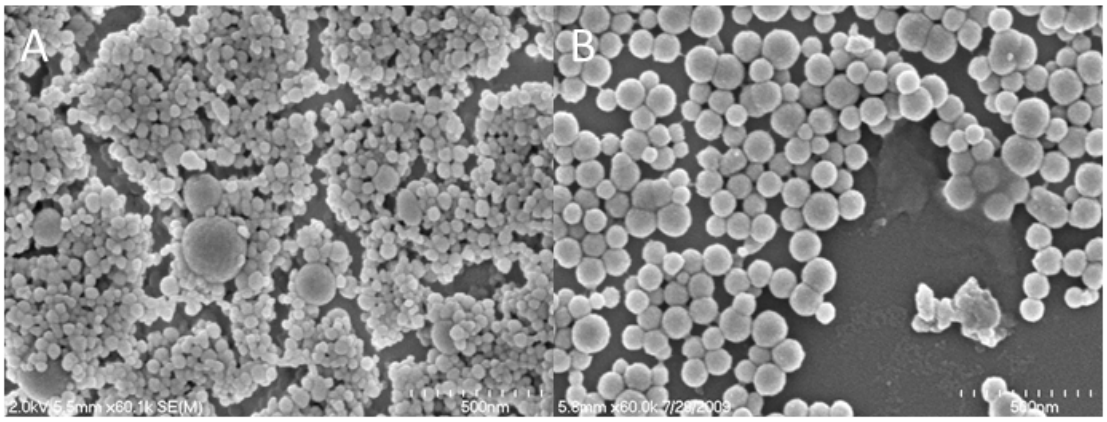

Figure 3-4: SEM micrographs of **3.5** (A) and **3.6** (B).

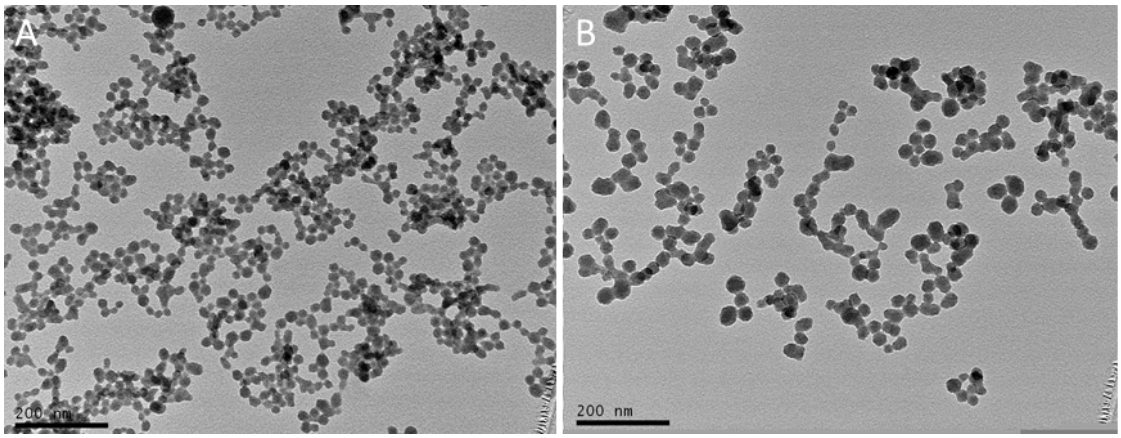

Figure 3-5: TEM micrographs of **3.5** (A) and **3.6** (B).

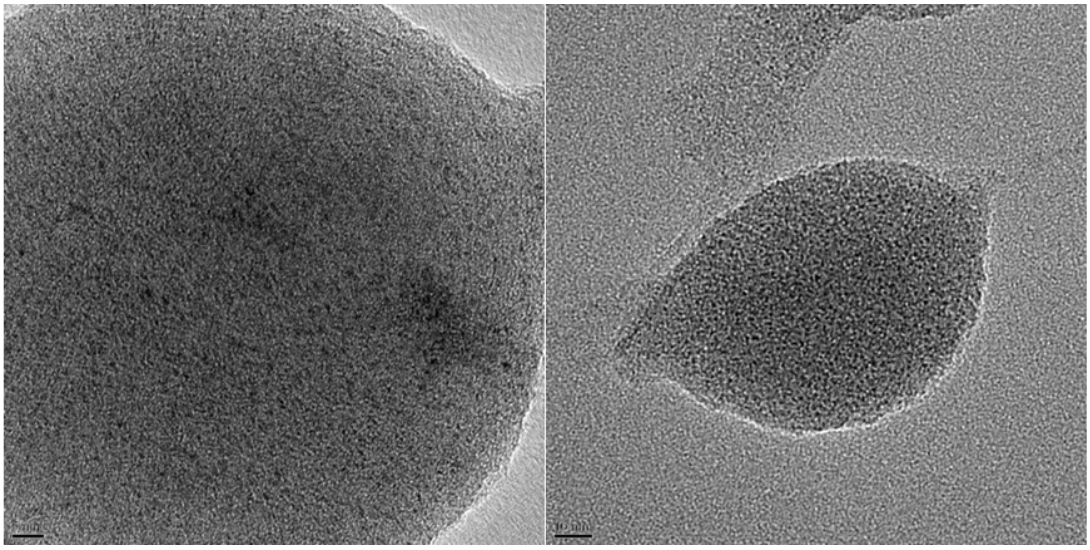

Figure 3-6: High resolution TEM images of **3.6**. Scale bar is 5 nm for the left image and 10 nm for the right image.

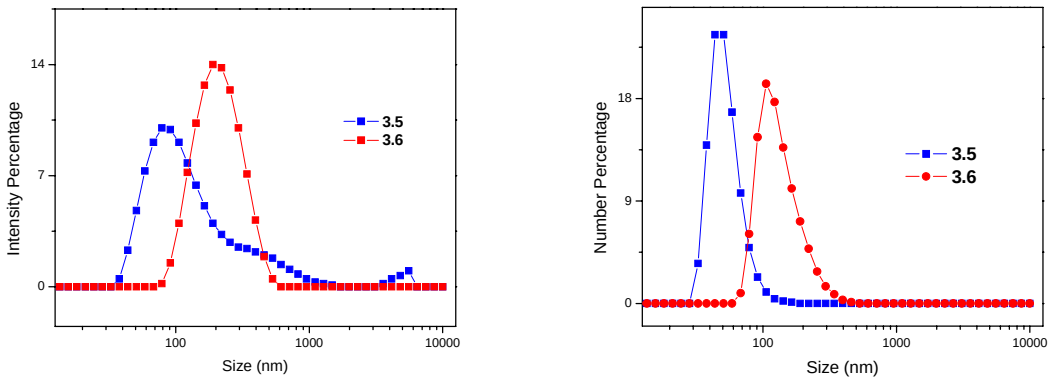

Figure 3-7: Intensity (left) and number (right) weighted DLS spectra of **3.5** (blue) and **3.6** (red) obtained in 5mM PBS.

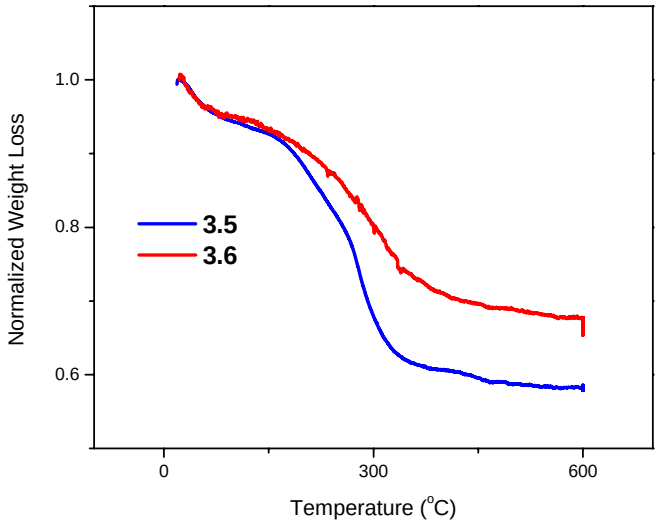

Figure 3-8: TGA weight loss curves for **3.5** (blue) and **3.6** (red)

3.2.3 cRGD Targeting of Nanoparticle 3.6

A variety of different strategies have been developed to post-synthetically modify silica nanoparticles.[16, 21, 25, 44] For covalent post-synthetic modification, silica nanoparticles can be modified through surface silanol groups with a variety of silyl-derived molecules. Alternatively, an orthogonal functional group can be placed onto the nanoparticle surface to allow for further modification. For the nanoparticles discussed in this chapter, the latter strategy is adapted since DSCP-Si, when condensed into the silica matrix, presents carboxylic acids on the nanoparticle surface.

Nanoparticle **3.6** was modified with a cancer targeted peptide, cRGDfK, by an amide coupling reaction between the surface carboxylic acids and the primary amine group on the peptide for conjugation (Scheme 3-3). The carboxylic acid groups are activated via the formation of an activated NHS ester intermediate, which then reacts with the amine group on

the peptide to form the amide bond. cRGD targets the $\alpha_v\beta_3$ integrin, which is overexpressed on a wide variety of different cancers. [45-47] There was no change in particle morphology by SEM (Figure 3-9) as a result of peptide modification. However, the nanoparticles were slightly larger by DLS, (Table 3-1, Figure 3-10) with a hydrodynamic diameter of 222 nm. The increase in hydrodynamic diameter is within the error range of the DLS (as a function of PDI), so cRGD conjugation has little, if any, effect on nanoparticle size. Peptide conjugation increased the zeta potential to -21.1 mV (Table 3-1) as a result of charge attenuation with the neutral cRGD peptide. The drug loading, measured by ICP-MS, also did not substantially change as a result of peptide conjugation.

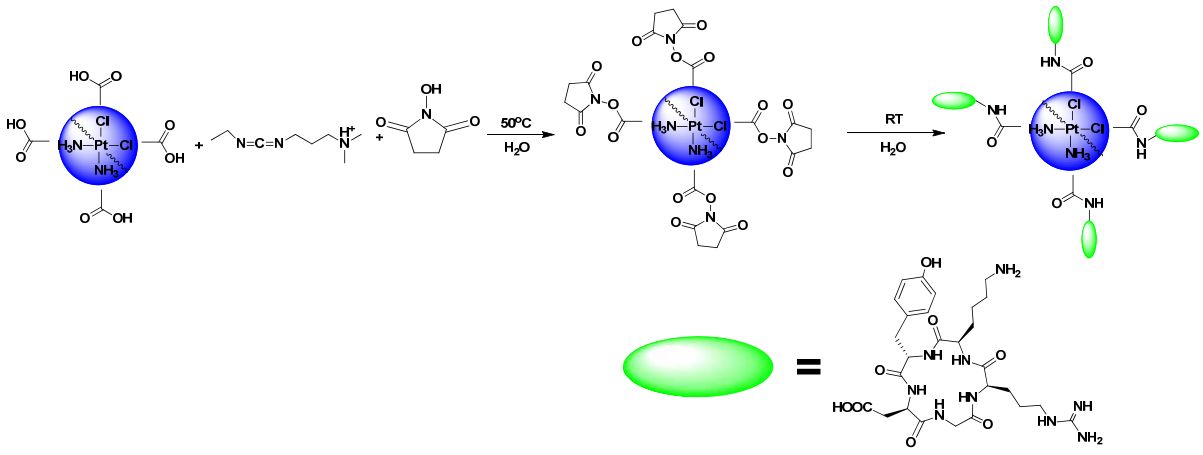

Scheme 3-3: Post-synthetic modification scheme of **3.6**. **3.6** is first activated to form an active NHS ester, which then reacts with amine groups on cRGDfK to create RGD-**3.6**

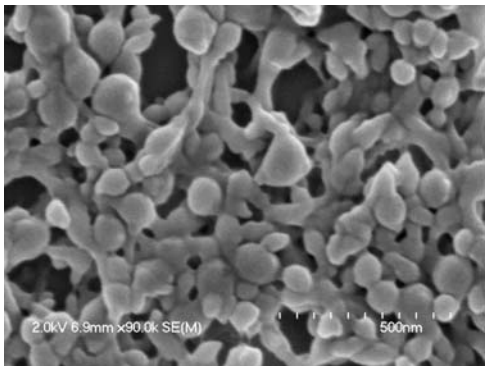

Figure 3-9: SEM image of RGD-**3.6**

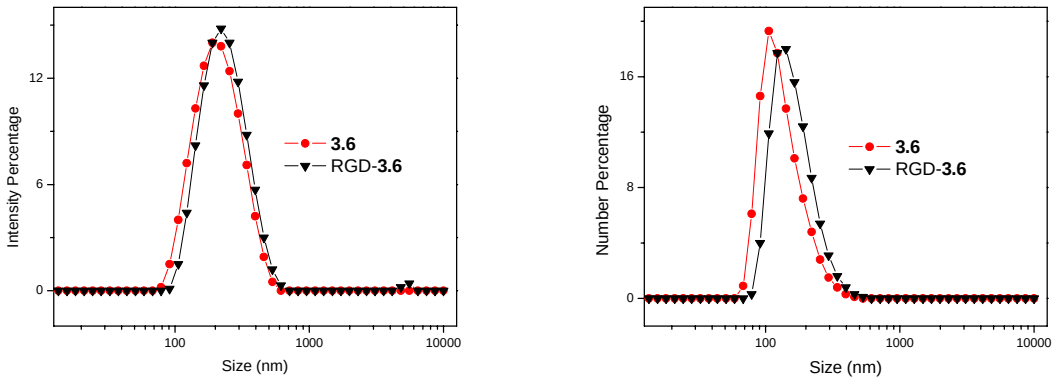

Figure 3-10: Intensity (left) and number (right) weighted DLS spectra of **3.6** (red) and RGD-**3.6** (black) obtained in 5mM PBS.

3.2.4 Platinum Release from Nanoparticle 3.6

We would expect the synthesized nanoparticles to be stable under normal physiological conditions due to the robust nature of the silica matrix. However, once the nanoparticles are internalized by cells or reach the tumor microenvironment, the platinum (IV) centers would be rapidly reduced by endogenous biomolecules, releasing cisplatin to exert its anticancer activity. As a proof of concept, we tested platinum release from **3.6** (Figure 3-11). In the absence in any reducing agent ($t<0$), there is no background platinum release from **3.6** due to the strong silsesquioxane linkages anchoring the platinum centers to the nanoparticle matrix. With the addition of 5mM glutathione, which would roughly correspond to intracellular concentrations of thiol-containing reducing agents, a rapid release of 44% of the total platinum payload was observed after 2 hours of incubation, followed by a more gradual release of remaining platinum over the next 4 days. This biphasic release has been previously observed in the development of oxaliplatin-based PSQ nanoparticles (as discussed in the previous chapter).[42] We believe that the first, initial burst release is

composed mostly of platinum centers found at or near the nanoparticle surface. The second, more sustained drug release comes from platinum centers located in the core, as glutathione would need to diffuse further into the silica matrix to reduce and release the platinum centers.

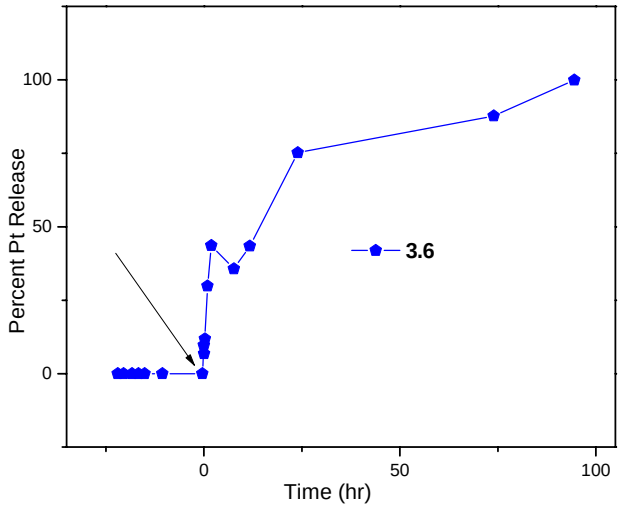

Figure 3.11: Platinum release from **3.6** can be triggered by the addition of an endogenous reducing agent (indicated by arrow) in this case 5mM glutathione.

3.2.5 *In Vitro* Cytotoxicity Assays

3.6 was evaluated *in vitro* against two human non-small cell lung cancer cell lines: A549 and NCI-H460. We chose to evaluate these nanoparticles against non-small cell lung cancer because that cisplatin is a widely used chemotherapeutic for lung cancer treatment and that lung cancer is the most common form of cancer in the US.[2] In the A549 cell line, **3.6** showed no activity across the concentration range evaluated (Figure 3-12). These results are not entirely unexpected, as **3.6** has a negative charge and would be unable to cross the cell membrane easily. If the nanoparticles are not internalized, then we would not expect to see any drug release due to the stability of **3.6** and the low concentrations of reducing agents in

cell media. Additionally, cell media does not possess a high concentration of reducing agents (typically sub-millimolar) to induce an appreciable amount of platinum release from **3.6** over the time-frame of the assay. Cisplatin was highly effective with an IC_{50} of 0.77 μM. A549 cells overexpress the $\alpha_v\beta_3$ integrin,[48-49] so RGD-**3.6** would be expected to provide an increase in efficacy over **3.6**. Indeed, RGD-**3.6** had an IC_{50} value of 1.18 μM, which is comparable to cisplatin, presumably due to the increase in nanoparticle uptake by receptor-mediated endocytosis. In the H460 cell line, **3.6** had modest efficacy with an IC_{50} of 13.85 μM, but was not nearly as effective as cisplatin, which possessed an IC_{50} of 1.86 μM (Figure 3.-3). The difference in efficacy is presumably due to the ineffective endocytosis of **3.6**. H460 cells also express the $\alpha_v\beta_3$ integrin,[50] so RGD-**3.6** (IC_{50}= 4.46 μM) was more effective than **3.6**, but it was not more effective than cisplatin. RGD targeting appears to have increased the extent of endocytosis, but not enough for equal efficacy as cisplatin.

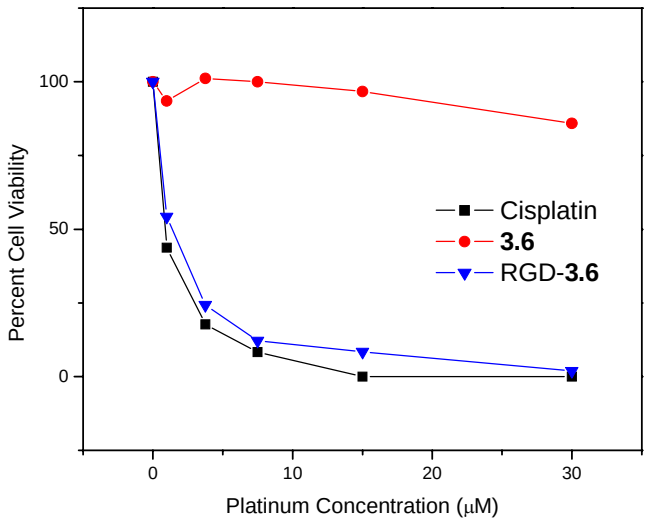

Figure 3-12: Cell viability assay of cisplatin (black), **3.6** (red), and RGD-3.6 (blue) evaluated against A549 human lung carcinoma cells.

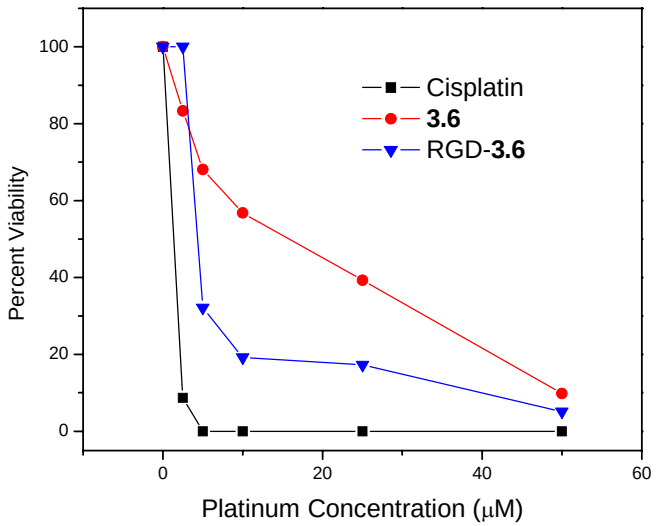

Figure 3-13: Cell viability assay of cisplatin (black), **3.6** (red), and RGD-3.6 (blue) evaluated against NCI-H460 human lung carcinoma cells.

3.3 Conclusion

In this chapter, a series of silica nanoparticles with co-condensed cisplatin prodrugs were synthesized. The nanoparticle size and drug loading could be controlled by varying the platinum to TEOS molar ratio in the synthesis or by changing the reaction time. Platinum release from these nanoparticles could be triggered by exposure to intracellular concentrations of biologically-relevant reducing agents such as glutathione. Nanoparticles with 10 molar equivalents of TEOS were targeted to cancer cells by conjugating a cyclic-RGD peptide onto the nanoparticle surface. These nanoparticles were evaluated *in vitro* against two human non-small cell lung cancer cell lines. The unfunctionalized nanoparticles possessed little activity against these cell lines as their negative charge would hinder endocytosis and cell media does not have enough reducing agents present to induce a significant extent of drug release. RGD targeting these nanoparticles could increase their

efficacy to that of cisplatin. Due to the development of a more promising cisplatin-PSQ nanoparticle (discussed in the next chapter) and the lack of an efficiently pegylated nanoparticle, the development of these co-condensed silica nanoparticles was halted after the initial *in vitro* studies. Further work would be needed to create an effectively pegylated species for *in vivo* evaluation.

3.4 Materials and Methods

3.4.1 General Materials and Methods

All chemicals were purchased from Fisher or Aldrich and used without purification unless noted. Cisplatin was purchased from AK Scientific. Tetrahydrofuran was dried by the sodium metal/benzophenone method. Dimethylformamide was dried by passing through an activated alumina column. Thermogravimetric analysis was performed using a Shimadzu TGA-50 equipped with a platinum pan and heated at 3°C per minute in air. A Hitachi 4700 field emission scanning electron microscope and a JEM 100CX-2 transmission electron microscope (TEM) were used to determine particle size and morphology. SEM and TEM samples were prepared from ethanolic suspensions of the nanoparticles dropped onto glass slides or amorphous carbon-coated copper grids. The solvent was then allowed to evaporate. A Cressington 108 Auto Sputter Coater equipped with an Au/Pd (80/20) target and a MTM-10 thickness monitor was used to coat SEM samples with a 4 nm thick conductive layer prior to obtaining SEM images. Dynamic light scattering (DLS) and zeta potential measurements were made using a Malvern Instruments Zetasizer Nano. Inductively-Coupled Plasma Mass Spectrometry (ICP-MS) measurements were made using a Varian 820-MS Inductively-Coupled Plasma Mass Spectrometer. ICP-MS samples were prepared by digesting a known

amount of sample in concentrated nitric acid overnight and then diluting with water to 2% nitric acid by volume.

3.4.2 Synthesis of Platinum Complexes

Synthesis of c,c,t-Pt(NH$_3$)$_2$Cl$_2$(OH)$_2$

The platinum complex *c,c,t*-Pt(NH$_3$)$_2$Cl$_2$(OH)$_2$ was synthesized by a previously reported method with minor changes.[14] A suspension of cisplatin (*cis*-Pt(NH$_3$)$_2$Cl$_2$) (2.50 g, 8.3 mmol) and 30 wt% hydrogen peroxide (H_2O_2) (14 mL, 125 mmol) in water (113 mL) was heated to 70°C for 5 hours in the dark. The heat was removed and stirring was continued overnight at room temperature. The resulting yellow suspension was concentrated under rotary evaporation to 10 mL and the product was allowed to precipitate at 4°C for several hours. The product was collected via filtration, washed with water, ethanol, and diethyl ether, and vacuum dried. The product was obtained as a bright yellow powder. Yield: 2.07 g (75% yield).

Synthesis of c,c,t-Pt(NH$_3$)$_2$Cl$_2$(triethoxysilylpropyl succinic acid)$_2$ (DSCPSi)

Two hundred milligrams of *c,c,t*-Pt(NH$_3$)$_2$Cl$_2$(OH)$_2$ (0.6 mmol) was suspended in 4 mL of anhydrous DMF. To this, 700 μL of triethoxysilylpropyl succinic anhydride was added (1.8 mmol). The resulting suspension was stirred under argon at 50°C for 3 days, yielding a clear yellow solution. Two volume equivalents of triethylamine was added to precipitate the product. The product was isolated by centrifugation and washed twice with diethyl ether before drying under high vacuum, yielding a yellow brown crystalline material. The product was stored at -20°C. Yield 440 mg (78%). ^{1}H NMR (DMSO-d^6): 6.25(6H, NH$_3$), 3.73 (12H,

OCH_2), 2.75 (4H, CH_2), 2.31 (2H, CH), 1.45 (4H, CH_2); 1.32 (4H, CH_2), 1.12 (18H, CH_3); 0.52 (4H, CH_2)

3.4. 3 Nanoparticle Synthesis

All nanoparticles were synthesized within a reverse microemulsion. An organic stock solution of 0.3 M Triton X-100 and 1.5 M 1-hexanol in cyclohexanes was created by mixing Triton X100 (93.75g, 0.15mol) and 1-hexanol (76.5 g, 0.75 mol) into a 500 mL volumetric flask. The flask was filled to the mark with cyclohexanes.

*Synthesis of **3-1**, **3-2**, **3-3**, and **3-4***

A solution of 0.3 M Triton X100 and 1.5 M 1-hexanol in cyclohexanes (35 mL) was placed into a 100 mL round bottom flask. DSCP-Si (22mg, 23μmol) was dissolved into 770 μL of water. The aqueous portion was added to the organic and X equivalents (X=5, 10,15,20) of TEOS were added. The resulting microemulsion was stirred for 10 minutes until optically transparent and 600 μL of aqueous ammonia was added (w=7.5). The microemulsion was stirred at room temperature in the dark for 3 hours and then an equal volume of ethanol was added to quench the reaction. The particles were isolated by centrifugation (13,000 rpm for 15 minutes) and washed with ethanol three times. The resulting nanoparticles were characterized by SEM, DLS and TGA.

*Synthesis of **3-5** and **3-6***

3-5 and **3-6** were synthesized by a slight modification of the procedure above. A solution of 0.3 M Triton X-100, 1.5 M 1-hexanol in cyclohexanes (35mL) was placed in a round bottom flask. DSCP-Si (22mg, 23 μmol) was dissolved into 770 μL of water. The aqueous solution

was added to the organic and either 5 or 10 equivalents of TEOS was then added. The microemulsion was stirred for 10 minutes and 600 μL of aqueous ammonium hydroxide was added. The microemulsion was then stirred for 24 hours at room temperature in the dark. An equal volume of ethanol was added to quench the reaction and the particles were isolated by centrifugation (13,000 rpm x 15 minutes) and washed with ethanol three times. The nanoparticles were stored in ethanol.

3.4.4 Nanoparticle Surface Modification

*Synthesis of cRGDfK targeted **3.6***

As-synthesized nanoparticles (10 mg) were resuspended into 4 mL of a freshly made 0.025 M NHS/EDC solution in water. The nanoparticle suspension was heated at 50°C for 2 hours to activate the acid as an NHS ester before the suspension was cooled to room temperature. cRGDfK (Peptides International, 0.6 mg, 0.96 μmol) was added and the suspension was stirred overnight. Nanoparticles were isolated by centrifugation and washed with water once and ethanol once. The particles were stored in ethanol.

3.4.5 Platinum Release from 3.6

Two milligrams of **3-6** was isolated by centrifugation and redispersed into 1mL 2mM HEPES buffer. The suspension was loaded into a 3500 MW weight cutoff dialysis bag and the bag was added to 479 mL of the same buffer. The solution was sparged with argon for 10 minutes and heated to 37°C. The solution was incubated under an Ar blanket for 24 hours, with aliquots of the dialysate periodically removed. After 24 hours, an oxygen free solution of glutathione was added to make a total glutathione concentraton of 5 mM. The solution was

incubated at 37°C with aliquots periodically removed. Platinum concentration within the dialysis aliquots was determined by ICP-MS.

3.4.6 *In Vitro Assays*

General: NCI-H460 human large cell lung carcinoma (ATCC# HTB-177), A549 human lung carcinoma cells (ATCC# CCL-185), and PC-3 human prostate adenocarcinoma cells (ATCC# CRL-1435) were all purchased from the Tissue Culture Facility of the Lineberger Comprehensive Cancer Center. All cell culture reagents were purchased from the Tissue Culture Facility in the Lineberger Comprehensive Cancer Center at UNC-Chapel Hill. All cells were maintained at 37°C with 5% CO_2 and were cultured according to ATCC recommendations.

Cell Viability Assay: A549 Cells

Confluent A549 cells were plated in 6 well plates at a density of 100,000 cells/well (3mL media). The plates were incubated overnight to promote cell attachment. After incubation, the plates were removed from the incubator and the media was removed once. Each well was washed once with PBS and refilled with 3 mL media with various concentrations of platinum. The plates were incubated for 72 hours and cell viability was determined by trypan blue dye exclusion.

Cell Viability Assay: H460 cells

Confluent H460 cells were plated in 6 well plates at a density of 50,000 cells/well (3mL media). The plates were incubated overnight to promote cell attachment. After incubation, the plates were removed from the incubator and the media was removed. Each well was

washed once with PBS and refilled with 3mL media with various concentrations of platinum. The plates were incubated for 72 hours, with the media removed and replaced on the second day. Cell viability was determined by trypan blue dye exclusion.

3.5 References

1. Rosenberg, B.; Van Camp, L.; Krigas, T., Inhibition of Cell Division in *Escherichia coli* by Electrolysis Products from a Platinum Electrode. *Nature* **1965,** *205* (4972), 698-699.

2. Alex, C., Chemotherapy, chemoresistance and the changing treatment landscape for NSCLC. *Lung Cancer* **2011,** *71* (1), 3-10.

3. Homma, A.; Inamura, N.; Oridate, N.; Suzuki, S.; Hatakeyama, H.; Mizumachi, T.; Kano, S.; Sakashita, T.; Onimaru, R.; Yasuda, K.; Shirato, H.; Fukuda, S., Concomitant Weekly Cisplatin and Radiotherapy for Head and Neck Cancer. *Jpn. J. Clin. Oncol.* **2011,** *41* (8), 980-986.

4. Kawai, K.; Akaza, H., Current status of chemotherapy in risk-adapted management for metastatic testicular germ cell cancer. *Cancer Sci.* **2010,** *101* (1), 22-28.

5. Kunos, C. A.; Waggoner, S.; von Gruenigen, V.; Eldermire, E.; Pink, J.; Dowlati, A.; Kinsella, T. J., Phase I Trial of Pelvic Radiation, Weekly Cisplatin, and 3-Aminopyridine-2-Carboxaldehyde Thiosemicarbazone (3-AP, NSC #663249) for Locally Advanced Cervical Cancer. *Clin. Cancer Res.* **2010,** *16* (4), 1298-1306.

6. Ott, I.; Gust, R., Preclinical and clinical studies on the use of platinum complexes for breast cancer treatment. *Anticancer Agents Med. Chem.* **2007,** *7* (1), 95-110.

7. Jung, Y.; Lippard, S. J., Direct Cellular Responses to Platinum-Induced DNA Damage. *Chem. Rev. (Washington, DC, U.S.)* **2007,** *107* (5), 1387-1407.

8. Wang, D.; Lippard, S. J., Cellular processing of platinum anticancer drugs. *Nat. Rev. Drug Discovery* **2005,** *4* (4), 307-320.

9. Kelland, L., The resurgence of platinum-based cancer chemotherapy. *Nat Rev Cancer* **2007,** *7* (8), 573-584.

10. Della Rocca, J.; Liu, D.; Lin, W., Are high drug loading nanoparticles the next step forward for chemotherapy? *Nanomedicine (London, U.K.)* **2012,** *Accepted*.

11. Alexis, F.; Pridgen, E.; Molnar, L. K.; Farokhzad, O. C., Factors Affecting the Clearance and Biodistribution of Polymeric Nanoparticles. *Mol. Pharmaceutics* **2008,** *5* (4), 505-515.

12. Li, S.-D.; Huang, L., Pharmacokinetics and Biodistribution of Nanoparticles. *Mol. Pharmaceutics* **2008,** *5* (4), 496-504.

13. Peer, D.; Karp, J. M.; Hong, S.; Farokhzad, O. C.; Margalit, R.; Langer, R., Nanocarriers as an emerging platform for cancer therapy. *Nat. Nanotechnol.* **2007,** *2* (12), 751-760.

14. Rieter, W. J.; Pott, K. M.; Taylor, K. M. L.; Lin, W., Nanoscale Coordination Polymers for Platinum-Based Anticancer Drug Delivery. *J. Am. Chem. Soc.* **2008,** *130* (35), 11584-11585.

15. Taylor-Pashow, K. M. L.; Della Rocca, J.; Xie, Z.; Tran, S.; Lin, W., Postsynthetic Modifications of Iron-Carboxylate Nanoscale Metal−Organic Frameworks for Imaging and Drug Delivery. *J. Am. Chem. Soc.* **2009,** *131* (40), 14261-14263.

16. Taylor-Pashow, K. M. L.; Della Rocca, J.; Huxford, R. C.; Lin, W., Hybrid nanomaterials for biomedical applications. *Chem. Commun. (Cambridge, U.K.)* **2010,** *46* (32), 5832-5849.

17. Lee, J. E.; Lee, N.; Kim, H.; Kim, J.; Choi, S. H.; Kim, J. H.; Kim, T.; Song, I. C.; Park, S. P.; Moon, W. K.; Hyeon, T., Uniform Mesoporous Dye-Doped Silica Nanoparticles Decorated with Multiple Magnetite Nanocrystals for Simultaneous Enhanced Magnetic Resonance Imaging, Fluorescence Imaging, and Drug Delivery. *J. Am. Chem. Soc.* **2009,** *132* (2), 552-557.

18. Kim, T.; Momin, E.; Choi, J.; Yuan, K.; Zaidi, H.; Kim, J.; Park, M.; Lee, N.; McMahon, M. T.; Quinones-Hinojosa, A.; Bulte, J. W. M.; Hyeon, T.; Gilad, A. A., Mesoporous Silica-Coated Hollow Manganese Oxide Nanoparticles as Positive T1 Contrast Agents for Labeling and MRI Tracking of Adipose-Derived Mesenchymal Stem Cells. *J. Am. Chem. Soc.* **2011,** *133* (9), 2955-2961.

19. Liu, R.; Zhang, Y.; Zhao, X.; Agarwal, A.; Mueller, L. J.; Feng, P., pH-Responsive Nanogated Ensemble Based on Gold-Capped Mesoporous Silica through an Acid-Labile Acetal Linker. *J. Am. Chem. Soc.* **2010,** *132* (5), 1500-1501.

20. Sajja, H. K.; East, M. P.; Mao, H.; Wang, Y. A.; Nie, S.; Yang, L., Development of Multifunctional Nanoparticles for Targeted Drug Delivery and Noninvasive Imaging of Therapeutic Effect. *Curr. Drug Discovery Technol.* **2009,** *6* (1), 43-51.

21. Yan, J. L.; Estevez, M. C.; Smith, J. E.; Wang, K. M.; He, X. X.; Wang, L.; Tan, W. H., Dye-doped nanoparticles for bioanalysis. *Nano Today* **2007,** *2* (3), 44-50.

22. Ashley, C. E.; Carnes, E. C.; Phillips, G. K.; Padilla, D.; Durfee, P. N.; Brown, P. A.; Hanna, T. N.; Liu, J.; Phillips, B.; Carter, M. B.; Carroll, N. J.; Jiang, X.; Dunphy, D. R.; Willman, C. L.; Petsev, D. N.; Evans, D. G.; Parikh, A. N.; Chackerian, B.; Wharton, W.; Peabody, D. S.; Brinker, C. J., The targeted delivery of multicomponent cargos to cancer cells by nanoporous particle-supported lipid bilayers. *Nat Mater* **2011,** *10* (5), 389-397.

23. Bagwe, R. P.; Yang, C.; Hilliard, L. R.; Tan, W., Optimization of Dye-Doped Silica Nanoparticles Prepared Using a Reverse Microemulsion Method. *Langmuir* **2004,** *20* (19), 8336-8342.

24. Botella, P.; Abasolo, I.; Fernández, Y.; Muniesa, C.; Miranda, S.; Quesada, M.; Ruiz, J.; Schwartz Jr, S.; Corma, A., Surface-modified silica nanoparticles for tumor-targeted delivery of camptothecin and its biological evaluation. *J. Controlled Release* **2011,** *156* (2), 246-257.

25. Liu, J.; Stace-Naughton, A.; Jiang, X.; Brinker, C. J., Porous Nanoparticle Supported Lipid Bilayers (Protocells) as Delivery Vehicles. *J. Am. Chem. Soc.* **2009,** *131* (4), 1354-1355.

26. Kim, J. S.; An, H.; Rieter, W. J.; Esserman, D.; Taylor-Pashow, K. M. L.; Sartor, R. B.; Lin, W.; Tarrant, T. K., Multimodal optical and Gd-based nanoparticles for imaging in inflammatory arthritis. *Clin. Exp. Rheumatol.* **2009,** *27* (4), 580-586.

27. Kim, J. S.; Rieter, W. J.; Taylor, K. M. L.; An, H.; Lin, W. L.; Lin, W. B., Self-assembled hybrid nanoparticles for cancer-specific multimodal imaging. *J. Am. Chem. Soc.* **2007,** *129* (29), 8962-8963.

28. Rieter, W. J.; Kim, J. S.; Taylor, K. M. L.; An, H. Y.; Lin, W. L.; Tarrant, T.; Lin, W. B., Hybrid silica nanoparticles for multimodal Imaging. *Angew. Chem., Int. Ed.* **2007,** *46* (20), 3680-3682.

29. Taylor, K. M. L.; Kim, J. S.; Rieter, W. J.; An, H.; Lin, W. L.; Lin, W. B., Mesoporous silica nanospheres as highly efficient MRI contrast agents. *J. Am. Chem. Soc.* **2008,** *130* (7), 2154-2155.

30. Vivero-Escoto, J. L.; Taylor-Pashow, K. M. L.; Huxford, R. C.; Della Rocca, J.; Okoruwa, C.; An, H.; Lin, W.; Lin, W., Multifunctional Mesoporous Silica Nanospheres with Cleavable Gd(III) Chelates as MRI Contrast Agents: Synthesis, Characterization, Target-Specificity, and Renal Clearance. *Small* **2011,** *7* (24), 3519-3528.

31. Benezra, M.; Penate-Medina, O.; Zanzonico, P. B.; Schaer, D.; Ow, H.; Burns, A.; DeStanchina, E.; Longo, V.; Herz, E.; Iyer, S.; Wolchok, J.; Larson, S. M.; Wiesner, U.; Bradbury, M. S., Multimodal silica nanoparticles are effective cancer-targeted probes in a model of human melanoma. *J. Clin. Invest.* **2011,** *121* (7), 2768-2780.

32. Barnes, K. R.; Kutikov, A.; Lippard, S. J., Synthesis, Characterization, and Cytotoxicity of a Series of Estrogen-Tethered Platinum(IV) Complexes. *Chem. Biol.* **2004,** *11* (4), 557-564.

33. Giandomenico, C. M.; Abrams, M. J.; Murrer, B. A.; Vollano, J. F.; Rheinheimer, M. I.; Wyer, S. B.; Bossard, G. E.; Higgins, J. D., Carboxylation of Kinetically Inert Platinum(IV) Hydroxy Complexes. An Entry into Orally Active Platinum(IV) Antitumor Agents. *Inorg. Chem.* **1995,** *34* (5), 1015-1021.

34. Arriagada, F. J.; Osseo-Asare, K., Phase and dispersion stability effects in the synthesis of silica nanoparticles in a non-ionic reverse microemulsion. *Colloid Surf.* **1992,** *69* (2–3), 105-115.

35. Arriagada, F. J.; Osseo-Asare, K., Synthesis of Nanosize Silica in a Nonionic Water-in-Oil Microemulsion: Effects of the Water/Surfactant Molar Ratio and Ammonia Concentration. *J. Colloid Interface Sci.* **1999,** *211* (2), 210-220.

36. Feazell, R. P.; Nakayama-Ratchford, N.; Dai, H.; Lippard, S. J., Soluble single-walled carbon nanotubes as longboat delivery systems for Platinum(IV) anticancer drug design. *J. Am. Chem. Soc.* **2007,** *129* (27), 8438-8439.

37. Kim, J.-H.; Kim, Y.-S.; Park, K.; Lee, S.; Nam, H. Y.; Min, K. H.; Gon Jo, H.; Park, J. H.; Choi, K.; Jeong, S. Y.; Park, R. W.; Kim, I.-S.; Kim, K.; Kwon, I. C., Antitumor efficacy of cisplatin-loaded glycol chitosan nanoparticles in tumor bearing mice. *J. Controlled Release* **2008,** *127* (1), 41-49.

38. Min, Y.; Mao, C.; Xu, D.; Wang, J.; Liu, Y., Gold nanorods for platinum based prodrug delivery. *Chem. Commun. (Cambridge, U.K.)* **2010,** *46* (44), 8424-8426.

39. Paraskar, A. S.; Soni, S.; Chin, K. T.; Chaudhuri, P.; Muto, K. W.; Berkowitz, J.; Handlogten, M. W.; Alves, N. J.; Bilgicer, B.; Dinulescu, D. M.; Mashelkar, R. A.; Sengupta, S., Harnessing structure-activity relationship to engineer a cisplatin nanoparticle for enhanced antitumor efficacy. *Proc. Natl. Acad. Sci. U.S.A.* **2010,** *107* (28), 12435-12440.

40. Aryal, S.; Hu, C.-M. J.; Zhang, L., Polymer−Cisplatin Conjugate Nanoparticles for Acid-Responsive Drug Delivery. *ACS Nano* **2009,** *4* (1), 251-258.

41. Nishiyama, N.; Okazaki, S.; Cabral, H.; Miyamoto, M.; Kato, Y.; Sugiyama, Y.; Nishio, K.; Matsumura, Y.; Kataoka, K., Novel cisplatin incorporated polymeric micelles can eradicate solid tumors in mice. *Cancer Res.* **2003,** *63* (12), 8977-8983.

42. Della Rocca, J.; Huxford, R. C.; Comstock-Duggan, E.; Lin, W., Polysilsesquioxane nanoparticles for targeted platin-based cancer chemotherapy by triggered release. *Angew. Chem., Int. Ed.* **2011,** *50* (44), 10330-10334.

43. Burger, K. N. J.; Staffhorst, W. H. M.; de Viglder, H. C.; Velinova, M. J.; Bomans, P. H.; Frederik, P. M.; de Kruijff, B., Nanocapsules: Lipid-coated aggregates of cisplatin with high cytotoxicity. *Nat. Med.* **2002,** *8* (1), 81-84.

44. van Schooneveld, M. M.; Vucic, E.; Koole, R.; Zhou, Y.; Stocks, J.; Cormode, D. P.; Tang, C. Y.; Gordon, R. E.; Nicolay, K.; Meijerink, A.; Fayad, Z. A.; Mulder, W. J. M., Improved Biocompatibility and Pharmacokinetics of Silica Nanoparticles by Means of a Lipid Coating: A Multimodality Investigation. *Nano Lett.* **2008,** *8* (8), 2517-2525.

45. Schottelius, M.; Laufer, B.; Kessler, H.; Wester, H.-J. r., Ligands for Mapping αvβ3-Integrin Expression in Vivo. *Acc. Chem. Res.* **2009,** *42* (7), 969-980.

46. Temming, K.; Schiffelers, R. M.; Molema, G.; Kok, R. J., RGD-based strategies for selective delivery of therapeutics and imaging agents to the tumour vasculature. *Drug Resist. Updates* **2005,** *8* (6), 381-402.

47. Chen, K.; Chen, X. Y., Integrin Targeted Delivery of Chemotherapeutics. *Theranostics* **2011,** *1*, 189-200.

48. Jiang, T.; Zhang, C. F.; Zheng, X.; Xu, X. F.; Xie, X.; Liu, H. C.; Liu, S. Y., Noninvasively characterizing the different alpha v beta 3 expression patterns in lung cancers with RgD-USPIO using a clinical 3.0T MR scanner. *International Journal of Nanomedicine* **2009,** *4*, 241-249.

49. Zhou, Y.; Kim, Y. S.; Chakraborty, S.; Shi, J. Y.; Gao, H. J.; Liu, S., (99m)Tc-Labeled Cyclic RGD Peptides for Noninvasive Monitoring of Tumor Integrin alpha(v)beta(3) Expression. *Mol. Imaging* **2011,** *10* (5), 386-397.

50. Albert, J. M.; Cao, C.; Geng, L.; Leavitt, L.; Hallahan, D. E.; Lu, B., Integrin αvβ3 Antagonist Cilengitide Enhances Efficacy of Radiotherapy in Endothelial Cell and Non-Small-Cell Lung Cancer Models. *Int. J. Radiation Oncology Biol. Phys.* **2006,** *65* (5), 1536-1543.

Chapter 4:

Cisplatin-containing Polysilsesquioxane Nanoparticles for Chemotherapy and Chemoradiotherapy of Lung Cancer

4.1 Introduction

Our laboratory has recently developed a new nanoparticle platform, known as polysilsesquioxane (PSQ), for anticancer drug delivery.[1] PSQ is a type of hybrid material composed of siloxane networks with organic or metal organic bridging ligands. These materials are synthesized from bis(trialkoxysilanes) ($(R'O)_3Si\text{-}R\text{-}Si(OR')_3$) by sol-gel synthesis.[2-3] Our laboratory incorporated a derivative of the anticancer drug oxaliplatin into PSQ nanoparticles at very high loadings (up to 47 wt%). Preliminary *in vivo* evaluations demonstrated that oxaliplatin-PSQ nanoparticles possessed improved efficacy over oxaliplatin in a pancreatic cancer xenograft model.

We wished to extend the PSQ platform to deliver the platinum anticancer drug cisplatin, as cisplatin receives more general use than oxaliplatin. Cisplatin is used for the treatment of a variety of cancers, including testicular, lung, breast, and ovarian cancers.[4-5] In addition, it is used for the chemoradiotherapy treatment of head and neck, esophageal, lung, cervical, and anal cancers.[6-9] However, cisplatin treatment has limitations, most notably its high general toxicity and resistance against some cancers.[10-11] This chapter reports the extension of the PSQ nanocarrier for the delivery of cisplatin to cancer cells. We have carried

out the detailed physiochemical characterization and demonstrated triggered drug release, *in vitro* cytotoxicity, and *in vivo* efficacy of cisplatin-containing PSQ nanoparticles.

4.2 Results and Discussion

4.2.1 Platinum Complex Synthesis

The platinum complex DSCP-Si (DSCP-Si= *c,c,t*-Pt$(NH_3)_2Cl_2$(triethoxysilylpropyl succinate)$_2$) was synthesized as described in the previous chapter, starting from commercially available cisplatin (Scheme 3-1). DSCP-Si has two triethoxysilyl groups to allow for polymerization into PSQ nanoparticles and two carboxylic acid groups to allow for further nanoparticle surface modification.

4.2.2 Synthesis of Nanoparticle 4.1

PSQ particle **4.1** was synthesized via a base catalyzed sol-gel polymerization in a mixture of ethanol, water, and ammonia and then purified by ion-exchange chromatography, dialysis, and centrifugation (Scheme 4-1). The nanoparticle synthesis is similar to the classical Stöber synthesis of silica nanoparticles.[12-13] The isolated nanoparticles were characterized by transmission electron microscopy (TEM), scanning electron microscopy (SEM), dynamic light scattering (DLS), thermogravimetric analysis (TGA), and inductively coupled - plasma mass spectrometry (ICP-MS). **4.1** is 64 nm in diameter by TEM (Figure 4-1), with SEM showing a similar diameter (Figure 4-2). Under physiological conditions, **4.1** shows hydrogel-like behavior and swells to a diameter of 134.2 nm (Figure 4-3, Table 4-1) by DLS. **4.1** possesses a highly negative zeta potential (Table 4-1) due to deprotonation of surface silanol and carboxylic acid groups. TGA of **4.1** (Figure 4-4) gave the expected weight loss for the completely condensed nanoparticle, indicating that **4.1** was a

homopolymer of completely polymerized DSCP-Si. TGA measurements suggested a cisplatin loading of 42 wt%, which was confirmed by ICP-MS measurements of the platinum content. This impressive cisplatin loading corresponds to approximately $1.15x10^5$ cisplatin molecules/ nanoparticle. The cisplatin loading is higher, by up to 4 orders of magnitude, than other cisplatin nanoparticle drug delivery platforms. [14-21] For example, Lippard and coworkers reported two carbon nanotube-based systems, containing between 65-82 Pt centers, to deliver Pt(IV) prodrugs similar to DSCP-Si.[16, 20] The cisplatin loading of **4.1** is slightly less than that of the PSQ nanoparticles for oxaliplatin delivery on a per weight basis because of the higher molecular weight of the oxaliplatin prodrug, but has a similar agent loading on a per number basis.[1]

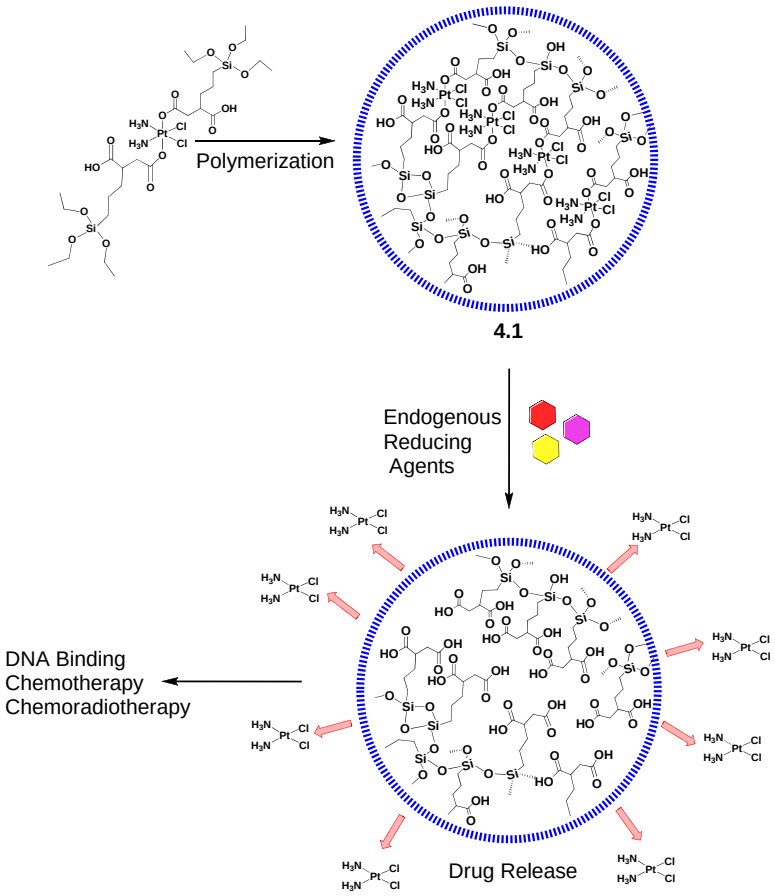

Scheme 4-1: Schematic of the synthesis of **4.1**. Drug release can be triggered by endogenous reducing agents with the released drug leading to various anticancer effects.

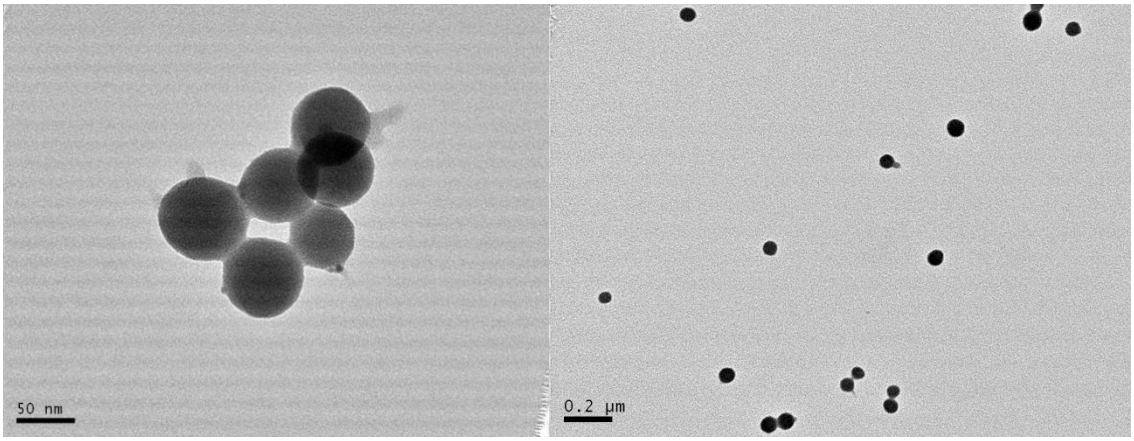

Figure 4-1: TEM micrographs of **4.1**.

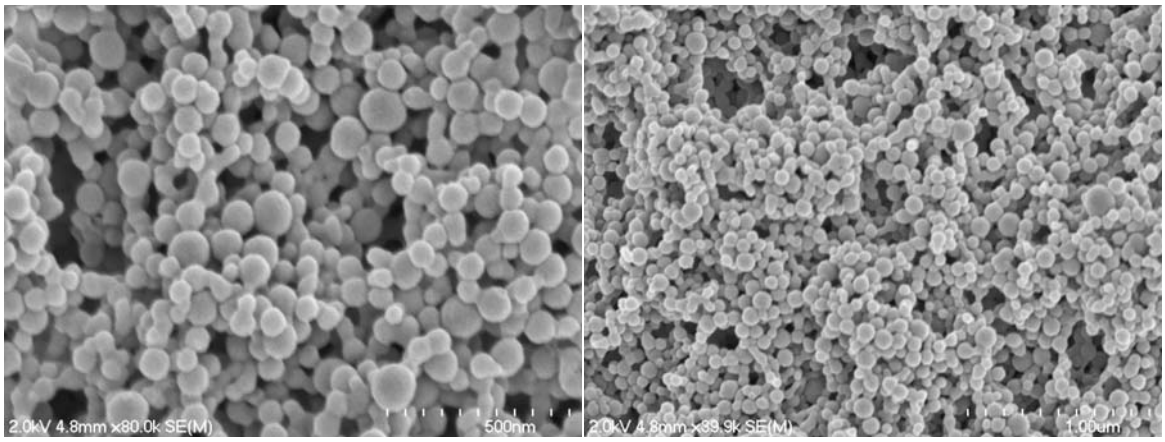

Figure 4-2: SEM micrographs of **4.1**.

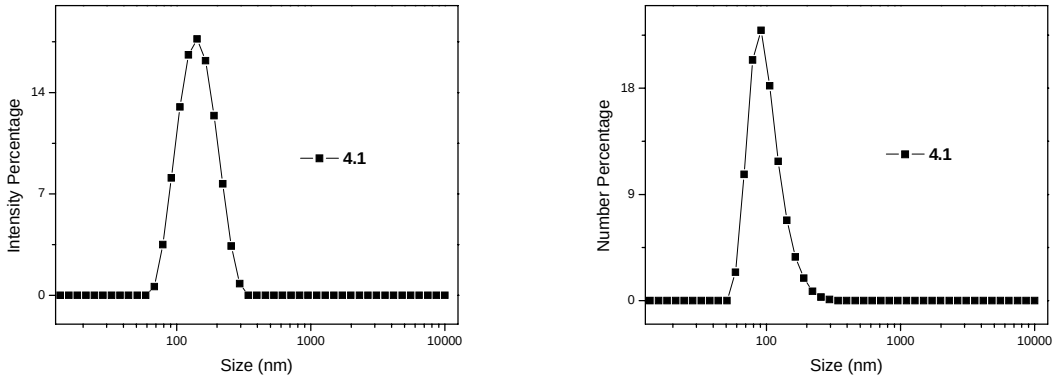

Figure 4-3: Intensity (left) and number (right) weighted DLS spectra for **4.1** obtained in 5 mM PBS.

Table 4-1: Hydrodynamic diameters and zeta potentials of various forms of **4.1**. All DLS measurements were obtained in 5 mM PBS and are the average of 3 measurements.

Particle ID	Z Average (nm)	PDI	Intensity Average (nm)	Number Average (nm)	Zeta Potential (mV)
4.1	135.2 ± 0.5	0.07 ± .01	147.9 ± 0.8	101.5 ± 1.2	-41.9 + 2.4
RGD-**4.1**	129.1± 0.4	0.10 ± 0.01	142.7 ± 1.5	95.2 ± 1.8	-17.7 ± 0.6
PEG2k-**4.1**	195.9 ± 2	0.13 ± 0.02	217.7 + 2.3	147.9 ± 3.1	-2.9 ± 1.5
APEG2k-**4.1**	201.3 ± 1.1	.09 + ± 0.01	221.2 + 1.6	165.4 ± 2.2	-3.9 +2.3
PEG5k-**4.1**	150.3 ± 5	0.09 ± 0.01	165.9 ± 5.8	114.0 ± 5.3	-6.5 ± 0.4

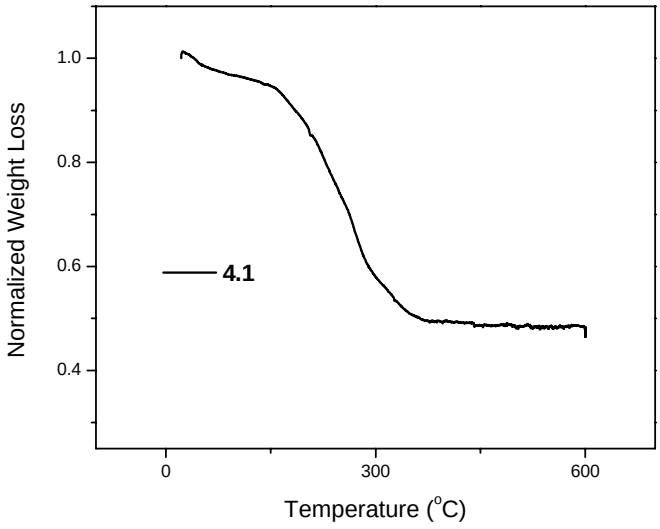

Figure 4-4: TGA weight loss curve for **4.1.**

4.2.3 Cisplatin Release from Nanoparticle 4.1

Nanoparticle **4.1** was designed to show minimal drug release under normal physiological conditions, but to rapidly release cisplatin within the tumor microenvironment or upon cellular internalization (Scheme 4-1). Platinum release from **4.1** was measured by ICP-MS (Figure 4-5) in the presence of *L*-cysteine, a surrogate cellular reducing agent. In the absence of any reducing agent, **4.1** shows a burst release of 9-15% of the total payload, but no additional release is observed after the initial release. This is most likely due to some weakly physisorbed DSCP-Si on the nanoparticle surface. In the presence of 15 μM of *L*-cysteine (Figure 4-5, red line), there is a very slow, sustained release of platinum from **4.1**, with only 30% of the total amount of platinum released after 73 hours of incubation. However, in the presence of 5 mM *L*-cysteine (Figure 4-5, blue line), 45% of the total platinum is released within 5 hours, with the remaining platinum released gradually over the next 50 hours. The biphasic release is due to the covalent nature of the PSQ matrix. We

believe that the initial burst release of platinum arises from platinum centers at or near the nanoparticle surface. The longer sustained platinum release arises from platinum centers in the core of the nanoparticle, as *L*-cysteine would need to diffuse progressively further into the nanoparticle interior to reduce and release the platinum. These results suggest that **4.1** would show minimal drug release in circulation, but when placed in a highly reducing environment, such as the tumor microenvironment or upon cellular internalization, cisplatin would be rapidly released from the PSQ matrix, leading to more pronounced antitumor effects.

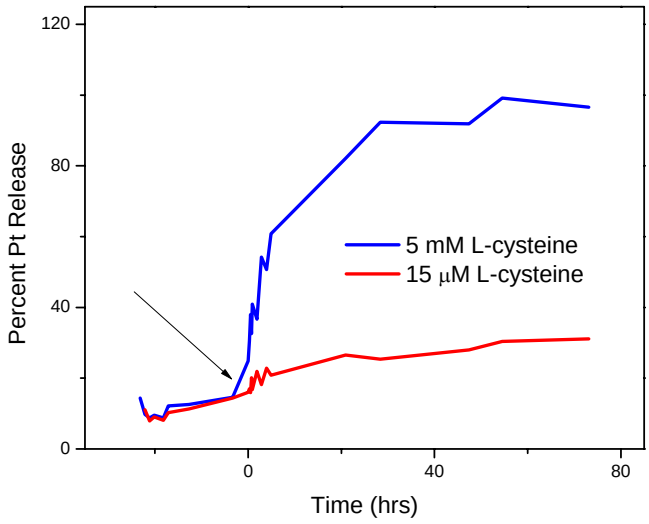

Figure 4-5: Platinum Release from **4.1** in the presence of low (15 μM, red line) or high (5 mM, blue line) concentrations of *L*-cysteine as a model reducing agent. *L*-cysteine was added at time zero, as indicated by the black arrow.

4.2.4 cRGD targeting

The presence of carboxylic acids on the surface of **4.1** allows the nanoparticles to be post-synthetically modified to further improve its surface properties. First, the cRGD peptide

was conjugated to **4.1** via an amide linkage to afford RGD-**4.1** (Scheme 4-2). The cRGD peptide primarily targets the $\alpha_v\beta_3$ integrin, which is upregulated on a variety of different tumor types.[22-23] cRGD conjugation to **4.1** (RGD-**4.1**) was accomplished by pre-activating the carboxylic acids on **4.1** with EDC (1-ethyl-3-(3-dimethylaminopropyl) carbodiimide) and NHS (N-hydroxysuccinimide) to form a more reactive NHS ester, which would then form an amide bond with the lysine residue on cRGDfK. The lysine residue was engineered onto the peptide for conjugation, so the activity of the peptide would not be compromised. RGD-**4.1** showed no difference in particle morphology by SEM (Figure 4.6). By DLS, RGD-**4.1** was actually slightly smaller than **4.1** (Figure 4.7, Table 4.1), but the differences in the two values are within experimental error. The zeta potential of RGD-**4.1** shifted to a more neutral value of -17.7 mV, indicating coating by the neutral cRGD peptide (Table 4.1). The drug loading, measured by ICP-MS, was unaffected by peptide conjugation.

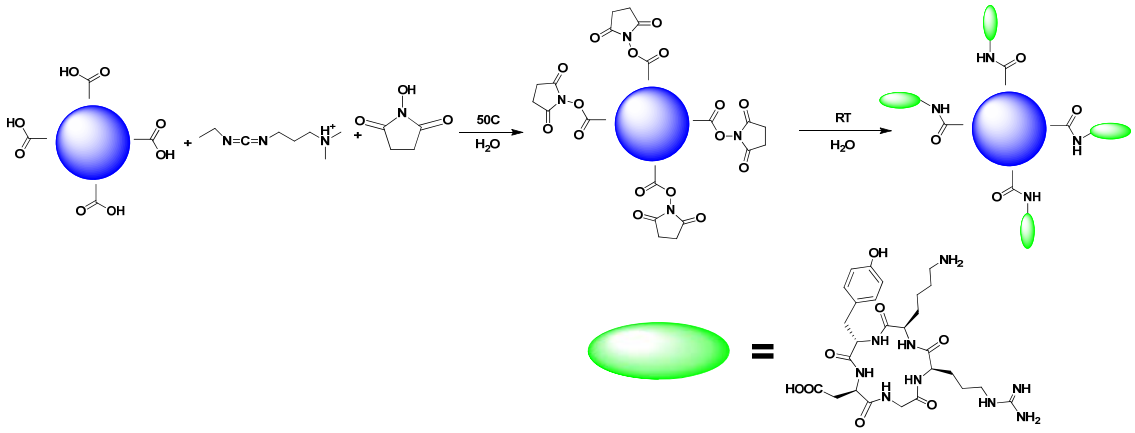

Scheme 4-2: Post-synthetic modification of **4.1** to form RGD-**4.1**

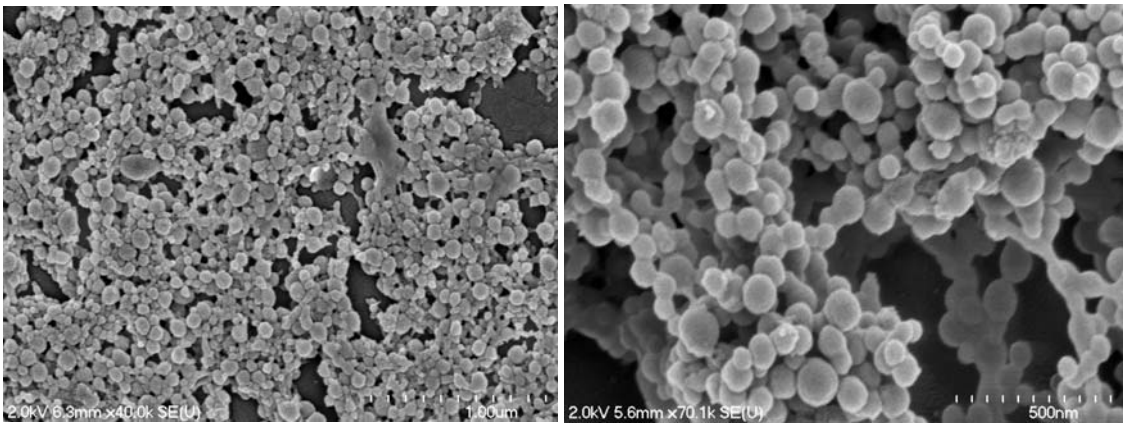

Figure 4-6: SEM micrographs of RGD-**4.1**.

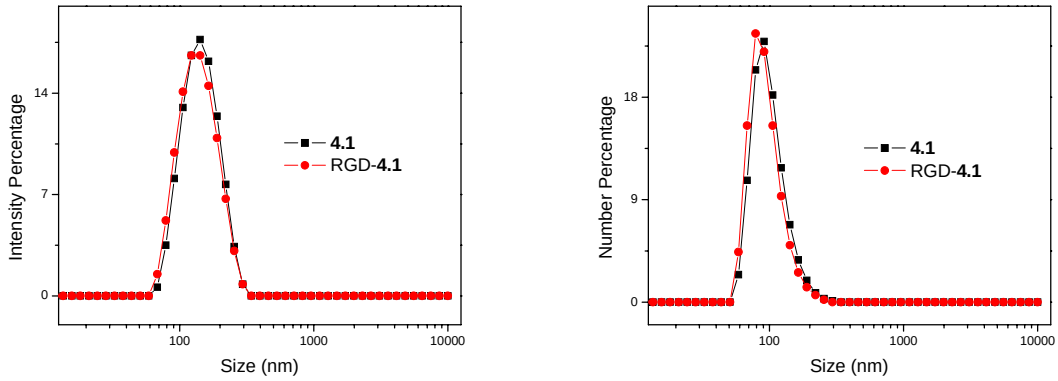

Figure 4-7: Intensity (left) and number (right) weighted DLS spectra of **4.1** (black) and RGD-**4.1** (red) obtained in 5 mM PBS.

4.2.5 *In Vitro* Cytotoxicity of 4.1 and RGD-4.1

4.1 and RGD-**4.1** were evaluated *in vitro* against 3 cancer cell lines: A549 lung adenocarcinoma, NCI-H460 large cell lung carcinoma, and PC-3 prostate adenocarcinoma. We chose to evaluate these nanoparticles against models of lung and prostate cancer as cisplatin is part of the standard of care for these two cancers.[24-25] In the A549 cell line, **4.1** was nearly twice as effective as cisplatin (Figure 4-8, Table 4-2). The $\alpha_v\beta_3$ integrin is overexpressed in A549 cells,[26] so RGD-**4.1** had an IC_{50} value one-half that of **4.1** and nearly one-quarter of cisplatin (Table 4-2). Cisplatin was more cytotoxic than **4.1** in H460 cells;

however, RGD-**4.1** possessed nearly 4 fold-better efficacy than **4.1**, and slightly better cytotoxicity than cisplatin itself (Figure 4-9, Table 4-2) as H460 cells overexpress the $\alpha_v\beta_3$ integrin.[27] PC-3 cells do not overexpress the $\alpha_v\beta_3$ integrin, so RGD targeting would not be effective.[28] Indeed, RGD-**4.1** had nearly identical efficacy as **4.1**, both of which were 2.5 times more effective than cisplatin (Figure 4-10, Table 4-2).

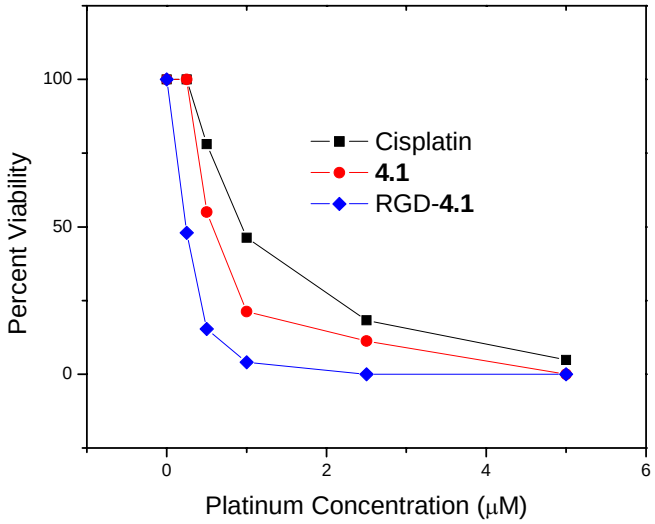

Figure 4-8: Cell viability assay of A549 lung adenocarcinoma cells treated with cisplatin (black), **4.1** (red) or RGD-**4.1** (blue).

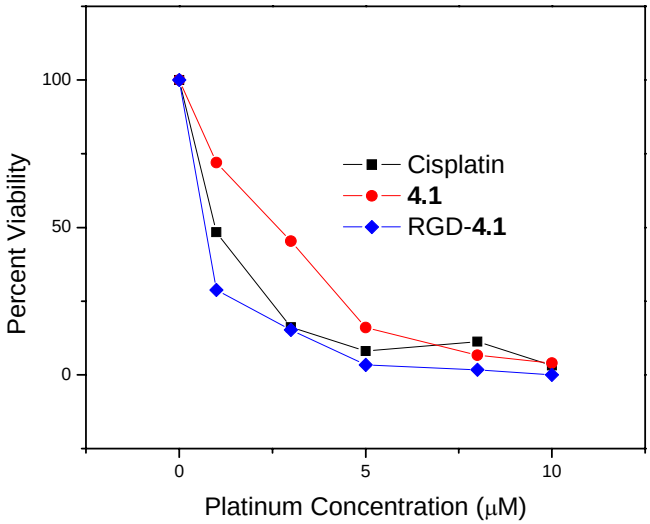

Figure 4-9: Cell viability assay of H460 large cell lung carcinoma cells treated with cisplatin (black), **4.1** (red) or RGD-**4.1** (blue).

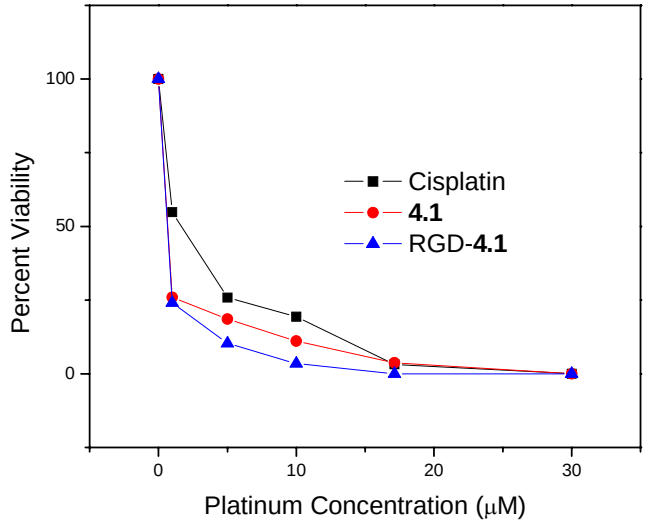

Figure 4-10: Cell viability assay of PC-3 prostate adenocarcinoma cells treated with cisplatin (black), **4.1** (red) or RGD-**4.1** (blue).

Table 4-2: IC_{50} values of cisplatin, **4.1**, and RGD-**4.1** evaluated against three cancer cell lines.

Cell Line	Cisplatin IC_{50} (μM)	Cisplatin-PSQ IC_{50} (μM)	RGD-Cisplatin-PSQ IC_{50} (μM)
A549	0.95	0.55	0.25
NCI-H460	0.96	2.65	0.702
PC-3	1.66	0.675	0.659

4.2.6 Pegylation of 4.1

Encouraged by the initial results, which demonstrated that **4.1** possessed triggered drug release and *in vitro* efficacy against a panel of cancer cell lines, we decided to evaluate **4.1** *in vivo* against murine cancer models. First, polyethylene glycol (PEG) was also conjugated to the surface of **4.1**. PEG is an inert, biocompatible polymer which is widely used to improve the biocompatibility, to reduce mononuclear phagocytic system (MPS) uptake, and to improve efficacy of nanomaterials.[29-32] Amine-terminated polyethylene glycol monomethyl ether (MW=2000) first was synthesized by an established procedure with minor modifications.[33] This PEG could be conjugated to **4.1** by an EDC-mediated amide coupling to form PEG2k-**4.1**. As-synthesized PEG2k-**4.1** demonstrated no change in particle morphology by SEM (Figure 4-11). Under physiological conditions, PEG2k-**4.1** has a larger hydrodynamic diameter [d(Z_{avg}) = 195.9 nm] than **4.1** ([d(Z_{avg}) = 134.2 nm] (Figure 4-12, Table 4-1). An increase in hydrodynamic diameter would be expected due to the PEG chains extending away from the nanoparticle surface, but it would not be expected to alter the size to this extent. There also may be a very slight increase in aggregation as a result of PEG conjugation. The zeta potential after PEG conjugation increased to -2.9 mV, which would be indicative of a PEG surface layer shielding the negative charge of the nanomaterial (Table 4-1).[30] TGA measurements of PEG2k-**4.1** showed an increase in weight loss of 20%, attributable to the PEG layer on the nanoparticle surface (Figure 4-13). This weight loss would correspond to a dense PEG surface coverage of 1.02 PEG/ nm^2. At this coverage density, PEG would be expected to adopt the desired brush confirmation to resist plasma protein binding and would allow the particle to evade the MPS system for efficient *in vivo* applications.[32]

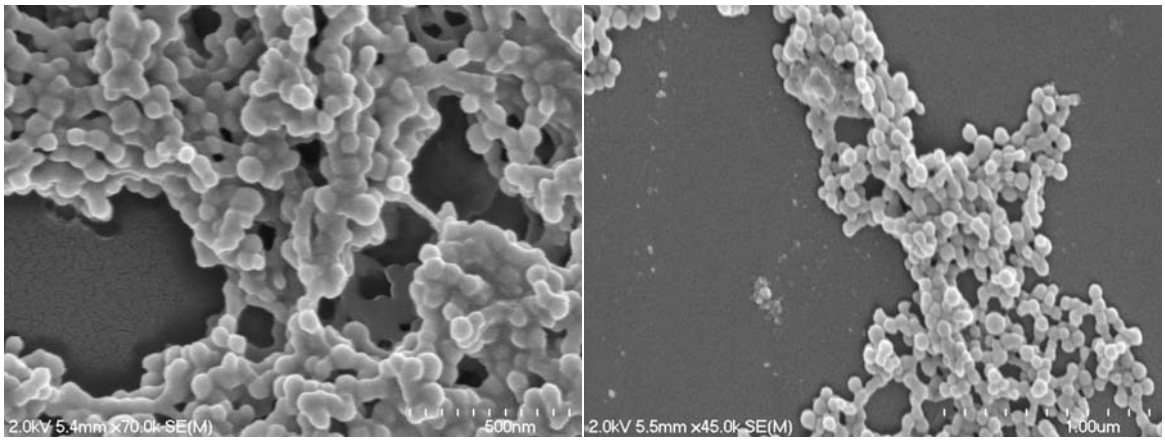

Figure 4-11: SEM micrographs of PEG2k-**4.1** (left) and APEG2k-**4.1** (right).

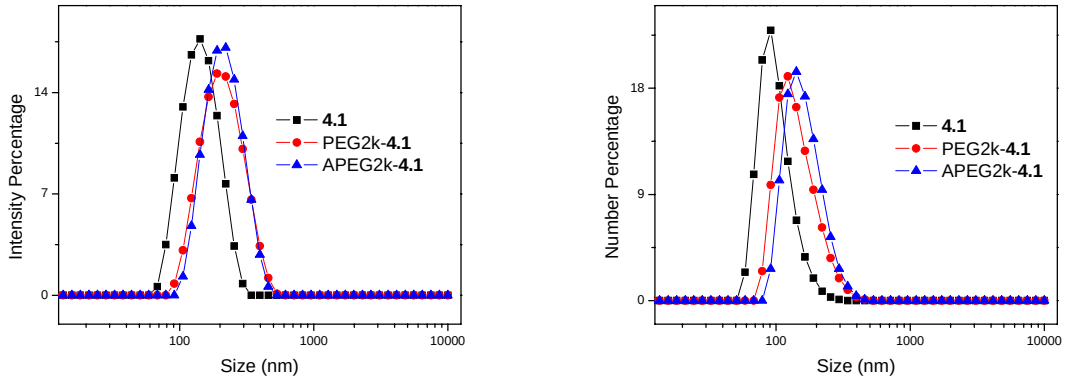

Figure 4-12: Intensity (left) and number (right) weighted DLS spectra of **4.1** (black), PEG2k-**4.1** (red) and APEG2k-**4.1** (blue) obtained in 5mM PBS.

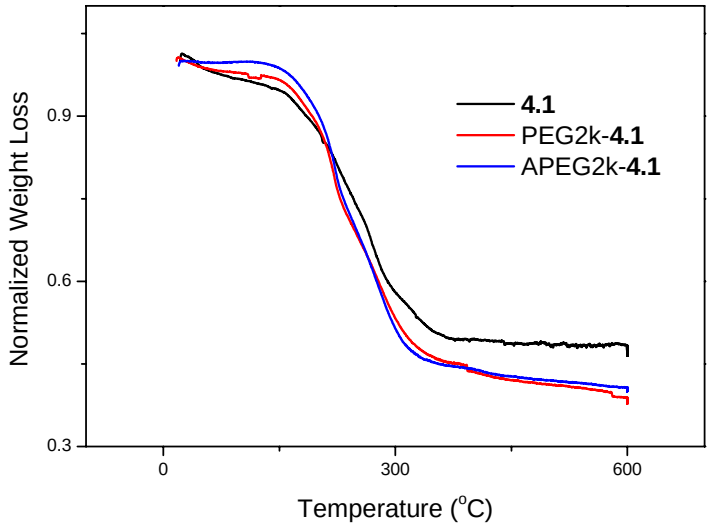

Figure 4-13: TGA weight loss curves for **4.1** (black), PEG2k-**4.1**(red), and APEG2k-**4.1** (blue).

An anisamide targeted, pegylated version of **4.1** (APEG2k-**4.**1) was synthesized as well. The anisamide ligand targets the sigma receptor, an opioid receptor overexpressed on a variety of cancer cells.[34-38] PEG with one anisamide and one amine end group was synthesized by an amide coupling between *p*-methoxybenzoic acid and diamminopolyethylene glycol (MW= 2000). The desired PEG was isolated from the reaction byproducts by column chromatography. To synthesize APEG2k-**4.1**, the same procedure for the preparation of PEG2k-**4.1** was followed except that 10 mol% anisamide PEG was added. Only 10 mol % of the APEG2k agent was used as prior studies suggest that about 10 mol % targeting ligand is necessary to achieve targeting *in vivo* and higher fractions may reduce the shielding effects of PEG.[39-40] APEG2k-**4.1** was characterized by SEM, DLS, zeta potential, TGA and ICP-MS (Figures 4-11 - 4-13, Table 4-1) and had no appreciable differences from PEG2k-**4.1**.

4.2.7 *In vitro* cytotoxicity of PEG2k-4.1 and APEG2k-4.1

PEG2k-**4.1** and APEG2k-**4.1** were evaluated *in vitro* against two non-small cell lung cancer lines: A549 and H460. In the A549 cell line, PEG2k-**4.1** was highly effective, but it was not quite as effective as cisplatin under the same conditions (Figure 4-14, Table 4-3). Previous assays had demonstrated that the unmodified **4.1** was much more effective than cisplatin (Figure 4-8, Table 4-2), so the PEG layer, which is designed to prevent nanoparticle uptake by MPS organs, lessened the degree of endocytosis and reduced efficacy in A549 cells. PEG2k-**4.1**, APEG2k-**4.1** and **4.1** were evaluated in H460 cells (Figure 4-15, Table 4-3). H460 cells overexpress the sigma receptor, so using an anisamide targeted nanoparticle would be appropriate.[41-42] All three forms of **4.1** showed better efficacy than cisplatin with **4.1** and PEG2k-**4.1** having comparable IC_{50} values. Anisamide targeting increased the efficacy approximately 3 times compared to the other nanoparticles and 6 times over cisplatin. Based on these promising *in vitro* results, PEG2k-**4.1** and PEG5k-**4.1** were chosen for further *in vivo* evaluations.

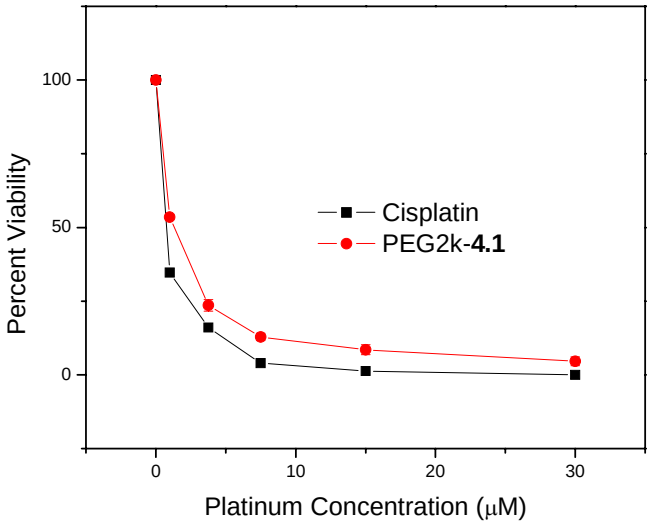

Figure 4-14: Cell viability assay of A549 lung adenocarcinoma cells treated with either cisplatin (black) or PEG2k-**4.1** (red).

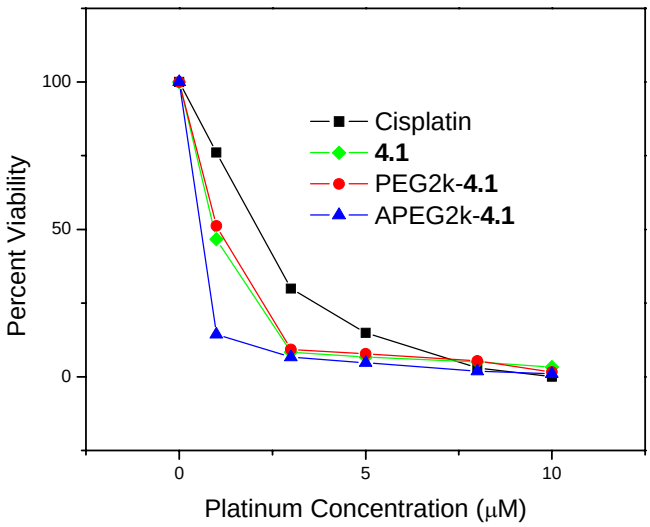

Figure 4-15: Cell Viability assay of H460 large cell lung carcinoma cells treated with either cisplatin (black), **4.1** (green), PEG2k-**4.1** (red) or APEG2k-**4.1** (blue).

Table 4-3: IC_{50} values of cisplatin, **4.1**, PEG2k-**4.1**, and APEG2k-**4.1** evaluated against two NSCLC cell lines.

Cell Line	Cisplatin (μM)	**4.1** (μM)	PEG2k-**4.1** (μM)	APEG2k-**4.1** (μM)
A549	0.676	N.A.	1.27	N.A.
H460	2.04	0.92	1.03	0.33

4.2.8: *In Vivo* Efficacy of PEG2k-4.1 and APEG2k-4.1

Based on the encouraging *in vitro* results which demonstrated that both PEG2k-**4.1** and APEG2k-**4.1** were efficacious in multiple cancer cell lines, we evaluated chemotherapeutic efficacy of the PSQ particles *in vivo* against a H460 lung cancer xenograft model (Figure 4-16). Nu/Nu mice were implanted with H460 cells subcutaneously and the tumors were allowed to grow until palpable. The mice were randomly split into 4 groups (7-8 mice per group) and received either saline control, cisplatin (4 mg/kg), PEG2k-**4.1** (4 mg cisplatin/kg equivalent), APEG2k-**4.1** (4 mg cisplatin/kg equivalent) on days 0, 2 and 4. Tumor growth was measured by caliper measurements and the study was terminated when the control mice reached the maximum allowed size by the IACUC guidelines. Mice receiving no treatment showed rapid tumor growth, reaching the allowed size limits 15 days after commencement of the study. Mice receiving all of the platinum treatments demonstrated statistically significant tumor growth inhibition over the control mice, but all platinum treatment provided nearly identical tumor growth inhibition. Unfortunately, the treatments with all of the platinum formulations were too aggressive and treatment related deaths were observed in all treatment groups (Table 4-4). Surviving mice weights remained relatively constant, with some weight gain throughout the study (Figure 4-17). After the conclusion of the study, the tumors were resected and analyzed by histology (Figures 4-18 - 4-20). Mice receiving no treatment showed large tumors with viable and necrotic regions.

The necrotic regions are due to a lack of nutrients in the core of the tumor. Cisplatin treatment increased the area of the necrotic tumor regions compared to the control mice, but did not eradicate all of the cells in the tumor region. On the other hand, mice receiving PEG2k-**4.1** or APEG2k-**4.1**treatment had tumors composed of large necrotic centers, with viable cells found only on the periphery of the tumor. The histology results suggest that the PSQ particles are highly effective chemotherapeutics, but that the treatments were too harsh and resulted in death caused by the toxicity of the platinum formulations.

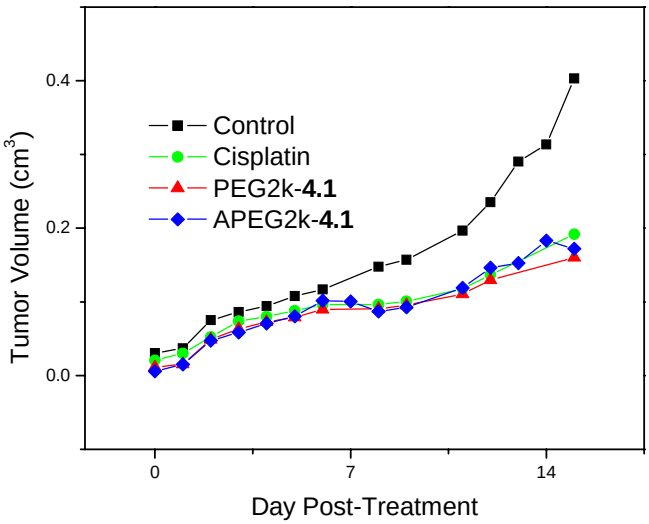

Figure 4-16: Tumor growth inhibition in a H460 large cell lung carcinoma subcutaneous xenograft model. Mice received either saline control (black), cisplatin (green, 4 mg/kg), PEG2k-**4.1** (red, 4 mg cisplatin/kg equivalent), or APEG2k-**4.1** (blue, 4mg cisplatin/kg equivalent) on days 0, 2, and 4.

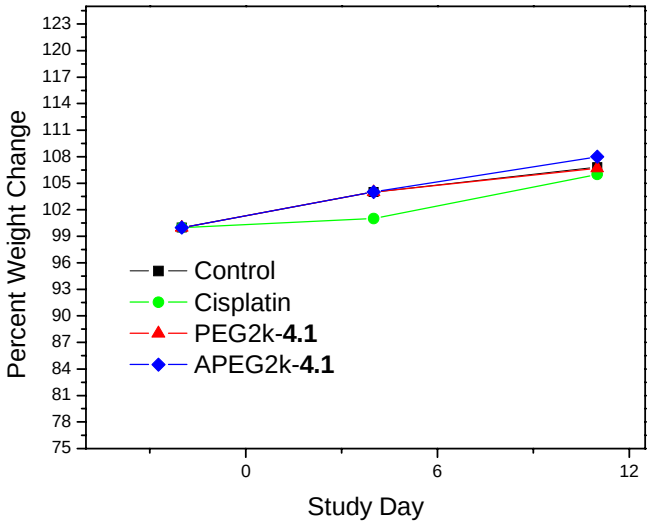

Figure 4-17: Mouse body weight changes during the course of the study. Mice received either saline control (black), cisplatin (green, 4 mg/kg), PEG2k-**4.1** (red, 4 mg cisplatin/kg equivalent), or APEG2k-**4.1** (blue, 4 mg cisplatin/kg equivalent) on days 0, 2, and 4.

Table 4-4: Mouse survival statistics as a result of platinum chemotherapy

Treatment Group	Treatment Related Deaths	Death Percentage
Control	0/7	0%
Cisplatin	3/7	43%
PEG2k-**4.1**	3/7	43%
APEG2k-**4.1**	3/7	43%

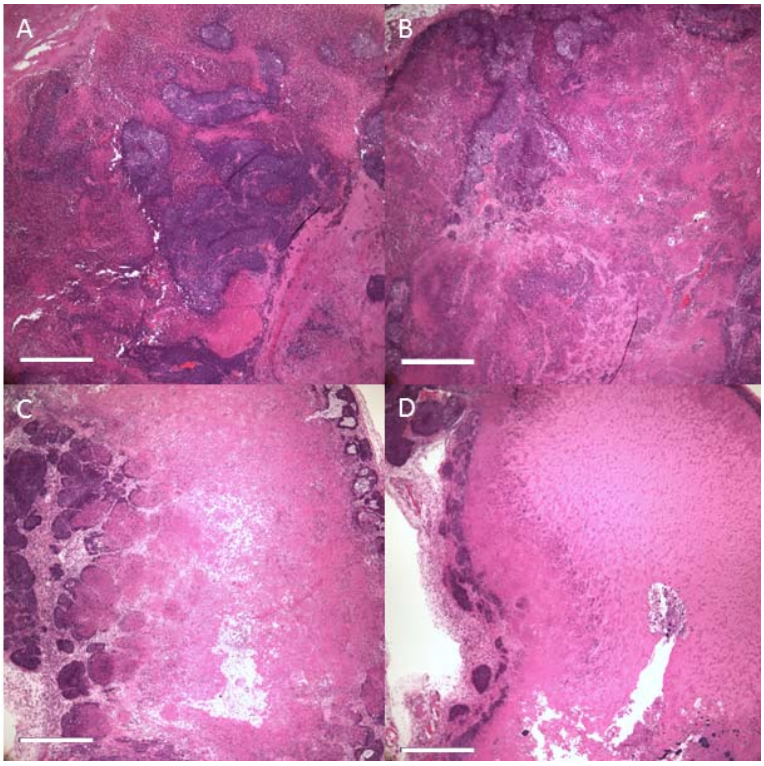

Figure 4-18: Histological images of resected H460 tumors with H&E staining at 4x magnification. Mice received either saline control (A), cisplatin (B), PEG2k-**4.1** (C), or APEG2k-**4.1**(D) on study days 0, 2, and 4. The blue-purple dots result from nuclear staining of viable cancer cells whereas the pinkish areas are necrotic regions containing no viable tumor tissue. Scale bar indicates 0.5 mm.

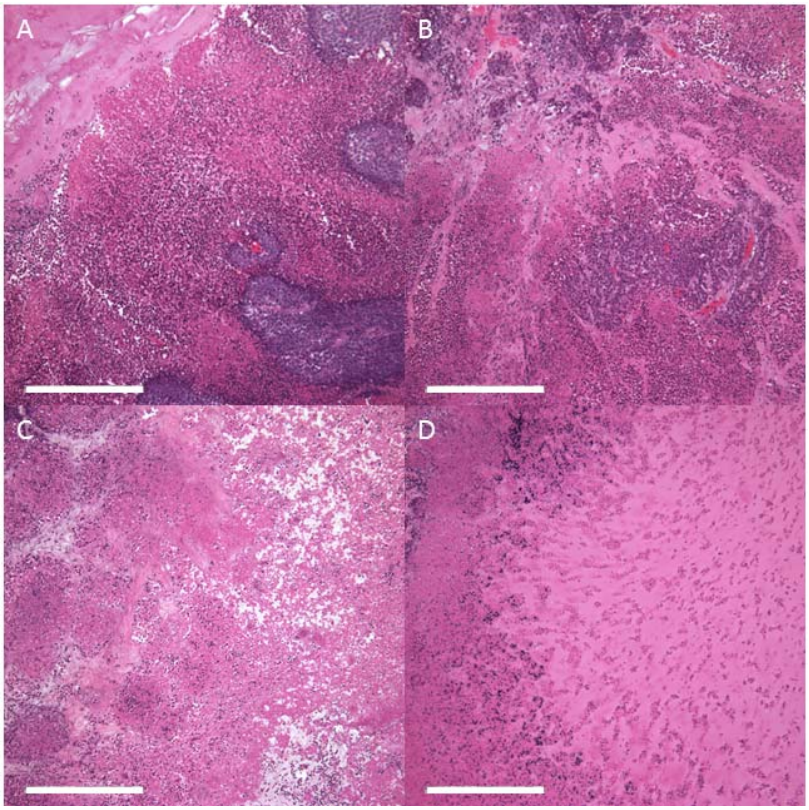

Figure 4-19: Histological images of resected H460 tumors with H&E staining at 10x magnification. Mice received either saline control (A), cisplatin (B), PEG2k-**4.1** (C), or APEG2k-**4.1**(D) on study days 0, 2, and 4. The blue-purple dots result from nuclear staining of viable cancer cells whereas the pinkish areas are necrotic regions containing no viable tumor tissue. Scale bars indicate 0.5 mm.

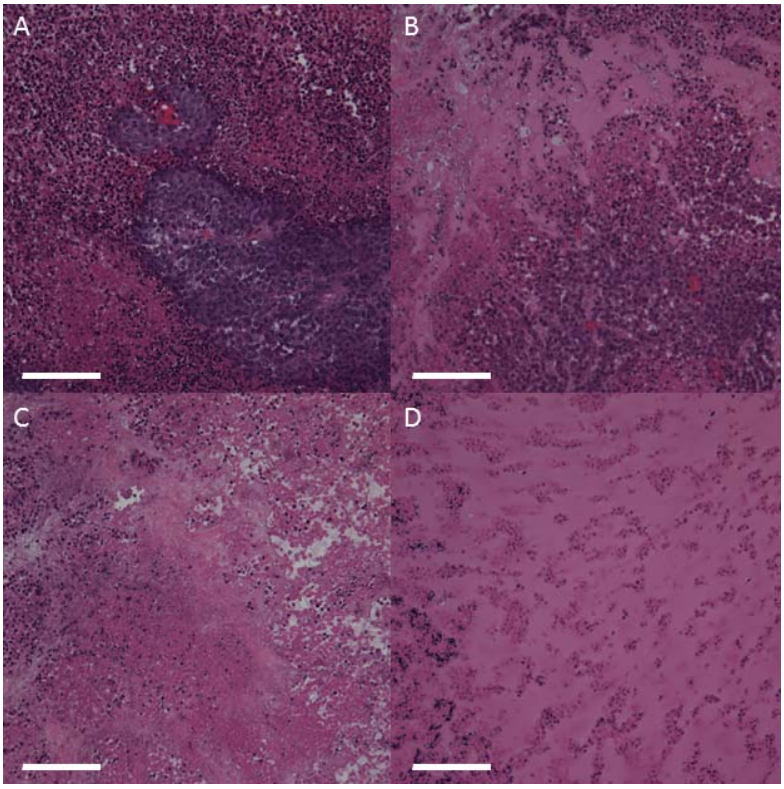

Figure 4-20: Histological images of resected H460 tumors with H&E staining at 20x magnification. Mice received either saline control (A), cisplatin (B), PEG2k-**4.1** (C), or APEG2k-**4.1**(D) on study days 0, 2, and 4. The blue-purple dots result from nuclear staining of viable cancer cells whereas the pinkish areas are necrotic regions containing no viable tumor tissue. Scale bars indicate 120 μm.

4.2.9 Maximum Tolerated Dose Studies of PEG2k-4.1

In order to avoid the toxicity-related mouse death observed in the previous xenograft study, maximum tolerated dose (MTD) studies were performed on PEG2k-**4.1**. MTD is defined as the highest dose level that does not cause death, a body condition score less than or equal to two,[43] or greater than 20% body weight loss. Violation of the latter two parameters would result in the immediate euthanasia of the mouse due to the IACUC guidelines. Non-tumor bearing mice were administered a single i.v. dose of PEG-**4.1** and mice were monitored daily. Survival, with no adverse effects, for two weeks post-injection was considered a safe dose level. The MTD of cisplatin, under this injection schedule was 10

mg/kg.[44-45] PEG2k-**4.1** possessed a much lower MTD than cisplatin, with animal death observed at a 4 mg/kg cisplatin dose (Table 4-5). These results suggest that PEG2k-**4.1** has high, off target organ toxicity, which would limit its clinical application. ICP-MS analysis of the resected MPS system organs demonstrated that the liver had the highest platinum accumulation post-injection, which was further verified by liver histology (Figure 4-21). The liver from the mouse receiving PEG2k-**4.1** had large necrotic regions, with a significant amount of red blood cells leaving circulation and pooling in the liver. Due to this toxicity, **4.1** was reformulated to attempt to improve its *in vivo* performance.

Table 4-5: MTD study results of non-tumor bearing nude mice treated with PEG2k-**4.1**

Dose (Cisplatin equivalent)	Toxic Deaths	Time after injection
8 mg/kg	2/2	4 days
6 mg/kg	2/2	4 days
4 mg/kg	2/2	4 days

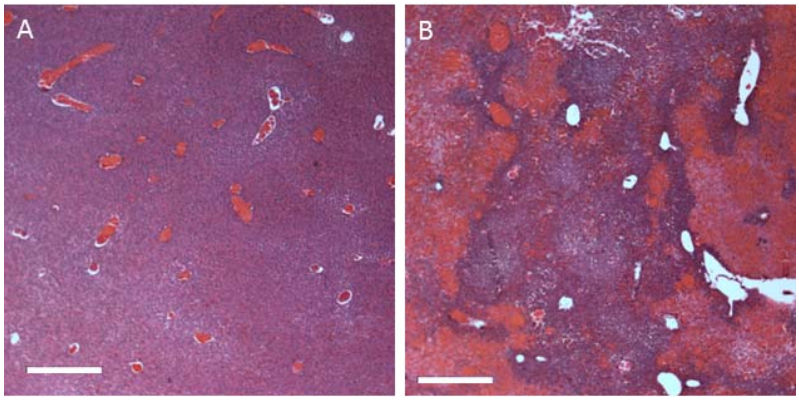

Figure 4-21: Liver histology results of mice treated with saline (A) or PEG2k-**4.1** (B) with H&E staining at 4x magnification. Purple areas indicate viable cells, pink areas indicate dead cells, and red circles indicate red blood cells. Scale bars indicate 0.5 mm.

4.2.10 Pegylation (MW: 5000) of 4.1

As PEG chain length and PEG density can play an important role in optimizing the pharmacokinetics and biodistribution of **4.1**,[29, 31-32] we modified the PEG grafting strategy in

order to endow **4.1** with better stealth properties. Amino-PEG (MW 5000) monomethyl ether was synthesized through end group modification of PEG (MW 5000) monomethyl ether. Numerous attempts to couple PEG5k-NH_2 to **4.1** by EDC mediated couplings were unsuccessful, so a HBTU-based coupling in acetonitrile was used to synthesize PEG5k-**4.1**(Scheme 4-3). PEG5k-**4.1** showed no change in particle morphology by SEM and TEM (Figures 4-22 and 4-23); however the hydrodynamic size increased to 150.3 nm (Figure 4-24, Table 4-1). This increase in hydrodynamic size was due to a dense layer of conjugated PEG chains extending away from the nanoparticle surface. The zeta potential of **4.1** was -6.5 mV due to the shielding of the nanoparticle surface charge by the PEG corona. PEG5k-**4.1** contained 22 wt% PEG by TGA (Figure 4-25). This would correspond to a PEG coverage density of 1 PEG/ 4.5 nm^2, which would allow the PEG to adopt a brush confirmation extending away from the nanoparticle surface and provide PEG5k-**4.1** with the optimum stealth properties.[32]

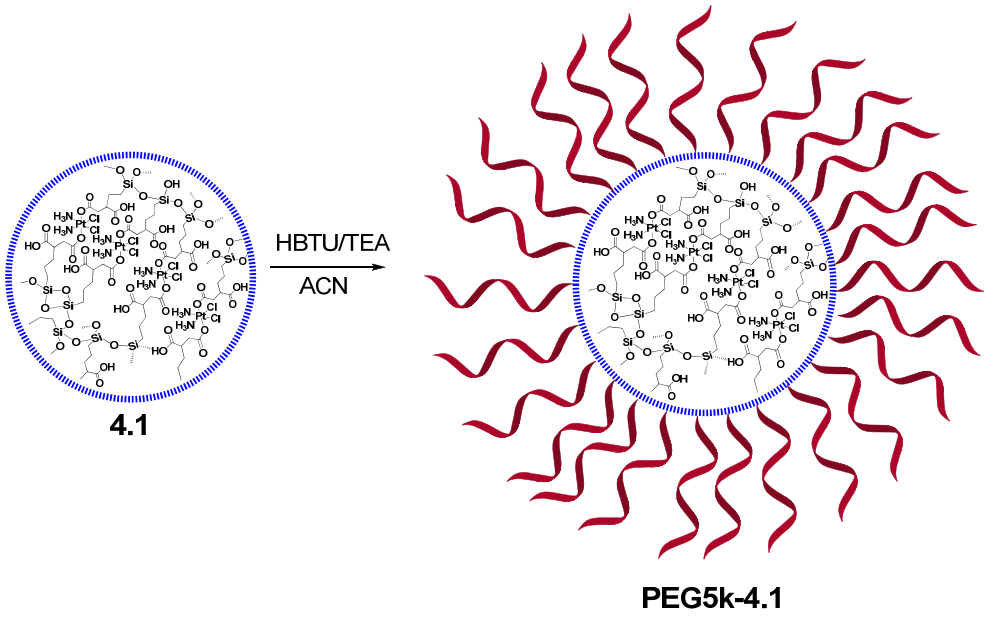

Scheme 4-3: Schematic of pegylation of **4.1** to PEG5k-**4.1**.

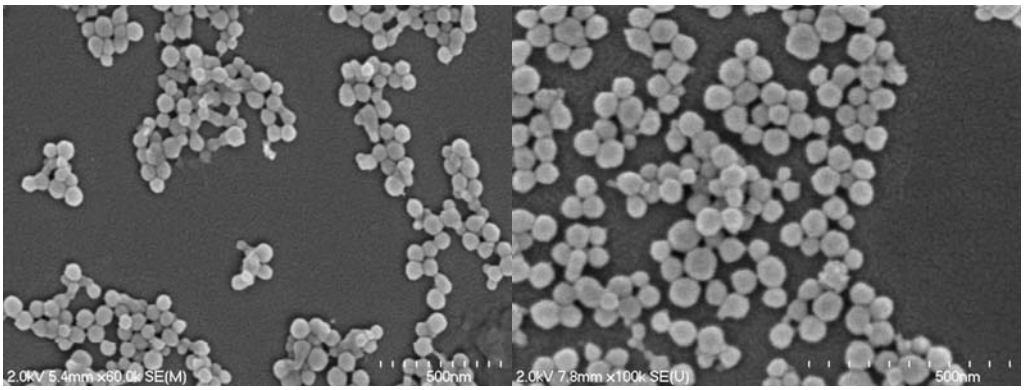

Figure 4-22: SEM micrographs of PEG5k-**4.1**.

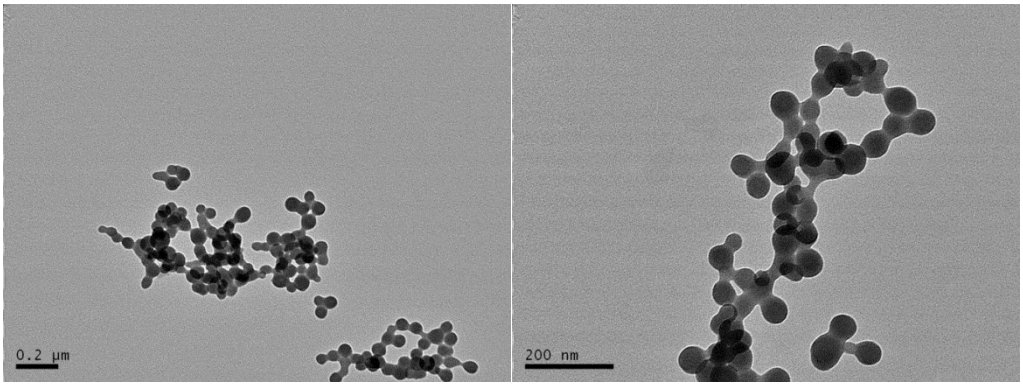

Figure 4-23: TEM micrographs of PEG5k-**4.1**.

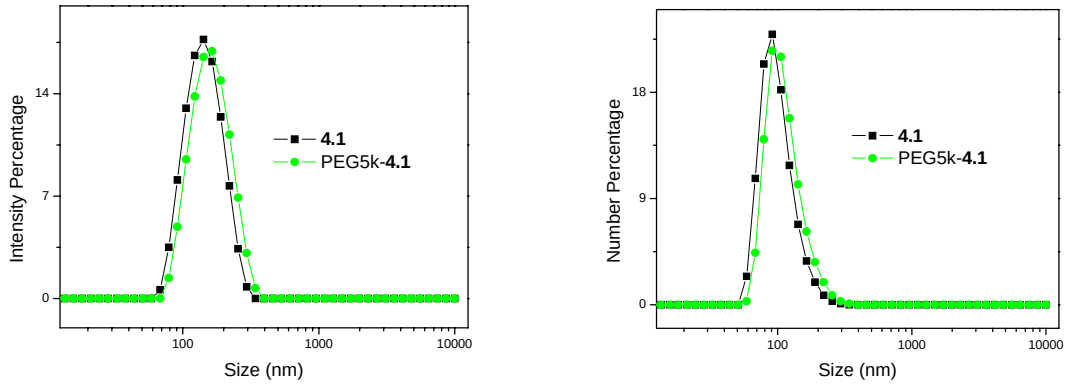

Figure 4-24: Intensity (left) and number (right) weighted DLS spectra of **4.1** (black) and PEG5k-**4.1** obtained in 5mM PBS.

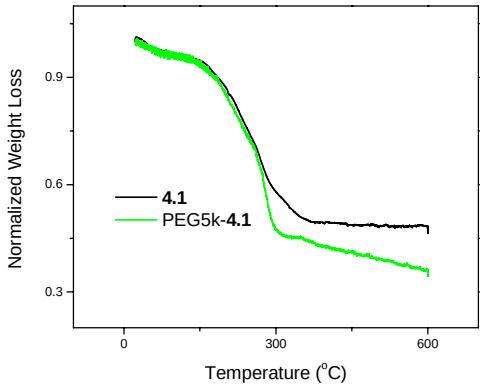

Figure 4-25: TGA weight loss curves for **4.1** (black) and PEG5k-**4.1** (green)

4.2.11 Nonspecific Protein Binding and Colloidal Stability in Plasma

Nonspecific plasma protein binding to the nanoparticle surface is one of the first steps for the MPS system to recognize and thus uptake the nanoparticles, thus playing a major role in determining nanoparticle biodistribution.[46] A well pegylated nanoparticle should be able to resist protein absorption, which would extend systemic circulation. To this end, the colloidal stability of **4.1** and PEG5k-**4.1** in the presence of bovine serum albumin (BSA), the most common type of plasma protein, was investigated. If BSA was bound to the nanoparticle surface, the size of the nanoparticles would increase and would also cause them to quickly precipitate from the suspension. The sizes of various nanoparticle suspensions (under conditions that were shown to be colloidally stable without BSA over the time frame) were determined by DLS immediately before adding 500 wt% BSA. Nanoparticle sizes were measured every 10 minutes for 3 hours. For unpegylated **4.1**, the nanoparticle size immediately increased by approximately 100 nm (Figure 4-26) after BSA addition and remained relatively constant over the course of the experiment. The instrument count rate, which corresponds to the particle concentration of the suspension, gradually decreased over

the course of the experiment, suggesting that the nanoparticles are precipitating from the suspension (Figure 4-27). Size distribution data also confirmed the presence of larger, up to 1 micron, particle agglomerates in solution due to the aggregation (and eventual precipitation) of **4.1** with BSA (Figure 4-28). PEG5k-**4.1** nanoparticles were also evaluated by this method. In contrast to **4.1**, the d(Z_{avg}), count rate, and intensity distribution of PEG5k-**4.1** remained consistent over the experiment (Figures 4-26, 4-27, 4-29) indicating that the PEG layer on the nanoparticles prevented nonspecific protein absorption. Both experimental results are reproducible with different nanoparticle batches.

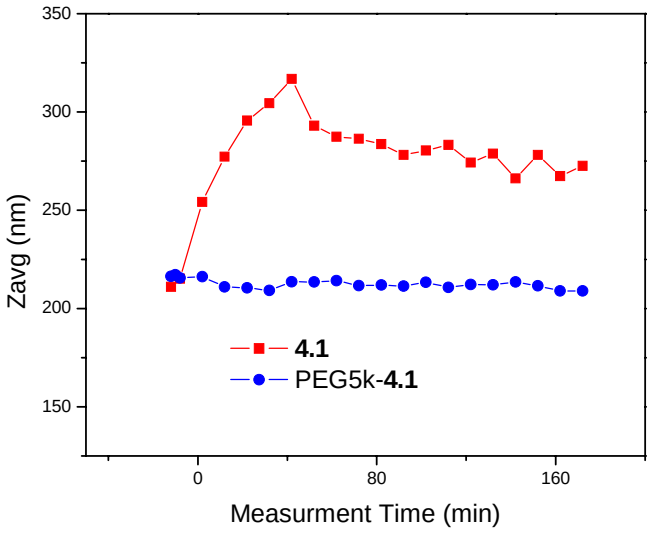

Figure 4-26: d(Z_{avg}) trends as a function of exposure to BSA for **4.1** (red) and PEG5k-**4.1** (blue). BSA was added at t =0.

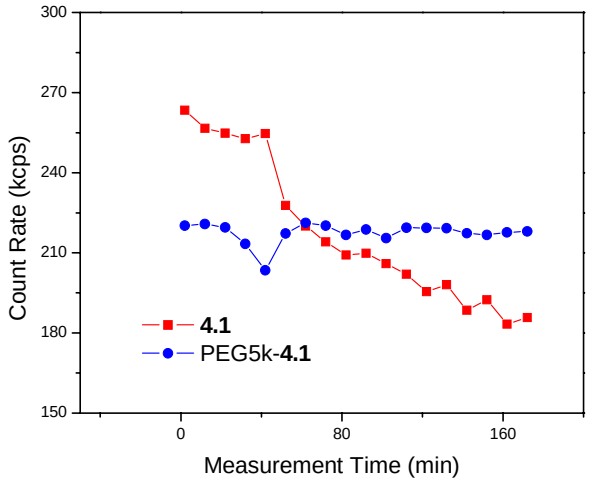

Figure 4-27: DLS count rate trends of **4.1** (red) and PEG5k-**4.1** (blue) as a function of time after exposure to BSA.

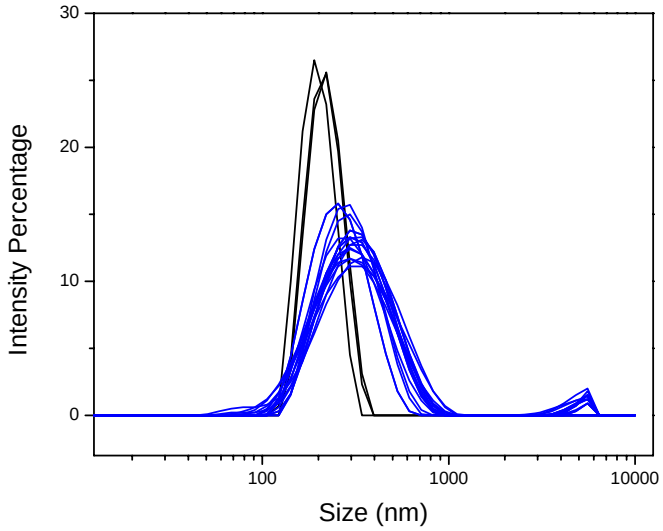

Figure 4-28: Intensity-weighted DLS curves of **4.1** before (black) and after (blue) BSA addition. After curves were obtained every 10 minutes for 3 hours.

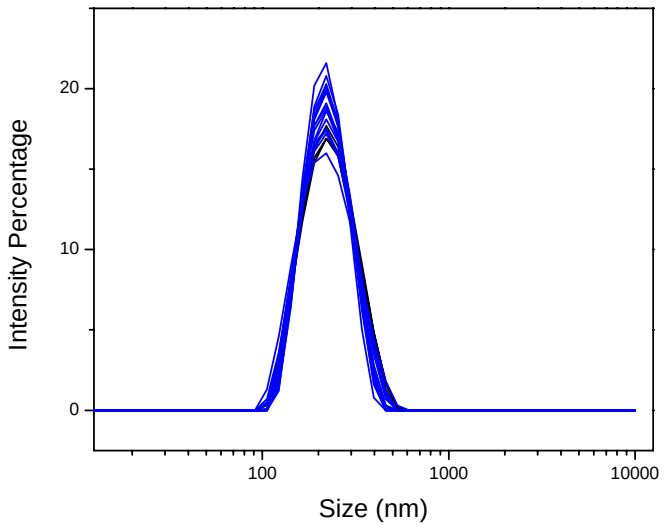

Figure 4-29: Intensity-weighted DLS curves of PEG5k-**4.1** before (black) and after (blue) BSA addition. After curves were obtained every 10 minutes for 3 hours.

Due to some of the biodistribution results obtained in the next sections, the colloidal stability in rat plasma was investigated by DLS. PEG5k-**4.1**was suspended into 1mL undiluted rat plasma and DLS measurements were obtained every 10 minutes for 2 hours (Figures 4-30 and 4-31) for two different samples of PEG5k-**4.1** (PEG5k-**4.1**(A) and PEG5k-**4.1**(B)). In both curves, the smaller peaks (under 50 nm) are due to plasma proteins present in solution, so only the larger intensity peaks are indicative of nanoparticle behavior. For PEG5k-**4.1**(A), the intensity size distribution shifted outward to larger hydrodynamic diameters, indicating that the nanoparticles are aggregating as a result of plasma protein binding (Figure 4.34). For PEG5k-**4.1**(B), the particle intensity distribution remained relatively unchanged from plasma incubation, indicating a better pegylated nanoparticle (Figure 4.35). Both batches of nanoparticles were identical by prior physiochemical characterization and could resist BSA binding; however, subtle differences in the PEG corona lead to varying degrees of colloidal stability in plasma. This effect was reproducible

within the same batch, but the degree of the control in synthesizing the PEG corona has not yet been achieved to reach batch to batch reproducibility. Future *in vivo* studies will attempt to utilize nanoparticles that are colloidally stable in plasma. It is important to mention that this assay was developed in response to the *in vivo* results obtained in the next sections, so some of the studies were performed with batches that were later found to lack stability in plasma.

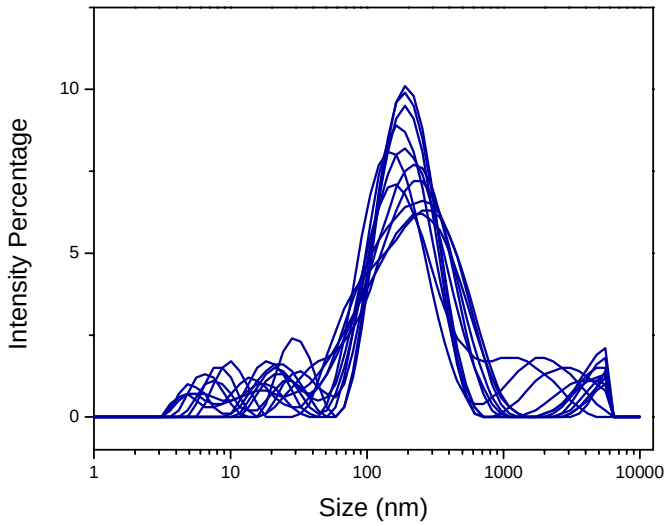

Figure 4-31: Colloidal stability measurements of PEG5k-**4.1** (A) in rat plasma.

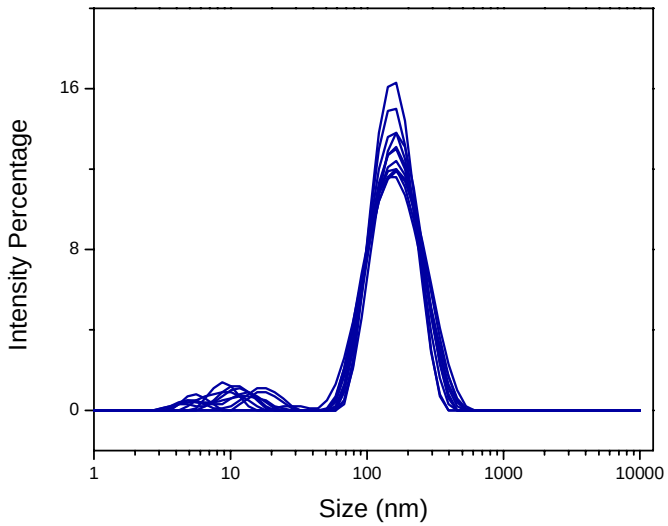

Figure 4-31: Colloidal stability of PEG5k-**4.1** (B) in rat plasma.

4.2.12 Maximum Tolerated Dose **of PEG5k-4.1**

Before starting efficacy studies, the MTD of PEG5k-**4.1** was determined. These studies were performed using a batch of nanoparticles that was later found to slightly aggregate in plasma and the study was conducted as described in section **4.2.9**. PEG5k-**4.1** has a MTD of greater than 20 mg/kg (Table 4-6). These studies are still ongoing, so the true MTD of this nanoparticle formulation has not yet been reached. The mouse weights remained relatively consistent, with only slight (<10%) weight loss observed initially. At the termination of the study, all dose levels had regained any lost weight (Figure 4-32). The MTD of PEG5k-**4.1** is at least twice as high as cisplatin[44-45] and more than five times higher than PEG2k-**4.1** (Table 4-5), suggesting that PEG5k-**4.1**is better tolerated in mice due to the improved PEG shell. The liver and spleen of MTD mice receiving 0, 4 mg/kg, 10 mg/kg and 15 mg/kg doses were also examined by histology (Figures 4-33- 4-36). There were no gross morphological changes in the liver as a result of treatment with various doses of PEG5k-**4.1** (Figures 4-33 and 4-34) in contrast to administration of PEG2k-**4.1**. Spleen morphology changes were observed at the 15 mg/kg dose level, indicating that spleen toxicity may play a

role in the MTD of PEG5k-**4.1**; however, further study is needed to determine both the MTD and the dose limiting toxicity (Figures 4-35 and 4-36).

Table 4-6: MTD study results of non-tumor bearing nude mice receiving different dose levels of PEG5k-**4.1**.

Dose (Cisplatin equivalent)	Toxic Deaths
4mg/kg	0/2
6mg/kg	0/2
10mg/kg	0/2
12mg/kg	0/2
15 mg/kg	0/2
20 mg/kg	0/2

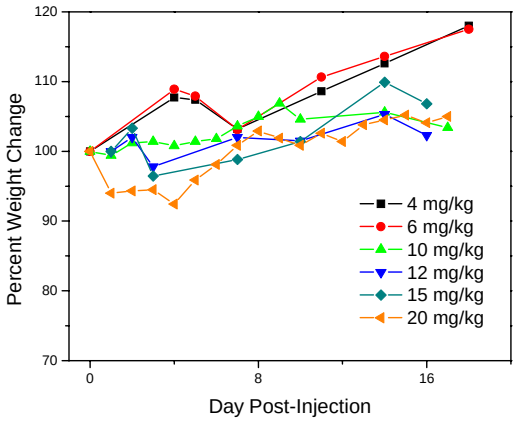

Figure 4-32: Percent mouse body weight changes after administration of 4 mg/kg (black), 6 mg/kg (red), 10 mg/kg (green) 12 mg/kg (blue), 15 mg/kg (cyan) or 20 mg /kg (orange) doses of PEG5k-**4.1** in non-tumor bearing nude mice. All doses are cisplatin equivalent.

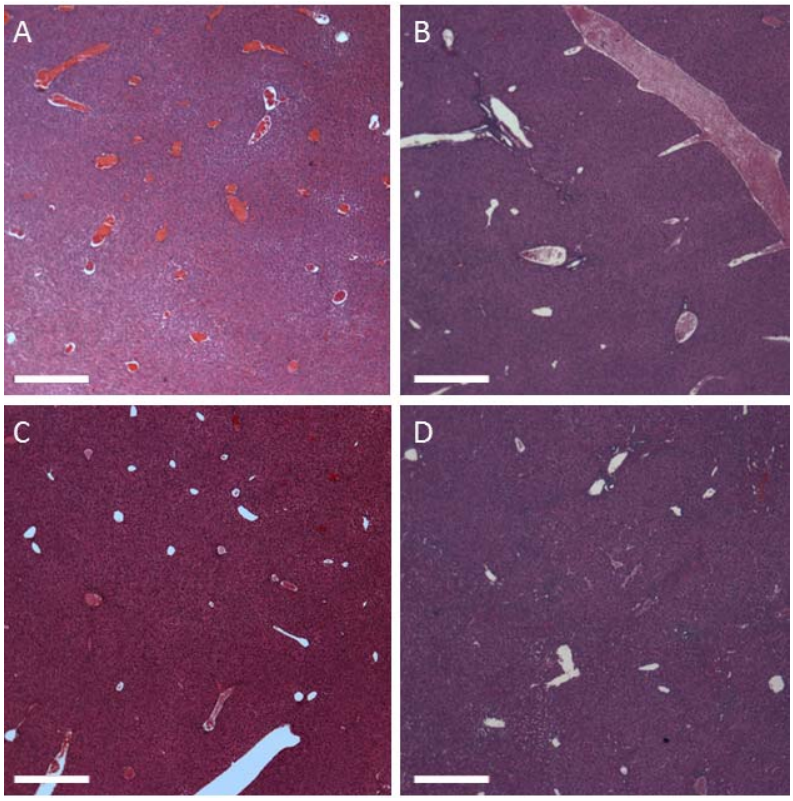

Figure 4-33: Liver histological images (with H& E staining) obtained at 4 x magnification of mice receiving either 0 mg/kg (A), 4 mg/ kg (B), 10 mg/kg (C) or 15 mg /kg (D) doses of PEG5k-**4.1**. All doses are expressed as cisplatin equivalent doses. Scale bars indicate 0.5 mm.

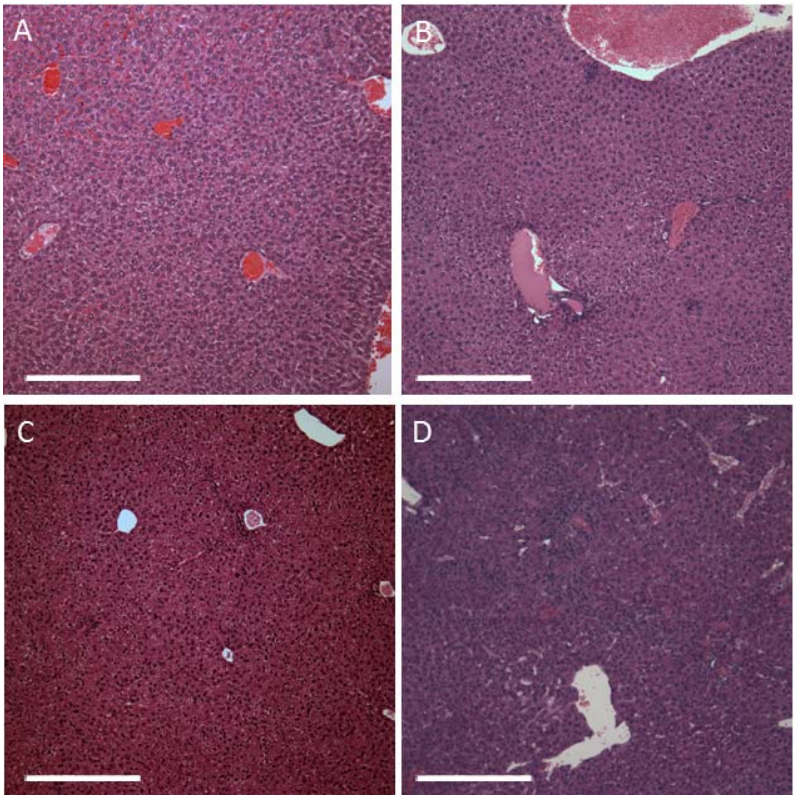

Figure 4-34: Liver histological images (with H& E staining) obtained at 10x magnification of mice receiving either 0 mg/kg (A), 4 mg/ kg (B), 10 mg/kg (C) or 15 mg /kg (D) doses of PEG5k-**4.1**. All doses are expressed as cisplatin equivalent doses. Scale bars indicate 500 μm.

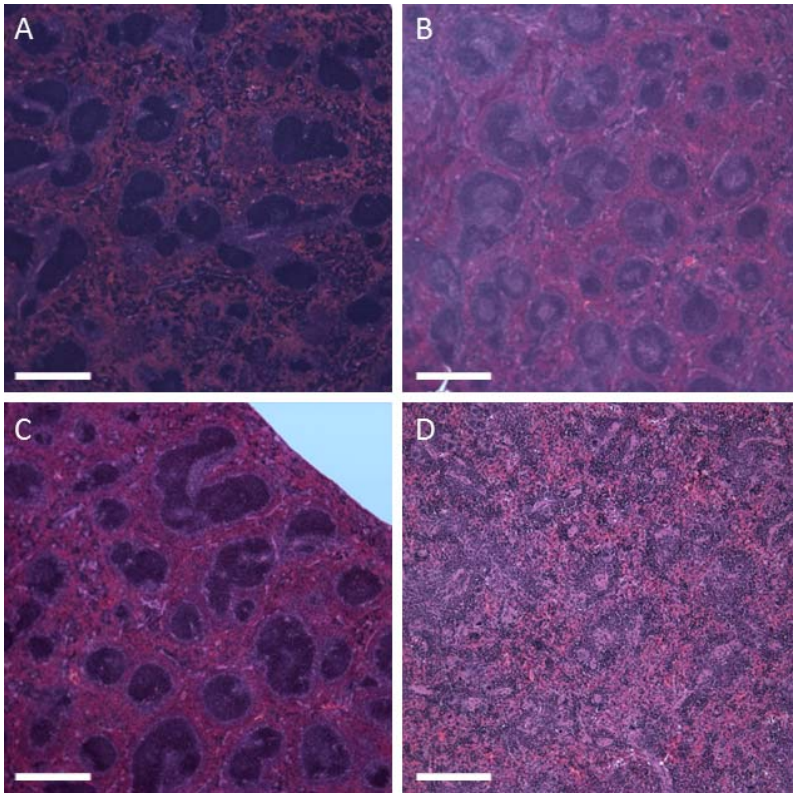

Figure 4-35: Spleen histological images (with H& E staining) obtained at 4x magnification of mice receiving either 0 mg/kg (A), 4 mg/ kg (B), 10 mg/kg (C) or 15 mg /kg (D) doses of PEG5k-**4.1**. All doses are expressed as cisplatin equivalent doses. Scale bar indicates 0.5 mm.

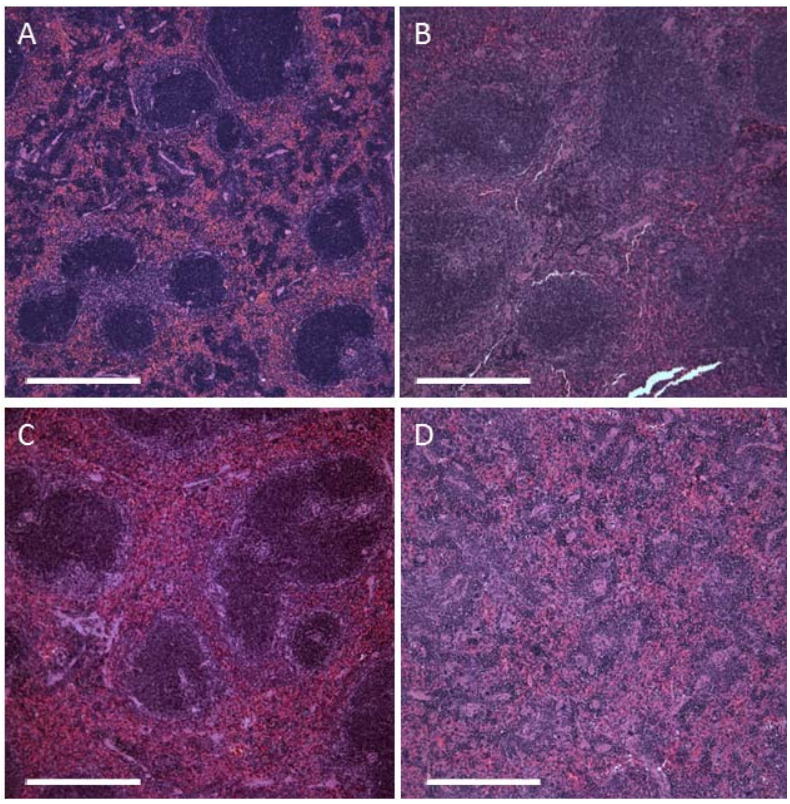

Figure 4-36: Spleen histological images (with H& E staining) obtained at 10x magnification of mice receiving either 0 mg/kg (A), 4 mg/ kg (B), 10 mg/kg (C) or 15 mg /kg (D) doses of PEG5k-**4.1**. All doses are expressed as cisplatin equivalent doses. Scale bar indicates 500 µm.

4.2.13 Biodistribution of PEG5k-4.1

The biodistribution of PEG5k-**4.1** was investigated in nu/nu mice bearing H460 s.c xenografts (Figures 4-37 and 4-38). Mice were administered PEG5k-**4.1**(A) i.v. at a 4 mg/kg cisplatin dose and were sacrificed 5 minutes, 1 hour, 6 hours and 24 hours post-injection. The blood, MPS organs (liver and spleen), kidneys and tumors were harvested. Organs were digested in concentrated nitric acid and platinum content was determined by ICP-MS. Tumor concentrations of platinum were quite high, reaching a maximum concentration of 14 µg Pt/g tissue (Figure 4-37, black), which is a much higher concentration than what is typically observed for cisplatin (1-2 µg/g).[44, 47-48] However, tumor platinum concentrations were highly variable presumably due to differences in tumor sizes between individual mice.

Clearance of PEG5k-**4.1** (A) occurred through the major MPS organs (liver and spleen) with the highest platinum concentrations observed in the spleen (Figure 4-37, blue), but the bulk of the injected dose accumulating within the liver (Figure 4-38, red). High splenic uptake was initially surprising, as the macrophages in the spleen primarily clear larger nanoparticles than what was observed for PEG5k-**4.1**.[29] However, considerable aggregation of PEG5k-**4.1** (A) was observed by DLS in the presence of rat plasma (Figure 4-31), so high splenic accumulation was probably due to the aggregation of PEG5k-**4.1** (A) in the plasma. PEG5k-**4.1** (A) was also used for the MTD studies above, which also suggested high spleen concentrations of platinum. Cisplatin is primarily cleared through the kidneys, resulting in dose limiting renal toxicity.[49] In contrast, administration of PEG5k-**4.1** caused very low renal platinum concentrations, typically under 2 μg/g. The circulation properties of PEG5k-**4.1** (A) appear to have a rapid distribution phase and a slow elimination phase, as there is a rapid decline in blood concentration to 1 hour post injection, followed by a slower decline afterwards (Figure 4-37, pink; Figure 4-38). There was still a detectable amount of platinum present in the bloodstream 24 hours post-injection.

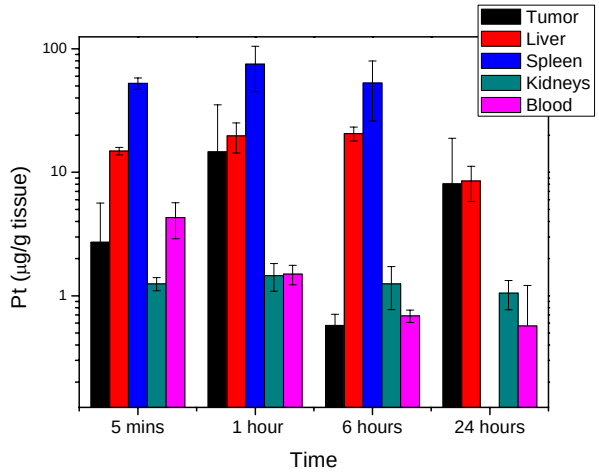

Figure 4-37: Platinum concentrations in the tumor (black), liver (red), spleen (blue), kidneys (cyan), and blood (pink) after administration of PEG5k-**4.1** (A) to mice bearing H460 s.c. xenografts.

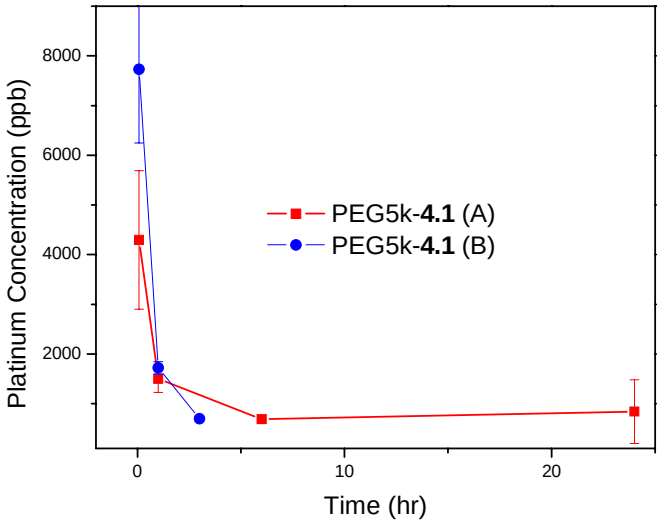

Figure 4-38: Blood platinum concentration levels over time after administration of PEG5k-**4.1** (A) (red) and PEG5k-**4.1** (B) to nu/nu mice.

Due to the tendencies of PEG5k-**4.1** (A) to aggregate in plasma, the biodistribution study was repeated with PEG5k-**4.1** (B) (Figures 4-38 and 4-39) PEG5k-**4.1** (B) did not aggregate in plasma (Figure 4-31). The blood circulation properties of both batches of nanomaterials were similar. PEG5k-**4.1** (B) had a higher platinum concentration at 5 minutes

post-injection, but are within error of each other after 1 hour (Figure 4-38). It appears that plasma aggregation does not have a dramatic effect on the circulation time of PEG5k-**4.1**. However, much less spleen uptake was observed for PEG5k-**4.1** (B) at concentrations roughly equivalent to hepatic concentrations (Figure 4-39, red and blue). Kidney uptake of PEG5k-**4.1** (B) remained low.

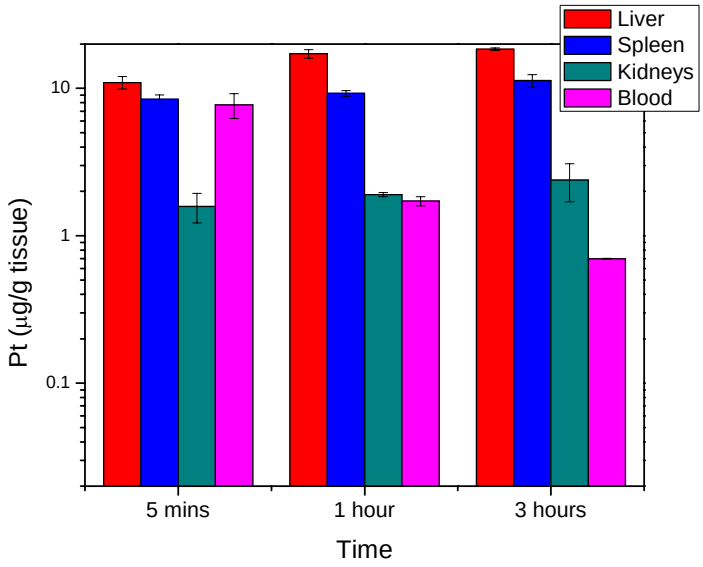

Figure 4-39: Platinum concentrations in liver (red), spleen (blue), kidneys (cyan), and blood (pink) after administration of PEG5k-**4.1** (B) to mice.

The biodistribution profile of PEG5k-**4.1** demonstrates some advantages over conventional cisplatin administration. First, PEG5k-**4.1** was able to accumulate in the tumor region to a much higher extent than normally observed with cisplatin. Nanoparticle incorporation also altered the platinum biodistribution profile. Cisplatin demonstrates high renal uptake, leading to dose limiting toxicity. PEG5k-**4.1** delivered little platinum to the kidneys, with the majority being cleared through hepatic pathways. This may present a more favorable toxicity profile than cisplatin and alleviate some of its side effects. The circulation time of PEG5k-**4.1** was fairly short, which may limit its *in vivo* efficacy. However, we feel

that the altered biodistribution and increased MTD of PEG5k-**4.1** gives it distinct advantages over cisplatin.

4.2.14 Chemotherapeutic Efficacy of PEG5k-4.1

PEG5k-**4.1** was also evaluated for its efficacy as a chemotherapeutic against mice bearing H460 xenografts (Figure 4-40). Mice were administered saline control (black), cisplatin (4mg/kg, red) or PEG5k-**4.1** (4mg cisplatin/kg, blue) via i.v. injection on days 0, 4, and 8. Tumor growth was monitored daily and the study concluded when the mice reached the maximum allowed size. Mice receiving saline control demonstrated rapid tumor growth, reaching the maximum allowed size 15 days after the start of the study. PEG5k-**4.1** both demonstrated significant tumor growth inhibition, limiting the tumor size to approximately 40% of the untreated control mice. Cisplatin was slightly more effective, limiting tumor growth to 30% of the untreated control. The two platinum treatment arms were within error of each other. Mouse weights remained unchanged as a result of platinum treatment (Figure 4-41). However, PEG5k-**4.1** can be administered at a higher dose than cisplatin, we should be able to achieve superior tumor growth inhibition than cisplatin in xenograft models. Additional tumor growth inhibition with higher doses of PEG5k-**4.1** are being planned in order to assess its true chemotherapeutic efficacy.

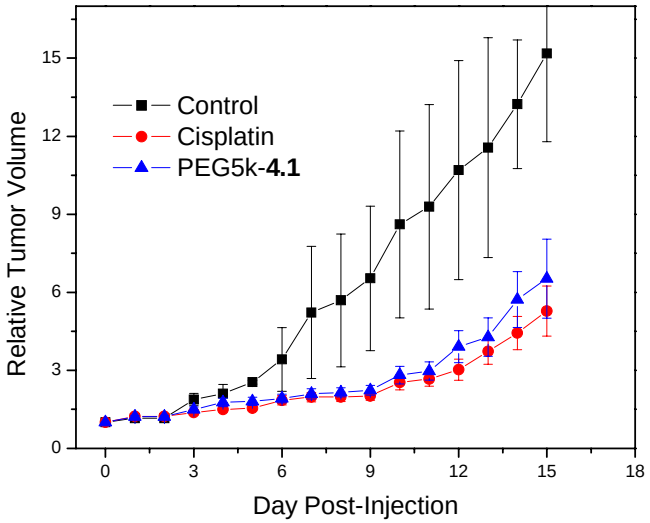

Figure 4-40: Chemotherapeutic efficacy study in mice with H460 s.c. xenografts receiving either saline control (black), cisplatin (red, 4mg/kg) or PEG5k-**4.1** (blue, 4 mg/kg cisplatin) on days 0, 4 and 8.

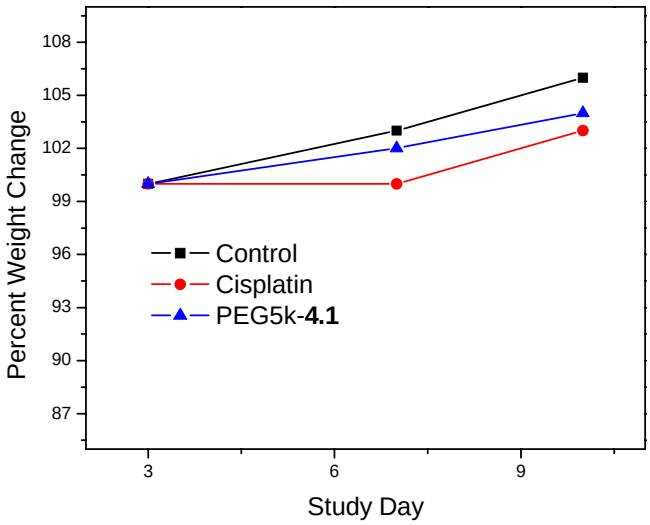

Figure 4-41: Body weight changes in mice with H460 s.c. xenografts receiving either saline control (black), cisplatin (red) or PEG5k-**4.1** (blue).

4.2.15 Lung Cancer Chemoradiotherapy with PEG5k-4.1

Chemoradiotherapy, the concurrent administration of chemotherapy and radiotherapy, has emerged as an additional option to traditional chemotherapy. Chemoradiotherapy is the standard of care for many difficult to treat solid cancers, including brain, head and neck, esophageal, gastric, pancreatic, lung, rectal, anal, and cervical cancers.[6, 50-53] Chemoradiotherapy has shown consistently improved local tumor control and rates of cancer cure compared to either sequential treatment or sole administration of chemotherapy or radiotherapy. Chemoradiotherapy is, however, not without limitations; the concurrent use of both chemotherapy and radiotherapy has significantly higher toxicities when compared to either treatment alone or sequential use. [54-55] The higher toxicity profile of chemoradiotherapy limits the administered dose and restricts the patients who are eligible for treatment. Furthermore, patients who receive chemoradiotherapy often cannot tolerate further treatment, limiting the cure of their disease. Cancer treatment by either chemotherapy or chemoradiotherapy can be improved by delivering the chemotherapeutic selectively to the tumor region, while minimizing drug exposure to healthy tissue.

PEG5k-**4.1** was evaluated in vivo as a chemoradiotherapy agent. Nanotherapeutics have received a lot of attention as chemotherapeutic or imaging contrast agents,[56-57] but have received scant attention as chemoradiotherapeutics[49, 58-62] even though nanotherapeutics possess many properties that make them ideally suitable for chemoradiotherapy. PEG5k-**4.1** was evaluated as a chemradiotherapy agent *in vivo* against mice bearing either A549 (Figure 4-42) or H460 (Figure 4-43) lung cancer xenografts. Mice received either no treatment, 10 Gy radiation, cisplatin (1 mg/kg) 6 hours prior to 10 Gy radiation, or PEG5k-**4.1** (1 mg

cisplatin/kg) 6 hours prior to 10 Gy radiation. For the A549 xenograft (Figure 4-42), all treatment groups gave statistically significant tumor growth inhibition compared to the untreated control (Table 4-7). Cisplatin did not show any significant effects ($\alpha \leq 0.05$) over radiation alone over the course of the study, while PEG5k-**4.1** demonstrated a significant ($\alpha \leq 0.05$) increase in efficacy over radiation alone from day 8 onwards and a significant increase over cisplatin at day 22. The endpoint time (5x tumor volume increase for 1 mouse in group) was extended from 22 days for radiation only and for cisplatin plus radiation to 30 days for PEG5k-**4.1** plus radiation. For the H460 xenograft (Figure 4-43), all treatment groups showed significant tumor growth inhibition compared to the control (Table 4-8). Cisplatin demonstrated insignificant chemoradiosensitization effects over the course of the study. PEG5k-**4.1** demonstrated statistically significant ($\alpha \leq 0.05$) increases in tumor growth inhibition over radiation alone over the entire study period and over cisplatin from days 4-8 and 14-16 (Table 4-8). These results suggest that PEG5k-**4.1** is a highly potent chemoradiotherapy agent for lung cancer treatment.

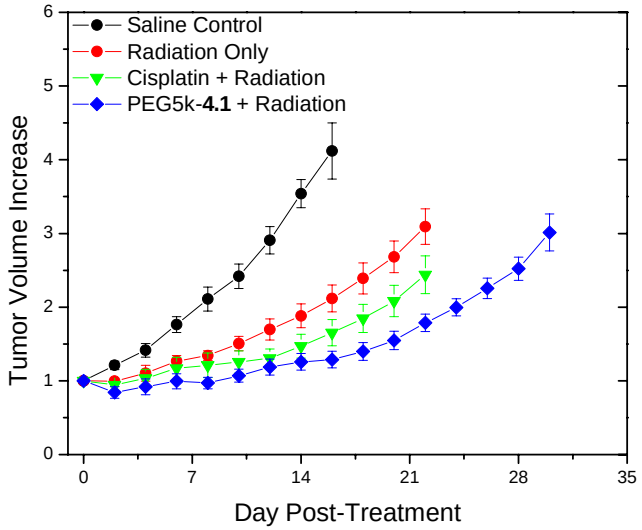

Figure 4-42: Chemoradiotherapy efficacy assay against mice bearing A549 lung cancer xenografts. Mice received either saline control (black), 10 Gy radiation (red), cisplatin (1mg/kg) 6 hours prior to 10 Gy radiation (green) or PEG5k-**4.1** (1mg cisplatin/kg) 6 hours prior to radiation (blue).

Table 4-7: Comparison of α values of different treatment arms of A549 chemoradiotherapy efficacy study by students t-test.

Comparison	Day 6	Day 8	Day 10	Day 12	Day 14	Day 16	Day 18	Day 20	Day 22
XRT vs Control	0.00331	0.002484							
XRT vs Cisplatin	0.576	0.486	0.190	0.064	0.097	0.094	.080	0.071	0.087
XRT vs PEG5k-**4.1**	0.059	0.0036	0.0059	0.015	0.0093	0.0031	0.0025	0.0012	.0010
Cisplatin vs PEG5k-**4.1**	0.353	0.2235	0.315	0.491	0.302	0.116	0.077	0.055	0.0471

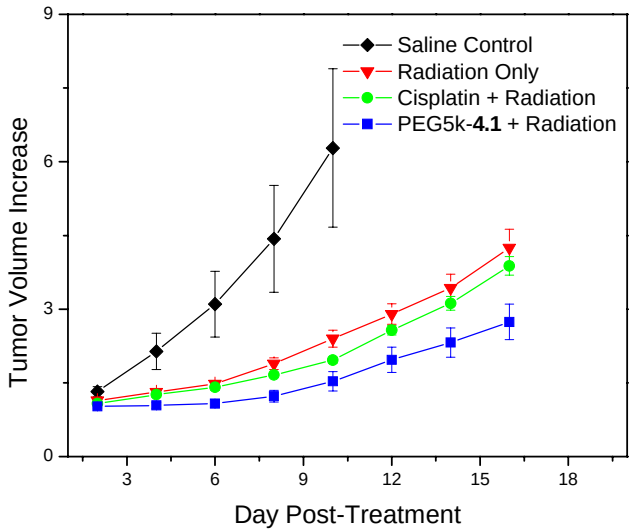

Figure 4-43: Chemoradiotherapy efficacy assay against mice bearing H460 lung cancer xenografts. Mice received either saline control (black), 10 Gy radiation (red), cisplatin (1mg/kg) 6 hours prior to 10 Gy radiation (green) or PEG5k-**4.1** (1mg cisplatin/kg) 6 hours prior to radiation (blue).

Table 4-8: Comparison of α values of different treatment arms of H460 chemoradiotherapy efficacy study by students t-test.

Comparison	Day 4	Day 6	Day 8	Day 10	Day 12	Day 14	Day 16
XRT vs Control	0.064	0.052	0.059	0.060			
XRT vs Cisplatin	0.519	0.437	0.113	0.039	0.189	0.336	0.419
XRT vs PEG5k-**4.1**	0.0052	0. 0015	0.0024	0.0060	0.0165	0.0194	0.0161
PEG5k-**4.1** vs cisplatin	0.0165	0.0051	0.0119	0.0784	0.0630	0.0419	0.0210

4.3 Conclusions

A new type of polysilsesquioxane nanoparticle containing cisplatin, **4.**1, was synthesized. As-synthesized **4.1** was 64 nm in diameter by electron microscopy, but showed hydrogel-like behavior in aqueous solution, swelling to 134 nm in diameter under physiological conditions. **4.1** had an exceptionally high drug loading of 42 wt% cisplatin and

drug release can be triggered by endogenous reducing agents. Abundant surface carboxylic acid groups on **4.1** allowed for the post-synthetic modification with cancer targeting peptides (cRGD) or passivating polymers (PEG). *In vitro* efficacy of **4.1** and RGD-**4.1** was evaluated against 3 different cancer cell lines. **4.1** possessed comparable cytotoxicity as cisplatin against all three cell lines, with RGD targeting providing an increase in efficacy in $\alpha_v\beta_3$ overexpressing cell lines.

PEG chains of varying lengths (MW= 2000 or 5000) could be conjugated to **4.1** through amide coupling reaction and a targeted, pegylated nanoparticle could be synthesized by adding a fraction of anisamide PEG2k to the pegylation reaction. PEG2k-**4.1** and APEG2k-**4.1** demonstrated comparable *in vitro* efficacy as cisplatin, with APEG2k-**4.1** increasing efficacy in the sigma-receptor over-expressing H460 cell line. Initial *in vivo* evaluations of PEG2k-**4.1** and PEG5k-**4.1** were performed in a lung cancer xenograft model. All platinum treatment modalities demonstrated nearly identical tumor growth inhibition. *Ex vivo* tumor histology demonstrated that the nanoparticle treatment groups were highly effective, creating large regions of necrotic tissue in the center of the tumor. However, mice in all three platinum treatment arms showed toxicity-related death, so the treatments might have been too aggressive. The MTD of PEG2k-**4.1** was less than 4mg/kg, a value well below that of cisplatin and PEG2k-**4.1** was revealed to cause a significant amount of liver damage by histology.

PEG5k-**4.1** was developed to improve the *in vivo* performance of **4.1**. PEG5k-**4.1** was much better tolerated in mice with a MTD of at least 20 mg/kg. Liver toxicity was greatly diminished in PEG5k-**4.1** with splenic damage observed at the highest doses. Biodistribution studies revealed that PEG5k-**4.1** had very high tumor uptake, approximately 10 times what is

typically observed with cisplatin. Renal platinum uptake was greatly diminished, with PEG5k-**4.1** primarily removed by the liver and the spleen. PEG5k-**4.1** was evaluated as a chemotherapy and chemoradiotherapy agent *in vivo*. As a chemotherapy agent, PEG5k-**4.1** demonstrated similar tumor growth inhibition as cisplatin; but future studies can utilize the fact that PEG5k-**4.1** can be administered at a higher dose than cisplatin to achieve superior tumor growth inhibition. PEG5k-**4.1** was evaluated as a chemoradiotherapy agent in two lung cancer xenograft models. The nanoparticles had statistically significant radiosensitization effects, while cisplatin provided no statistically significant effects. Nanoparticles **4.1** show considerable promise in the treatment of lung cancer by various modalities, but more systemic *in vivo* evaluations must be performed to elucidate the clinical potential of this novel nanotherapeutic.

4.4 Materials and Methods

4.4.1 General Materials and Methods

All chemicals were purchased from Fisher or Aldrich and used without further purification unless noted. Cisplatin was purchased from AK scientific. Tetrahydrofuran was dried by the sodium metal/benzophenone method. Dimethylformamide was dried by activated alumina. Thermogravimetric analysis was performed using a Shimadzu TGA-50 equipped with a platinum pan and heated at 3°C per minute in air. A JEM 100CX-2 transmission electron microscope (TEM) and a Hitachi S-4700 scanning electron microscope (SEM) were used to determine particle size and morphology. TEM and SEM samples were prepared from ethanolic suspensions of the nanoparticles dropped onto amorphous carbon coated copper grids. The solvent was then allowed to evaporate. Dynamic light scattering (DLS) and zeta

potential measurements were made using a Malvern Instruments Zetasizer Nano. Inductively-Coupled Plasma Mass Spectrometry (ICP-MS) measurements were made using a Varian 820-MS Inductively-Coupled Plasma Mass Spectrometer. ICP-MS samples were prepared by digesting a known amount of sample in concentrated nitric acid overnight, and then diluted with water to 2% nitric acid by volume.

4.4.2 Synthesis of Platinum Compounds

Synthesis of all platinum compounds was as previously described in chapter 3 of this dissertation.

4.4.3 Synthesis of Polyethylene Glycol (PEG) derivatives

Synthesis of amino-polyethylene glycol (MW= 2000) monomethyl ether

Methoxy-PEG_{2000}-amine was synthesized as described in Chapter 2.

Synthesis of anisamide-PEG_{2000}-NH_2

Anisamide-PEG_{2000}-NH_2 was synthesized as described in Chapter 2.

Synthesis of amino-polyethylene glycol (MW= 5000) monomethyl ether

Amino-Polyethylenegylcol (MW=5000) monomethyl ether was synthesized through a modification of an established protocol.[33] Polyethylene glycol (MW=5000) monomethylether (30g) was dried under vacuum at 90°C overnight to remove moisture. Anhydrous tetrahydrofuran (360 mL) was added with 3.6 mL (46.5 mmol) of methanesulfonyl chloride. The solution was cooled to 0°C on an ice bath and 6.9 mL tryethylamine dissolved in 60mL THF was added dropwise. The resulting solution was

stirred under nitrogen from 0°C to room temperature overnight. Water (150 mL) was added and the solution was cooled back to 0°. A sodium bicarbonate solution (1M, 15mL) and sodium azide (3.9g, 60mmol) were added. The THF was removed by rotary evaporation and the remaining aqueous solution was refluxed for 24 hours. PEG-azide was extracted with dichloromethane (4x100 mL). The organic layers were collected, concentrated, and extracted with brine. The organic solution was then dried with magnesium sulfate, filtered and then the dichloromethane was removed by rotary evaporation. (21.2g, 70% yield) ^{1}H NMR ($CDCl_3$) δ 2.93(2H), 3.33 (3H), 3.42 (3H), 3.50 (4H), 3.53-3.75(410H), 3.77 (4H). The monomethyl PEG-azide complex (6.083g) was heated to 80°C before being dissolved into 115mL THF and triphenylphosphine (3.174 g, 12.1mmol) was added. The solution was stirred at room temperature for 12 hours. Water (9.1mL) was then added and the solution was stirred for 18 hours. The THF solvent was removed by rotary evaporation and the residue was redissolved in water (150mL), precipitating triphenylphosphine oxide. The triphenylphosphine byproducts were removed by filtration and the water removed by rotary evaporation. (3.95g, 65% yield).

4.4.4 Nanoparticle 4.1 Synthesis

Sixty milligrams of DSCPSi ($6.36X10^{-5}$ mol) were dissolved into 3 mL 33% ammonium hydroxide, 4.5 mL water and 6 mL of ethanol. The yellow solution was stirred vigorously at room temperature for 1 hour, yielding a bluish white suspension. The suspension was loaded onto an amberlite IRC-50 cation exchange column and the nanoparticles were eluted using water. The nanoparticle containing fractions were loaded into a 3500 MW cutoff dialysis bag and dialyzed against 500mL water for 3 hours, changing water hourly. **4.1** was concentrated by centrifugation, washed with ethanol once and stored as an ethanolic suspension.

4.4.5 Platinum Release Assays

Four hundred milliliters of 2mM HEPES buffer (pH=7.4) was placed in a 2-neck round bottom flask, sparged with nitrogen gas and prewarmed to 37 °C. Two milligrams of **4.1** (1.84 μmol Pt) was suspended into 2mL of the buffer solution. The nanoparticle suspension was then added to the large buffer sink and the system was incubated at 37°C under N_2 blanket. Periodically, 1.2mL aliquots of the solution were removed. After 1 day of incubation, a solution of L-cysteine in 2mM HEPES buffer was added to make the total reducing agent concentration either 5mM or 15 μM. The resulting system was incubated at 37°C, with 1.2 mL aliquots periodically removed. The removed aliquots were processed by filtering the suspensions through a Costar Spin-X centrifuge tube filter (0.22 μm cellulose acetate). The filtrate was collected and analyzed by ICP-MS.

4.4.6 Nanoparticle Surface Modification

*Conjugation of cRGDfK to **4.1** (RGD-**4.1**)*: The cRGDfK peptide was conjugated to the surface of **4.1** through surface carboxylate groups. Briefly, 3 mg of **4.1** was redispersed into 2 mL of a freshly prepared solution of 25 mM EDC and 25 mM NHS (EDC= 1-ethyl-3-(3-dimethylaminopropyl)carbodiimide, NHS= N-hydroxysuccinimide). The suspension was heated at 50°C for 2 hours to form the NHS ester, then the suspension was cooled to room temperature. cRGDfK (0.5 mg, 0.8 μmol) was then added to the suspension and the suspension was stirred overnight at room temperature to form RGD-**4.1**. RGD-**4.1** was isolated by centrifugation and washed with water 1x and ethanol 2x. RGD-**4.1** was stored as an ethanolic suspension.

*Conjugation of PEG (MW: 2000) amine to **4.1** (PEG2k-**4.1**):* Nine milligrams of **4.1** were redispersed into 4mL of DMF (2.25 mg/mL). EDC (36 mg, $1.87x10^{-4}$ mol) and amino-poly(ethylene)glycol monomethyl ether (MW=2000)(86 mg, $4.3x10^{-5}$ mol) were dissolved into the suspension. The suspension was vigorously stirred, covered, at room temperature overnight. An equal volume of ethanol was added to dilute the suspension and PEG2k-**4.1** was isolated by centrifugation. PEG2k-**4.1** was washed with ethanol 3x and stored as an ethanolic suspension.

*Conjugation of Anisamide-PEG (MW: 2000) to **4.1** (APEG2k-**4.1**):* Anisamide-targeted **4.1** (APEG2k-**4.1**) was synthesized by the same procedure as PEG2k-**4.1**, except that a fraction, typically 10 wt% of anisamide-PEG_{2000}-NH_2 was added to the PEG feed.

*Conjugation of PEG (MW: 5000) amine to **4.1** (PEG5k-**4.1**):* **4.1** was pegylated through the surface carboxylic acids. **4.1** (15mg) was suspended into acetonitrile (15 mL). To the **4.1** suspension, aminopolyethylene glycol monomethyl ether (MW=5000, 75mg), triethylamine (37.5 μL) and HBTU (45mg) were added. The suspension was stirred at room temperature for 24 hours before the nanoparticles were isolated by centrifugation and washed with acetonitrile twice and ethanol once. PEG5k-**4.1** was stored as an ethanolic suspension.

4.4.7 Colloidal Stability in Biological Media

Bovine Serum Albumin nonspecific binding: In order to determine the ability of the synthesized nanoparticles to resist plasma protein absorption, we performed colloidal stability tests in the presence of BSA. Various forms of **4.1** were dispersed into a 5mM PBS solution at 0.5 mg NP/mL. The nanoparticle size was measured by dynamic light scattering. BSA (2.5 mg, 5x weight) was then dissolved into the nanoparticle suspension. DLS

measurements were obtained every 10 minutes for 3 hours to size the suspension. Differences in the Z_{avg} and count rate of the solution were used to determine extent of protein binding and sedimentation.

Rat Plasma stability: Colloidal stability in rat plasma was also determined by DLS. Various forms of **4.1** (0.45 mg) were dispersed into 1mL rat plasma (Innovative Research, Novi, MI). DLS measurements were taken every 10 minutes for 2 hours. Changes in intensity weighted size distributions and count rate were used to determine the colloidal stability.

4.4.8 *In vitro assays*

General: NCI-H460 human large cell lung carcinoma (ATCC# HTB-177), A549 human lung carcinoma cells (ATCC# CCL-185) and PC-3 human prostate adenocarcinoma cells (ATCC# CRL-1435) were all purchased from the Tissue Culture Facility of the Lineberger Comprehensive Cancer Center. All cells were maintained at 37°C with 5% CO_2. Cisplatin was purchased from AK Scientific and stored in PBS. All nanoparticle suspensions were freshly made from sterile PBS. NCI-H460 cells were cultured in RPMI-1640 medium (Gibco) supplemented with 10% FBS (Mediatech) and 2% Penicillin- Steptomycin solution (Mediatech). PC-3 cells were cultured in Ham's F-12 media (Gibco) supplemented with 10% FBS (Mediatech) and 2% Penicillin- Streptomycin solution (Mediatech). A549 cells were cultured in MEM (Gibco) supplemented with 10% FBS (Mediatech) and 2% Penicillin-Streptomycin solution (Mediatech)

Cell Viability Assay: NCI-H460 cells: NCI-H460 cells were plated in 6 well plates at a concentration of 300,000 cells/well and incubated in 3 mL media for 12 hours to promote cell attachment. The plates were then washed once with 2mL PBS and subsequently given 2 mL

media containing varying drug concentrations. The plates were incubated at 37°C for 48 hours and cell viability was determined by the trypan blue dye exclusion method.

Cell Viability Assay: A549 Cells: Confluent A549 cells were trypsinized and counted via a hematocytometer. Cells were plated into 6-well plates at a cell density of 1.0×10^5 cells/well and 3 mL total volume (RPMI-1640 complete growth medium). The cells were incubated overnight at 37°C and 5% CO_2. Media was removed from the wells and aliquots of free drug (or particles) and media (5% phosphate buffered saline, PBS) were added to each well to ensure final drug concentrations of 0, 0.25, 0.5, 1, 2.5, and 5 μM. The plates were incubated (37°C, 5% CO_2) for 72 hours with a media switch being done on the second day. Each well was washed with 2 mL PBS, trypsinized, and cell viability determined by the trypan blue exclusion assay.

Confluent A549 cells were trypsinized and counted via a hematocytometer. Cells were plated into 6-well plates at a cell density of 1.0×10^5 cells/well and 3 mL total volume (RPMI-1640 complete growth medium). The cells were incubated overnight at 37°C and 5% CO_2. Media was removed from the wells and aliquots of free drug (or particles) and media (5% phosphate buffered saline, PBS) were added to each well. The plates were incubated (37°C, 5% CO_2) for three days. Each well was washed with 2 mL PBS, trypsinized, and cell viability determined by the trypan blue exclusion assay.

Cell Viability Assay: PC-3 Cells: PC-3 cells were plated in 6 well plates at a concentration of 300,000 cells/well and incubated in 3 mL media for 12 hours to promote cell attachment. The plates were then washed once with 2mL PBS and subsequently given 2 mL media

containing varying drug concentrations. The plates were incubated at 37°C for 48 hours and cell viability was determined by the trypan blue dye exclusion method.

4.4.9: *In vivo assays*

General: Mice (male nu/nu, 4-6 weeks old) were purchased from the animal colony at the UNC Lineberger cancer center unless noted. Mice were housed in an AALAC accredited facility in sterile housing at UNC Chapel Hill. All animal work was approved and monitored by The University of North Carolina at Chapel Hill Animal Care and Use Committee.

Maximum Tolerated Dose: Maximum tolerated dose (MTD), defined as the highest possible dose resulting in no animal deaths and less than 20% weight loss was evaluated for PEG2k-**4.1** and PEG5k-**4.1**. Non-tumor bearing mice (nu/nu) were injected with varying amounts of PEG-cis-PSQ in PBS by tail vein injection. The mice were weighed and observed daily for any change in physical activity. Weight loss greater than 20% and/or lethargy were interpreted as signs of toxicity and the mice were euthanized immediately.

Biodistribution Studies-H460 Tumor Bearing Mice: NCI-460 cells were inoculated in the right flank of nu/nu mice at 500,000 cells/ mouse (200 µL of cell media). Tumors were allowed to grow until each was between 100-200 mg. PEG5k-**4.1** was injected at 4mg cisplatin/kg (80µL saline) via the tail vein. Mice were euthanized 5 minutes, 1 hour, and 24 hours post-injection (2-3 mice per time point). The tumor, liver, spleen, intestines, lungs, kidney, and heart were removed. All organs were flash-frozen and stored at -20°C. Blood was removed by cardiac puncture prior to euthanasia and stored in EDTA-treated tubes. All blood samples were stored at 4°C prior to analysis. Tissues were weighed prior to digestion in concentrated nitric acid overnight. Digestate (150 µL) was placed in a vial and diluted to

4mL total volume with water. The solution was then filtered used a 0.45 μm PTFE filter to remove undissolved species. Platinum concentrations was determined by ICP-MS.

Biodistribution Studies-non-Tumor Bearing Mice: Studies were performed as above, except with non-tumor bearing nu/nu mice.

In vivo efficacy: H460 Xenograft Study 1: Athymic nude mice were purchased from Jackson Laboratories. Mice were cared for according to an approved protocol by the institutional animal care and use committee at the University of North Carolina. H460 cells were suspended in a 50% matrigel (BD Biosciences) and 50% RPMI-1640 media at 5 million cells/mL. Mice were injected subcutaneosusly in the right flank with 200 μL of the cell suspension (1 million cells). Tumor growth was measured daily and treatment commenced when tumors were measurable in each flank. Mice were divided randomly into 4 groups (4-5 mice/group) and received either control (PBS), cisplatin (4mg/kg), Peg2k-**4.1** (4mg cisplatin/kg), or APEG2k-**4.1** (4mg cisplatin/kg). All injections were administered through the tail vein with 100 μL total injection volume. Mice received treatments on days 0, 2, and 4. Tumor growth was measured daily until the mice reached the maximum allowed tumor size. Tumor volume was calculated by the formula (axbxc)/2, where a, b, and c are the three tumor dimensions. Mice weights were recorded weekly. The mice were euthanized by CO_2 inhalation followed by cervical dislocation and the tumors were removed and stored in formalin.

In vivo efficacy: H460 Xenograft Study 2: Anthymic nude mice (male 4-6 weeks old) were obtained from the Lineberger Cancer Center colony. All animal care was done in accordance with an approved protocol by UNC Institutional Animal Care and Use Committee. NCI-

H460 cells (5 million cells) were suspended in a 1:1 media:matrigel mixture and implanted subcutaneously in the right flank of each mouse (200 μL total volume). Tumor size was measured daily and the study commenced when tumors were palpable (2-4 days after tumor implantation). Mice were divided randomly into 3groups (9 mice per group) and received either saline control, cisplatin (4mg/kg), or PEG5k-**4.1** (4mg cisplatin/kg). All injections were performed on days 0, 4, and 8 through the tail vein (100 μL) total volume. Tumors were measured daily until the mice reached the maximum allowed tumor size. Tumor volume was calculated by the formula (axbxc)/2, where a, b, and c are the three tumor dimensions. Mice weights were recorded weekly. The mice were euthanized by CO_2 inhalation followed by cervical dislocation. The tumors were removed and stored in formalin.

In vivo efficacy: Chemoradiotherapy: A549 or H460 cells ($1x10^6$ cells in 200 μL 1:1RPMI-1640 and matrigel) were subcutaneously in the upper dorsal region of 6-8 week-old Nu/Nu mice. Twelve days after inoculation, the mice were randomly distributed into different groups for subsequent treatment (NP cisplatin, free cisplatin, XRT Only, and control). NP cisplatin or free cisplatin in water was tail vein i.v. injected at a dose of 1mg/Kg. Six hours post injection, the tumors were subjected to a dose of 10 Gy with XRAD 320. Mice were shielded with a lead shield allowing radiation of the tumor site and minimal radiation to other organs. Tumor volumes were calculated by measuring two perpendicular diameters with a caliper and using the formula of $V=0.5 \times a \times b^2$, where 'a' and 'b' are the larger and smaller diameters, respectively. The tumor volumes are measured every 2 days, and the relative percent change in tumor volume was calculated using the relation $100^* (V_i-V_o)/V_{o,}$ where V_i is the volume calculated and V_o is the initial volume on day 1.

Tissue Histology: All evaluated organs were received in a neutral buffered formalin (10%) solution. Organs were placed in labeled cassettes and flushed with water for 20 minutes. The cassettes were stored in a 70% ethanol solution and were processed (placed in paraffin, sectioned, H&E stained, and mounted) at the UNC Lineberger Cancer Center Animal Histopathology Core Laboratory. Stained organs were images at the UNC Microscopy Services Laboratory using an Olympus BX61 Upright Fluorescence Microscope equipped with Improvision's Volocity software. Images were captured using a QImaging RETIGA 4000R color camera.

4.5 References

1. Della Rocca, J.; Huxford, R. C.; Comstock-Duggan, E.; Lin, W., Polysilsesquioxane Nanoparticles for Targeted Platin-Based Chemotherapy by Triggered Release. *Angew. Chem. Int. Ed.* **2011,** *50* (44), 10330-10334.

2. Hu, L.-C.; Shea, K. J., Organo-silica hybrid functional nanomaterials: how do organic bridging groups and silsesquioxane moieties work hand-in-hand? *Chem. Soc. Rev.* **2011,** *40* (2), 688-695.

3. Shea, K. J.; Loy, D. A., Bridged Polysilsesquioxanes. Molecular-Engineered Hybrid Organic−Inorganic Materials. *Chem. Mater.* **2001,** *13* (10), 3306-3319.

4. Kelland, L., The resurgance of platinum-based cancer chemotherapy. *Nat. Rev. Cancer* **2007,** *7* (8), 573-584.

5. Wheate, N. J.; Walker, S.; Craig, G. E.; Oun, R., The status of platinum anticancer drugs in the clinic and clinical trials. *Dalton Trans.* **2010,** *39* (35), 8113-8127.

6. Chandana, S. R.; Conley, B. A., Neoadjuvant chemotherapy for locally advanced squamous cancers of the head and neck: current status and future prospects. *Curr. Opin. Oncol.* **2009,** *21* (3), 218-223.

7. Baas, P.; Belderbos, J. S. A.; van den Heuvel, M., Chemoradiation therapy in nonsmall cell lung cancer. *Curr. Opin. Oncol.* **2011,** *23* (2), 140-149.

8. Lim, F.; Glynne-Jones, R., Chemotherapy/chemoradiation in anal cancer: A systematic review. *Cancer Treat. Rev.* **2011,** *37* (7), 520-532.

9. Staal, E.; Aleman, B. M. P.; Boot, H.; van Velthuysen, M. L. F.; van Tinteren, H.; van Sandick, J. W., Systematic review of the benefits and risks of neoadjuvant chemoradiation for oesophageal cancer. *Br. J. Surg.* **2010,** *97* (10), 1482-1496.

10. Galanski, M.; Jakupec, M. A.; Keppler, B. K., Update of the preclinical situation of anticancer platinum complexes: Novel design strategies and innovative analytical approaches. *Curr. Med. Chem.* **2005,** *12* (18), 2075-2094.

11. Wang, D.; Lippard, S. J., Cellular Processing of Platinum Anticancer Drugs. *Nat. Rev. Drug Discovery* **2005,** *4* (5), 308-320.

12. van Blaaderen, A.; Vrij, A., Synthesis and Characterization of Colloidal Model Particles Made from Organoalkoxysilanes. In *Colloidal Silica: Fundamentals and Applications*, Bergna, H. E.; Roberts, W. O., Eds. Taylor and Francis Group, LLC: Boca Raton, FL., 2006; pp 65-80.

13. Stöber, W.; Fink, A.; Bohn, E., Controlled growth of monodisperse silica spheres in the micron size range. *J. Colloid Interface Sci.* **1968,** *26* (1), 62-69.

14. Avgoustakis, K.; Beletsi, A.; Panagi, Z.; Klepetsanis, P.; Karydas, A. G.; Ithakissios, D. S., PLGA-mPEG nanoparticles of cisplatin: in vitro nanoparticle degradation, in vitro drug release and in vivo drug residence in blood properties. *J. Controlled Release* **2002,** *79* (1-3), 123-135.

15. Burger, K. N. J.; Staffhorst, W. H. M.; de Viglder, H. C.; Velinova, M. J.; Bomans, P. H.; Frederik, P. M.; de Kruijff, B., Nanocapsules: Lipid-coated aggregates of cisplatin with high cytotoxicity. *Nat. Med.* **2002,** *8* (1), 81-84.

16. Feazell, R. P.; Nakayama-Ratchford, N.; Dai, H.; Lippard, S. J., Soluble single-walled carbon nanotubes as longboat delivery systems for Platinum(IV) anticancer drug design. *J. Am. Chem. Soc.* **2007,** *129* (27), 8438-8439.

17. Nishiyama, N.; Okazaki, S.; Cabral, H.; Miyamoto, M.; Kato, Y.; Sugiyama, Y.; Nishio, K.; Matsumura, Y.; Kataoka, K., Novel cisplatin incorporated polymeric micelles can eradicate solid tumors in mice. *Cancer Res.* **2003,** *63* (12), 8977-8983.

18. Rieter, W. J.; Pott, K. M.; Taylor, K. M. L.; Lin, W., Nanoscale Coordination Polymers for Platinum-based Anticancer Drug Delivery. *J. Am. Chem. Soc.* **2008,** *130* (35), 11584-11585.

19. Dhar, S.; Kolishetti, N.; Lippard, S. J.; Farokhzad, O. C., Targeted delivery of a cisplatin prodrug for safer and more effective prostate cancer therapy in vivo. *Proc. Natl. Acad. Sci. U.S.A.* **2011,** *108* (5), 1850-1855.

20. Dhar, S.; Liu, Z.; Thomale, J.; Dai, H. J.; Lippard, S. J., Targeted single-wall carbon nanotube-mediated Pt(IV) prodrug delivery using folate as a homing device. *J. Am. Chem. Soc.* **2008,** *130* (34), 11467-11476.

21. Taylor-Pashow, K. M. L.; Della Rocca, J.; Xie, Z.; Tran, S.; Lin, W., Post-synthethic Modifications of Iron-Carboxylate Nanoscale Metal Organic Frameworks for Imaging and Drug Delivery. *J. Am. Chem. Soc.* **2009,** *131* (40), 14261-14263.

22. Temming, K.; Schiffelers, R. M.; Molema, G.; Kok, R. J., RGD-based strategies for selective delivery of therapuetics and imaging agents to the tumor vasculature. *Drug Resist. Updates* **2005,** *8*, 381-402.

23. Zhou, Y.; Kim, Y. S.; Chakraborty, S.; Shi, J. Y.; Gao, H. J.; Liu, S., (99m)Tc-Labeled Cyclic RGD Peptides for Noninvasive Monitoring of Tumor Integrin alpha(v)beta(3) Expression. *Mol. Imaging* **2011,** *10* (5), 386-397.

24. Reungwetwattana, T.; Eadens, M. J.; Molina, J. R., Chemotherapy for Non-Small-Cell Lung Carcinoma: From a Blanket Approach to Individual Therapy. *Semin Respir Crit Care Med* **2011,** *32* (01), 078,093.

25. Boulikas, T.; Vougiouka, M., Recent clinical trials using cisplatin, carboplatin, and their combination chemotherapy drugs. *Oncol. Rep.* **2004,** *11* (3), 559-595.

26. Ye, Y. P.; Bloch, S.; Xu, B. G.; Achilefu, S., Design, synthesis, and evaluation of near infrared fluorescent multimeric RGD peptides for targeting tumors. *J. Med. Chem.* **2006,** *49* (7), 2268-2275.

27. Albert, J. M.; Cao, C.; Geng, L.; Leavitt, L.; Hallahan, D. E.; Lu, B., Integrin αvβ3 Antagonist Cilengitide Enhances Efficacy of Radiotherapy in Endothelial Cell and Non-Small-Cell Lung Cancer Models. *Int. J. Radiation Oncology Biol. Phys.* **2006,** *65* (5), 1536-1543.

28. Liu, Z.; Li, Z. B.; Cao, Q.; Liu, S.; Wang, F.; Chen, X., Small animal PET of tumors with ^{64}Cu-Labeled RGD-Bombesin Heterodimer. *J. Nucl. Med.* **2009,** *50* (7), 1168-1177.

29. Alexis, F.; Pridgen, E.; Molnar, L. K.; Farokhzad, O. C., Factors Affecting the Clearance and Biodistribution of Polymeric Nanoparticles. *Mol. Pharmaceutics* **2008,** *5* (4), 505-515.

30. Li, S.-D.; Huang, L., Pharmacokinetics and Biodistribution of Nanoparticles. *Mol. Pharmaceutics* **2008,** *5* (4), 496-504.

31. Owens III, D. E.; Peppas, N. A., Opsonization, biodistribution and pharmacokinetics of polymeric nanoparticles. *Int. J. Pharm.* **2006,** *307* (1), 93-102.

32. Jokerst, J. V.; Lobovkina, T.; Zare, R. N.; Gambhir, S. S., Nanoparticle PEGylation for imaging and therapy. *Nanomedicine (London)* **2011,** *6* (4), 715-728.

33. Kikkeri, R.; Lepenies, B.; Adibekian, A.; Laurino, P.; Seeberger, P. H., In Vitro Imaging and in Vivo Liver Targeting with Carbohydrate Capped Quantum Dots. *J. Am. Chem. Soc.* **2009,** *131* (6), 2110-2112.

34. Aydar, E.; Palmer, C. P.; Djamgoz, M. B. A., Sigma Receptors and Cancer. *Cancer Res.* **2004,** *64* (15), 5029-5035.

35. Banerjee, R.; Tyagi, P.; Li, S.; Huang, L., Anisamide-targeted stealth liposomes: A potent carrier for targeting doxorubicin to human prostate cancer cells. *Int. J. Cancer* **2004,** *112* (4), 693-700.

36. John, C. S.; Vilner, B. J.; Geyer, B. C.; Moody, T.; Bowen, W. D., Targeting Sigma Receptor-binding Benzamides as in Vivo Diagnostic and Therapeutic Agents for Human Prostate Tumors. *Cancer Res.* **1999,** *59* (18), 4578-4583.

37. Nakagawa, O.; Ming, X.; Huang, L.; Juliano, R. L., Targeted Intracellular Delivery of Antisense Oligonucleotides via Conjugation with Small-Molecule Ligands. *J. Am. Chem. Soc.* **2010,** *132* (26), 8848-8849.

38. Vilner, B. J.; John, C. S.; Bowen, W. D., Sigma-1 and Sigma-2 Receptors Are Expressed in a Wide Variety of Human and Rodent Tumor Cell Lines. *Cancer Res.* **1995,** *55* (2), 408-413.

39. Wang, A. Z.; Gu, F.; Zhang, L.; Chan, J. M.; Radovic-Moreno, A.; Shaikh, M. R.; Farokhzad, O. C., Biofunctionalized targeted nanoparticles for therapeutic applications. *Expert Opin. Biol. Ther.* **2008,** *8* (8), 1063-1070.

40. Farokhzad, O. C.; Jon, S.; Khademhosseini, A.; Tran, T.-N. T.; LaVan, D. A.; Langer, R., Nanoparticle-Aptamer Bioconjugates. *Cancer Res.* **2004,** *64* (21), 7668-7672.

41. Chen, Y. C.; Sen, J.; Bathula, S. R.; Yang, Q.; Fittipaldi, R.; Huang, L., Novel Cationic Lipid That Delivers siRNA and Enhances Therapeutic Effect in Lung Cancer Cells. *Mol. Pharmaceutics* **2009,** *6* (3), 696-705.

42. Li, S. D.; Chen, Y. C.; Hackett, M. J.; Huang, L., Tumor-targeted delivery of siRNA by self-assembled nanoparticles. *Mol. Ther.* **2008,** *16* (1), 163-169.

43. Ullman-Cullere, M. H.; Foltz, C. J., Body Condition Scoring: A Rapid and Accurate Method for Assessing Health Status in Mice. *Lab. Anim. Sci.* **1999,** *49* (3), 319- 323.

44. Zamboni, W. C.; Gervais, A. C.; Egorin, M. J.; Schellens, J. H. M.; Hamburger, D. R.; Delauter, B. J.; Grim, A.; Zuhowski, E. G.; Joseph, E.; Pluim, D.; Potter, D. M.; Eiseman, J. L., Inter-and Intratumoral Disposition of Platinum in Solid Tumors after Administration of Cisplatin. *Clin. Cancer Res.* **2002,** *8* (9), 2992-2999.

45. Caron, W.; Clewell, H.; Dedrick, R.; Ramanathan, R.; Davis, W.; Yu, N.; Tonda, M.; Schellens, J.; Beijnen, J.; Zamboni, W., Allometric scaling of pegylated liposomal anticancer drugs. *J. Pharmacokinet. Pharmacodyn.* **2011,** *38* (5), 653-669.

46. Aggarwal, P.; Hall, J. B.; McLeland, C. B.; Dobrovoskaia, M. A.; McNeil, S. E., Nanoparticle Interaction with Plasma Proteins as it Relates to Particle Biodistribution, Biocompatibility, and Therapeutic Efficacy. *Adv. Drug Delivery Rev.* **2009,** *61* (6), 428-437.

47. Newman, M. S.; Colbern, G. T.; Working, P. K.; Engbers, C.; Amantea, M. A., Comparative pharmacokinetics, tissue distribution, and therapeutic effectiveness of cisplatin encapsulated in long-circulating, pegylated liposomes (SPI-077) in tumor bearing mice. *Cancer Chemother. Pharmacol.* **1999,** *43* (1), 1-7.

48. Staffhorst, W. H. M.; van der Born, K.; Erkelens, C. A. M.; Hamelers, I. H. L.; Peters, G. J.; Boven, E.; de Kroon, A. I. P. M., Antitumor activity and biodistribution of cisplatin

nanocapsules in nude mice bearing human ovarian carcinoma xenografts. *Anticancer Drugs* **2008,** *19* (7), 721-727.

49. Boulikas, T., Clinical overview on Lipoplatin™: a successful liposomal formulation of cisplatin. *Expert Opin. Investig. Drugs* **2009,** *18* (8), 1197-1218.

50. Brandsma, D.; Stalpers, L.; Taal, W.; Sminia, P.; van den Bent, M., Clinical features, mechanisms, and management of pseudoprogression in malignant gliomas. *Lancet Oncol.* **2008,** *9* (5), 453-461.

51. Ohe, Y., Chemoradiothreapy for Lung Cancer. *Expert Opin. Pharmacother.* **2005,** *6* (16), 2793-2804.

52. Seiwert, T. Y.; Salama, J. K.; Vokes, E. E., The concurrent chemoradiation paradigm: general principles. *Nat Clin Prac Oncol* **2007,** *4* (2), 86-100.

53. Willett, C. G.; Czito, B. G., Chemoradiotherapy in Gastrointestinal Malignancies. *Clin. Oncol.* **2009,** *21* (7), 543-556.

54. Cooper, J. S.; Pajak, T. F.; Forastiere, A. A.; Jacobs, J.; Campbell, B. H.; Saxman, S. B.; Kish, J. A.; Kim, H. E.; Cmelak, A. J.; Rotman, M.; Machtay, M.; Ensley, J. F.; Chao, K. S. C.; Schultz, C. J.; Lee, N.; Fu, K. K., Postoperative Concurrent Radiotherapy and Chemotherapy for High-Risk Squamous-Cell Carcinoma of the Head and Neck. *N. Engl. J. Med.* **2004,** *350* (19), 1937-1944.

55. Udagawa, H., Chemoradiotherapy: Its effectiveness tocivity and perspective in the treatment of esophageal cancer. *Ann. Thorac. Cariovasc. Surg.* **2009,** *15* (6), 359-361.

56. Heidel, J.; Davis, M., Clinical Developments in Nanotechnology for Cancer Therapy. *Pharm. Res.* **2011,** *28* (2), 187-199.

57. Peer, D.; Karp, J. M.; Hong, S.; Farokhzad, O. C.; Margalit, R.; Langer, R., Nanocarriers as an emerging platform for cancer therapy. *Nat Nano* **2007,** *2* (12), 751-760.

58. Jin, C.; Bai, L.; Wu, H.; Liu, J.; Guo, G.; Chen, J., Paclitaxel-loaded poly(D,L-lactide-co-glycolide) nanoparticles for radiotherapy in hypoxic human tumor cells in vitro. *Cancer Biol. Ther.* **2008,** *7* (6), 911-916.

59. Wang, A. Z.; Yuet, K.; Zhang, L.; Gu, F. X.; Huynh-Le, M.; Radovic-Moreno, A. F.; Kantoff, P. W.; Bander, N. H.; Langer, R.; Farokhzad, O. C., ChemoRad Nanoparticles: a novel multifunctional nanoparticle platform for targeted delivery of concurrent chemoradiation. *Nanomedicine (London)* **2010,** *5* (3), 361-368.

60. Werner, M. E.; Copp, J. A.; Karve, S.; Cummings, N. D.; Sukumar, R.; Li, C.; Napier, M. E.; Chen, R. C.; Cox, A. D.; Wang, A. Z., Folate-Targeted Polymeric Nanoparticle

Formulation of Docetaxel Is an Effective Molecularly Targeted Radiosensitizer with Efficacy Dependent on the Timing of Radiotherapy. *ACS Nano* **2011,** *5* (11), 8990-8998.

61. Werner, M. E.; Karve, S.; Sukumar, R.; Cummings, N. D.; Copp, J. A.; Chen, R. C.; Zhang, T.; Wang, A. Z., Folate-Targeted Nanoparticle Delivery of Chemo-and radiotherapeutics for the treatment of ovarian cancer peritoneal metastasis. *Biomaterials* **2011,** *32* (33), 8548-8554.

62. Zhang, X.; Yang, H.; Gu, K.; Chen, J.; Rui, M.; Jiag, G.-L., In vitro and in vivo study of a nanoliposomal cisplatin as a radiosensitizer. *Int. J. Nanomed.* **2011,** *6*, 437-444.